THERMODYNAMIC PROPERTIES OF Na-Al-O, Ni-Al-O, AND Fe-Al-O SYSTEMS

By

FAWZI ABDELKADER ABDELLATIEF ELREFAIE

A Thesis

Submitted to the School of Graduate Studies

in Partial Fulfilment of the Requirements

for the Degree

Doctor of Philosophy

McMaster University

October, 1979

THERMODYNAMIC PROPERTIES

OF Na-Al-O, Ni-Al-O, AND Fe-Al-O SYSTEMS

DOCTOR OF PHILOSOPHY (1979) McMASTER UNIVERSITY
(Metallurgy) (Hamilton, Ontario)

TITLE: Thermodynamic properties of Na-Al-O, Ni-Al-O, and Fe-Al-O systems

AUTHOR: Fawzi Abdelkader Abdellatief Elrefaie,
B. Met. Eng., Hons.
(Cairo University, Egypt)

SUPERVISOR: Professor W.W. Smeltzer

NUMBER OF PAGES: xx, 263

ABSTRACT

Before utilizing the two phase mixture of β- and α-Al_2O_3 as solid electrolytes in oxygen probes that can monitor very low oxygen potentials, the chemical stability of β-Al_2O_3($Na_2O \cdot 11Al_2O_3$) was studied by determining the sodium oxide activity in α-Al_2O_3, β-Al_2O_3 coexistence using electrochemical cells of the type

$$Pt|W_{(s)},WS_{2(s)},Na_2S_{(s)}|\beta\text{- and }\alpha\text{-}Al_2O_3|M_{(s)},M_xO_{(s)}|Pt$$

where M stands for Cu, Ni or Fe. The over-all cell reaction for these cells can be written as

$$W_{(s)} + 2Na_2S_{(s)} + M_xO_{(s)} = 2Na_2O_{(\beta)} + WS_{2(s)} + xM_{(s)}$$

By considering the following reaction

$$Na_2O_{(\beta)} = 2Na_{(g)} + \frac{1}{2}O_{2(g)}$$

the measured values of Na_2O activity in α-Al_2O_3,β-Al_2O_3 coexistence were used to evaluate the variation of sodium vapor pressure over this coexistence, $P_{Na(\alpha-\beta)}$, with temperature and oxygen pressure. The results indicate that $P_{Na(\alpha-\beta)}$ reaches one atmospheric pressure at 1076°C in environments with Al,Al_2O_3(α) imposed-oxygen potentials, and at 1834°C in atmospheres with Fe,FeO imposed-oxygen potentials.

The activities of Na_2O in Al,Na,β-Al_2O_3 coexistence and β-Al_2O_3,β"-Al_2O_3 equilibria were also determined using the fol-

lowing cells

$$Ta|Al_{(s \text{ or } \ell)},Na_{(\ell)}|\beta\text{-}Al_2O_3|NiO_{(s)},Ni_{(s)}|Pt|Ta,$$

and

$$Pt|W_{(s)},WS_{2(s)},Na_2S_{(s)}|\beta\text{- and }\beta''\text{-}Al_2O_3|Ni_{(s)},NiO_{(s)}|Pt,$$

respectively. The results obtained as well as the available thermodynamic data in the literature for the Na-Al-O system were used to partially represent the equilibrium oxygen pressure diagram of Na-Al-O system at 1000K.

To establish the reliability of using the two phase mixture of β- and α-Al_2O_3 as a solid electrolyte in oxygen probes, galvanic cells using solid electrolyte tubes fabricated from this mixture with electrodes of fixed oxygen chemical potentials were developed. Experimental results indicated that this solid electrolyte responded reversibly to oxygen potentials as high as those of Cu,Cu_2O equilibria between 600°C and 1000°C, and as low as those of $Al,\alpha\text{-}Al_2O_3,\beta\text{-}Al_2O_3$ coexistence between 550°C and 800°C.

The thermodynamic parameters and phase compositions in the Ni-Al-O and Fe-Al-O systems at temperatures in the range 850°C-1150°C have been also investigated using electrochemical technique, electron microprobe analyses, and X-ray powder diffraction studies. Results showed that, about one ppm of Al in Ni or Fe is sufficient to stabilize α-Al_2O_3. Electrochemical cells with calcia stabilized zirconia as solid electrolyte and working electrodes of the type Ni(or Fe)-Al alloy, $Al_2O_{3(\alpha)}$ had

shown electrical instability which was not amenable to correction by coulometric disturbance or by temperature cycling. When β- and α-Al_2O_3 solid electrolyte was used in combination with Ni (or Fe)-Al,$Al_2O_{3(\alpha)}$ electrodes, steady and reproducible potentials were measured at 940°C which enabled the equilibrium oxygen pressures over these electrodes to be calculated. The values obtained for the oxygen pressures were outside the electrolytic domain of calcia stabilized zirconia which explain the instability problems of cells with this electrolyte.

Quantitative results have been obtained for the phase compositions in the ternary systems Ni-Al-O, and Fe-Al-O. These results have been used to construct the 1000°C Ni-Al-O isotherm, and to modify and extend the NiO-Al_2O_3 quasibinary system given previously in the literature. The equilibrium oxygen pressure diagrams of the Ni-Al-O and Fe-Al-O systems have been constructed at 1000°C based on the results of this investigation as well as the available data in the literature.

ACKNOWLEDGMENTS

I wish to thank my supervisor, Dr. W. W. Smeltzer, for suggesting the problems considered here and for his continuous guidance, help and encouragement throughout the course of this study. The interest and encouragement shown by Dr. D.A.R. Kay and Dr. O.E. Hileman, Jr., who both were members of the supervisory committee, is gratefully acknowledged. I am indebted to my wife, Mrs. H.Z. Elrefaie, for her limitless help, support, and assistance.

Thanks are also due to the staff of the Department of Metallurgy and Materials Science, post-doctoral fellows, and graduate students. The invaluable technical advice and help of the technical staff in the department is greatly appreciated. The thesis was typed with skill and very remarkable patience by Mrs. H. Kennelly, to whom I give special thanks.

The author gratefully acknowledges the Department of Metallurgy and Materials Science and the Aluminum Company of Canada for their financial support for this project.

TABLE OF CONTENTS

		Page
ABSTRACT		iii
ACKNOWLEDGEMENTS		vi
TABLE OF CONTENTS		vii
LIST OF ILLUSTRATIONS		xii
LIST OF TABLES		xviii
CHAPTER 1	INTRODUCTION	1
CHAPTER 2	REVIEW OF THE THEORMODYNAMICS OF Ni-Al-O, Fe-Al-O, and $Na_2O.Al_2O_3$-Al_2O_3 SYSTEMS	5
2.1	The Nickel-Oxygen System	5
2.2	The Aluminum-Oxygen System	6
2.3	The Nickel-Aluminum System	7
2.4	Nickel Oxide-Aluminum Oxude System	10
2.5	The Iron-Oxygen System	15
2.6	The Aluminum-Iron System	19
2.7	The Iron-Aluminum-Oxygen System	21
2.8	Sodium Aluminate-Aluminum Oxide System	23
CHAPTER 3	APPLICATIONS OF SOLID ELECTROLYTES TO HIGH TEMPERATURE-THERMODYNAMIC MEASUREMENTS	32
3.1	Introduction	32
3.2	Electrical Conductivity, Transference Number, and Electrolytic Domain of a Solid Electrolyte	32
3.3	Calcia Stabilized Zirconia	35
3.4	Beta-Alumina ($Na_2O.11Al_2O_3$)	43
3.5	Solid Electrolyte-Electrochemical Cell Design for High Temperature Thermodynamic Measurements	46

			Page
	3.6	Limitations and Experimental Considerations in the Use of Solid State Galvanic Cells	52
	3.6.1	Electronic Conduction in the Electrolyte	52
	3.6.2	Maintaining a Fixed Chemical Potential at the Electrode-Electrolyte Interface	53
	3.6.3	Experimental Uncertainties	54
	3.6.4	Experimental Considerations	54
	3.7	Summary	56
CHAPTER 4		EXPERIMENTAL TECHNIQUES	57
	4.1	Materials	57
	4.2	Solid-Electrolyte Tube Fabrication	60
	4.3	Sample Preparation	71
	4.3.1	Aluminum, α-Alumina, β-Alumina System	71
	4.3.2	Nickel Oxide-Aluminum Oxide System	73
	4.3.3	Nickel-Aluminum-Oxygen System	74
	4.3.4	Iron-Aluminum-Oxygen System	78
	4.3.5	Nickel-Aluminum and Iron-Aluminum Systems	81
	4.4	Metallography	81
	4.5	Wet Chemical Analyses	82
	4.6	X-ray Analyses	82
	4.7	Electron Probe Analysis	82
	4.8	The Electrochemical Cells "Design and Operation"	88
CHAPTER 5		STABILITY OF THE FAST IONIC CONDUCTING PHASES, β- and β"-Al_2O_3, IN $NaAlO_2$-Al_2O_3 SYSTEM	105
	5.1	Introduction	105
	5.2	Experimental Results	107

			PAGE
	5.2.1	Chemical Equilibration	107
	5.2.2	EMF Results	107
	5.3	Discussion	114
	5.3.1	Sodium Oxide Activity in Al, α-Al_2O_3, β-Al_2O_3 Coexistence	114
	5.3.2	Sodium Oxide Activity in α-Al_2O_3, β-Al_2O_3 Coexistence	122
	5.3.3	Sodium Oxide Activity in Al, Na, β-Al_2O_3 Coexistence	131
	5.3.4	Sodium Oxide Activity in β-Al_2O_3, β"-Al_2O_3 Coexistence	132
	5.4	The Equilibrium Oxygen Pressure Diagram for Na-Al-O System at 1000 K	133
CHAPTER 6		EMF MEASUREMENTS ON CELLS INVOLVING A MIXTURE OF BETA AND ALPHA ALUMINA AS SOLID ELECTROLYTE WITH ELECTRODES FIXING OXYGEN CHEMICAL POTENTIALS "RESULTS AND DISCUSSION"	137
	6.1	Introduction	137
	6.2	Electrochemical Cell Measurements	138
	6.3	Discussion	149
	6.4	Summary	160
CHAPTER 7		NICKEL-ALUMINUM-OXYGEN SYSTEM "RESULTS AND DISCUSSION"	161
	7.1	Electrochemical Cell Measurements	161
	7.2	Metallography	165
	7.3	X-ray Analysis	177
	7.4	Electron Probe Microanalyses	177
	7.5	Discussion	190

			PAGE
	7.5.1	Nickel Oxide-Aluminum Oxide System	190
	7.5.2	Nickel-Aluminum-Oxygen Isotherm at 1000°C	194
	7.5.3	Cell Electromotive Force Analyses	197
	7.5.4	Free Energy of Formation of Nickel Spinel	199
	7.5.5	Thermodynamic Properties of Nickel-Aluminum Alloys	202
	7.5.6	Equilibrium Oxygen Pressure Diagram for Ni-Al-O System at 1000°C	203
CHAPTER 8		IRON-ALUMINUM-OXYGEN SYSTEM "RESULTS AND DISCUSSION"	207
	8.1	Electrochemical Cell Measurements	207
	8.2	Metallography	212
	8.3	The Electron Microprobe Analyses	215
	8.4	Discussion	222
	8.4.1	Introduction	222
	8.4.2	Standard Free Energy of Formation of $FeAl_2O_4$	224
	8.4.3	Thermodynamic Properties of Fe-Al Alloys	227
	8.4.4	The Equilibrium Oxygen Pressure Diagram of Fe-Al-O System at 1000°C	228
CHAPTER 9		GENERAL DISCUSSION AND CONCLUSIONS	235
	9.1	Stability of β-Al_2O_3	235
	9.2	β- and α-Al_2O_3 Mixture as Solid Electrolyte for Oxygen Probe	239
	9.3	Aluminum, α-Alumina, β-Alumina Equilibrium	244

		PAGE
9.4	The Equilibrium Oxygen Pressure Diagram of Na-Al-O System at 1000K	246
9.5	Nickel Oxide-Aluminum Oxide System	247
9.6	Nickel-Aluminum-Oxygen Isotherm at 1000°C	248
9.7	Iron-Aluminum-Oxygen System	249
9.8	Nickel-Nickel Oxide-Spinel Phase Field	249
9.9	Iron-Wustite-Spinel Phase Field	250
9.10	Nickel-Spinel-Aluminum Oxide Phase Field	251
9.11	Iron-Spinel-Aluminum Oxide Phase Field	252
9.12	Nickel (or Iron)-Aluminum Alloy, Aluminum Oxide Coexistence	252
9.13	Equilibrium Oxygen Pressure Diagram for Ni-Al-O System at 1000°C	255
9.14	Equilibrium Oxygen Pressure Diagram for Fe-Al-O System at 1000°C	255
REFERENCES		257

LIST OF ILLUSTRATIONS

FIGURE	SUBJECT	PAGE
2-1	Al-Ni system (8).	8
2-2	Activity data in Ni-Al binary system at 1000°C (28).	11
2-3	Free energy of mixing in the Al-Ni system at 1000°C (29).	12
2-4	Equilibrium diagram for the system $NiO-Al_2O_3$ (31).	13
2-5	Equilibrium diagram for the system $NiO-Al_2O_3$ (32).	14
2-6	The Fe-O phase diagram (35,36).	16
2-7	Variation of wustite composition with O_2 pressure and temperature.	18
2-8	Fe-Al system (8).	20
2-9	Change in O_2 partial pressure and its effect on subsolidus equilibria in $Fe_2O_3-Al_2O_3$ system (48).	22
2-10	Fe-Al-O isotherms proposed in reference (49) at 1000°C (a), 1250°C (b), and 1350°C (c).	24
2-11	$NaAlO_2-Al_2O_3$ system as proposed by De Vries and Roth (63).	29
2-12	Equilibrium diagram for the system $NaAl_2O_2-Al_2O_3$ (65).	31
3-1	Schematic representation of concentration of ionic and electronic defects as a function of P_{X_2} for the hypothetical compound MX_2.	36
3-2	Schematic representation of the electrical conductivity for the hypothetical compound MX_2.	37
3-3	Schematic representation of ionic transference number for the MX_2 compound.	38

FIGURE	SUBJECT	PAGE
3-4	Electrolytic domains of ZrO_2(+CaO) and ThO_2(+$YO_{1.5}$).	38
3-5	Conductivity of ZrO_2(+CaO) as function of composition (81).	41
3-6	Crystal structure of β-Al_2O_3 as proposed by Beevers and Ross (59).	44
3-7	Ionic arrangement in loosely packed layer of β-Al_2O_3.	45
3-8	Non-separate electrode assembly (6,7).	48
3-9	H-type electrochemical cell (90).	48
3-10	Separate electrode assembly, designed by using a solid electrolyte tube (91).	49
3-11	Separate electrode assembly designed by pressing one side of the electrolyte against a polished end of an alumina tube (91).	49
3-12	Electrochemical cell assembly, designed for use with dynamic vacuum on both electrode compartments, utilizing a calcia stabilized zirconia tube (40).	50
3-13	Electrochemical cell assembly, designed for use with static vacuum in the inner compartment, utilizing a calcia stabilized zirconia tube (92).	51
4-1	Dimensions of a typical plaster mould.	66
4-2	The appearance of five β- and α-Al_2O_3 green tubes after removing from the plaster moulds,	68
4-3	A composite photograph illustrating the arrangement of the green tubes inside the α-Al_2O_3 crucible prepared for sintering the tubes.	69
4-4	The temperature-time curve for a typical sintering run of the ceramic tubes at 1800°C.	70

FIGURE	SUBJECT	PAGE
4-5	5 sintered-electrolyte tubes of β- and α-Al_2O_3; the tubes were sintered at 1800°C for 3 hours.	72
4-6	The electrochemical cell assembly utilizing β- and α-Al_2O_3 solid electrolyte tube.	96
4-7	The potential decay curve obtained at 650°C for cell (6-V).	102
4-8	The potential decay curve obtained at 725°C for cell (6-VI).	103
5-1	Variation of emf with temperature for cell (5-I)	111
5-2	Variation of emf with temperature for cell (5-II).	112
5-3	Variation of emf with temperature for cell (5-III).	113
5-4	Variation of emf with temperature for cell (5-IV).	118
5-5	Variation of emf with temperature for cell (5-V).	119
5-6	The equilibrium oxygen pressure diagram of Na-Al-O system at 1000 K.	136
6-1	Variation of emf with temperature for cell (6-I)	144
6-2	Variation of emf with temperature for cell (6-II).	145
6-3	The dependence of emf on temperature for cell (6-III).	146
6-4	Variation of emf with temperature for cell (6-VI).	147
6-5	The variation of the emf with temperature for cells (6-V) and (6-VI).	148
6-6	Temperature dependence of emf for Ni,NiO||Cu_2O, Cu cell.	150

FIGURE	SUBJECT	PAGE
6-7	Temperature dependence of emf for Fe,FeO||NiO, Ni cell.	151
7-1	The variation of emf with temperature for cell (7-I).	163
7-2	The variation of emf with temperature for cell (7-II).	164
7-3	Photograph showing the upper surface (a), the lower surface (b), and the cross section (c) of air annealed NiO-$NiAl_2O_4$ tablet at 1600°C.	167
7-4	Photograph showing the surface and the cross section of NiO-$NiAl_2O_4$ pellet after annealing at 1800°C in argon atmosphere for 20 hours.	168
7-5	Photograph showing the upper surface (a) and the lower surface (b) of air annealed NiO-$NiAl_2O_4$ at 1800°C.	169
7-6	Photograph showing the surface and the cross section of air annealed spinel-$Al_2O_{3(\alpha)}$ tablet at 1700°C.	170
7-7	Photograph showing the contact region of α-Al_2O_3 crucible with spinel-$Al_2O_{3(\alpha)}$ pellet after air annealing at 1700°C.	171
7-8	The contact region of the α-Al_2O_3 crucible with NiO-$NiAl_2O_4$ pellet after air annealing at 1700°C.	172
7-9	The surface and the cross section of spinel-$Al_2O_{3(\alpha)}$ tablet after annealing at 1800°C under argon atmosphere for 14 hours.	173
7-10	The surface and the cross section of spinel-$Al_2O_{3(\alpha)}$ tablet after annealing at 1920°C in argon atmosphere for three hours.	174
7-11	a) Scanning electron micrograph of the Ni,spinel,$Al_2O_{3(\alpha)}$ sample. b) Ni-K_α radiation mapping. c) Al-K_α radiation mapping.	175
7-12	a) Scanning electron micrograph of the 0.15 a/o Al-Ni alloy, $Al_2O_{3(\alpha)}$ sample. b) Ni-K_α radiation mapping c) Al-K_α radiation mapping.	176

FIGURE	SUBJECT	PAGE
7-13	Micriprobe scan along the cross section of air annealed NS16 tablet.	185
7-14	Microprobe scan along the cross section of spinel-$Al_2O_{3(\alpha)}$ pellet annealed at 1700°C.	186
7-15	Microprobe scan along the surface of annealed NS18AR sample.	187
7-16	Ni and Al profiles obtained from the surface (a) and the cross section (b) of annelaed SA18AR tablet.	188
7-17	Electron microprobe scan obtained from the cross section of annealed SA19AR pellet.	189
7-18	Equilibrium diagram for the system $NiO-Al_2O_3$.	193
7-19	Al-Ni-O isotherm at 1000°C.	196
7-20	Equilibrium oxygen pressure diagram for Ni-Al-O system at 1000°C.	206
8-1	Variation of emf with temperature for cell (8-I)	209
8-2	Variation of emf with temperature for cell (8-II).	210
8-3	Variation of emf with temperature for cell (8-III).	211
8-4	a) Scanning electron micrograph of the Fe, wustite,spinel sample that annealed at 1000°C. b) Fe-K_α radiation mapping. c) Al-K_α radiation mapping.	213
8-5	a) Scanning electron migrograph of the IA0.1A sample. b) Fe-K_α radiation mapping. c) Al-K_α radiation mapping.	214
8-6	Microprobe scan along the sample.	216

FIGURE	SUBJECT	PAGE
8-7	The equilibrium oxygen pressure diagram for Fe-Al-O system at1000°C.	232
9-1	The variation of $P_{Na(\alpha-\beta)}$ with temperature and oxygen pressure.	238
9-2	The free energy of formation of nickel spinel from NiO and Al_2O_3.	253

LIST OF TABLES

TABLE	TITLE	PAGE
4-1	Materials used in this investigation	58
4-2	Synthesis of β''-Al_2O_3 from α-Al_2O_3 and Na_2CO_3 mixture as determined by X-ray diffraction analysis	61
4-3	Starting materials used in preparing suspensions for slip casting the ceramic tubes	65
4-4	Annealing conditions of NiO-$NiAl_2O_4$ and spinel-$Al_2O_{3(\alpha)}$ samples	75
4-5	Starting composition of mixtures belonging to Ni-Al-O system	77
4-6	Starting constituents of mixture belonging to Fe-Al-O system	79
4-7	Wet chemical analyses of Ni-Al alloys	83
4-8	Wet chemical analyses of Fe-Al alloys	84
4-9	The electron probe results for the Ni-Al alloys	86
4-10	The electron probe results for the Fe-Al alloys	87
4-11	The purposes and the cell reactions of the electrochemical cells that designed in this investigation.	90
5-1	Sodium contents in the metallic phase of the coexistence Al,α-Al_2O_3,β-Al_2O_3	108
5-2	The variation of cell emf with temperature for cell (5-I), cell (5-II), and cell (5-III)	109
5-3	Least squares analyses of emf data from cells (5-I), (5-II), and (5-III)	110
5-4	Variation of cell emf with temperature for cell (5-IV)	116
5-5	Emf data for cell (5-V)	117
5-6	Data used in calculating $\Delta G^o_f(\beta\text{-}Al_2O_{3(s)})$	117
5-7	The standard free energy of formation of β-Al_2O_3	121

TABLE	TITLE	PAGE
5-8	The activity of sodium oxide in the equilibrium Al, α-Al_2O_3, β-Al_2O_3	121
5-9	Thermochemical data used in this investigation	124
5-10	The variation of cell emf with temperature for cell (5-VII)	129
5-11	The dependence of emf on temperature for cell (5-VIII)	129
6-1	The emf-temperature data for cells (6-I) and (6-II)	140
6-2	Least squares analyses of the emf data of cell (6-I) and cell (6-II)	141
6-3	The emf-temperature data for cells (6-III) and (6-IV)	141
6-4	The emf-temperature data for cells (6-V) and (6-VI)	142
6-5	Least squares analyses of emf data of cells (6-III), (6-IV), (6-V), and (6-VI)	143
6-6	The free energy of formation of nickel spinel from $NiO_{(s)}$ and $Al_2O_{3(\alpha)}$ (33)	153
7-1	The dependence of emf on temperature for cells (7-I) and (7-II)	162
7-2	X-ray powder diffraction results of annealed samples from NiO-Al_2O_3 system	178
7-3	Electron probe results for samples from NiO-Al_2O_3 system	180
7-4	Electron probe results for samples from Ni-Al-O system	183
7-5	Phase relations in NiO-Al_2O_3 system over the temperature range 1000°C-1900°C	192
7-6	The activities of the aluminum of the alloy of the invariant system Ni-spinel-$Al_2O_{3(\alpha)}$	200
7-7	Dissociation of α-Al_2O_3 in equilibrium with Ni-Al alloys at 1000°C.	205

TABLE	TITLE	PAGE
8-1	Variation of cell emf with temperature for cells (8-I), (8-II), and (8-III)	208
8-2	Emf-T relations obtained for cell (8-I), cell (8-II) and cell (8-III)	208
8-3	Electron microprobe analyses for Fe-Al-O samples	217
8-4	The composition data of iron spinel equilibrated with wustite and iron	221
8-5	The equilibrium oxygen pressures over HSA, WSI, and SAI electordes	223
8-6	Activities of Al of the alloy phase which is in equilibrium with $FeAl_2O_4$ and α-Al_2O_3	226
8-7	The standard free energy of formation of $FeAl_2O_4$	226
8-8	The thermodynamic functions of Al in Fe-Al solid alloys (referred to liquid aluminum)	229
8-9	Dissociation pressure of α-Al_2O_3 in equilibrium with Fe-Al alloys at 1000°C	231

CHAPTER 1

INTRODUCTION

Metals and alloys are essential structural materials because of their excellent formability, mechanical strength and corrosion resistance. Iron, nickel, cobalt and chromium alloys serve as structural materials up to 1000°C in oxidizing atmospheres. The corrosion resistance of these alloys is improved by the addition of aluminum as an alloying element and by alloy coatings containing aluminum to the extent that they may be utilized at temperatures up to 1200°C.

An essential problem in developing these alloys is associated with improvements in their mechanical and corrosion properties. Accordingly, basic thermodynamic data of the alloy-environment systems are of great importance. From thermodynamic data one can predict the nature and number of phases that are stable in a system under specified conditions while the rate of formation of these phases is a kinetic problem. Several models have been developed for diffusion-controlled binary alloy oxidation (1-5). Thermodynamic data as well as phase compositions of the M_1-M_2-O systems are essential parameters in these models.

One of the useful methods for determining thermodynamic data is the electromotive force (emf) technique. Providing that the temperature and pressure are constant and the electrolyte

behaves ionically, the thermodynamics of the cell reaction can be determined by the basic principles of electrochemistry when a reversible potential between the electrodes is measured. The emf technique was limited to low temperatures because it was difficult to obtain a suitable electrolyte at elevated temperatures until about two decades ago, when Kiukkola and Wagner (6,7) introduced calcia stabilized zirconia, ZrO_2(+CaO), as a solid electrolyte. This electrolyte behaves ionically over a wide range of temperatures and oxygen pressures. New solid electrolytes as well as several applications in thermodynamics, kinetics, and controlling processes have been developed since that time. Wagner* has pointed out that high temperature thermodynamic functions obtained from solid electrolyte electrochemical measurements may be more reliable in some cases than those calculated by combining calorimetric measurements at 25°C with high-temperature enthalpy increments.

The main purpose of this work is the evaluation of the thermodynamic parameters of the Ni-rich corner and the Fe-rich corner of the Ni-Al-O and Fe-Al-O systems by using solid electrochemical cells and the determination of the phase properties of these systems up to 50 a/o Al by electron probe microanalyses.

At oxygen potentials lower than those imposed by

---

*This statement is reported in reference (99).

Cr, Cr_2O_3 equilibria, calcia stabilized zirconia shows electron conduction which limits its use as a solid electrolyte. Available thermodynamic data for the binary Ni-Al and Fe-Al systems indicate that the equilibrium oxygen pressures of coexistences of the type $Al_2O_{3(\alpha)}$, Ni(or Fe)-rich alloy are much lower than those of Cr, Cr_2O_3. The lack of an oxygen-solid electrolyte which can reversibly monitor very low oxygen potentials makes the development of a new solid electrolyte which is stable, conducts ionically, and reacts reversibly to oxygen potentials as low as those defined by $Al, Al_2O_{3(\alpha)}$ equilibria of great importance.

In this investigation, the chemical stability of β-Al_2O_3 ($Na_2O.11Al_2O_3$) was studied by determining the activity of sodium oxide in the coexistence α-Al_2O_3, β-Al_2O_3. Emf measurements using β- and α-Al_2O_3 solid electrolyte tubes and chemical equilibration techniques were used for this purpose. The activity of Na_2O in the coexistences Al, Na, β-Al_2O_3 and β-Al_2O_3, β''-Al_2O_3 was also determined by using β-Al_2O_3 and β- and β''-Al_2O_3 tubes, respectively, as solid electrolytes in galvanic cells. The experimental results obtained in this investigation as well as the data available in the literature were used to partially construct the equilibrium oxygen pressure diagram of Na-Al-O system at 1000 K.

Electromotive force measurements in our investigation were also carried out on cells involving solid electrolyte tubes

fabricated from a mixture of β- and α-Al_2O_3 together with electrodes fixing oxygen chemical potentials over the temperature range 600-900°C. The cells were designed to investigate the applicability of using this solid electrolyte to sense reversibly oxygen pressures as high as those of Cu, Cu_2O coexistence and as low as those of Al, α-Al_2O_3, β-Al_2O_3 coexistence.

Thermodynamic properties and phase compositions in Ni-Al-O and Fe-Al-O systems at temperatures in the range 850-1150°C were investigated by using galvanic cells which utilized the calcia stabilized zirconia electrolyte or the two-phase mixture of β- and α-Al_2O_3 as solid electrolyte prepared in this laboratory as tubes by slip casting and sintering techniques.

A review is presented of the thermodynamics of the Ni-Al-O, Fe-Al-O, and $Na_2O.Al_2O_3$-Al_2O_3* systems (Chapter 2), and solid electrolytes and their application to high temperature thermodynamic measurements (Chapter 3). Chapter 4 describes the experimental techniques used in the investigation. In Chapters 5, 6, 7 and 8, the experimental results and their discussion are summarized. General conclusions are formulated in Chapter 9. The energy unit used in this thesis is the calorie unless otherwise specified.

*Al_2O_3 is used to imply α-Al_2O_3.

CHAPTER 2

REVIEW OF THE THERMODYNAMICS OF Ni-Al-O, Fe-Al-O, AND $Na_2O.Al_2O_3$-Al_2O_3 SYSTEMS

2.1 The Nickel-Oxygen System

The Ni-O system has been extensively studied by numerous investigators. The results are compiled in references (8-10). The solid phases in this system are solid solution of oxygen in Ni, NiO, NiO-Ni_2O_3 solid solution, Ni_2O_3, and NiO_2 (11). NiO_2 can be prepared by heating the hydroxide to constant weight at 250-300°C in the presence of O_2 at sufficiently higher pressure. If the hydroxide or NiO_2 is heated to a constant weight in the same temperature range in air, Ni_2O_3 is the stable phase. Solid solutions of NiO in Ni_2O_3 are formed by heating NiO_2 to constant weight in air at higher temperature and over a wide temperature range. The percentage of NiO increases from 0.0 w/o at 250°C to 100 w/o at 1000°C. There have been a number of investigations to determine the vapor pressures and the heats of vaporization of solid and liquid Ni. The "best values" of the parameters in the vapor pressure equations of solid and liquid Ni, the heat of vaporization of Ni, heat of vaporization of $NiO_{(s)}$, and heats of dissociation of $NiO_{(g)}$ and $Ni_{2(g)}$ are reported (12). Steele (13) has proposed that the standard free energy of formation of NiO is given by

$$\Delta G_f^\circ(NiO_{(s)}) = -55,965+20.29T(K) \quad [900\text{-}1400K]. \quad (2.1)$$

Equation (2.1) is based on a least squares analysis of the published emf data of the cell

$$Fe,FeO|O^{--} \text{ conducting solid electrolyte}|Ni,NiO$$

2.2 The Aluminum-Oxygen System

Al_2O_3 is the only stable solid oxide in the Al-O system (14). Yanagida and Kroger (14) have reported that the high-temperature X-ray diffraction patterns previously attributed to crystalline Al_2O and AlO (15) are actually those of Al_4C_3 and $AlTaO_4$, respectively, and the melting curve observed by Baur and Brunner (16), suggesting the existence of the Al_8O_9 phase, corresponds to the pseudobinary system Al_2O_3-Al_4C_3. The existence of the aluminum suboxides AlO and Al_2O in the vapor phase is well established (17-19).

The standard free energy of formation of Al_2O_3 was determined (20) at aluminum extraction temperature using a molten-salt galvanic cell with alumina-saturated cryolite as a liquid electrolyte. Ghosh and Kay (21) have determined, recently, the standard free energy of formation of Al_2O_3 in the temperature range 1350-1550°C by studying the reaction

$$2Al_{(\ell)} + \frac{3}{2} O_{2(g)} = Al_2O_{3(\alpha)}$$

using the electrochemical cells

$$Pt_{(s)}\text{-}Al_2O_{3(s)}|Al_{(\ell)}|Al_2O_3 \text{ in liquid slag}|O_{2(g)}|Pt_{(s)}$$

and

$$C_{(s)},Al_{(\ell)}|Al_2O_{3(\alpha)}|\text{ionic oxide slag}|Al_2O_{3(\alpha)}|Fe\text{-}C_{(\ell)},CO_{(g)},C_{(s)}$$

in which the activity of Al_2O_3 in the electrolyte is unity. Choudhury (22) has combined the emf data for the solid-state galvanic cells

$$Ni_{(s)},NiF_{2(s)},NaF_{(s)}|\beta\text{-}Al_2O_3|Cu_{(s)},Cu_2O_{(s)}$$

and

$$Al_{(s)}\ |\beta\text{-}Al_2O_3|Ni_{(s)},NiF_{2(s)},NaF_{(s)}$$

in the temperature range 560-660°C and has obtained the emf values that correspond to the open-circuit emf between Al,Al_2O_3 and Cu,Cu_2O electrodes. The values of $\Delta G_f^o(Al_2O_{3(\alpha)})$ proposed by Ghosh and Kay are given by the expression

$$\Delta G_f^o(Al_2O_{3(\alpha)}) = -394,680+77.8T(K) \qquad (2.2)$$

and those determined by Choudhury are given by the relation

$$\Delta G_f^o(Al_2O_{3(\alpha)}) = -404,800+81T(K). \qquad (2.3)$$

2.3 The Nickel-Aluminum System

The aluminum-nickel system, shown in figure (2-1), is well established. Aluminum and nickel have f.c.c. structures. The atomic radius of Al is 14.9% larger than that of Ni (23). The solid solubility of Ni in Al is reported to be 0.05 w/o at 640°C (8). Up to 14 a/o of Al at 1000°C can be dissolved in Ni giving a disordered f.c.c. solid solution (γ). The lattice parameters of γ phase have been reported (24). Four intermetallic compounds are formed in this system, a γ' phase,

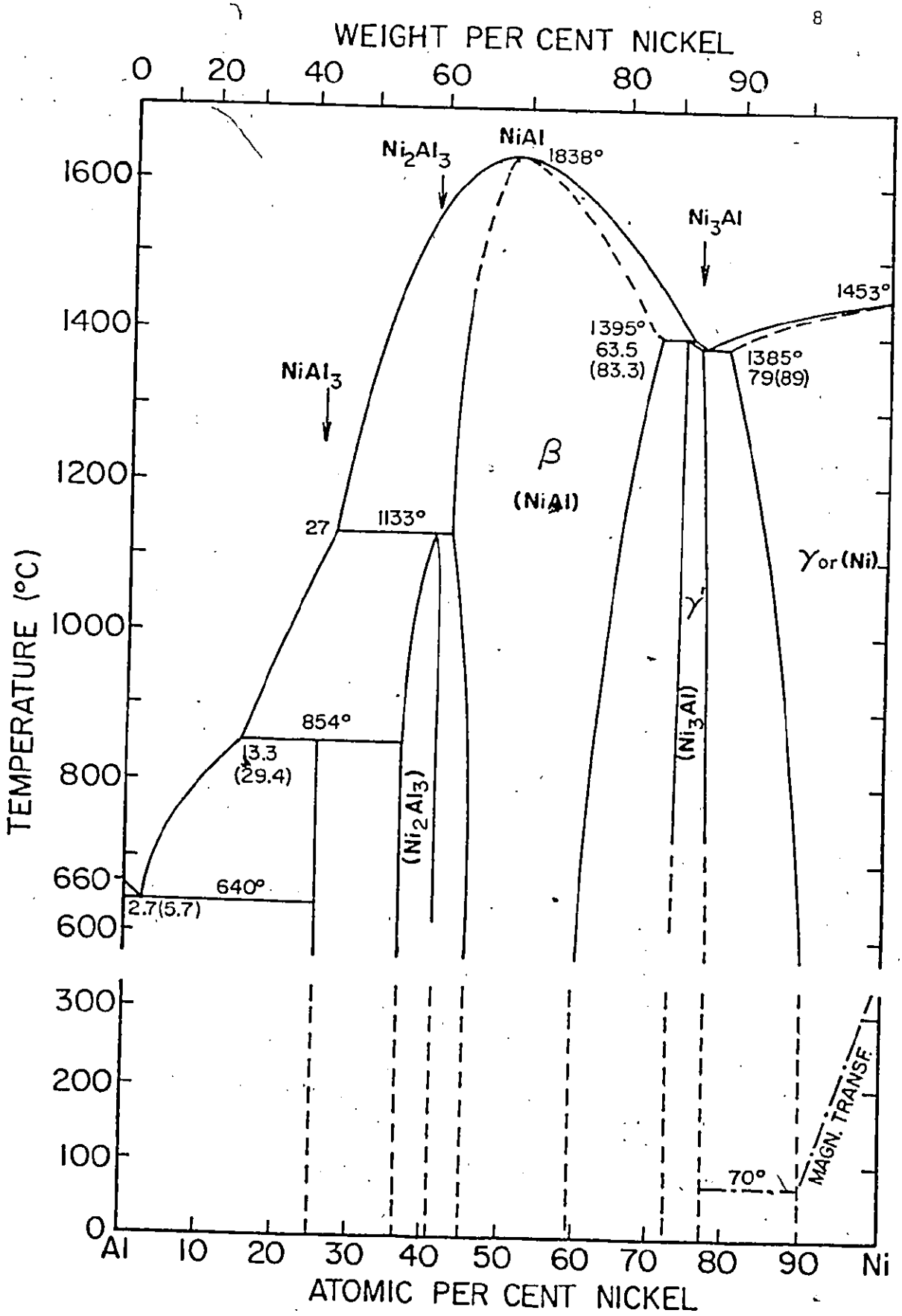

Figure (2-1) Al-Ni System (8).

based on Ni_3Al, a β phase, based on NiAl, a δ phase, based on Ni_2Al_3, and $NiAl_3$ phase. With the exception of $NiAl_3$, which has a singular composition, the other intermetallics have a range of homogeneity. The intermetallic $NiAl_3$ (42.03 w/o Ni), which is formed through a peritectic reaction at 840°C has an orthorhombic structure; the δ phase is hexagonal with $a = 4.036$ A^o and $c/a = 1.214$ at the stoichiometric composition (8). The change in the lattice parameters of the δ phase with composition has been studied by Taylor and Doyle (25). The β phase is a congruent melting compound with the highest melting point, 1638°C, in this system. It has a b.c.c. structure of the CsCl type. Taylor and Doyle (25) have measured also the change in lattice parameters of the β phase with composition using X-ray diffraction technique: the lattice parameters have the highest value at the stoichiometric composition and fall linearly within the Ni or Al-rich sides. The same investigators have claimed that the number of atoms per unit cell is 2 at the stoichiometric and Ni-rich compositions while it falls to 1.817 at the Al-rich side boundary. They concluded that on the Al-rich side vacancies are created in the Ni sites. These results are indicated also by Hughes et al. (26). The γ' phase has f.c.c. structure of the Cu_3Al type.

Activities of Al in solid Ni-Al alloys have been determined at 1000°C between 15 a/o Al and 60 a/o Al by equilibrating Ni specimens, heated in a temperature gradient,

with Al vapor in a closed system (27). The activity of Ni at 1000°C in the Ni-Al binary system has been calculated (28) from these Al-activity results using the Gibbs-Duhem equation; the activity data of both Ni and Al are shown in figure (2-2). Schaefer (29) has measured the activities of Al in Al-Ni alloys containing 0.54 to 30.04 a/o Ni using a molten salt-galvanic cell. Figure (2-3) gives the free energy of mixing in Al-Ni system at 1000°C as reported by Schaefer. The heat of formation of aluminides was determined calorimetrically (30). NiAl has the most negative heat of formation, -14,100 cal/g.atom.

2.4 Nickel Oxide-Aluminum Oxide* System

Experimental data on the phase relationships in the $NiO-Al_2O_3$ system are sparse. Figure (2-4) shows the equilibrium diagram for the system $NiO-Al_2O_3$ as proposed by Philips et al. (31). According to this diagram only one intermediate compound, nickel spinel ($Ni_{1-x}Al_{2+y}O_4$), is encountered in this system; however, the formation of another stable phase, δ_{Ni} ($NiO.13\ Al_2O_3$) has been suggested (32). Figure (2-5) shows the $NiO-Al_2O_3$ diagram as proposed by LeJus (32). The mutual solubility between NiO and Al_2O_3 is very small; according to Philips et al. (31), NiO dissolves 1 m/o Al_2O_3 at 1650°C while Al_2O_3 may not dissolve NiO. The spinel phase exhibits a range of homogeneity. The spinel/(spinel+NiO) limit is at 50 m/o Al_2O_3 and is independent of temperature. Al_2O_3 is partially soluble in the spinel; however, the spinel/(spinel+Al_2O_3) limit is not well established.

*Unless otherwise specified, aluminum oxide implies α-Al_2O_3.

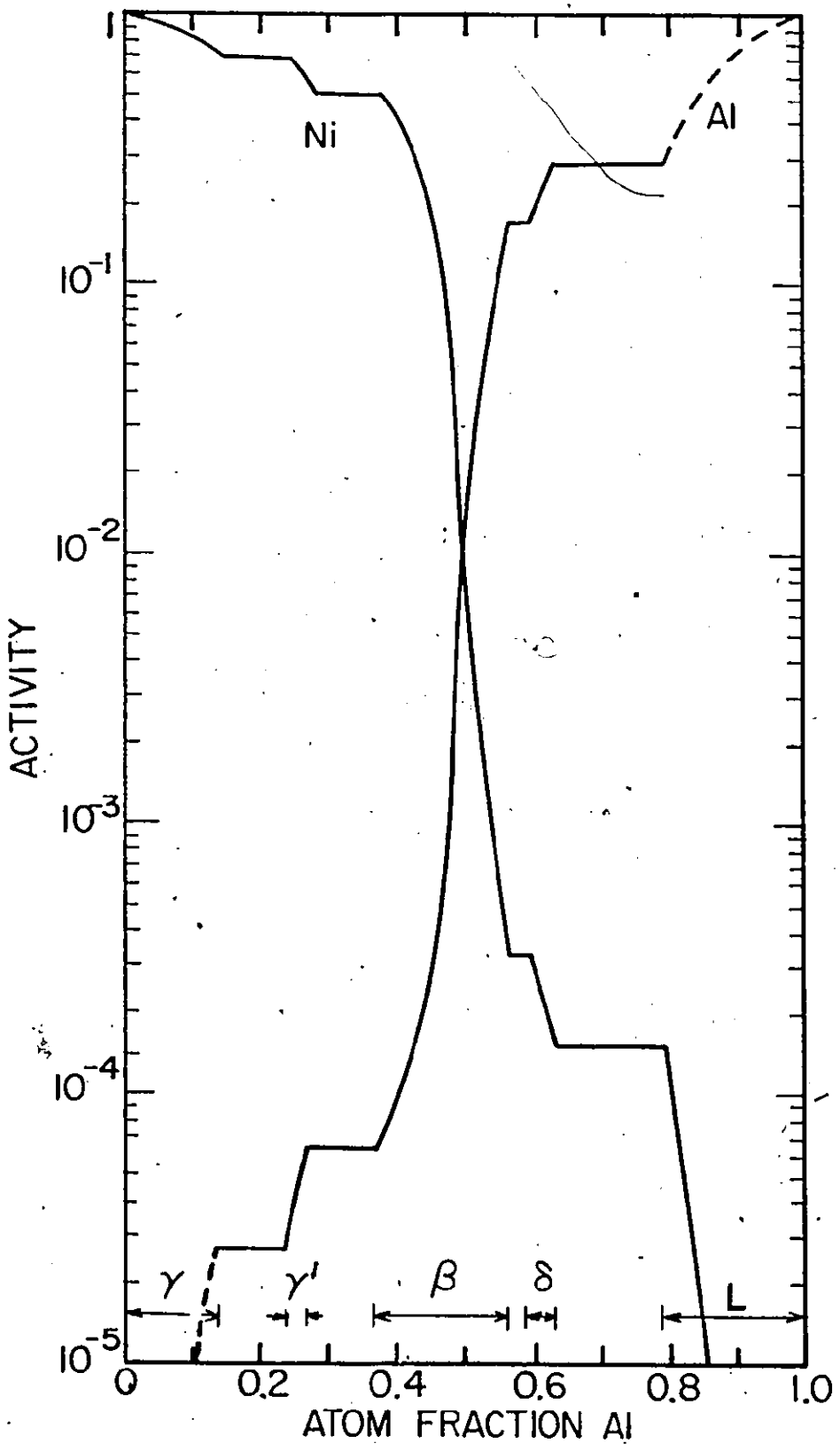

Figure (2-2) Activity data in Ni-Al binary system at 1000°C (28).

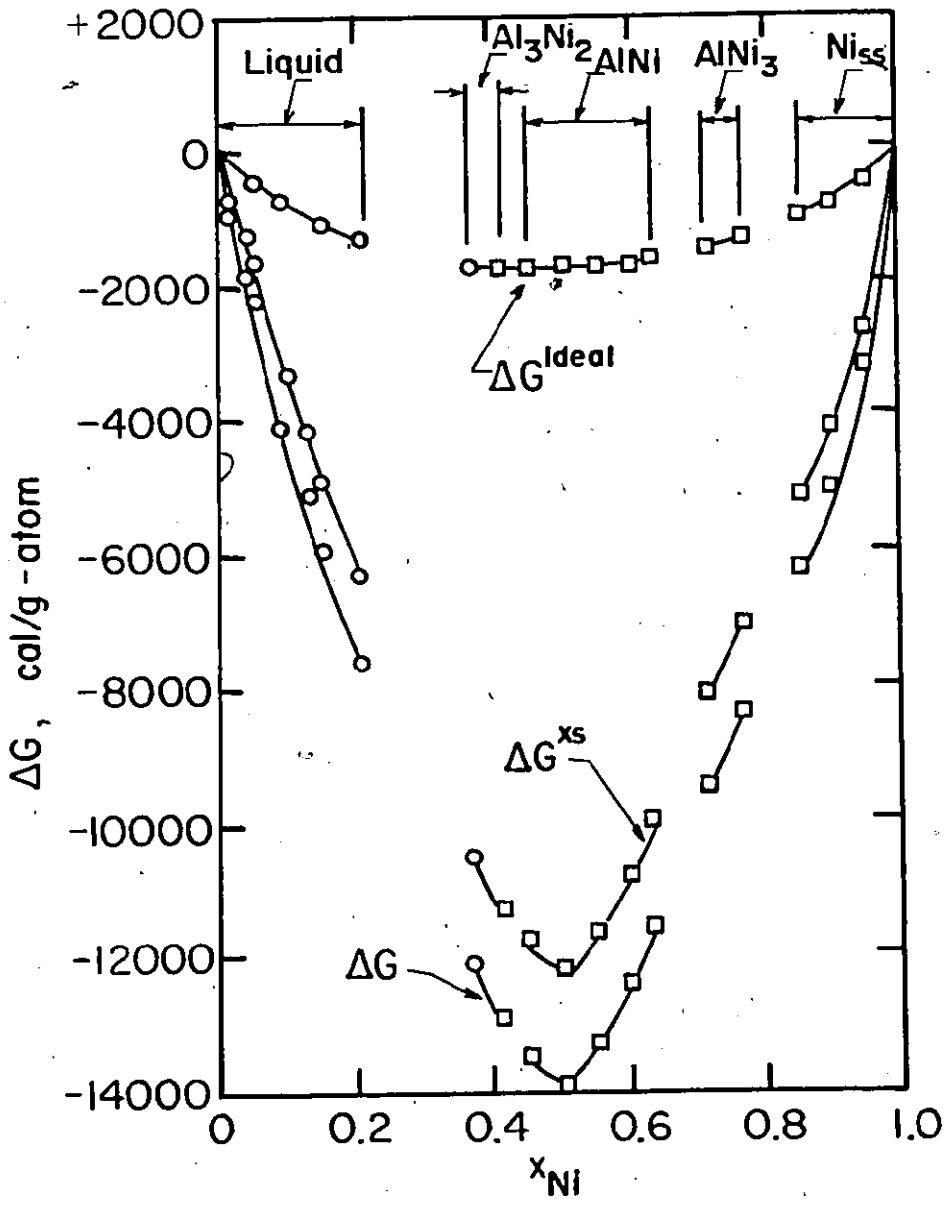

Figure (2-3) Free energy of mixing in the Al-Ni system at 1000°C (49).

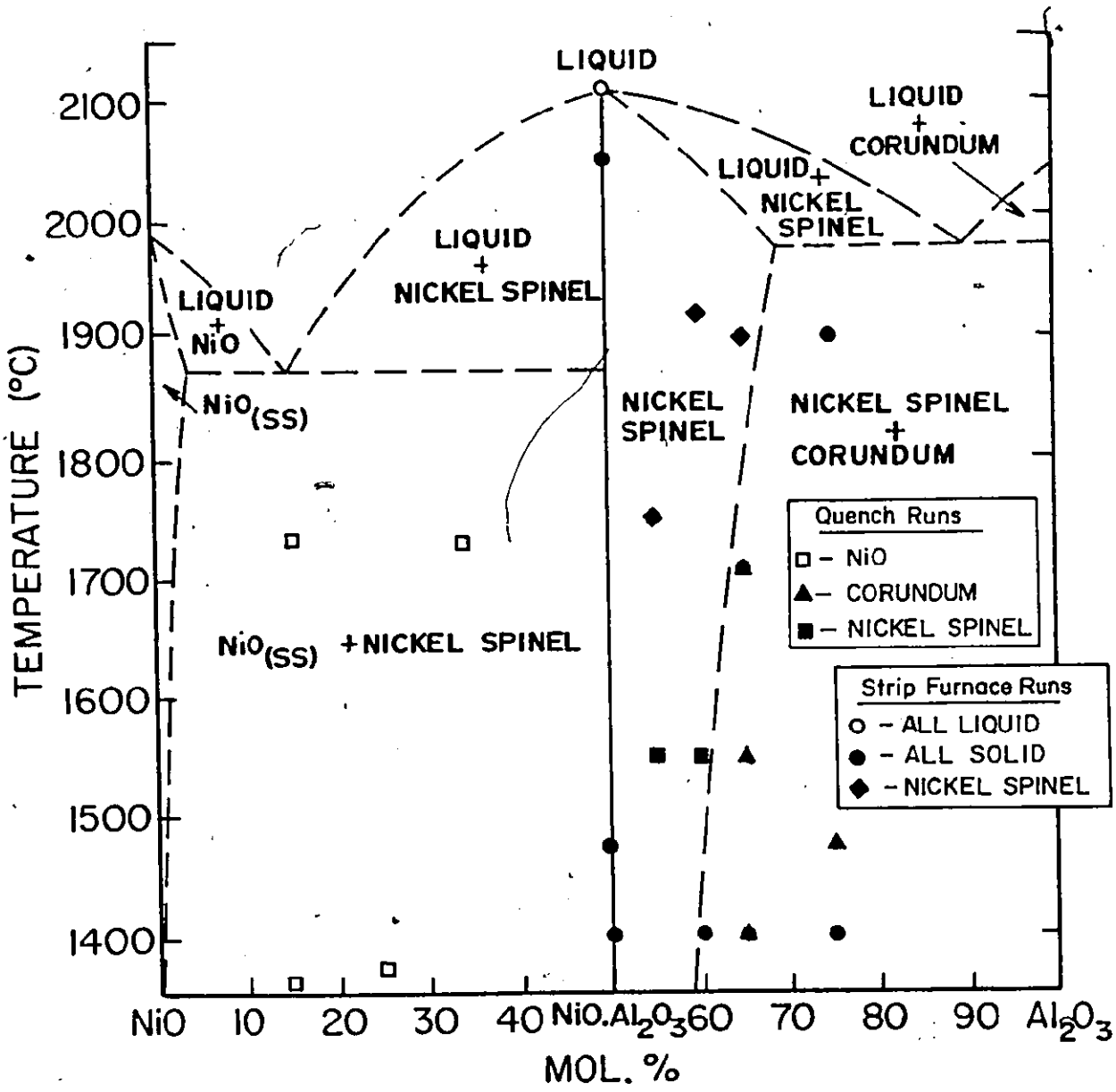

Figure (2-4) Equilibrium diagram for the system $NiO-Al_2O_3$ (31).

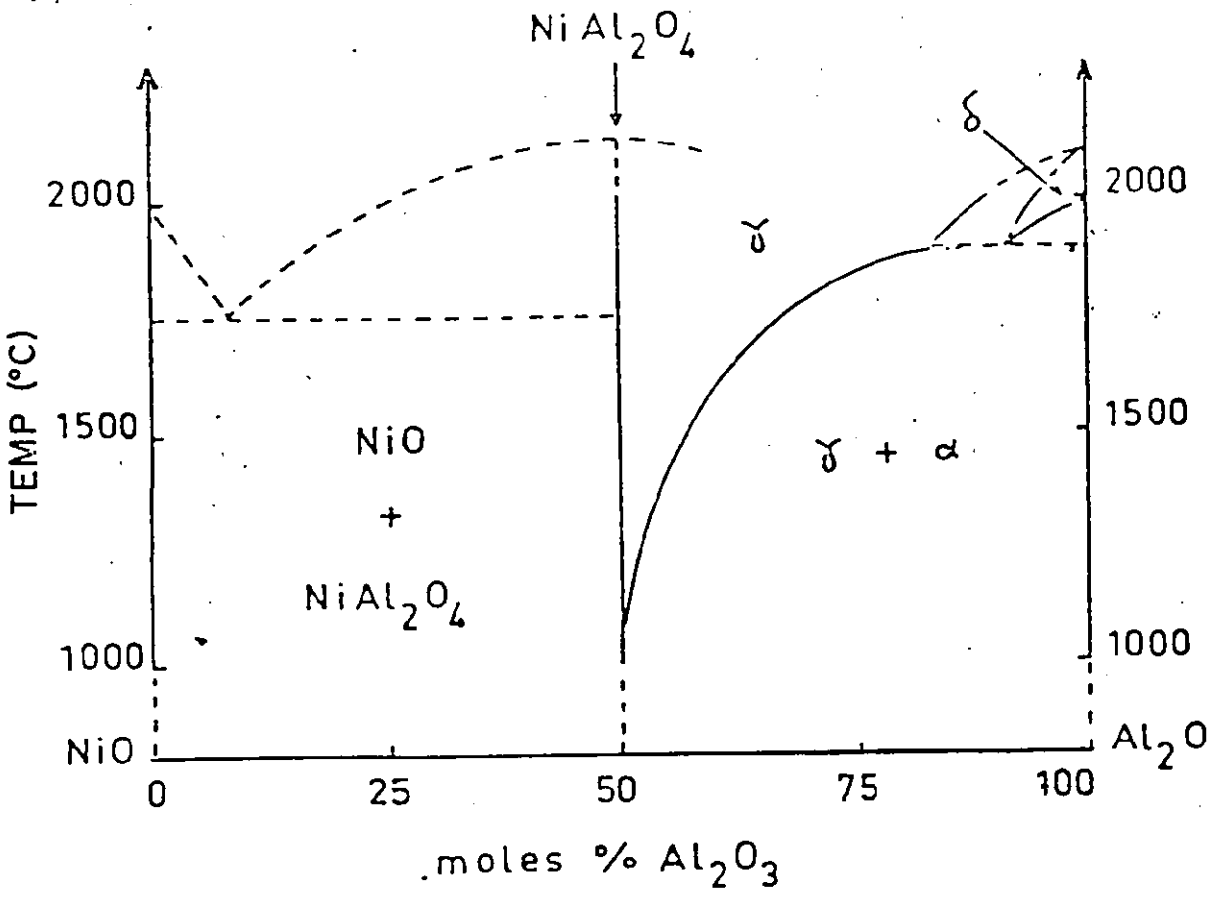

Figure (2-5) Equilibrium diagram for the system NiO-Al_2O_3 (32). γ is the spinel phase and α is α-Al_2O_3.

The free energy of formation of nickel spinel from its binary oxides has been measured using a solid state electrochemical technique (33,34), but the available results are contradictory. Tretjakow and Schmalzeried (33) have shown that the standard free energy of formation of spinel from its binary oxides increases with temperature while the values of the free energy of formation of nickel spinel from the binary oxides as proposed by Jacob and Alcock (34) are given by the relation

$$\Delta G = -1,499-2.31T(K) \quad . \qquad (2.4)$$

2.5 The Iron-Oxygen System

The Fe-O phase diagram, as proposed by Darken and Gurry (35,36), is shown in figure (2-6). This system contains three oxides; wustite ($Fe_{1-\delta}O$), magnetite (Fe_3O_4), and hematite (Fe_2O_3).

Wustite ($Fe_{1-\delta}O$) has an NaCl-type structure with a large range of nonstoichiometry which does not include the stoichiometric composition. The composition of wustite in equilibrium with iron is virtually independent of temperature and it has the minimum value of δ (0.051±0.002). The nonstoichiometry of wustite in equilibrium with magnetite increases from 0.065 at 600°C to 0.120 at 1000°C. The nonstoichiometry of wustite as a function of temperature and partial pressure of oxygen have been extensively investigated.

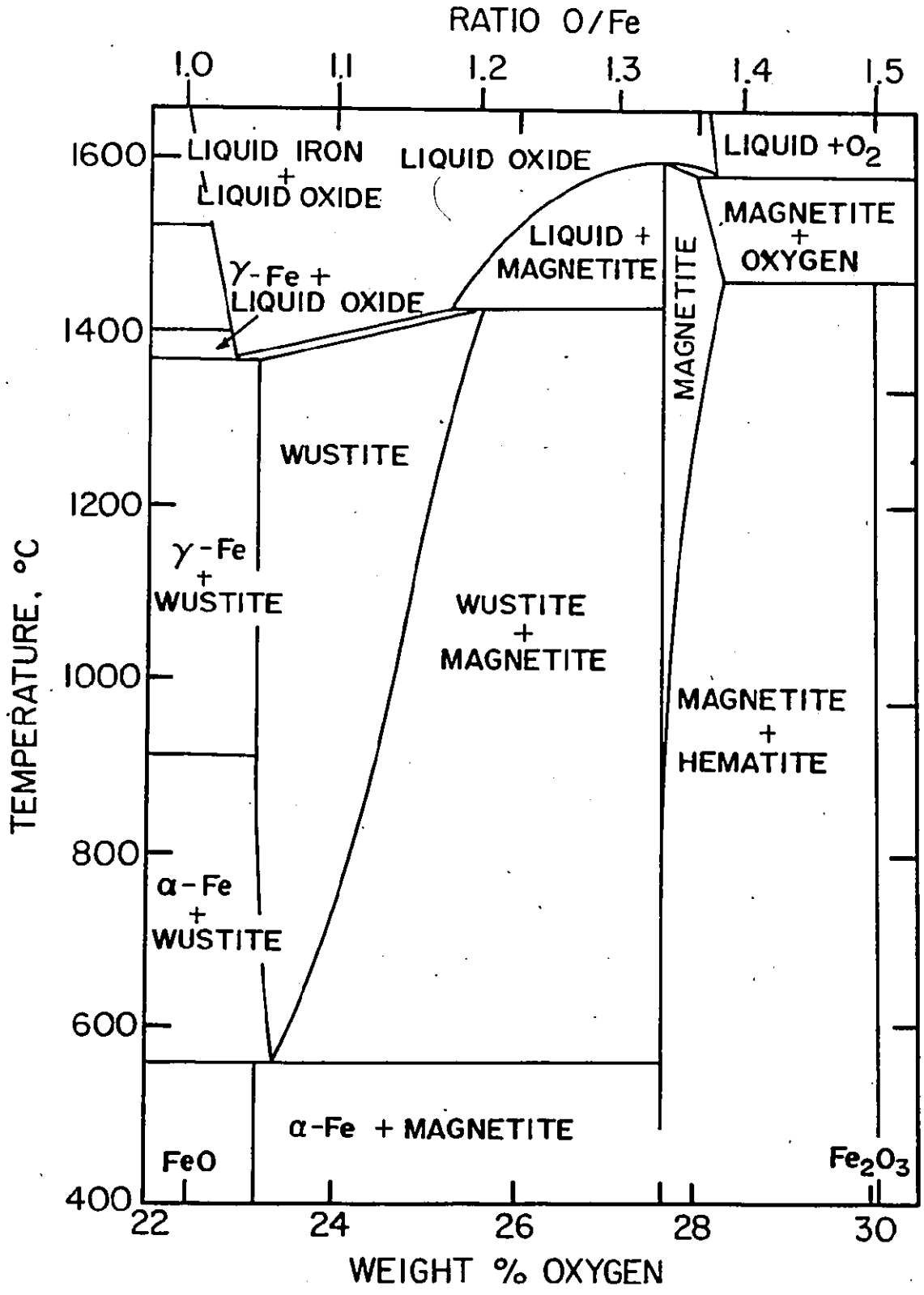

Figure (2-6) The Fe-O phase diagram (35,36).

The results of four separate investigations (35,37,38,39) are shown in figure (2-7).

Steele (13) analyzed the available data for the oxygen pressure in equilibrium with iron and wustite to obtain

$$\log p_{O_2} \text{ (atm)} = - \frac{27,637}{T(K)} + 6.831 \ . \qquad (2.5)$$

Davis (40) has obtained the expression

$$\log p_{O_2} \text{ (atm)} = - \frac{33,685}{T(K)} + 13.683 \qquad (2.6)$$

for the oxygen pressure in equilibrium with wustite and magnetite by a least squares analysis of the available data for the wustite-magnetite equilibria. Equations (2.5) and (2.6) were solved (40) for the euteqtoid temperature at which iron, wustite, and magnetite are in equilibrium. The calculated temperature is 610±40°C.

Magnetite has an inverse spinel structure at room temperature but at higher temperatures the cations are randomly distributed over the occupied octahedral and tetrahedral sites. Magnetite is essentially stoichiometric at the magnetite/wustite boundary and becomes increasingly cation deficient with increasing partial pressure of oxygen and its formula may be written as $Fe_{3-x}O_4$. It is reported that the point defects are cation vacancies (41).

Bryant and Smeltzer (42) investigated the magnetite-hematite equilibrium using a solid state electrochemical cell

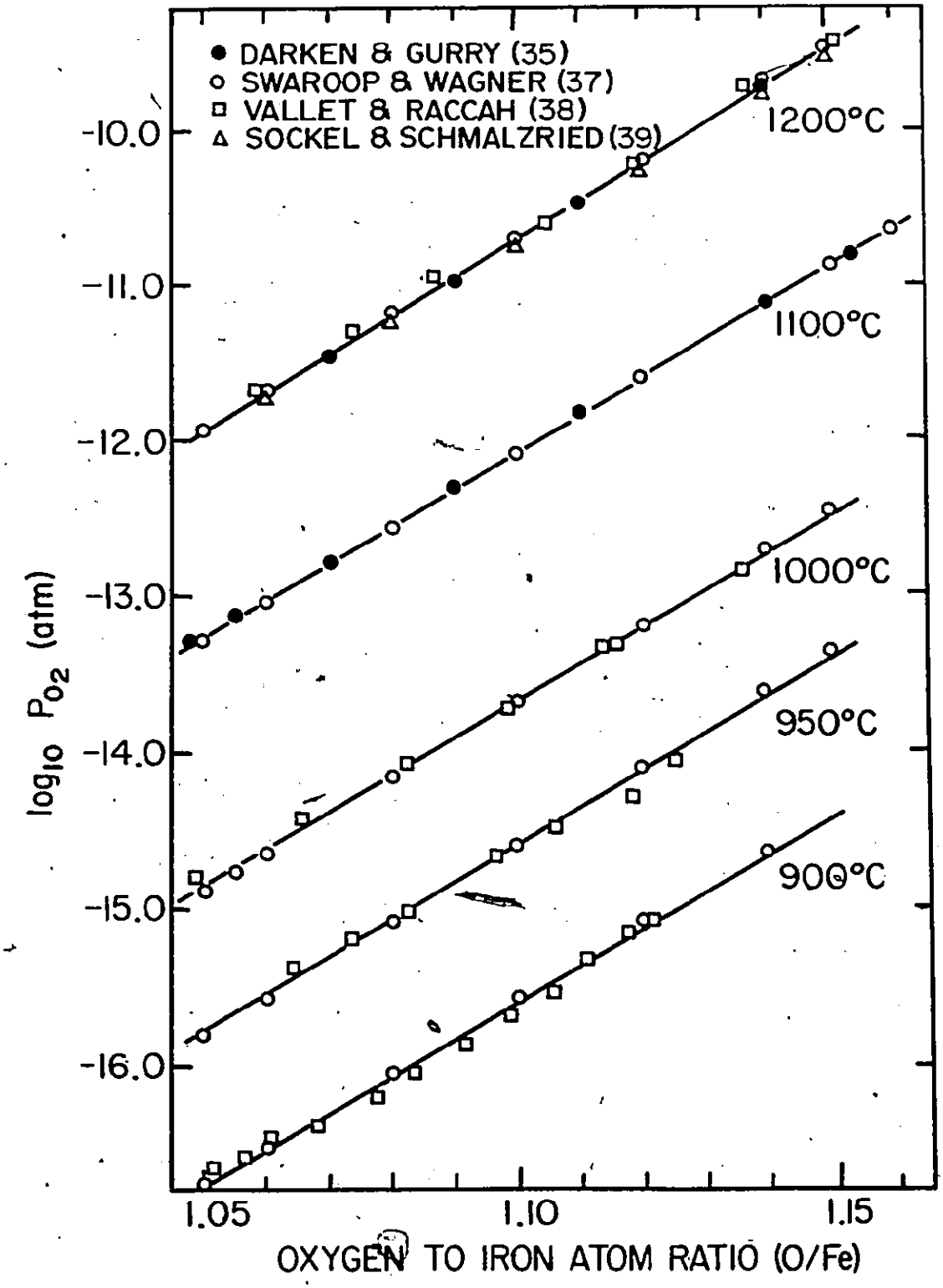

Figure (2-7) Variation of wustite composition with O_2 pressure and temperature.

and reported the dissociation pressure of hematite as

$$\log p_{O_2}\ (\text{atm}) = -\frac{25{,}908(\pm 215)}{T(K)} + 14.862(\pm 0.007) \quad (2.7)$$

over the temperature range 960-1740K.

Hematite has a corundum structure which is anion deficient (41). For Fe_2O_{3-y} in equilibrium with magnetite, y ranges from 0.0015 at 1000°C to 0.01 at 1504°C.

2.6 The Aluminum-Iron System

The results for the aluminum-iron system are compiled in references (8-10). Figure (2-8) illustrates the Al-Fe phase diagram as given in Hansen (8). The $\gamma/(\gamma+\alpha)$ and $\alpha/(\alpha+\gamma)$ boundaries extend from about 1.0 w/o to about 2.0 w/o Al, respectively, at about 1150°C. The Al-rich limit of the α solid solution is at about 52 a/o Al. The lattice parameter change, in the α region, with composition is reported (43). The existence of two superlattices, based on Fe_3Al and FeAl, in the α region is indicated by several investigators (43-45); however, these results do not permit the construction of a definite phase field for Fe_3Al and FeAl. The ε phase, the ξ phase, based on $FeAl_2$, the η phase, based on Fe_2Al_5, and the θ phase, based on $FeAl_3$, are the solid phases formed in this system.

Eldridge and Kommark (46) have determined the activity data of Al in solid Fe-Al alloys between 5 and 75 a/o Al and 1100K and 1400 K by equilibrating iron specimens, heated in

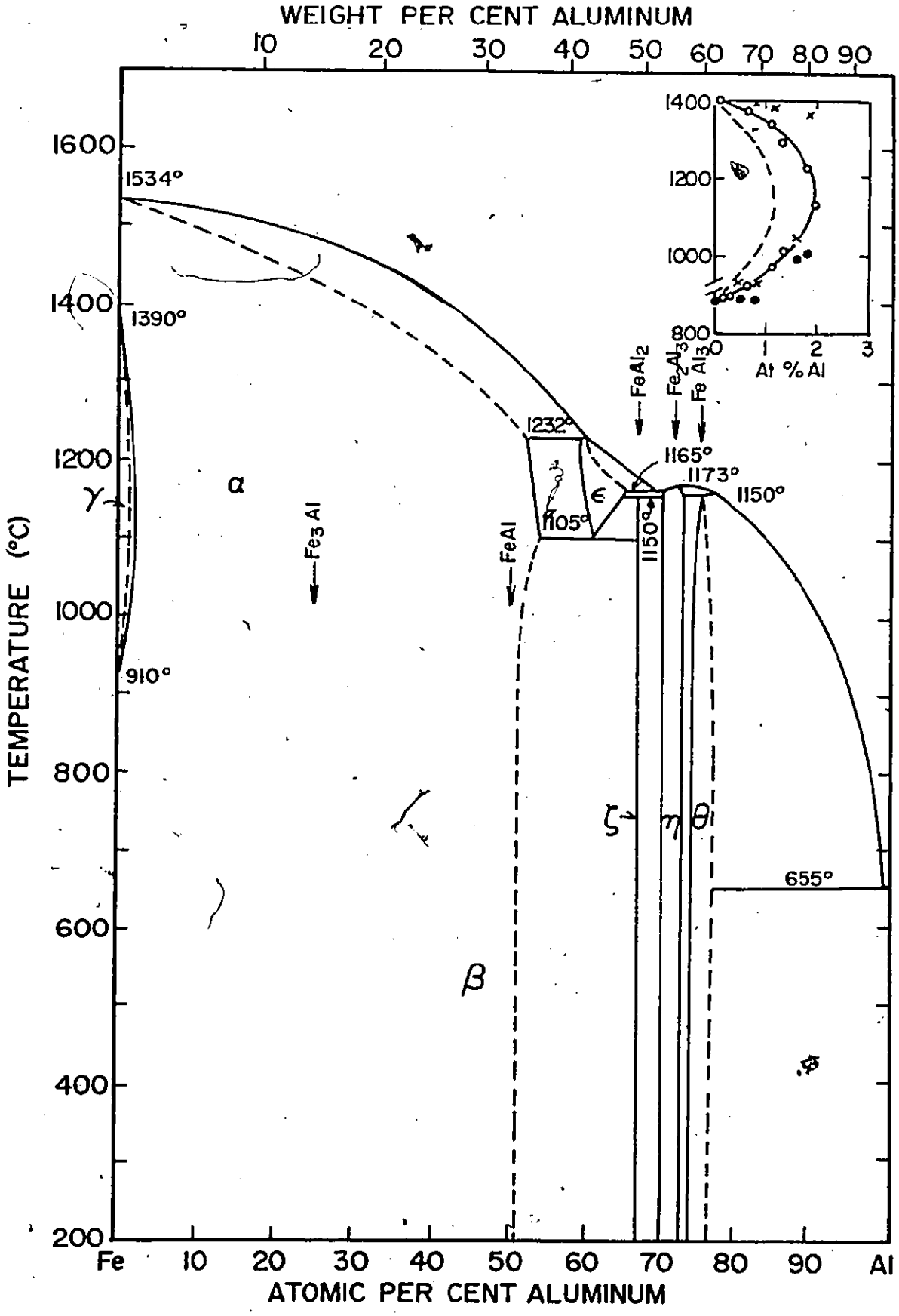

Figure (2-8) Fe-Al system (8).

a temperature gradient, with Al vapor in a closed system. Their results indicate that only one phase, α, may be found over the composition range 5 a/o to 52 a/o Al. The thermodynamic properties of solid Fe-Al alloys have been determined also by Radcliffe et al. (47) in the vicinity of 900°C and over the composition range 5 a/o to 75 a/o Al by emf measurements, using a molten chloride electrolyte.

2.7 The Iron-Aluminum-Oxygen System

Figure (2-9) shows the iron oxide-Al_2O_3 quasi-binary phase system as proposed by Muan (48). The first two diagrams in this figure (a and b) show phase relationships in the system iron oxide-Al_2O_3 at 1 atm. O_2 (a) and in air (b), respectively. The diagrams a and b illustrate that the compound $Fe_2O_3.Al_2O_3$ decomposes to a-hematite solid solution and a corundum solid solution below 1318°C. The diagrams in c and d are sketches intended to show the disappearance of the $Fe_2O_3.Al_2O_3$ phase at oxygen pressure less than 0.03 atm. Coexistence of the phases hematite solid solution, spinel, $Fe_2O_3.Al_2O_3$, and corundum solid solution at 1318°C and an O_2 partial pressure of 0.03 atm. corresponds to an invariant system in the Fe-Al-O system. Figure (2-9) illustrates that Fe_2O_3 and Al_2O_3 have limited mutual solubility while a complete solid solution occurs between Fe_3O_4 and the iron spinel.

Atlas and Sumida (49) have studied the phase relationships in the sub-solidus region of the Fe-Al-O system; from

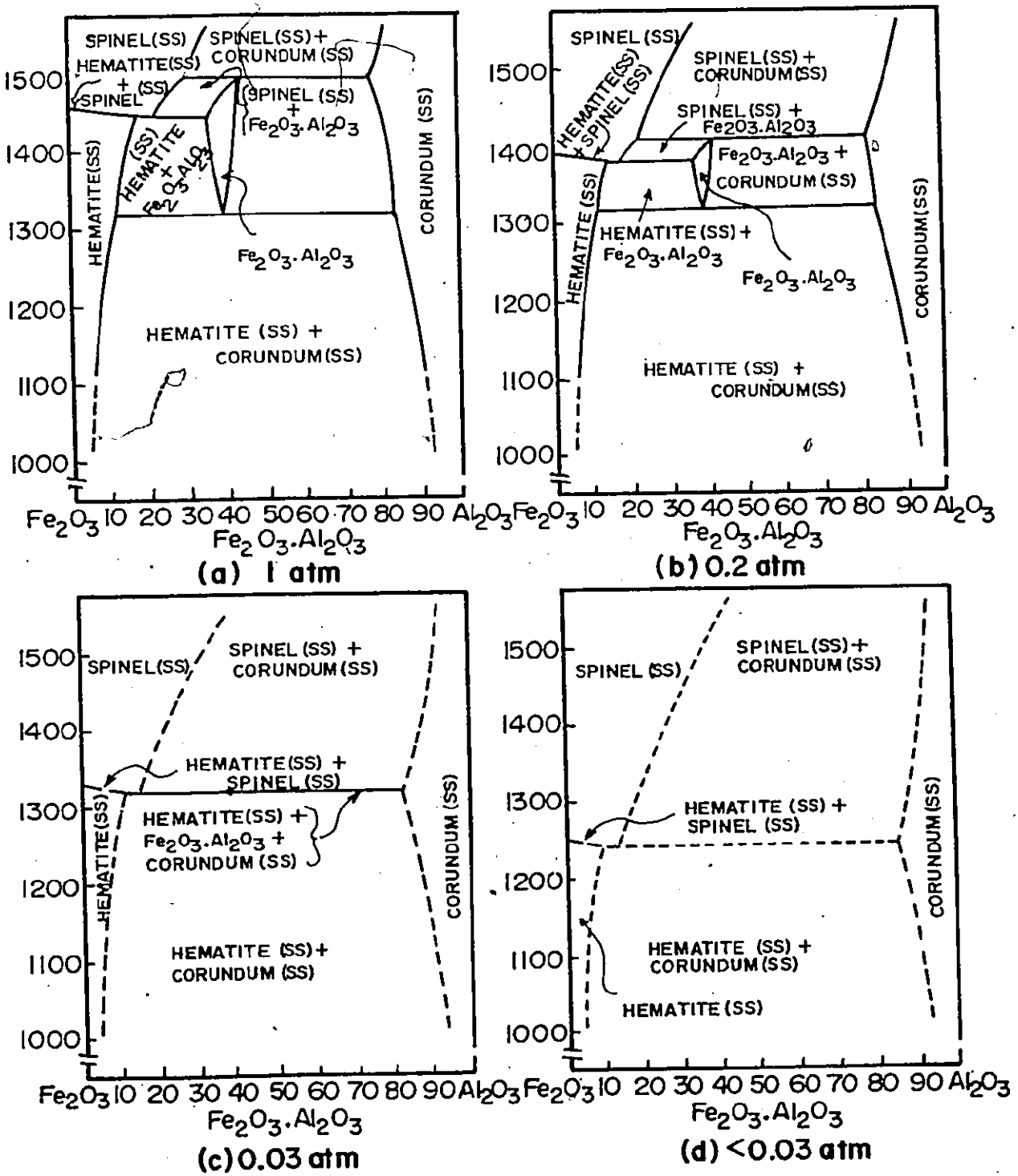

Figure (2-9) Change in O_2 partial pressure and its effect on subsolidus equilibria in Fe_2O_3-Al_2O_3 system (48).

their results and the available data in the literature they proposed the Fe-Al-O isotherms shown in figure (2-10). They also concluded from their investigation that wustite dissolves up to about 1 w/o Al and that Fe-Al alloys are compatible only with Al_2O_3 containing very little dissolved iron.

The standard free energy of the reaction

$$2Fe_{(s,\ell)} + O_{2(g)} + 2Al_2O_{3(\alpha)} = 2\ FeO.Al_2O_{3(s)}$$

has been determined by several investigators (50-53). Recently Chan et al (50) have given the expressions

$$\Delta G^{\circ} = -\ 139{,}790 + 32.73T(K) \qquad [750°C\text{-}1536°C] \quad (2.8)$$

$$\Delta G^{\circ} = -\ 146{,}390 + 36.48T(K) \qquad [1536°C\text{-}1700°C] \quad (2.9)$$

for the standard free energy of this reaction. They (50) utilized solid oxide galvanic cells using $CaO\text{-}ZrO_2$ and $CaO\text{-}ZrO_2$ in combination with $YO_{1.5}\text{-}ThO_2$ as solid electrolytes.

2.8 Sodium Aluminate-Aluminum Oxide System

The development of a Na-S battery by the Ford Motor Company (54) gave a particular emphasis to the study of the stability of the fast ionic-conducting phases, $\beta\text{-}Al_2O_3$ and $\beta''\text{-}Al_2O_3$, in the $Na_2O.Al_2O_3\text{-}Al_2O_3$ phase diagram. It was originally believed that $\beta\text{-}Al_2O_3$ was an allotropic form of $\alpha\text{-}Al_2O_3$ stabilized by adding a small amount of MgO, or Na_2O, to $\alpha\text{-}Al_2O_3$ (55). The

Figure (2-10) Fe-Al-O isotherms proposed in reference (49) at 1000°C (a), 1250°C (b), and 1350°C (c).

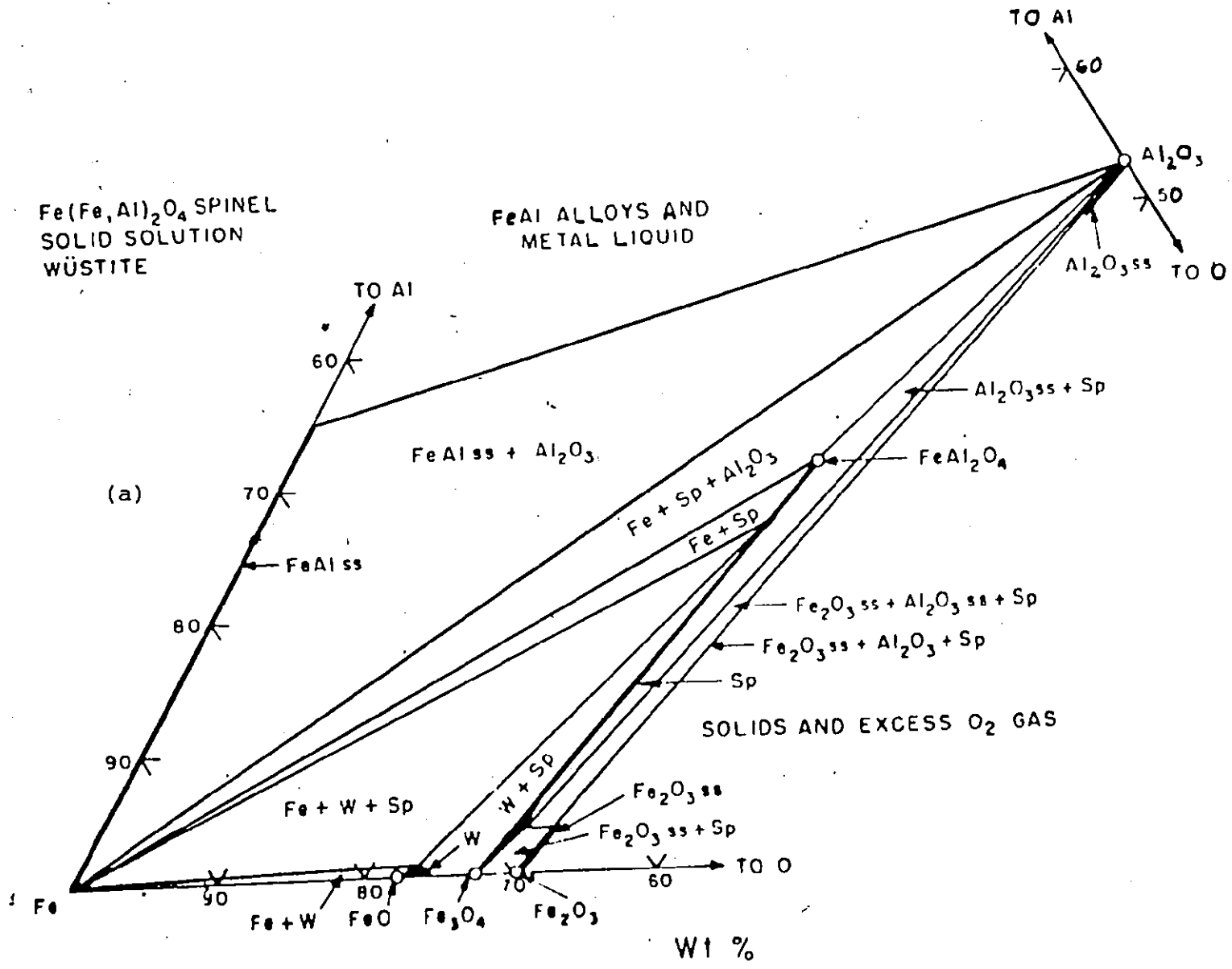
Sp Fe(Fe,Al)2O4 SPINEL
ss SOLID SOLUTION
W WÜSTITE
FeAl ALLOYS AND METAL LIQUID
TO Al
60
50
Al2O3
Al2O3ss
TO O
(a)
70
80
90
FeAl ss
FeAl ss + Al2O3
Fe + Sp + Al2O3
Fe + Sp
Al2O3ss + Sp
FeAl2O4
Fe2O3 ss + Al2O3 ss + Sp
Fe2O3ss + Al2O3 + Sp
Sp
SOLIDS AND EXCESS O2 GAS
Fe + W + Sp
W + Sp
Fe2O3 ss
Fe2O3 ss + Sp
W
Fe
90
80
70
60
TO O
Fe + W
FeO
Fe3O4
Fe2O3
Wt %

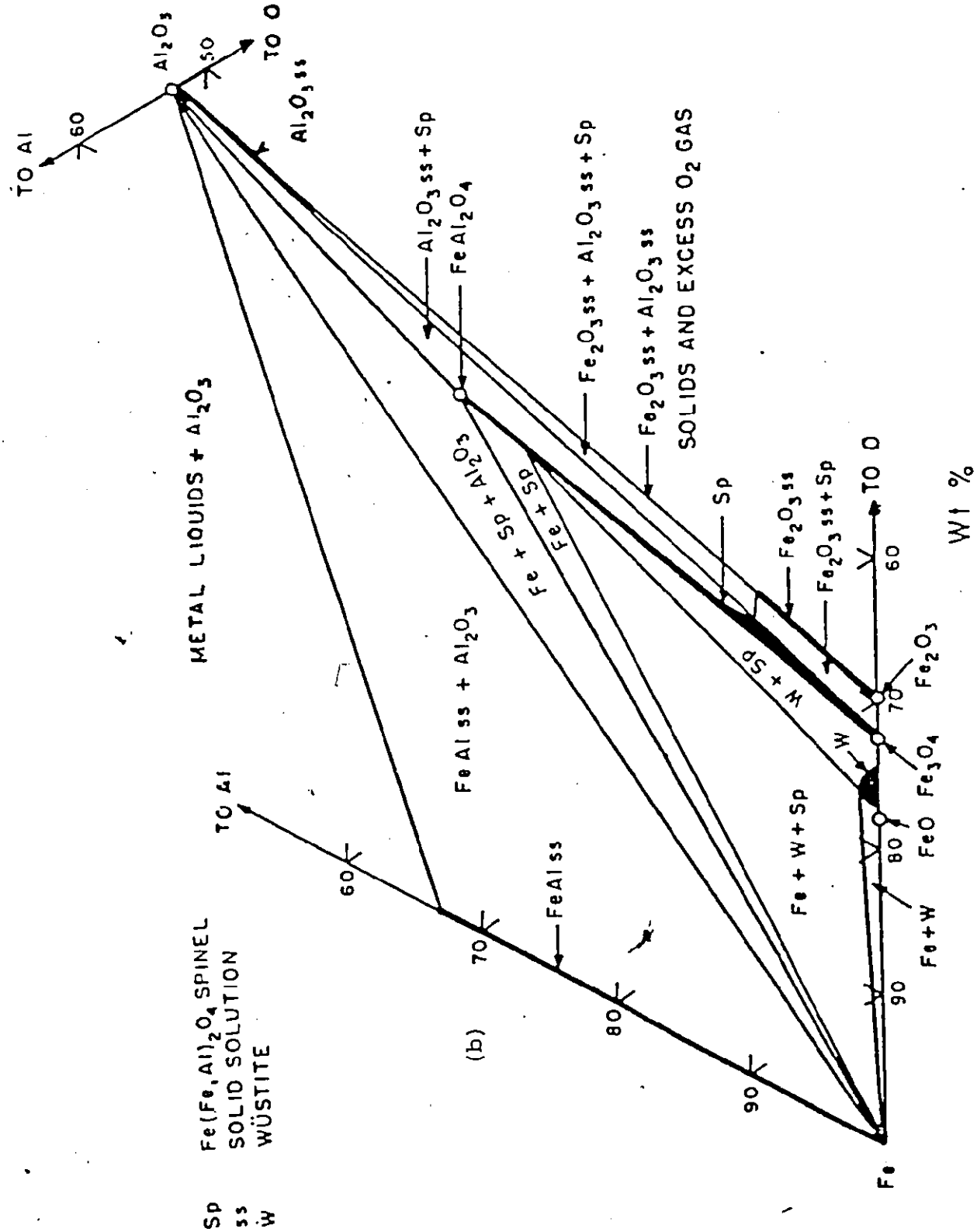
TO Al
60
Al_2O_3
50
TO O
Al_2O_3 ss
METAL LIQUIDS + Al_2O_3
Al_2O_3 ss + Sp
$FeAl_2O_4$
Fe_2O_3 ss + Al_2O_3 ss + Sp
Fe_2O_3 ss + Al_2O_3 ss
SOLIDS AND EXCESS O_2 GAS
Sp
Fe_2O_3 ss
Fe_2O_3 ss + Sp
TO O
60
Fe Al ss + Al_2O_3
Fe + Sp + Al_2O_3
Fe + Sp
W + Sp
W
Fe_2O_3
Fe_3O_4
FeO
Fe + W
Fe
TO Al
60
70
80
90
FeAl ss
Fe + W + Sp
(b)
Wt %
Sp Fe(Fe, Al)$_2$O$_4$ SPINEL
ss SOLID SOLUTION
W WÜSTITE

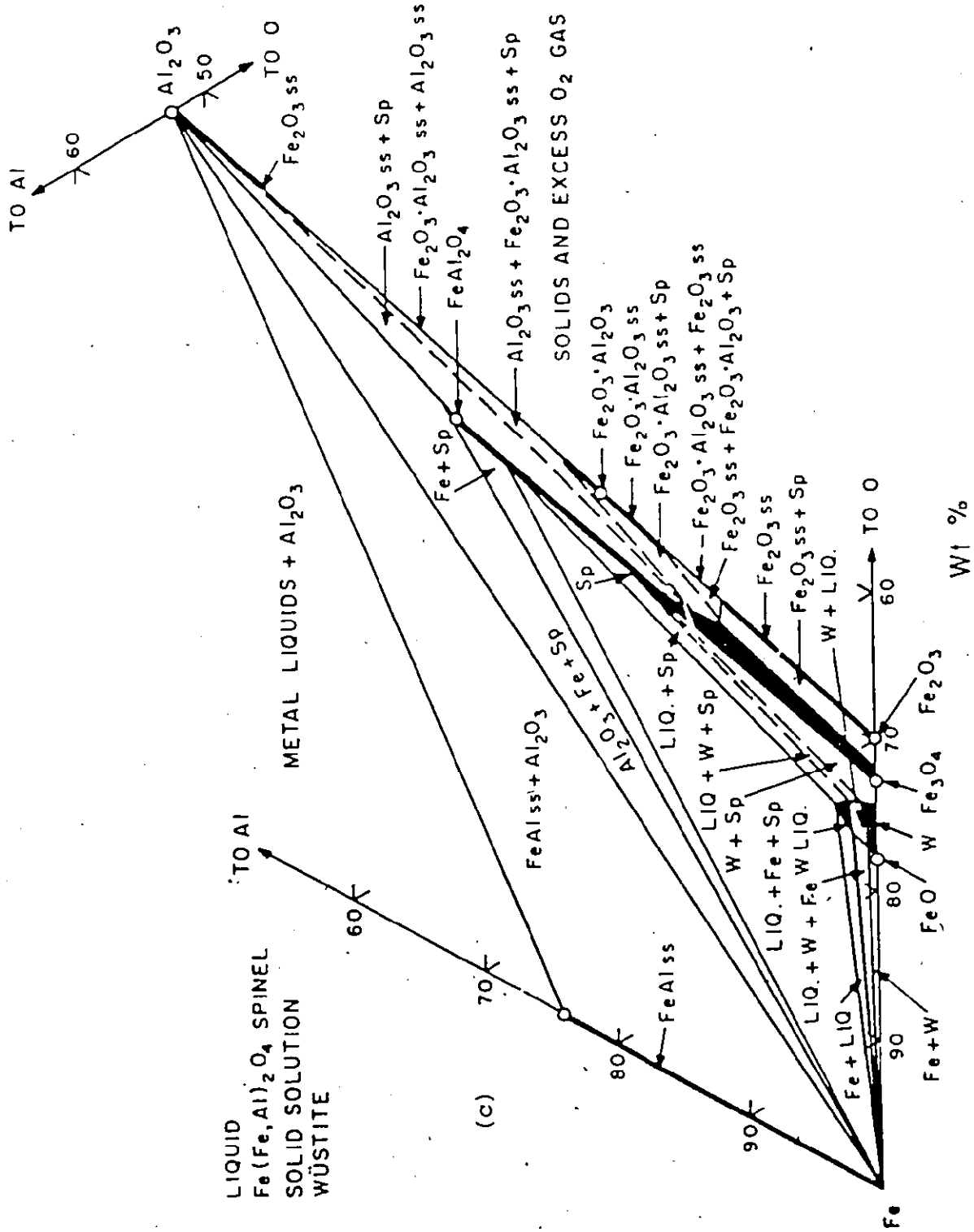
LIQ LIQUID
Sp Fe(Fe,Al)2O4 SPINEL
ss SOLID SOLUTION
W WÜSTITE
METAL LIQUIDS + Al2O3
SOLIDS AND EXCESS O2 GAS
TO Al
TO O
Al2O3
Fe2O3 ss
Al2O3 ss + Sp
Fe2O3·Al2O3 ss + Al2O3 ss
FeAl2O4
Fe + Sp
Al2O3 ss + Fe2O3·Al2O3 ss + Sp
Fe2O3·Al2O3
Fe2O3·Al2O3 ss
Fe2O3·Al2O3 ss + Fe2O3 ss
Fe2O3 ss + Fe2O3·Al2O3 + Sp
Fe2O3 ss
Fe2O3 ss + Sp
W + LIQ.
Sp
Al2O3 + Fe + Sp
LIQ. + Sp
LIQ + W + Sp
W + Sp
LIQ. + Fe + Sp
LIQ. + W + Fe
W LIQ.
FeAl ss + Al2O3
FeAl ss
Fe + LIQ
Fe + W
FeO
W Fe3O4 Fe2O3
Fe
50
60
70
80
90
(c)
Wt %

formation of a new phase, β-Al_2O_3, in the Na_2O-Al_2O_3 system by adding Na_2O to α-Al_2O_3 was then pointed out by several investigators (56,57); from chemical analysis the composition of $Na_2O.12Al_2O_3$ was reported (58) but a 1:11 ratio was found to be more representative of the crystal structure as proposed by Beevers and Ross (59).

Yao and Kummer (60) have found that the β-Al_2O_3 fused cast refractory from Harbison Carborundum contains 6.0 to 6.7 w/o Na_2O, compared to the theoretical 5.24 w/o Na_2O for the 1:11 composition, which is equivalent to the formula $Na_2O.9Al_2O_3$. Weber and Venero (61) investigated the composition range of the β-Al_2O_3 phase to a limited degree. They found that at 1750°C the soda to alumina ratio ranges from 1:8.1 to 1:9.2, as opposed to the ratio 1:11 in the idealized form.

A new compound with a β-Al_2O_3 like structure was prepared by Thery and Briancen (62) by reacting $NaAlO_2$ or Na_2CO_3 with α-Al_2O_3 above 1050°C; the new compound has the formula $Na_2O.5Al_2O_3$.

De Vries and Roth (63) made a critical evaluation of the literature data on β-Al_2O_3 and related phases and they concluded that there are at least two β-Al_2O_3 like phases, one at about $Na_2O.11Al_2O_3$ (possibly 1:9) and another in the 1:5 to 1:7 range; they also concluded that, although it is difficult to synthesize the β-Al_2O_3 phase from its compound oxides

below about 1650°C in reasonable time, once it is formed at higher temperatures, β-Al_2O_3 can exist at all temperatures below 2000°C. Figure (2-11) shows the phase diagram for the system $Na_2O.Al_2O_3$-Al_2O_3 as proposed by De Vries and Roth. The diagram (a) of figure (2-11) is the version for the case where β-Al_2O_3 is considered to be metastable below about 1500°C while the diagram (b) is for the case where β-Al_2O_3 is stable at all temperatures up to its incongruent melting point.

In contradiction to De Vries and Roth conclusions, Poulief et al (64) have claimed to synthesize β-Al_2O_3 at 1250°C by heating a mixture of γ-Al_2O_3+Na_2CO_3+1 w/o F in NaF form; they have not detected a β"-Al_2O_3 phase in the above mixture after the heat treatment. They also reported that at 0.1 w/o F only β"-Al_2O_3 is detected while at 0.5 w/o F both β- and β"-Al_2O_3 are found. Le Cars et al (65) have studied also the phase relationships in the $NaAlO_2$-Al_2O_3 system. The methods used to synthesize the fast ionic-conducting phases were by sodium oxide vapor loss and a solid state reaction between α-Al_2O_3 and Na_2CO_3; they found that β"-Al_2O_3 prepared by the solid state reaction is always present with β-Al_2O_3 in the temperature range 1050°C-1550°C. Above 1400°C the proportion of β-Al_2O_3 in the mixture increases and at 1550°C or higher only β-Al_2O_3 is obtained. In disagreement with De Vries and Roth, they argue that only one β-Al_2O_3 like phase, β-Al_2O_3, is stable in the $Na_2O.Al_2O_3$-Al_3O_3 system while the other one, β"-Al_2O_3,

Figure (2-11) $NaAlO_2$-Al_2O_3 system as proposed by De Vries and Roth (63). 2Bβ is β-Al_2O_3 and 3Bβ is β"-Al_2O_3.

(a)

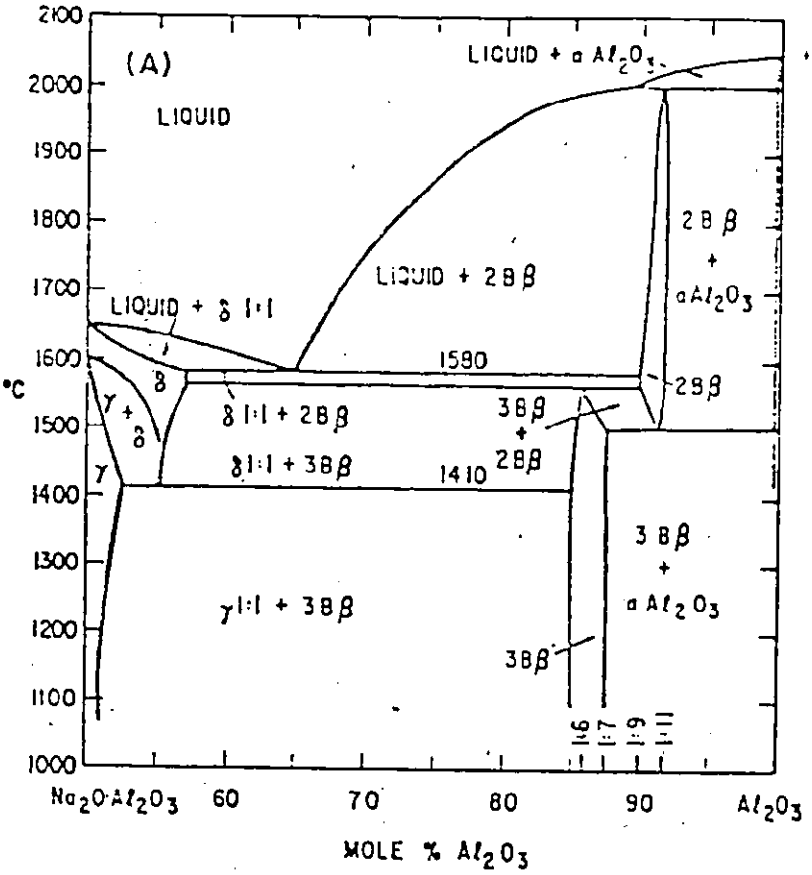
(A)
LIQUID
LIQUID + α Al_2O_3
LIQUID + 2Bβ
LIQUID + δ 1:1
2Bβ + αAl_2O_3
2Bβ
δ 1:1 + 2Bβ
3Bβ + 2Bβ
δ1:1 + 3Bβ
1590
1410
γ1:1 + 3Bβ
3Bβ + αAl_2O_3
3Bβ
γ + δ
δ
γ
°C
2100
2000
1900
1800
1700
1600
1500
1400
1300
1200
1100
1000
Na_2O-Al_2O_3
60
70
80
90
Al_2O_3
MOLE % Al_2O_3

(b)

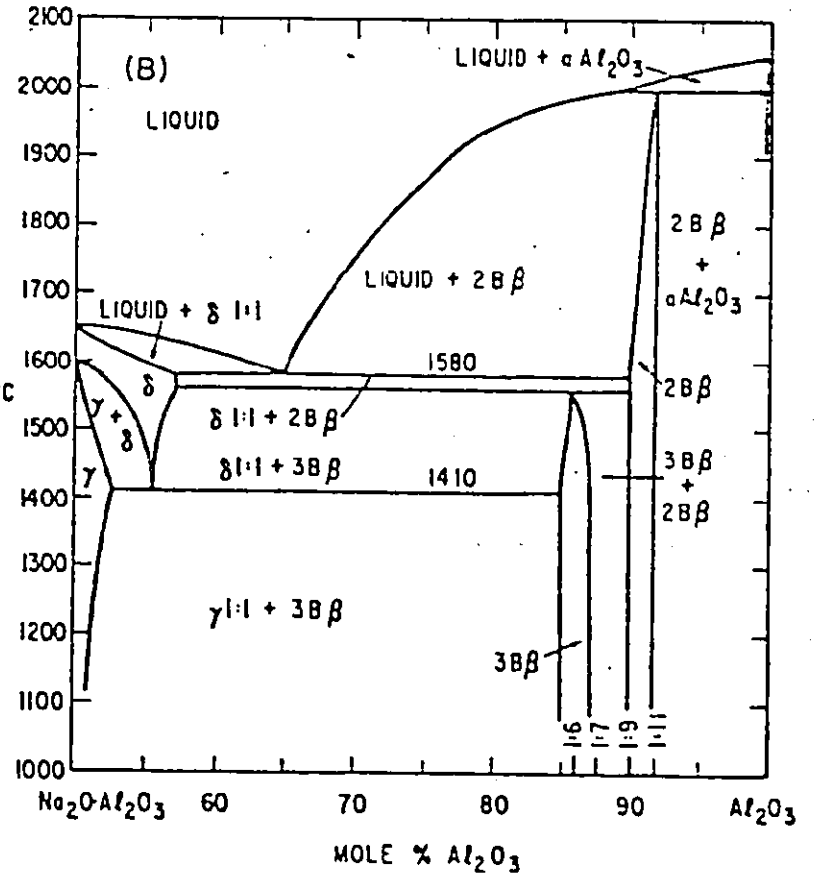
(B)
LIQUID
LIQUID + α Al_2O_3
LIQUID + 2Bβ
LIQUID + δ 1:1
2Bβ + αAl_2O_3
2Bβ
δ 1:1 + 2Bβ
3Bβ + 2Bβ
δ1:1 + 3Bβ
1580
1410
γ1:1 + 3Bβ
3Bβ
γ + δ
δ
γ
°C
2100
2000
1900
1800
1700
1600
1500
1400
1300
1200
1100
1000
Na_2O-Al_2O_3
60
70
80
90
Al_2O_3
MOLE % Al_2O_3

is metastable. The domain of the stable phase extends from $Na_2O \cdot 5.33Al_2O_3$ to $Na_2O.8.5Al_2O_3$ at 1400°C. Figure (2-12) shows the phase relationships in the system $Na_2O.Al_2O_3$-Al_2O_3 as proposed by Le Cars et al. (65).

The stability of β-Al_2O_3 in a reducing atmosphere is directly related to its sodium oxide activity. Many investigators (22,66,67,68) had reported the activity of Na_2O in the coexistence α-Al_2O_3,β-Al_2O_3; however, the different results show a discrepancy of up to several orders of magnitude at 700°C.

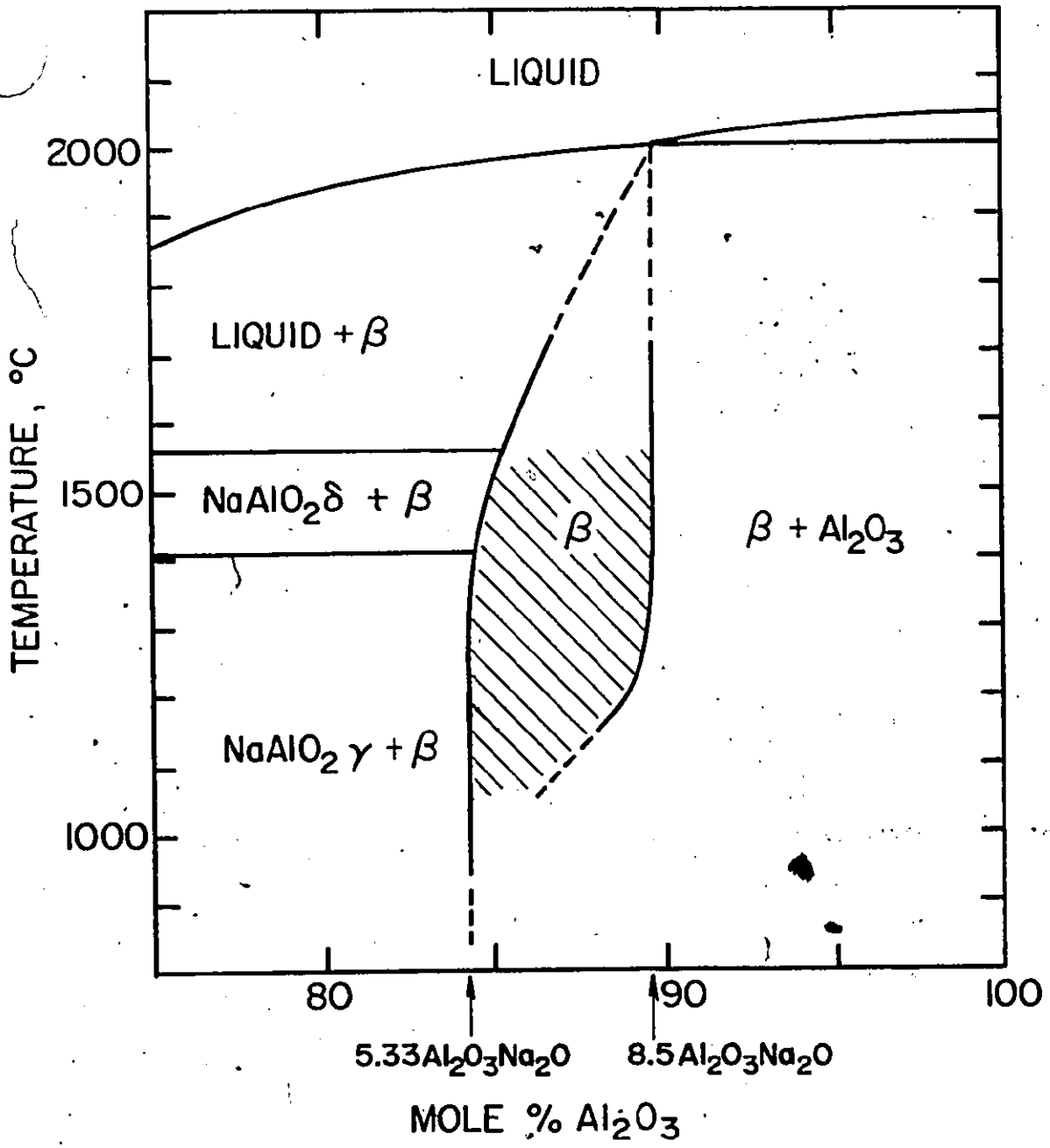

Figure (2-12) Equilibrium diagram for the system $NaAlO_2$-Al_2O_3 (65).

CHAPTER

APPLICATIONS OF SOLID ELECTROLYTES TO HIGH TEMPERATURE-THERMODYNAMIC MEASUREMENTS

3.1 Introduction

In 1957 Wagner and Kiukkola (6,7) introduced calcia stabilized zirconia as a solid oxide electrolyte which exhibits ionic conduction over a wide range of oxygen atmospheric pressure at 870°C. Within the last two decades electrochemical cells using solids as electrolyte used to measure extensively thermodynamic properties of solid,liquid, and gaseous electrodes. Thermodynamic data obtained using galvanic cells with solid electrolytes have been reviewed in references (13,69,70).

3.2 Electrical Conductivity, Transference Number, and Electrolytic Domain of a Solid Electrolyte

A compound is considered a solid electrolyte if it exhibits predominant ionic conduction over a wide range of temperatures. Crystalline compounds exhibit electronic defects, free electrons and/or positive holes, and ionic defects, anionic and/or cationic. In response to an electrochemical potential difference across the solid, the ionic and electronic defects migrate through the lattice. The partial conductivity for the defect species j, σ_j, is given by

$$\sigma_j = C_j q_j^2 \beta_j \qquad (3.1)$$

where:

C_j is the concentration of defect species j in particles/m^3

q_j is the electrical charge of the defect species j in coulombs/particle

β_j is the absolute mobility of defect species j in particle-m^2/sec-joule.

By definition, the ionic transference number, t_i, is defined as

$$t_i = \frac{\sum_{\text{ionic}} \sigma_j}{\sum_j \sigma_j} \qquad (3.2)$$

where $\sum_{\text{ionic}}$ indicates the summation over all the ionic defect species while $\sum_j$ indicates the summation over all the electronic and ionic defect species.

Equation (3.1) shows that the contribution of electronic and ionic conduction to the electrical conductivity depend on the concentration and mobility of the defect species. Mobilities of electronic defects in ionic solids are 10^2-10^4 times larger than mobilities of ionic defects (70); therefore, ionic conduction in these solids can be only obtained when the electronic defect concentration is negligible.

Electrical neutrality in these compounds requires that summation over all negative charges must equal to summation over all positive charges. As an example, consider a hypothetical compound of the type MX_2 which exhibits anionic defects. Electroneutrality requires that

$$[h^{\cdot}] + 2[V_X^{\cdot\cdot}] = [e'] + 2[X_i^{''}] \qquad (3.3)$$

where $X_i^{''}$ is an interstitial anion, $V_x^{\cdot\cdot}$ is a vacant anion site, $h^{\cdot}$ is a positive hole, and e' is a free electron. The notation of Kröger and Vink has been used in writing equation (3.3). Let us also consider that MX_2 exhibits predominant anti-Frenkel disorder at stoichiometry. The dependence of defect concentration on P_{X_2} is shown schematically in figure (3-1). Figures (3-2) and (3-3) are schematic representations of electrical conductivity and ionic transport number of MX_2 obtained by applying equations (3.1) and (3.2) to figure (3-1).

Defect concentrations and consequently the ionic transport number in MX_2 may be altered greatly by doping aliovalent ions into the lattice. As an example, consider introduction of soluble trivalent ions, m^{3+}, into the cationic lattice. The electroneutrality condition requires,

$$[h^{\cdot}] + 2[V_X^{\cdot\cdot}] = [e'] + 2[X_i^{''}] + [m_M^{'}] \; . \qquad (3.4)$$

For any m^{3+} concentration greater than trace amount, $[m_M^{'}]$

will be the predominant term. At the same time, introduction of the trivalent cation m^{3+} to M^{4+} lattice must be compensated by creation of vacancies in the anionic lattice to maintain the constant cationic to anionic ratio of the compound. Under such conditions the electroneutrality condition will be

$$2[V_X^{\cdot\cdot}] = [m_M'] \quad . \tag{3.5}$$

Equation (3.5) indicates that this introduction to trivalent cations to the MX_2 lattice will give rise to an enlarged electrolytic zone, zone II in figure (3-3).

The most common solid electrolytes are extensively reviewed in references (70,71). In 1971 Patterson (72) suggested the use of log P_{X_2} - $\frac{1}{T}$ space to represent the electrolytic domain, $t_i \geq 0.99$, of a solid electrolyte. Figure (3-4) illustrates the electrolytic domains of some useful solid electrolytes.

3.3 Calcia Stabilized Zirconia

Pure zirconia (ZrO_2) is of monoclinic form up to approximately 1200°C and then transforms to a tetragonal structure accompanied by 7% shrinkage (73,74). A fluorite structure can be stabilized by adding CaO (or MgO, Y_2O_3, La_2O_3) (75-77). This structure of calcia stabilized zirconia occurs near 15 m/o CaO but the phase boundaries are uncertain. Most investigators agree with 10 and between 20 and 30 m/o CaO as boun-

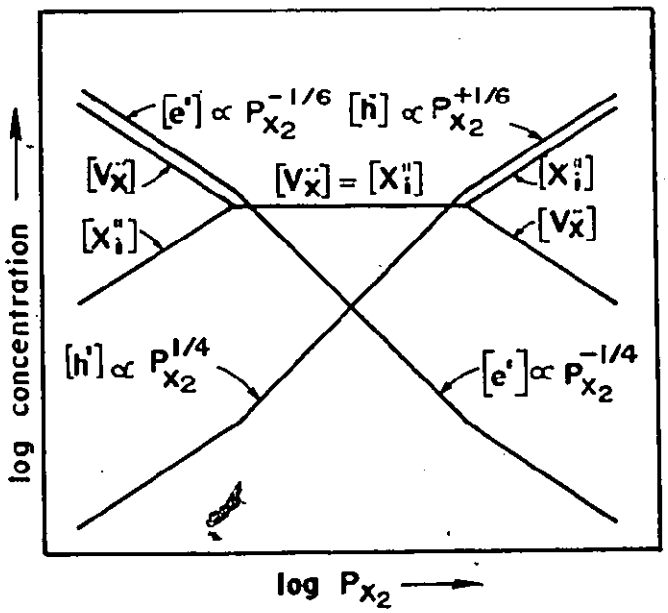

Figure (3-1) Schematic representation of concentration of ionic and electronic defects as a function of P_{X_2} for the hypothetical compound MX_2. [e'] is the free electron concentration, [h'] is the positive hole concentration, $[V_X^{\cdot\cdot}]$ is the vacancy concentration in the anionic lattice, and $[X_i^{''}]$ is the concentration of the interstitial anions.

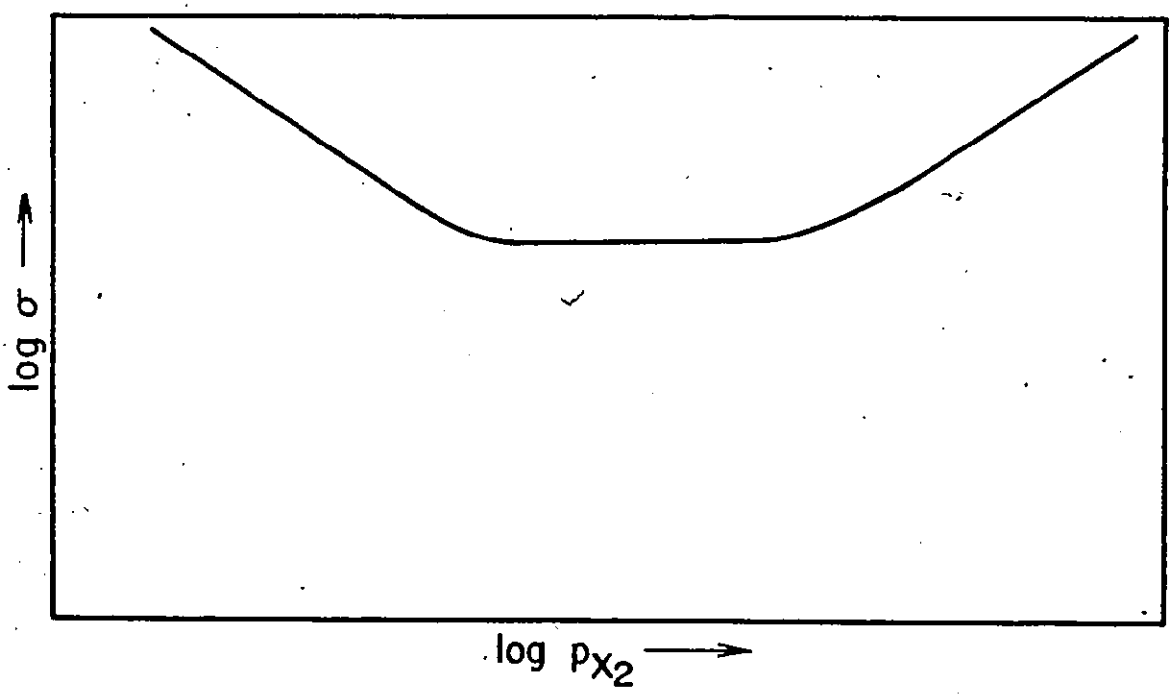

Figure (3-2) Schematic representation of the electrical conductivity for the hypothetical compound MX_2.

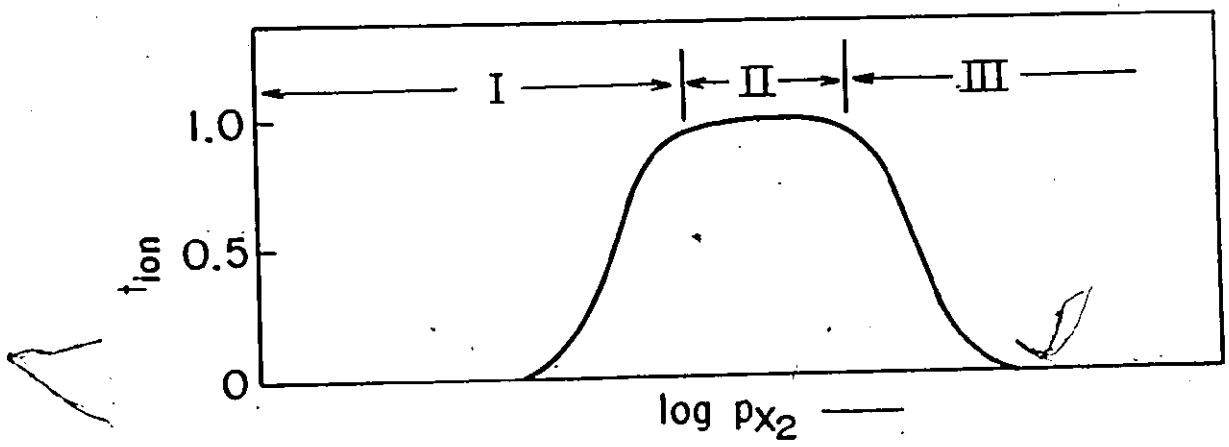

Figure (3-3) Schematic representation of ionic transference number for the MX_2 compound.
Zone I - n-type conduction zone.
Zone II - ionic conduction zone (solid electrolyte).
Zone III - p-type conduction zone.

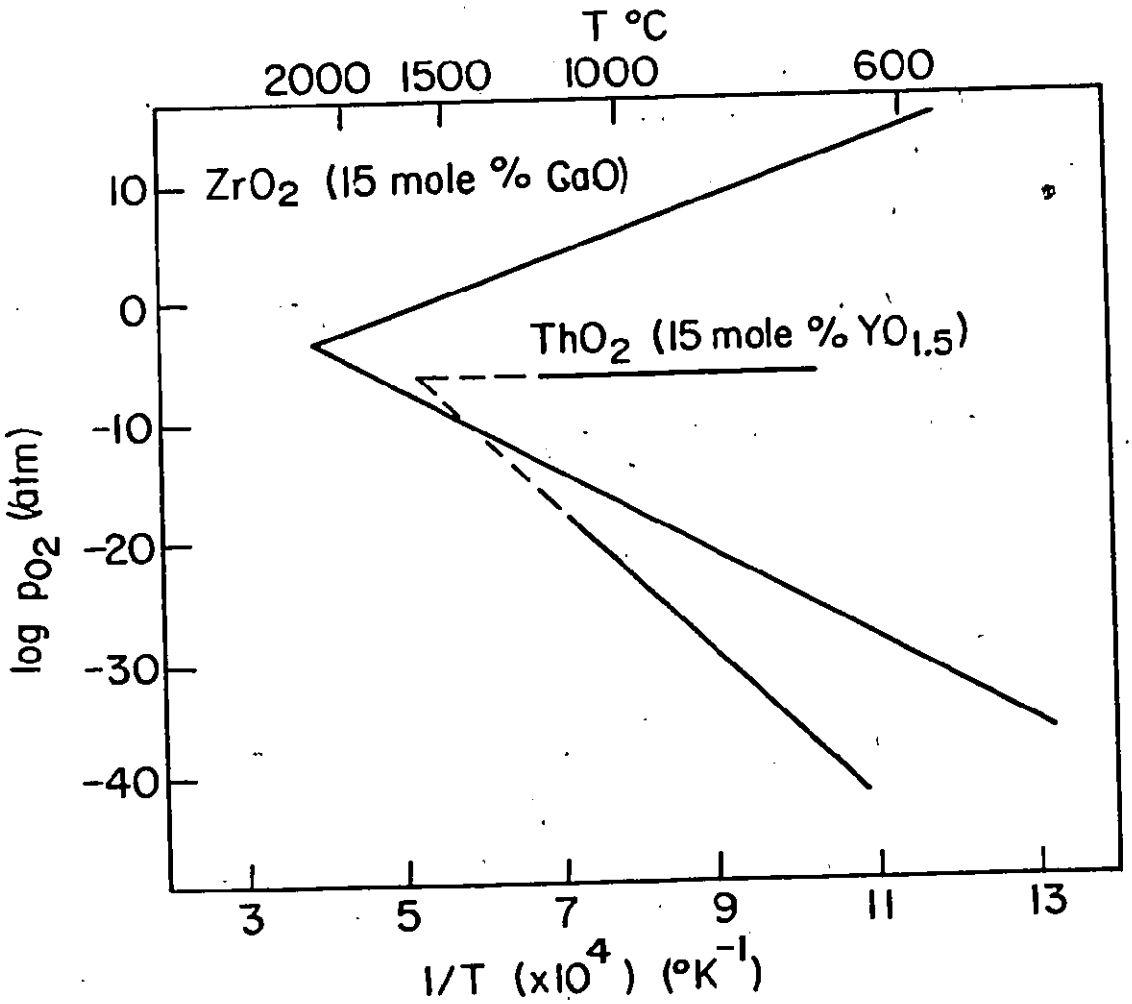

Figure (3-4) Electrolytic domains of ZrO_2(+CaO) and ThO_2 (+$YO_{1.5}$).

daries in the temperature range 1200-1600°C (78-81). Cacco (79) reported the boundaries at 1600°C to be 10.4 and 19.6 m/o CaO. The 19.6 boundary is independent on temperature while the 10.4 boundary moves to higher concentrations of CaO at lower temperatures. It is reported (80) that calcia stabilized zirconia exhibits eutectoid decomposition at 800°C into monoclinic zirconia and calcium zirconate.

Poulton and Smeltzer (82) reported that monoclinic zirconia has predominant anionic transport at 990°C between 10^{-10} and 10^{-18} atmospheric oxygen pressure. Two defect models have been postulated for stoichiometric monoclinic zirconia. Douglass and Wagner (83) proposed an anti-Frenkel disorder while Kroger (84) proposed a Schottky disorder of the type

$$nil = V_O^{\cdot\cdot} + (V_{Zr}V_O)''$$

where $(V_{Zr}V_O)''$ is a zirconium vacancy singly associated with an oxygen vacancy.

If this oxide is doped with lower valence cations, e.g. Ca^{2+}, the concentration of oxygen vacancies is enhanced and the solid solution may show a large range of predominant anionic transport. Several investigators (76,80,81) have suggested that calcium and zirconium are distributed in a completely filled cation lattice with sufficient anion vacancies for charge balance. Dines and Roy (80) found that between 10 and

15 m/o CaO, calcia stabilized zirconia quenched from 1800°C contains a full anion sublattice and a cation interstitial but when quenched from 1600°C the charge balance is due to anion vacancies. Carter and Roth (81) have measured the conductivity of this solid as a function of composition at one atmospheric pressure of oxygen and different temperatures. Their results, shown in figure (3-5), indicate that calcia stabilized zirconia exhibits a maximum in conductivity near 13-15 m/o CaO. Carter and Roth postulated that the increase in conductivity with calcia concentration agrees with the random anion vacancies model and the decrease in conductivity at large calcia concentration is due to vacancy ordering.

The electrolytic behaviour of calcia stabilized zirconia has been studied by several techniques, for example, emf measurements, electrical conductivity determination, and diffusion studies. The results of these investigations are compiled in reference (72).

Based on Wagner's analysis (85), the following expression

$$E = - \frac{1}{2F} \int_{\mu_0^c}^{\mu_0^a} t_0 -- d\mu_0 \qquad (3.6)$$

can be derived for the reversible potential, E, of the cell

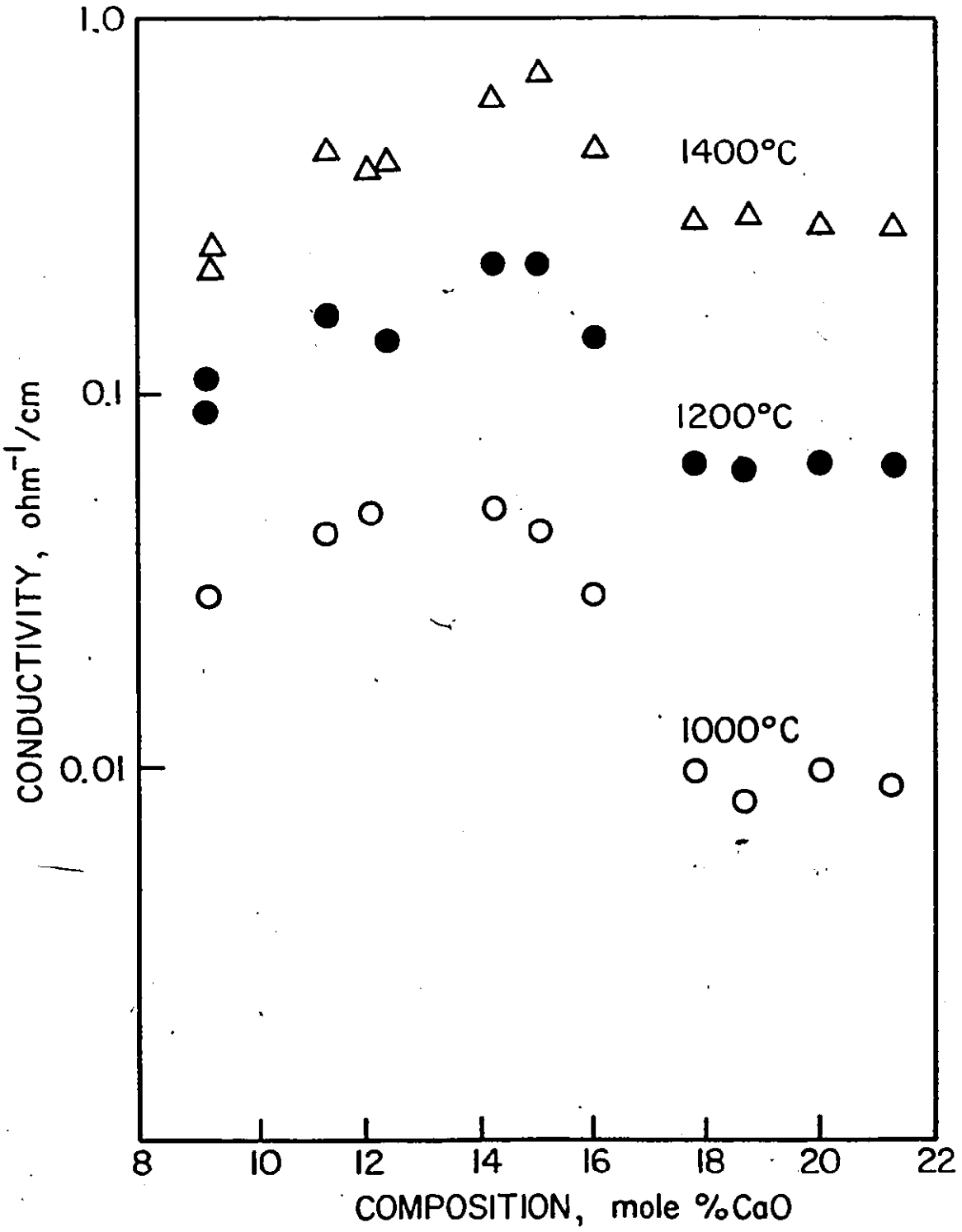

Figure (3-5) Conductivity of ZrO_2(+CaO) as function of composition (81).

TERMINAL 1 (PHASEα)	OXYGEN ELECTRODE 1 (ANODE)	ZrO_2(+CaO)	OXYGEN ELECTRODE 2 (CATHODE)	TERMINAL 2 (PHASEα)

If $t_{O^{--}} = 1.0$ expression (3.6) becomes

$$E = \frac{RT}{4F} \ln \frac{P^c_{O_2}}{P^a_{O_2}} . \qquad (3.7)$$

Calcia stabilized zirconia exhibits very small finite electronic conduction within its well-defined electrolytic domain. This electronic conduction may cause an electrolyte to show a significant permeability to oxygen, especially at high temperature (86,76). This could introduce some error in the emf measurements. The available data, however, indicate that calcia stabilized zirconia shows excellent behaviour as a solid electrolyte for the region where the electronic transference number is less than 0.01. The available data also indicate that oxygen activities imposed by the Cr, Cr_2O_3 coexistence define approximately the lower electrolytic domain boundary of calcia stabilized zirconia.

3.4 Beta-Alumina ($Na_2O.11Al_2O_3$)

β-Al_2O_3 , a fast ionic conductor, was initially suggested to be an allotropic form of α-Al_2O_3 stabilized by small amounts of MgO in α-Al_2O_3 (55). Later it was established that β-Al_2O_3 is a member of a new classification of compounds with the nominal composition of $A_2O \cdot 11M_2O_3$ (where A is Na,K,Pb, or Cs and M is Al,Fe or Ga).

The crystal structure of β-Al_2O_3 as proposed by Beevers and Ross (59) is shown in figure (3-6). The unit cell consists of two spinel blocks which are related to each other by a basal mirror plane of loosely packed oxygen and sodium ions. Each spinel-block consists of four layers of cubic-close packed oxygen ions. The Al^{3+} ions are located as in the spinel $MgAl_2O_4$. The idealized crystal structure proposed by Beevers and Ross has two sodium ions per unit cell in two possible sets of positions in the alkali plane, the first set is at $0,0,\frac{1}{4}$ and the other is at $\frac{2}{3},\frac{1}{3},\frac{1}{4}$. They concluded from their X-ray investigation that the sodium ions were located in the second set referred to as BR positions. The first set of positions was named aBR. These two sets of positions in the alkali plane are shown in figure (3-7).

Yao and Kummer (60) found that the sodium oxygen content in β-Al_2O_3 fused cast refractory is 6.0 to 6.7 w/o Na_2O. The sodium content in the structure of β-Al_2O_3, postulated by Beevers and Ross (59), is 5.24 w/o; therefore, Yao and Kummer (60)

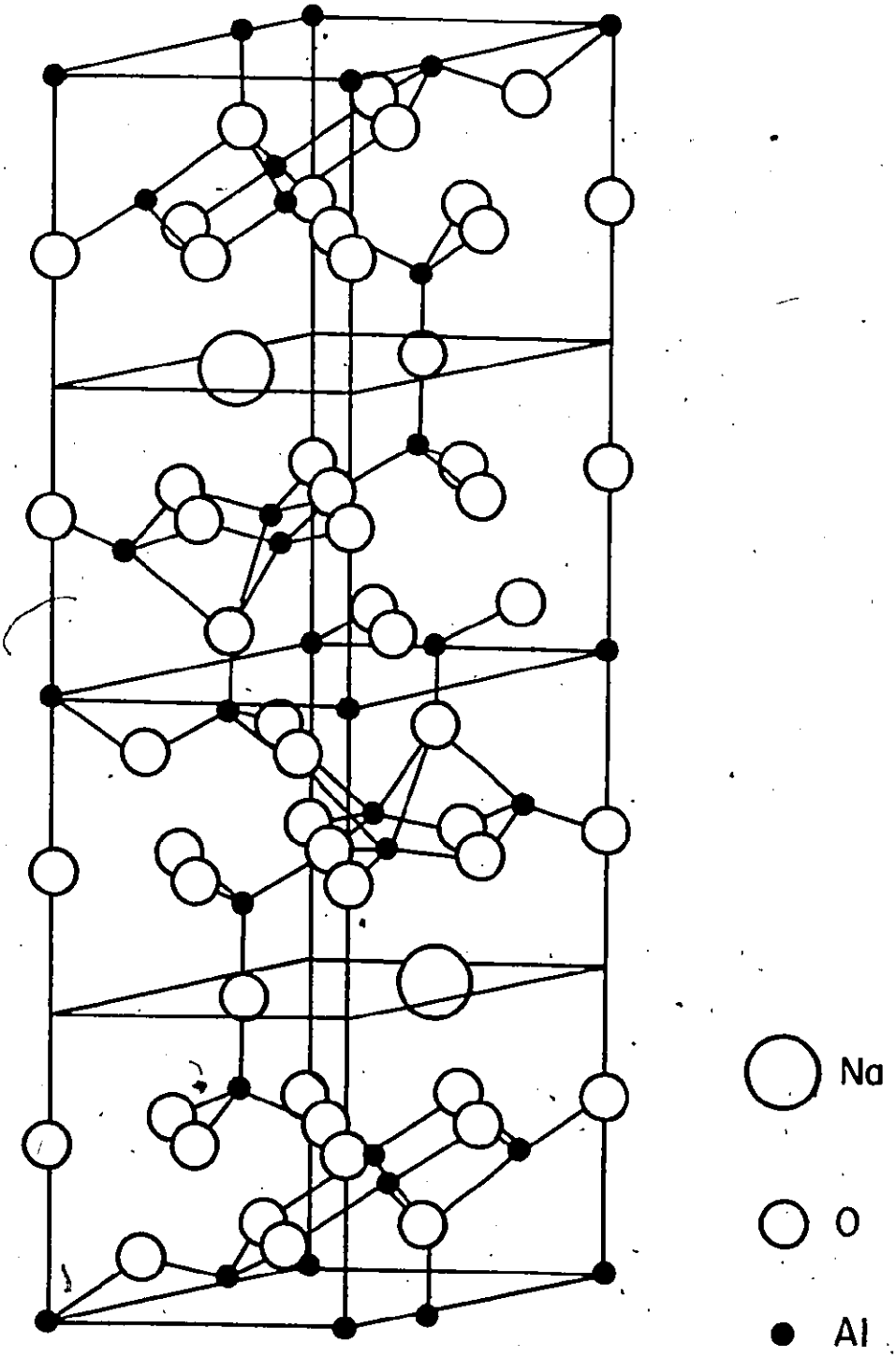

Figure (3-6) Crystal structure of β-Al_2O_3 as proposed by Beevers and Ross (59).

Figure (3-7) Ionic arrangement in loosely packed layer of β-Al_3O_3.

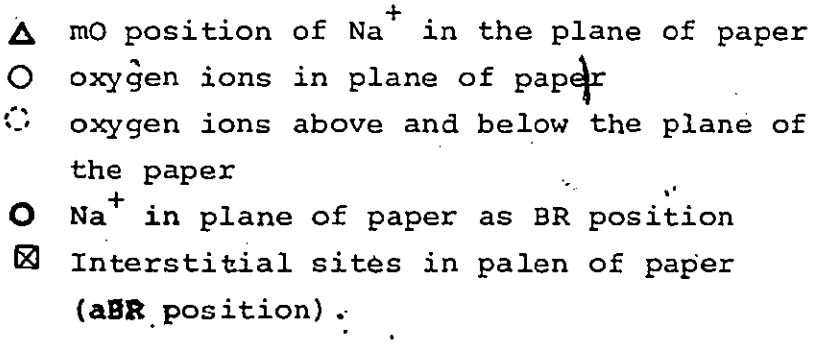

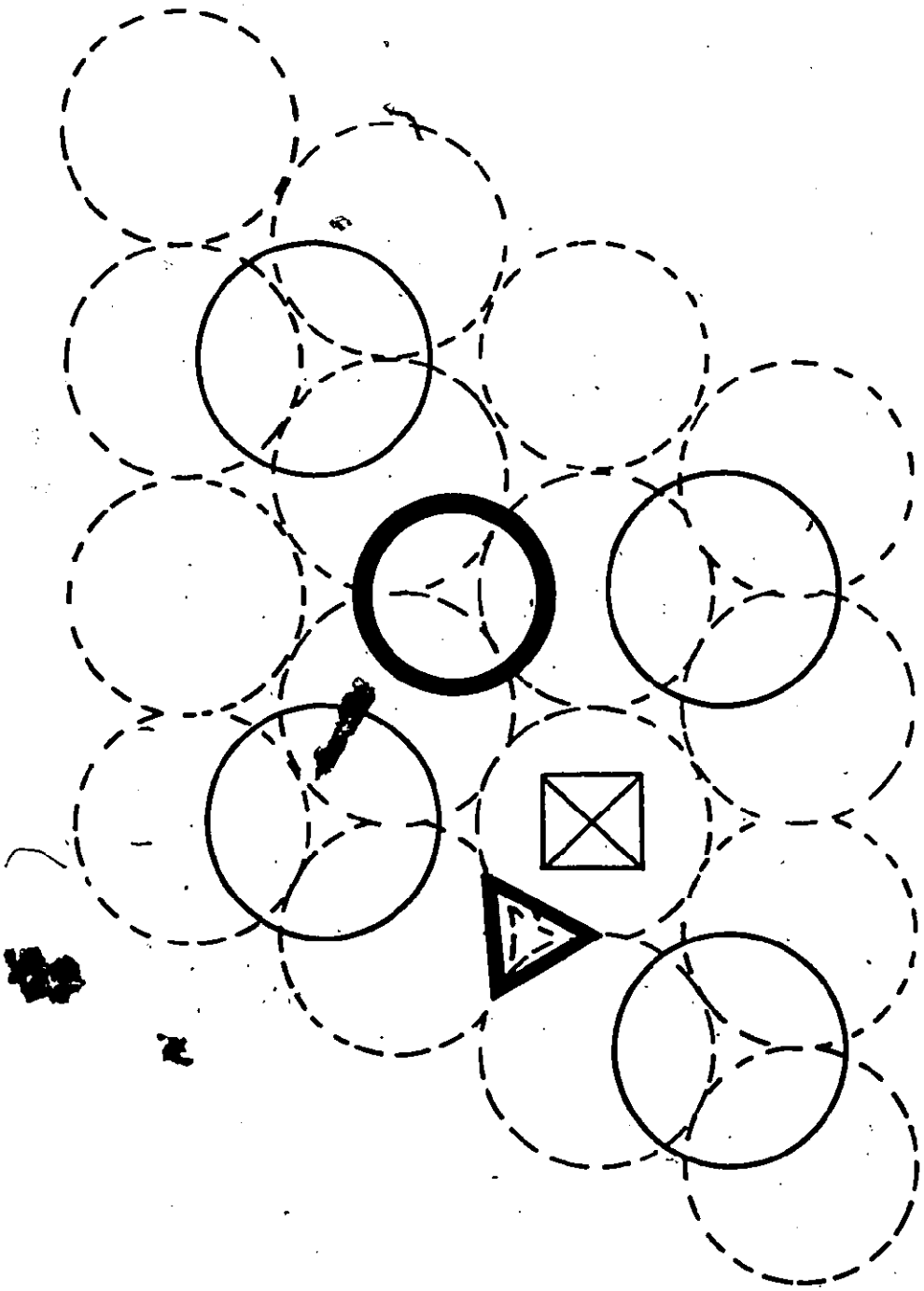

suggested that the unit cell should contain more than two sodium ions with the excess sodium ions in aBR interstitial positions. More recently, the number of sodium ions per unit cell has been studied by Peters et al (88). They found that the aBR positions were not occupied by excess Na^+ even though the Na^+ content per unit cell was 2.58±0.01. Also, they suggested the existence of another reasonable set of positions designated as mO positions for the sodium ions in the basal planes half-way between the oxygen columns. The same investigators suggested the presence of 1.06 sodium ions near the mO positions and 1.51 atoms near the BR position. The mO positions are shown in figure (3-7).

The excess sodium ions should be compensated by the formation of negative defects in the β-Al_2O_3 lattice. The formation of aluminum vacancies of effective charge -3 was suggested by Peters et al. (88) to compensate for the excess Na^+. Diffusional and electrical properties of β-Al_2O_3 have been studied by many investigators. The results of these investigations as well as the practical applications of β-Al_2O_3, are reviewed in reference (89).

3.5 Solid Electrolyte-Electrochemical Cell Design for High Temperature Thermodynamic Measurements

Many different cell designs have been developed, but in general they fall to one of the following two categories:

1 - Separate electrode compartments assembly.

2 - Non-separate electrode compartment assembly.

Kiukkola and Wagner (6,7) used a non-separate electrode compartment assembly. Their cell design is shown in figure (3-8). The cell consisted of a stack of sintered pellets and platinum leads mechanically pressed together. A continuous flow of a purified inert gas was used to minimize the interference of oxygen in the surrounding atmosphere to the equilibrium oxygen potentials established at the electrode-electrolyte interfaces. Rapp (90) found that the voltage of the cell

$$Pt \left| Mo_{(s)}, MoO_{2(s)} \right| Zr_2^{O}(+CaO) \left| Ni_{(s)}, NiO_{(s)} \right| Pt$$

is lower than the expected value by using this type of cell. A cell assembly containing separate electrode compartments gave acceptable emf values. In Rapp's design, shown in figure (3-9), the electrolyte was shaped into the form of 'H' and the electrodes pressed into the deep holes and then capped. The separate electrode compartments assembly could be designed either by using a solid electrolyte tube, figure (3-10), or by pressing one side of the electrolyte against a polished end of an alumina tube (91), figure (3-11).

The cell assembly can be designed for use with dynamic vacuum on both electrode compartments (40), figure (3-12), or with static vacuum in one compartment (92), figure (3-13). Davies (40) has reported that the latter assembly did not improve the emf accuracy, and it is more difficult to operate.

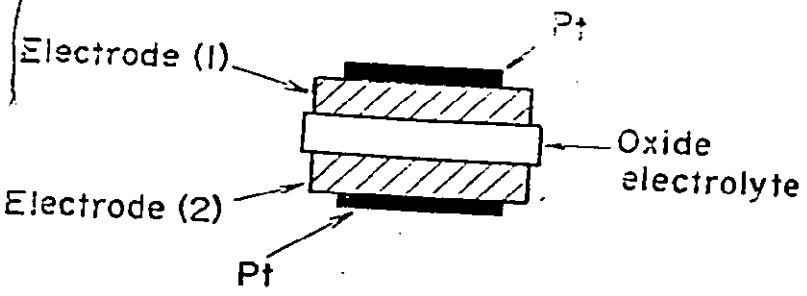

Figure (3-8) Non-separate electrode assembly (6,7).

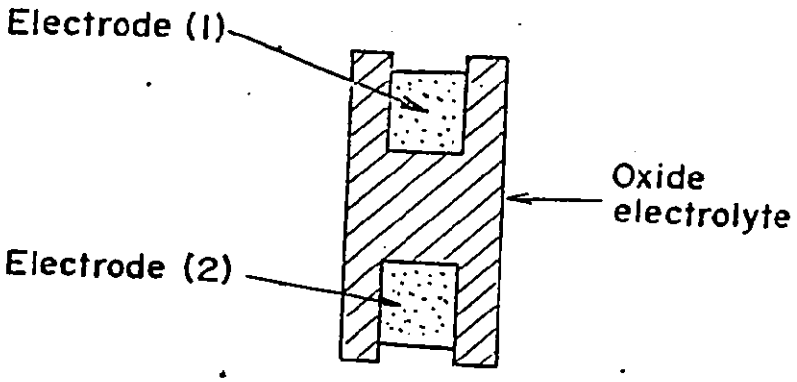

Figure (3-9) H-type electrochemical cell (90).

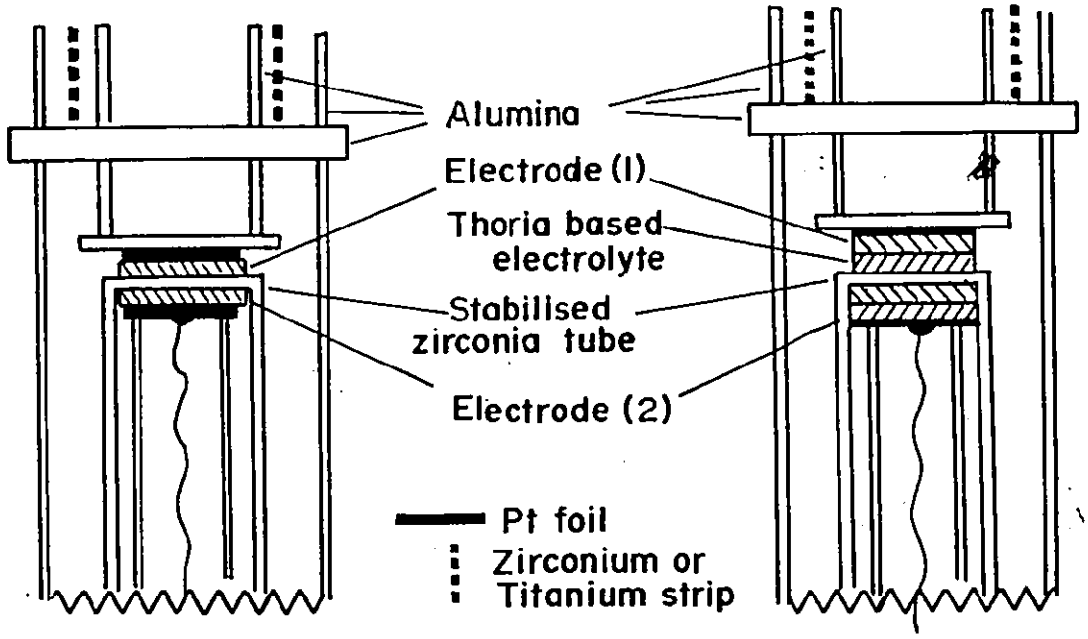

Figure (3-10) Separate electrode assembly, designed by using a solid electrolyte tube (91).

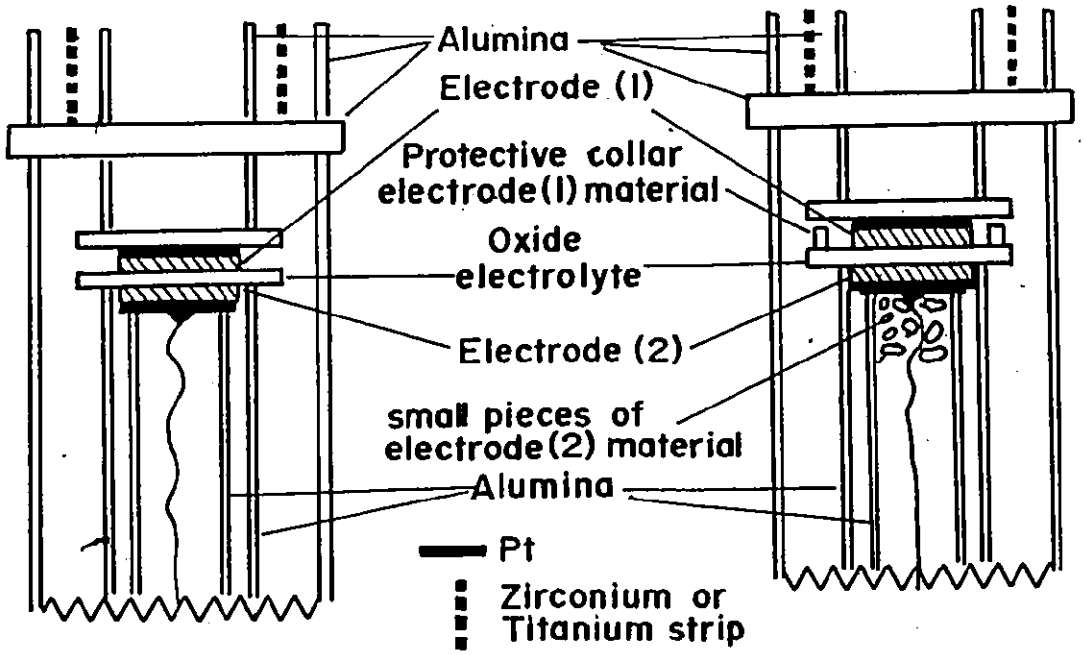

Figure (3-11) Separate electrode assembly, designed by pressing one side of the electrolyte against a polished end of an alumina tube (91).

Figure (3-12) Electrochemical cell assembly, designed for use with dynamic vacuum on both electrode compartments, utilizing a calcia stabilized zirconia tube (40).

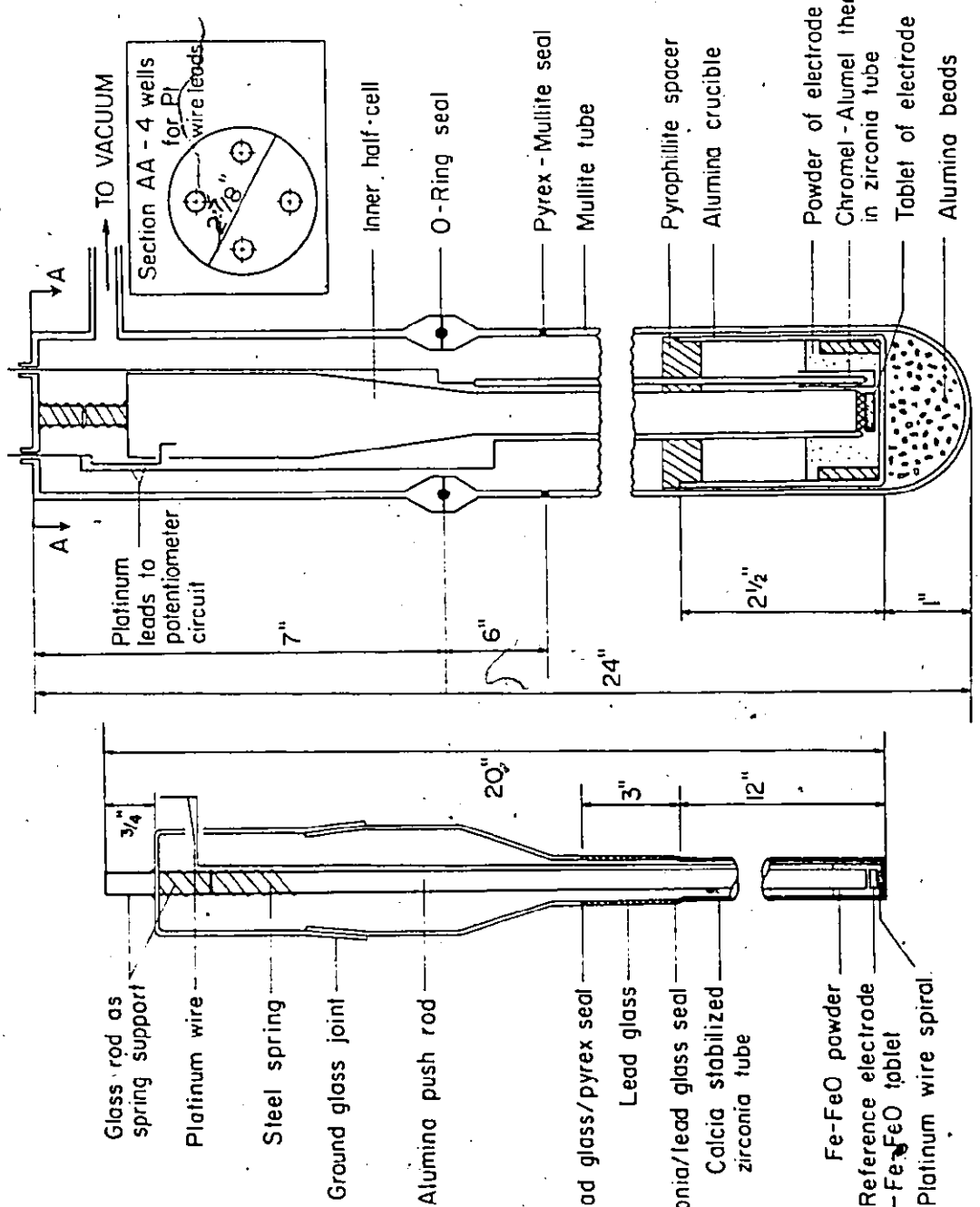
TO VACUUM
A
A
Section AA - 4 wells for Pt wire leads
2 3/8"
Platinum leads to potentiometer circuit
Inner half-cell
O-Ring seal
Pyrex - Mullite seal
Mullite tube
Pyrophillite spacer
Alumina crucible
Powder of electrode material
Chromel - Alumel thermocouple in zirconia tube
Tablet of electrode material
Alumina beads
7"
6"
24"
2½"
1"
20"
3"
12"
3/4"
Glass rod as spring support
Platinum wire
Steel spring
Ground glass joint
Alumina push rod
Lead glass/pyrex seal
Lead glass
Zirconia/lead glass seal
Calcia stabilized zirconia tube
Fe-FeO powder
Reference electrode - Fe-FeO tablet
Platinum wire spiral

Figure (3-13) Electrochemical cell assembly, designed for use with static vacuum in the inner compartment, utilizing a calcia stabilized zirconia tube (92).

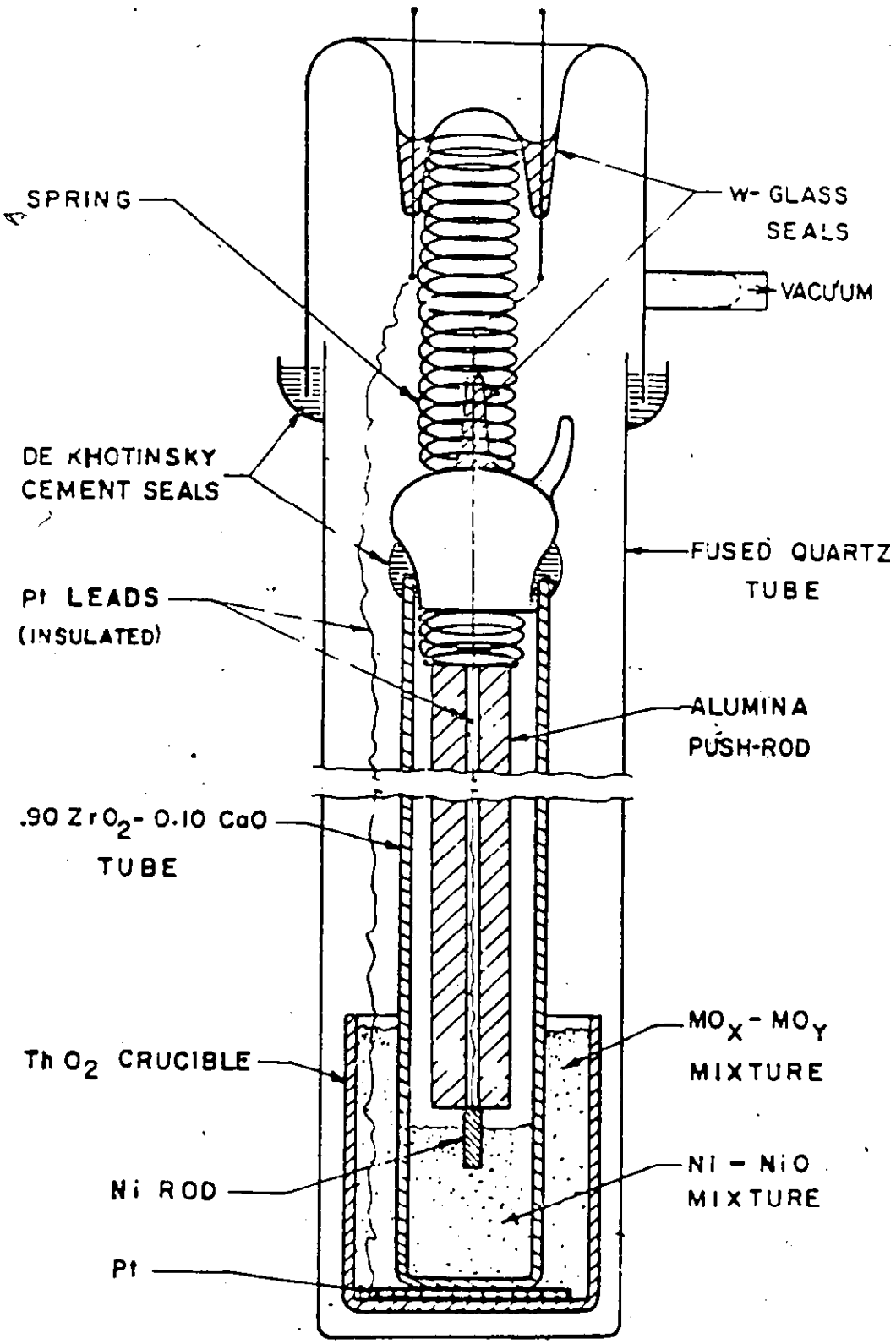
SPRING
W- GLASS SEALS
VACUUM
DE KHOTINSKY CEMENT SEALS
FUSED QUARTZ TUBE
Pt LEADS (INSULATED)
ALUMINA PUSH-ROD
.90 ZrO_2 - 0.10 CaO TUBE
MO_X - MO_Y MIXTURE
ThO_2 CRUCIBLE
Ni ROD
Ni - NiO MIXTURE
Pt

3.6 Limitations and Experimental Considerations in the Use of Solid State Galvanic Cells

Several factors limit the use of solid state galvanic cells for high temperature thermodynamic measurements. Such factors include, electronic conduction, difficulties in maintaining a fixed chemical potential at the electrode-electrolyte interfaces, and general experimental uncertainties. Consequently, several precautions in the experimental work must be taken into consideration.

3.6.1 Electronic Conduction in the Electrolyte

Within the electrolytic domain of a solid electrolyte, the electromotive force of a galvanic cell is a simple function of the chemical potentials at the electrode-electrolyte interfaces, relation (3.7). Outside this range the solid exhibits electronic conduction which must be taken into consideration in calculating the reversible emf. As a result, applications of solid oxide electrolytes are usually limited to the electrolytic domains.

According to Patterson and co-workers (93) calcia stabilized zirconia can be used for thermodynamic measurements at 1000°C over the oxygen pressure range 10^{-23} atm.-10^{5} atm. Baker and West (94) showed that the lower P_{O_2} limit is higher at the same temperature. Fruehan et al. (95) reported that the electrolytic domain boundary in ZrO_2(+CaO) is at about 3.8×10^{-13} atmospheric oxygen pressure at 1600°C.

Thoria doped yttria, ThO_2 ($+YO_{1.5}$), starts to exhibit positive hole conduction at oxygen pressure above 10^{-6} atm. at 1000°C but it remains as an ionic conductor at oxygen pressure down to 10^{-25} atm. (96).

Sodium β-Al_2O_3, with nominal composition $Na_2O.11Al_2O_3$, has been used to measure the chemical potential of monovalent cations; however, Choudhury (22) used the two phase mixture of sodium β-Al_2O_3 and α-Al_2O_3 as solid electrolytes in galvanic cells with electrodes that fix oxygen chemical potentials. Results indicated that this two-phase mixture can be used to measure the oxygen chemical potentials as low as those established by Al, Al_2O_3 coexistence ($P_{O_2} \approx 10^{-47}$ atm. at 1000K).

3.6.2 Maintaining a Fixed Chemical Potential at the Electrode-Electrolyte Interfaces

Unstable emfs will arise from a change of chemical potential at the electrode-electrolyte interface, this may arise from electronic conductivity in the solid electrolyte, reactions within the electrode, reaction between the electrode and the electrolyte or the electrical contact material, or interference from oxygen in the surrounding atmosphere. Because of the high chemical stabilities of ZrO_2(+CaO) and ThO_2($+YO_{1.5}$), an electrode-electrolyte reaction can occur only when a very stable ternary oxide compound is formed as a reaction product. Worell et al. (96) have detected from the examination of the X-ray diffraction patterns the formation of a $YFeO_3$ phase on ThO_2($+YO_{1.5}$) which indicated that a reaction between the

electrolyte and the Fe,FeO electrode occured. The precautions necessary to maintain a fixed chemical potential at the electrode-electrolyte interface are discussed in section (3.6.4).

3.6.3 Experimental Uncertainties

The average uncertainty in an electrochemical cell measurement is ± 1 mV, which is ± 46 cal. per gm. atm. of oxygen in the Gibbs free energy change. Because the temperature range of a typical emf investigation is narrow Schmalzried (97) has indicated that the uncertainties in ΔH is usually about ± 500 cal/g. atom; however, Wagner has pointed out that high temperature ΔH values obtained from electrochemical cell measurements may be more reliable in some cases than that calculated by combining calorimetric measurements at 25°C with high-temperature enthalpy increments.

3.6.4 Experimental Considerations

Unstable emfs in a solid state galvanic cell may arise from reactions within the electrodes during electrochemical measurements. This can be minimized by electrode equilibration before cell operation. Pressed electrode pellets of small particles decrease equilibration times. Also, as the number of electrode phases increases, more equilibration time is required because points of contact are limited. The electrode may have a certain distribution of components between the different phases when originally prepared, but when measurements are taken at different temperatures, phase equilibration must be

achieved by heating for some time.

Interaction between the electrical contact material and the electrode affect the cell emf and therefore a suitable lead must be chosen. Dias and Richardson (98) found that a commercial cermet consisting of 72% chromium and 28% Al_2O_3 was very satisfactory as a contact to solutions of oxygen in liquid copper while a Mo-Al_2O_3 cermet was heavily attacked.

To minimize the influence of oxygen in the surrounding atmosphere on the equilibrium chemical potential at the electrode-electrolyte interfaces, it is found preferable to make high-temperature electrochemical measurements in a flowing inert atmosphere rather than at very low pressure. The partial pressure of oxygen in the inert gas can be reduced to approximately 10^{-15} atm. by purification (99). An oxygen "getter" should be placed inside the reaction tube, upstream from the cell, particularly when the oxygen pressure fixed by the electrodes is below 10^{-20} atm. (99). An electrode-electrolyte interface should expose a minimum surface area to the cell atmosphere. This can be accomplished by polishing the electrode surface to have maximum contact at electrode-electrolyte interfaces, and also by covering the electrode-electrolyte interface with a powder of identical composition to that of the electrode.

Dias and Richardson (98) suggested that the decay of emf with time at constant temperature may be due to either gas transfer through pores and microcracks in the electrolyte or

electronic conduction in the electrolyte. They developed a technique of depolarizing a cell by applying an external voltage so as to increase the emf above the expected equilibrium value. When the external voltage was removed, the cell emf decayed rapidly to a steady reproducible value, which was the expected equilibrium value. It is reported that larger currents and shorter times of application cause a cell to remain depolarized for longer time periods (98).

3.7 Summary

The application of the emf technique to high temperature thermodynamic measurements has found broad useage since the introduction of calcia stabilized zirconia as a solid electrolyte exhibiting ionic behaviour, within a certain range of p_{O_2} and temperature. Recently, numerous solid electrolytes have been developed and a number of investigations based on this technique have been carried out. The cell design and several precautions must be taken into consideration to overcome problems encountered in the use of these solid state galvanic cells. Limitations in the use of this technique have given rise to several fruitful areas of research involving the problems of cell stability and the fabrication of solid electrolytes in the suitable form and size, development of new solid electrolytes, and studies of the thermodynamic properties of these materials.

CHAPTER 4

EXPERIMENTAL TECHNIQUES

4.1 Materials

The types and sources of materials used in this investigation are listed in table (4-1). Nickel spinel and β"-Al_2O_3 were prepared in this laboratory.

Nickel and aluminum nitrates were used to form the nickel spinel. The procedure used was as follows: $Ni(NO_3)_2.6H_2O$ and $Al(NO_3)_3.9H_2O$ crystals were dissolved in distilled water in proportions to give the stoichiometric Ni/Al composition of nickel spinel, $NiAl_2O_4$. The solution was then heated in a sand bath held at 200°C to evaporate water. The mixed solid was then heated at 700°C for 24 hours to decompose the nitrates. The weight of the product, after heating for 24 hours at 700°C, indicated that the nitrate decomposition was complete. X-ray powder analysis was carried out to identify the phases in the dried mixture. The diffraction patterns corresponded to pure NiO. The absence of other diffraction lines indicated the following: a) Aluminum oxide in the mixture was amorphous or microcrystalline. b) The spinel phase was not synthesized; or, if the spinel phase was formed, it was amorphous or microcrystalline.

Material	Source	Purity
Nickel Powder	Ventron, Alfa Products (00224)	>99.9%
Iron powder	Ventron, Alfa Products (00170)	>99.9%
Aluminum powder	Ventron, Alfa Products (00010)	99.8%
Nickel chunks	Falconbridge Company	99.99%
Electrolytic iron chips	*	≈99.9%
Aluminum chunks	Alcan Company	99.95%
Tungsten powder	Fisher Scientific Company (T-363,79808)	purified powder
Sodium Metal	Fisher Scientific Company (S-135)	>99.9%
Nickel oxide powder	Fisher Scientific Company (N-69)	>99.8%
Wustite powder	**	**
Magnetite powder	-	99.8%
Hematite powder	Ventron, Alfa Products (87319)	99.9%
Aluminum oxide powder (α)	Ventron, Alfa Products (87354)	99.99%
Nickel nitrate [$Ni(NO_3)_2 \cdot 6H_2O$]	Fisher Scientific Company (N-63)	>99.8%
Aluminum nitrate [$Al(NO_3)_3 \cdot 9H_2O$]	Fisher Scientific Company (A-586,70420)	99.0%
Tungsten sulfide powder (WS_2)	Ventron, Alfa Products (65103)	-
Sodium sulfide powder (Na_2S)	Ventron, Alfa Products (65122)	-
Nickel fluoride powder (NiF_2)	J. T. Backer Chemical Company (NX327-05)	-

Material	Source	Purity
Sodium fluoride powder (NaF)	J. T. Backer Chemical Company (1-3688)	>99.5%
Sodium Carbonate powder (Na_2CO_3)	Fisher Scientific Company (S-263)	>99.8%
β-alumina powder ($Na_2O.11Al_2O_3$)	ALCOA Superground-high quality grade Lot P-1750-18	-

Table (4-1) Materials used in this investigation.

*) Electrolytic iron chips were supplied by the metallurgy store of McMaster University with purity 99.9^{+}%.

**) Wustite powder was prepared by T. Elkasabgy; the preparation method and the purity of the material are reported in reference (122).

The diffraction lines were somewhat diffuse which indicated that NiO cyrstals in the mixture were very fine. The samples were then heated at 1300°C for a week and then air cooled. X-ray powder analysis indicated the presence of nickel spinel as the sole phase in the powder after heating for a week at 1300°C.

Materials for preparing β"-Al_2O_3 were α-Al_2O_3 and Na_2CO_3 mixed in the following proportions: 82.6 w/o Al_2O_3 and 17.4 w/o Na_2CO_3. The mixture was tumbled in a plastic bottle for 24 hours to ensure complete mixing and then heated in a Pt crucible at a temperature between 1000°C and 1400°C for a period of 3 - 15 hours followed by furnace cooling. The different phases identified using X-ray powder diffraction technique in the products are shown in table (4-2).

4.2 Solid-Electrolyte Tube Fabrication

Disks, pellets, tubes and crucibles of β-Al_2O_3 have been prepared in different laboratories using several procedures. Machining of the fused cast brick was used (100) to fabricate different shapes. Many investigators (101-103) have used hot and cold die pressing to prepare β-Al_2O_3 pellets and disks. The green material was sintered at temperatures as high as 1830°C (102). Electrophoresis has been used (104-108) to fabricate many shapes of β-Al_2O_3. Tubes (109,111) and disks and spheres (111) have been prepared by isostatic pressure moulding followed by

Temperature, °C	Time, hours	Phases
1000	3	α-Al_2O_3
	5	α-Al_2O_3
	15	α-Al_2O_3
1100	3	α-Al_2O_3
	5	α-Al_2O_3
	16	α-Al_2O_3 + β- and/or β"-Al_2O_3
1200	3	α-Al_2O_3 + β"-Al_2O_3
	5	α-Al_2O_3 + β-Al_2O_3 + β"-Al_2O_3
	14	β-Al_2O_3 + β"-Al_2O_3
1300	3	β-Al_2O_3 + β"-Al_2O_3
	5	β-Al_2O_3 + β"-Al_2O_3
	13	β-Al_2O_3 + β"-Al_2O_3
1350	15	β-Al_2O_3 + β"-Al_2O_3
1400	3	β-Al_2O_3 + β"-Al_2O_3
	5	β-Al_2O_3 + β"-Al_2O_3
	13	β-Al_2O_3 + β"-Al_2O_3

Table (4-2) Synthesis of β"-Al_2O_3 from α-Al_2O_3 and Na_2CO_3 mixture as determined by X-ray diffraction analysis.

sintering at high temperature. Liang and Elliott (112) prepared β-Al_2O_3 crucibles by drilling prefabricated rods. The rods were prepared by die pressing, then isostatic pressing followed by sintering at 1000°C for one hour while packed in coarse β-Al_2O_3 powder. The crucibles were then fired at 1750°C in air for a period of 20 - 30 minutes. An edge-defined film-fed growth technique has been used (113) to produce single-crystal β-Al_2O_3 tubes and ribbons. Byckalo et al. (114) used slip casting of a suspension in water to fabricate β-Al_2O_3 tubes. Plaster molds were used in this preparation and the green tubes were sintered at temperatures in the range 1600°C-1800°C. River and Pelton (115) slip cast β-Al_2O_3, using suspensions in methanol, in α-Al_2O_3 powder molds. The tubes obtained were then sintered at 1550°C for 2 hours.

The following three kinds of tubes were prepared in this investigation for electrochemical measurements:

1 - Single phase β-Al_2O_3 tubes.

2 - Two phase mixture of α-Al_2O_3 and β-Al_2O_3 tubes.

3- Two phase mixture of β-Al_2O_3 and β"-Al_2O_3 tubes.

The materials used in preparing these tubes were 99.99% α-Al_2O_3 received from Ventron (-200 mesh), XB-2 superground calcined β-Al_2O_3 powder received from Alcoa (-120 mesh), and the β- and β"-Al_2O_3 mixture prepared in this laboratory by heating a mixture of α-Al_2O_3 and Na_2CO_3 (-120 mesh) at 1350°C for 15 hours.

The XB-2 β-Al_2O_3 powder was ground in a ball mill with alumina balls. Fallah (89) reported that after 24 hours of grinding under isopropyl alcohol, about 98 w/o of the powder was less than 8 μm in diameter. River and Pelton (115) mentioned that the mean diameter of the particles was decreased to 0.5 μm after 72 hours of grinding under methanol. The two methods were used by the author to prepare the necessary amount of β-Al_2O_3 powder to fabricate the solid electrolyte tubes. The method recommended by River and Pelton was used to grind the two phase mixture of β- and β"-Al_2O_3 into a very fine powder. Each charge for the ball mill consisted of 200 g of the solid and 250 ml of the liquid. After grinding, the suspension was left in 600 ml pyrex beaker to dry in air for three days before drying in an oven at 120°C for 15 hours.

Solid electrolyte tubes were fabricated by slip casting an aqueous suspension of the desired composition. The plaster molds were prepared from an equal amount (by weight) of Pottery plaster and water. Water was placed initially in the 4000 ml pyrex beaker, then the plaster was added gradually while a mechanical stirrer was operating to mix the two constituents. It took about 3 minutes of stirring to obtain a homogeneous mixture. After removing entrapped bubbles by shaking the beaker, the mixture was then poured into a cylindrical-aluminum mold containing an aluminum rod as a core. The aluminum core as well as the inside of the aluminum mold were greased using glycerine before pouring to ensure smooth removal of the

plaster mold as well as the aluminum-rod core. This was normally done after 4 hours of pouring. The plaster mold dimensions are illustrated in figure (4-1).

Materials for preparing the different types of electrolyte tubes are summarized in table (4-3). The following procedure was found to be best for preparing a smooth slip:

1. Distilled water was charged first to the ball mill.
2. Darvin C followed by hydrochloric acid were then added and the ball mill shaken by hand to obtain a homogeneous solution.
3. In all cases β-Al_2O_3 powder was first added gradually to the solution then either α-Al_2O_3 or β- and β"-Al_2O_3 powder was charged. Before charging α-Al_2O_3 or β- and β"-Al_2O_3 the mixture was shaken by hand for a few minutes to obtain a homogeneous suspension of β-Al_2O_3 in water.
4. The mixture was then tumbled together for about 3 hours. The pH was checked each 15 minutes and readjusted to 8 for the β-Al_2O_3 and the β- and β"-Al_2O_3 suspension and to 7 for the α- and β-Al_2O_3 suspension in order to have smooth slips.
5. After these steps the suspension was transferred to a 500 ml pyrex beaker and cast into the plaster mold.

A plaster mold, which exhibited no visible cracks, was moderately wetted before casting to prevent very fast setting. The slip was poured into the mold, left for a period of 30 seconds, then the mold turned upside-down to remove excess slip.

Tube Type	Starting materials					
	α-Al_2O_3	β-Al_2O_3	β"-Al_2O_3	Distilled water	Hydrochloric acid	Darvin C*
β-Al_2O_3	-	400 g.	-	320 ml	8 ml	4 g.
β-and α-Al_2O_3	40 g.	360 g.	-	300 ml	6 ml	3 g.
β- and β"-Al_2O_3	-	150 g.	250 g.	350 ml	8 ml	5 g.

Table (4-3) Starting materials used in preparing suspensions for slip casting the ceramic tubes.

*) Darvin C is an ammonium salt of a polyelectrolyte; it was used as a defloculent in preparing the slips.

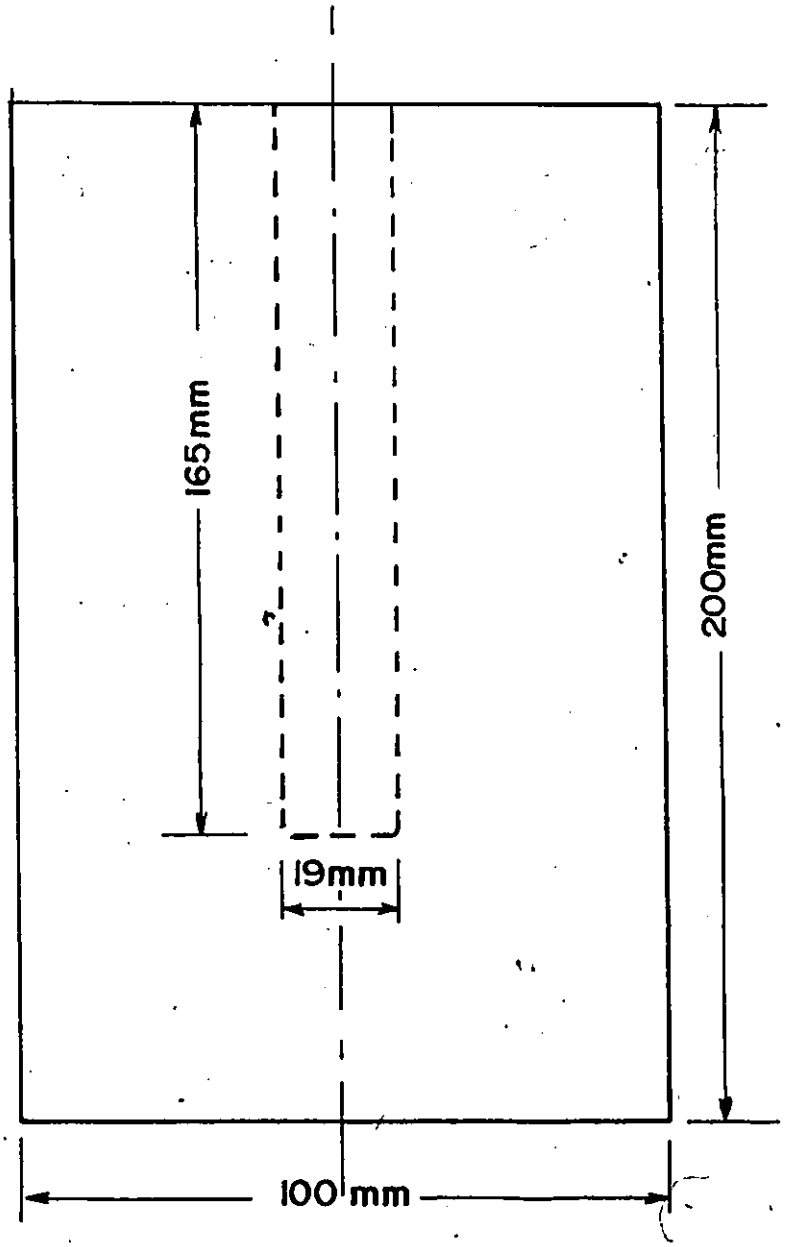

Figure (4-1) Dimensions of a typical plaster mold.

During the casting period, the slip level should be kept always at the top of the mold. Tube cracking was found to be minimal if the upper edge of a tube was removed from the mold using a spatula within 5 minutes of the casting. The tubes were then left in the plaster mold for a period of 48 hours to dry. The long drying period allowed easy tube removal. A shrinkage of about 10% in the length of the tubes was observed. The average wall thickness of the green tubes was approximately 2 mm. The tubes were left for at least a week in air at room temperature to allow for complete drying. Figure (4-2) shows a photograph of five green tubes.

Before sintering the tubes, the outer surfaces were polished using 320 grit emery paper and the upper edges trimmed and polished. Five tubes were then placed in an α-Al_2O_3 crucible which was then packed with a coarse powder having the same composition of the tubes. Figure (4-3) shows a composite photograph illustrating the arrangement of the green tubes inside the α-Al_2O_3 crucible, this was then covered by an α-Al_2O_3 cover. The whole unit was prefired at 700°C for 14 hours to allow complete drying before sintering. The β-Al_2O_3 tubes and the α- and β-Al_2O_3 tubes prepared from the less fine powder (grain size $\leq$ 10 µm were sintered at 1800°C for 3 hours. Figure (4-4) illustrates a typical heating and cooling curve of the sintering process. The β- and β''-Al_2O_3 tubes and α- and β-Al_2O_3 tubes prepared from the fine powders (mean grain size $\simeq$ 0.5 µm) were

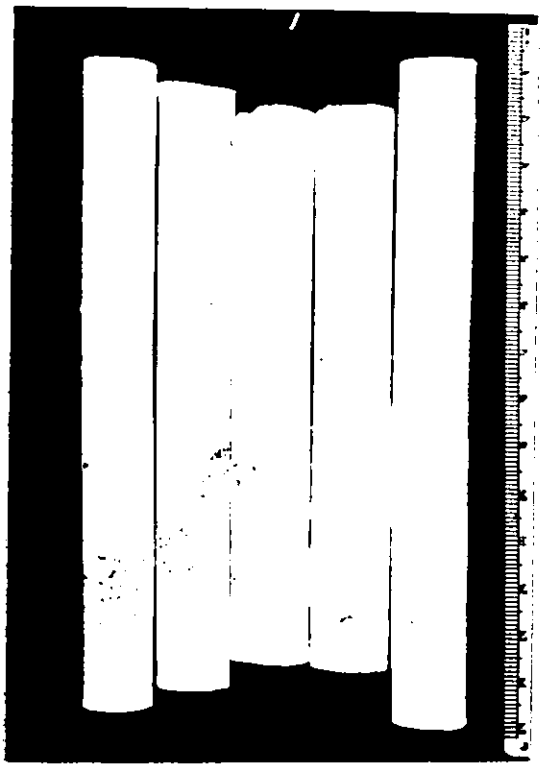

Figure (4-2) The appearance of five β- and α-Al_2O_3 green tubes after removing from the plaster moulds.

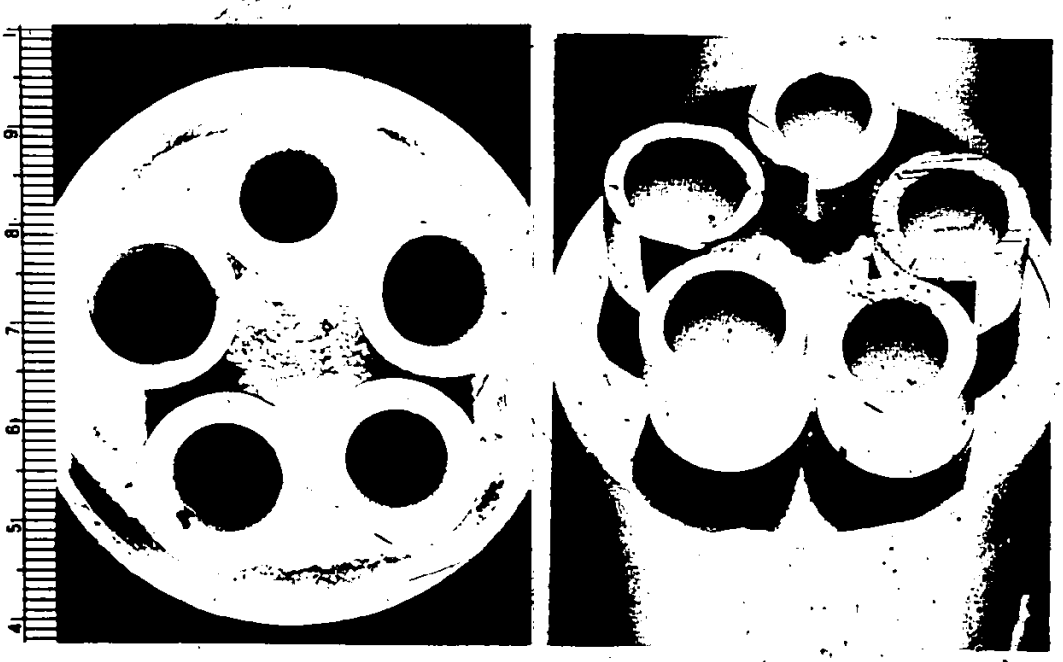

Figure (4-3) A composite photograph illustrating the arrangement of the green tubes inside the α-Al_2O_3 crucible prepared for sintering the tubes.

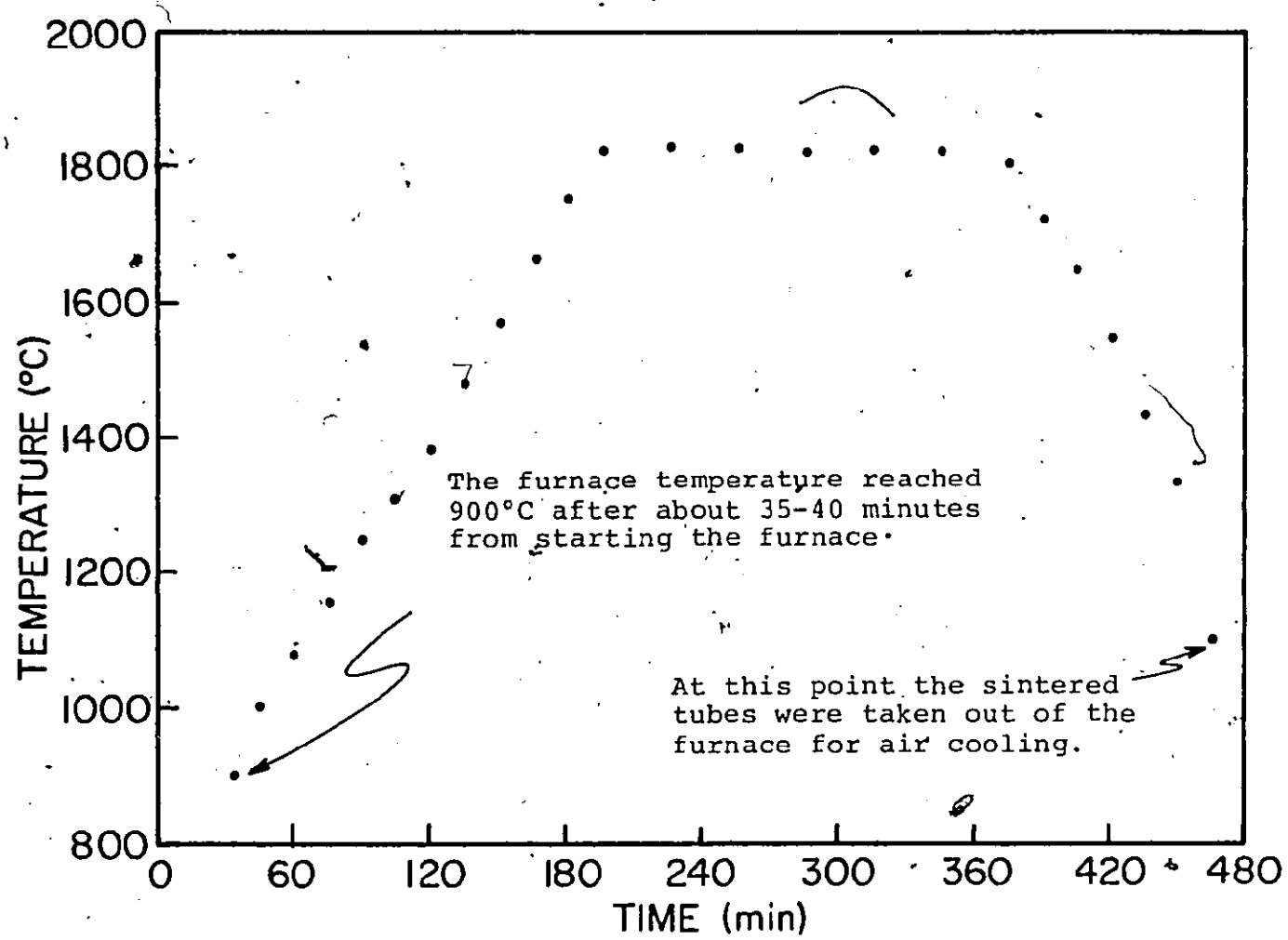

Figure (4-4) The temperature-time curve for a typical sintering run of the ceramic tubes at 1800°C.

sintered at 1550°C for 3 hours. Heating and cooling rates in this case were 300°C/hr. X-ray powder diffraction analyses confirmed the presence of only the desired phases in the several different kinds of tubes after the sintering procedure. A shrinkage of about 30% in the length and diameter of tubes occurred from sintering. Figure (4-5) shows a photograph of five tubes after sintering. About 80% of the sintered-α- and β-Al_2O_3 tubes exhibited a 10^{-8} Torr He-leakage resistance using a Varian MS-90 helium leak detector. Only one run was completed to prepare β-Al_2O_3 and β- and β"-Al_2O_3 electrolyte tubes. Of the 5 green tubes charged for sintering, two β-Al_2O_3 tubes and only one β- and β"-Al_2O_3 tube exhibited 10^{-8} Torr He-leakage resistance. Tubes sintered at 1800°C were fired in a combustion-gas furnace (Bickley Furnaces Inc. 1800 B) using propane as fuel. Tubes sintered at 1550°C were fired in an electric furnace (CM Inc., High Temperafure Furnace 78604) using molybdenum disilicide heating elements.

4.3 Sample Preparation

4.3.1 Aluminum, α-Alumina, β-Alumina System

To determine the sodium content in the Al phase of the Al, α-Al_2O_3, β-Al_2O_3 equilibria, α-Al_2O_3 tubes 8 mm in diameter and 50 mm in height were filled with a mixture of the above constituents as follows. One gram of Al powder (-200 mesh) was first placed in a tube and this layer was then covered by one

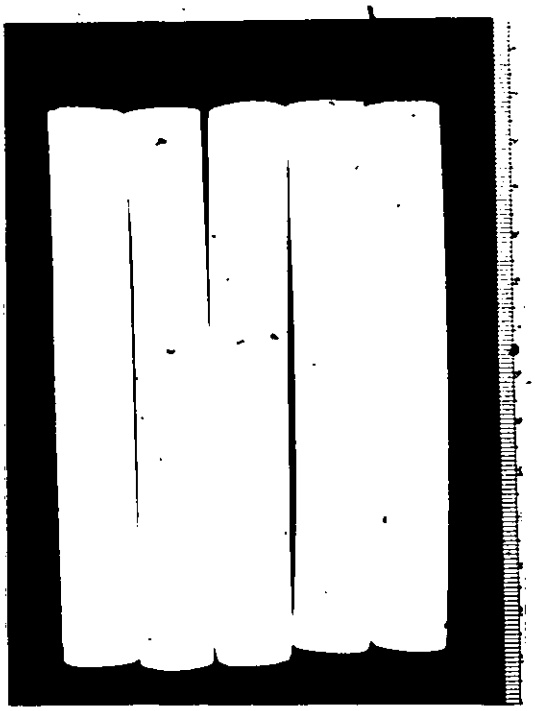

Figure (4-5) 5 sintered-electrolyte tubes of β- and α-Al_2O_3; the tubes were sintered at 1800°C for 3 hours.

gram of α- and β-Al_2O_3 mixture (-200 mesh). This mixture was prepared by tumbling equal weights of α-Al_2O_3 and β-Al_2O_3 powder in a plastic bottle for about 15 hours followed by firing at 1000°C for a week. After loading with oxide-powder mixture, the tubes were sealed using autostic cement, supplied by Carlton Brown and Partners Ltd. These samples were then annealed for 15 hours in tubular-electric furnace, Lindberg type, under flowing-purified argon atmosphere. The annealing temperatures were 700, 800, 900 and 1000°C and two samples were annealed at each temperature. The samples were air cooled to room temperature which was reached in about 5 minutes. X-ray powder analysis confirmed the presence of α-Al_2O_3 and β-Al_2O_3 as the only oxide phases. A single-metallic Al layer was found in all the tubes and its Na contents were determined by atomic absorption.

4.3.2 Nickel Oxide-Aluminum Oxide System

The compositions of nickel spinel equilibrated with NiO or α-Al_2O_3 at temperatures in the range 1000-1900°C were determined using the electron probe microanalyzer. The starting materials were NiO powder (-120 mesh), α-Al_2O_3 powder (-200 mesh), and $NiAl_2O_4$ (-200 mesh). Two types of mixtures were formed; the first was a mixture of NiO and $NiAl_2O_4$ with the molar ratio of 1:1, respectively, and the second was an α-Al_2O_3, and $NiAl_2O_4$ mixture with the molar ratio 4:1, respectively. Each mixture was tumbled for 24 hours in a plastic bottle to ensure complete mixing of

the constituents. Tablets, 3/8" in diameter and about 1/8" in thickness, were then pressed from each mixture using a silicon carbide die and a hydraulic press at 80,000-100,000 psi with no binder. The pellets were then annealed in between 1000°C and 1900°C at intervals of 100°C. The annealing conditions of the different pellets are summarized in table (4-4).

4.3.3 Nickel-Aluminum-Oxygen System

Alloy-oxide (or oxides) tablets belonging to the Ni-Al-O system were prepared for electrochemical and/or electron probe microanalyses. The compositions of the tablets corresponded to the following coexistences: a) Ni-NiO-$NiAl_2O_4$, b) Ni-spinel-$Al_2O_{3(\alpha)}$ and c) Ni-Al alloy, $Al_2O_{3(\alpha)}$. Materials used in preparing the pellets were Ni powder (-200 mesh), Al powder (-200 mesh), NiO powder (-120 mesh), $NiAl_2O_4$ powder (-200 mesh) and α-Al_2O_3 powder (-200 mesh). Table (4-5) describes the starting compositions of the mixtures used in preparing the different pellets. The mixtures were fabricated into pellets using the procedure described in the preceding section. The tablets were then annealed at 1000°C in a tubular electric furnace. After annealing, the pellets were air cooled, reaching room temperature in about 5 minutes. All the pellets of this system were annealed in an α-Al_2O_3 crucible except those belonging to Ni-NiO-$NiAl_2O_4$ system which were annealed while sitting on a stoichiometric-spinel pellet. During an annealing period,

Sample	Annealing Conditions	
	Temperature, °C	Period, hours
SA19AR	1920	3
SA19AI	1920	2
SA18AR	1800	14
SA18AI	1800	5
NS18AR	1800	20
NS18AI	1800	5
SA17	1700	124
NS17	1700	124
SA16	1600	100
NS16	1600	100
SA15	1500	168
NS15	1500	168
SA14	1400	168
NS14	1400	168
SA13	1300	168
NS13	1300	168
SA12	1200	168
NS12	1200	168
NS11	1100	168
SA11	1100	168
NS10	1000	168
SA10	1000	168

Table (4-4) Annealing conditions of $NiO-NiAl_2O_4$ and spinel-$Al_2O_{3(\alpha)}$ samples.

Notes:

a) Samples designated as SA were prepared from α-Al_2O_3-$NiAl_2O_4$ mixture while samples designated as NS were prepared from NiO-$NiAl_2O_3$ mixture.

b) All samples were annealed in air except samples SA19AR, SA18AR, and NS18AR which were annealed under atmospheric argon pressure.

c) Samples annealed at temperatures less than 1500°C were previously annealed at 1500°C for 168 hours.

d) Samples annealed at 1400°C or less were annealed in a tubular-electric furnace with SiC heating elements, Lindberg type; samples annealed at 1500-1700°C were annealed in a box-electric furnace with $MoSi_2$ heating elements, CM Inc., High Temperature Furnace 78604; samples annealed under argon atmosphere were annealed in an induction furnace, Arthur D. Little, Model MP, using RF induction heating; the remaining samples were annealed in a combustion-gas furnace, Bickley Furnace Inc. 1800 B.

e) Pellets annealed at 1500°C or less were air cooled, while samples annealed at 1600°C and 1700°C were furnace cooled down to 1500°C in about 10 minutes and then air cooled. The temperature of the gas furnace was brought to 1100°C in about 10 minutes, then the samples fired inside the gas furnace were air cooled. The induction-furnace temperature reached 250°C in about four minutes, then the samples sintered inside the furnace were argon cooled to room temperature.

Pellet*	The starting contents of the pellets in weight percent				
	Al	Ni	NiO	$NiAl_2O_4$	α-Al_2O_3
NSN	-	50	25	25	-
SAN	-	50	-	25	25
NA0.1A	0.05	49.95	-	-	50
NaO.5A	0.25	49.75	-	-	50
NA1.0A	0.50	49.50	-	-	50
NA2.3A	1.15	48.85	-	-	50
NA12A	6.00	44.00	-	-	50
NA22A	11.00	39.00	-	-	50
NA27A	13.50	36.50	-	-	50
NA30A	15.00	35.00	-	-	50
NA35A	17.50	32.50	-	-	50

Table (4-5) Starting compositions of mixtures belonging to Ni-Al-O systems.

*) The composition point of NSN pellets is Ni-NiO-$NiAl_2O_4$, SAN samples correspond to Ni-spinel-$Al_2O_{3(\alpha)}$ phase field, and the other samples belong to alloy-$Al_2O_{3(\alpha)}$ equilibria. NSN and SAN tablets were annealed at 1000°C for 60 days while the other samples were annealed for 30 days at 1000°C.

purified argon was kept flowing through the furnace. The argon was purified by passing it over Cu-Cu_2O mixture held at 180°C to oxidize CO and H_2 which were then absorbed by passage through ascarite, Ca SO_4, and silica gel. An oxygen getter, Zr chips, was placed inside the furnace tube, upstream from the sample, to prevent oxidation of the metallic phases in the different pellets.

4.3.4 Iron-Aluminum-Oxygen System

Tablets belonging to the Fe-Al-O system were prepared from Fe powder (-200 mesh), Al powder (-200 mesh), wustite powder (-100 mesh), Fe_3O_4 powder (-200 mesh), Fe_2O_3 powder (-200 mesh), and α-Al_2O_3 powder (-200 mesh). Table (4-6) summarizes the different kinds of prepared tablets and the compositions of the mixtures used in preparing these tablets. The method used in forming pellets from the powder mixtures was the same as that described in section (4.3.1). The samples were annealed under a flowing-purified argon atmosphere in a tubular electric furnace. The argon was purified in the manner described in the previous section. During an annealing period, the samples were placed inside an α-Al_2O_3 crucible except for the Fe-FeO-iron spinel tablets which were placed in a Pt crucible. The pellets were air cooled after annealing reaching ambient temperature in 5 minutes.

Sample*	The starting composition of the pellets in weight percent					
	Al	Fe	Wustite	Fe_3O_4	Fe_2O_3	α-Al_2O_3
HSA	-	-	-	30	30	40
WSI1, WSI2, WSI3	-	50	35	12	-	3
SAI1, SAI2, SAI3	-	50	10	-	-	40
IA0.1A	0.05	49.95	-	-	-	50
IA0.5A	0.25	49.75	-	-	-	50
IA1.5A	0.75	49.25	-	-	-	50
IA3.0A	1.50	48.50	-	-	-	50
IA10A	5.00	45.00	-	-	-	50
IA20A	10.00	40.00	-	-	-	50
IA25A	12.50	37.50	-	-	-	50
IA30A	15.00	35.00	-	-	-	50

Table (4-6) Starting constituents of mixtures belonging to Fe-Al-O systems.

*) The composition points of the different samples are: hematite - spinel-aluminum oxide for HSA samples, Fe-wustite-spinel for WSI pellets, Fe-$FeAl_2O_4$-$Al_2O_{3(\alpha)}$ for SAI tablets, and alloy-$Al_2O_{3(\alpha)}$ for the other samples. WSI1, WSI2, and WSI3 pellets were annealed at 1300°C for a week, then the samples WSI2 and

WSI3 were held at 1150°C and 1000°C respectively, for another week. SAI samples were subjected to the same annealing procedure. HSA tablets were annealed at 1000°C for a week. The other samples were annealed for a week at 1300°C then held at 1000°C for another week.

4.3.5 Nickel-Aluminum and Iron-Aluminum Systems

Ni (or Fe)-Al alloys used to calibrate the electron beam microprobe were prepared in a non-consumable tungsten electrodes arc furnace under 0.2 atmospheric pressure of argon. Each sample was remelted six times to ensure long range homogeneity. The alloy samples were approximately cylindrical, 40 mm long by 8 mm diameter. The rods were annealed at 1000°C for a week in a tubular-electric furnace under a purified-flowing argon atmosphere. The rods were then air cooled. Two disks 3 mm thick were sectioned, using a diamond blade cutter, from each rod for chemical and electron probe analyses. The disks were again annealed in an α-Al_2O_3 crucible at 1000°C for two weeks under purified argon atmosphere and then water quenched reaching room temperature in about two minutes.

4.4 Metallography

For electron probe analyses and microstructural observations, samples belonging to the NiO-Al_2O_3, Ni-Al-O, Fe-Al-O, Ni-Al, and Fe-Al systems were vacuum impregnated with cold-mounting epoxy resin. This resin was also used to mount the samples within 1" diameter plastic rings. To avoid severe damage of the oxide surfaces, specimens were sectioned using a diamond blade cutter and polished directly using 6 μm then 1 μm diamond paste on wheels covered with napless cloth lubricated with kerosene. This procedure produced a satisfactory surface for microprobe analyses. Some of these samples were metallographically examined using the scanning electron microscopy technique.

4.5 Wet Chemical Analysis

Ni-Al and Fe-Al alloys, which were used to calibrate the electron microprobe for quantitative analysis of the metallic phases of the Fe-Al-O and Ni-Al-O systems, were analyzed by wet chemical analyses. Ni in Ni-Al alloys was determined by the dimethylglyoxime method while Al was determined by the atomic absorption method. Fe-Al alloys were analyzed only for Fe, potassium dichromate titration technique being used to determine Fe contents in the alloys. Tables (4-7) and (4-8) give the results of the wet chemical analyses for Ni-Al and Fe-Al alloys.

Na in Al-Na alloys was determined also by the atomic absorption technique. The atomic absorption apparatus, Perkin-Elmer 303, used in this investigation was calibrated to directly read concentrations.

4.6 X-ray Analyses

The X-ray powder diffraction technique was used to identify the phases in samples belonging to $NiO-Al_2O_3$ and $NaAlO_2-Al_2O_3$ systems. Cu-K_α radiation was used in this investigation. The phases were identified by comparing the resultant patterns with standard ASTM data.

4.7 Electron Probe Analyses

A CAMECA MS-64 electron microprobe was used to determine the compositions of the equilibrated-tablet phases prepared

Weight of Starting material (g)		Nominal composition (w/o)		Wet Chemical Analysis* (w/o)	
Al	Ni	Al	Ni	Al	Fe
0.422	37.755	1.105	98.895	0.8	99.5
1.273	37.535	3.280	96.720	2.8	97.1
2.044	37.489	5.170	94.830	5.0	94.8
5.252	34.356	13.260	86.740	13.0	88.0
9.265	31.074	22.968	77.032	23.4	76.6
10.303	19.340	34.577	65.243	35.0	64.8

Table (4-7) Wet chemical analyses of Ni-Al alloys.

*) Each value reported for Al and Ni concentration is the average of the results from 3 analyses.

Weight of Starting material (g)		Nominal composition (w/o)		Wet Chemical Analysis* (w/o)
Al	Fe	Al	Fe	Fe
0.413	40.906	1	99	98.8
2.266	43.046	5	95	94.6
4.766	42.899	10	90	90.3
7.197	40.780	15	85	85.4
7.899	31.595	20	80	80.3
10.627	31.882	25	75	75.1
11.303	26.372	30	70	71.3

Table (4-8) Wet chemical analyses of Fe-Al alloys.

*) Each value reported for Fe concentration is the average of the results from three analyses.

as outlined in sections (4.3.2), (4.3.3), and (4.3.4). Theoretical aspects of using the electron probe in determining solid phase compositions are explained in reference (116). The electron-probe was operated under 15 kv acceleration voltage, 100-120 nanoamps specimen current, and a period of 20 seconds was used for X-ray pulses counting. The polished samples were covered by a thin layer of carbon to avoid charging of the specimens. Al, Ni and Fe-K_α lines were used to determine the concentration of Al, Ni and Fe, respectively. Pure Ni, Fe and Al were used as standards. Background, dead time, atomic number, absorption, and fluorescence corrections were applied to compute the chemical compositions of the different phases. Ni-Al and Fe-Al binary alloys were prepared and analyzed using wet chemical analyses as well as electron microprobe techniques to check the reliability of using the probe in determining the compositions of the metallic phases of the Ni-Al-O and Fe-Al-O systems. Results obtained from the standard alloys are listed in table (4-9) and table (4-10). To check the probe reliability in determining the compositions of the oxide phases, Ni, Fe, and Al concentrations in pure NiO, Fe_2O_3, and α-Al_2O_3 specimens, respectively, were determined. The values obtained were 49.9(±0.2) a/o, 39.9(±0.1) a/o, and 40.1(±0.2) a/o for Ni, Fe and Al, respectively.

Nominal Composition		Intensity Ratio*		Weight Percent	
Al (w/o)	Ni (w/o)	Al	Ni	Al	Ni
1.105	98.895	0.0033	0.9868	1.0	98.9
3.280	96.720	0.0098	0.9595	3.2	96.6
5.170	94.830	0.0159	0.9380	5.1	94.9
13.260	86.740	0.0425	0.8495	13.1	87.2
22.968	77.032	0.0734	0.7537	21.4	78.7
34.577	65.243	0.1312	0.6021	34.5	64.6

Table (4-9) The electron probe results for the Ni-Al alloys.

*) The ratios are given after background and dead time corrections. The intensity ratio is the ratio of the X-ray intensity obtained from the component j of a phase to that obtained from pure j. Each intensity value was the average of thirty-two values taken at different spots in the sample.

Nominal Composition		Intensity Ratio*		Weight Percent	
Al (w/o)	Fe (w/o)	Al	Fe	Al	Fe
1	99	0.0036	0.9881	0.9	99.0
5	95	0.0193	0.9386	5.0	95.0
10	90	0.0395	0.8780	10.1	89.9
15	85	0.0603	0.8210	15.0	84.8
20	80	0.0820	0.7677	19.9	80.1
25	75	0.1060	0.7103	24.9	74.9
30	70	0.1315	0.6577	29.9	70.1

Table (4-10) The electron probe results for the Fe-Al alloys.

*) Intensity ratios are given after background and dead time corrections.

4.8 The Electrochemical Cells "Design and Operation"

Electromotive force measurements were made for the following cells:

$Pt|W_{(s)},WS_{2(s)},Na_2S_{(s)}|\beta$- and α-$Al_2O_3|Cu_2O_{(s)},Cu_{(s)}|Pt$ (5-I)

$Pt|W_{(s)},WS_{2(s)},Na_2S_{(s)}|\beta$- and α-$Al_2O_3|NiO_{(s)},Ni_{(s)}|Pt$ (5-II)

$Pt|W_{(s)},WS_{2(s)},Na_2S_{(s)}|\beta$- and α-$Al_2O_3|FeO_{(s)},Fe_{(s)}|Pt$ (5-III)

$Ta|Al_{(s\text{ or }\ell)},Na_{(\ell)}|\beta$-$Al_2O_3|NiO_{(s)},Ni_{(s)}|Pt|Ta$ (5-IV)

$Pt|W_{(s)},WS_{2(s)},Na_2S_{(s)}|\beta$- and β"-$Al_2O_3|NiO_{(s)},Ni_{(s)}|Pt$ (5-V)

$Pt|W_{(s)},WS_{2(s)},Na_2S_{(s)}|\beta$- and α-$Al_2O_3|NaF_{(s)},NiF_{2(s)},Ni_{(s)}|Pt$ (5-VII)

$Pt|W_{(s)},WS_{2(s)},Na_2S_{(s)}|\beta$- and α-Al_2O_3(1550)$|FeO_{(s)},Fe_{(s)}|Pt$ (5-VIII)

$Pt|Ni_{(s)},NiO_{(s)}|\beta$- and α-$Al_2O_3|Cu_{(s)},Cu_2O_{(s)}|Pt$ (6-I)

$Pt|Fe_{(s)},FeO_{(s)}|\beta$- and α-$Al_2O_3|Ni_{(s)},NiO_{(s)}|Pt$ (6-II)

$Pt|W_{(s)},WS_{2(s)},Na_2S_{(s)}|\beta$- and α-$Al_2O_3|Ni_{(s)}$,spinel,$Al_2O_{3(\alpha)}|Pt$ (6-II

$Pt|W_{(s)},WS_{2(s)},Na_2S_{(s)}|\beta$- and α-$Al_2O_3|Fe_{(s)},FeAl_2O_{4(s)},Al_2O_{3(\alpha)}|Pt$ (6-IV)

$Pt|Al_{(s)}|\beta$- and α-$Al_2O_3|W_{(s)},WS_{2(s)},Na_2S_{(s)}|Pt$ (6-V)

$Pt|Ta|Al_{(\ell)}|\beta$- and α-$Al_2O_3|W_{(s)},WS_{2(s)},Na_{2(s)}|Pt$ (6-VI)

$Pt|Ni_{(s)},NiO_{(s)}\ NiAl_2O_{4(s)}|ZrO_2$(+CaO)$|Ni_{(s)},NiO_{(s)}|Pt$ (7-I)

$Pt|Ni_{(s)}$,spinel,$Al_2O_{3(\alpha)}|ZrO_2$(+CaO)$|Ni_{(s)},NiO_{(s)}|Pt$ (7-II)

$Pt|$Ni-Al alloy (0.15 a/o Al),$Al_2O_{3(\alpha)}|ZrO_2$(+CaO)$|Ni_{(s)},NiO_{(s)}|Pt$ (7-III)

$Pt|$Ni-Al alloy (0.15 a/o Al),$Al_2O_{3(\alpha)}|\beta$- and α-$Al_2O_3|W_{(s)},WS_{2(s)},Na_2S_{(s)}|Pt$ (7-IV)

$$Pt\left|\begin{matrix}\text{Ni-Al alloy}\\(1.19\ \text{a/o Al})\end{matrix},Al_2O_{3(\alpha)}\right|\beta\text{- and }\alpha\text{-}Al_2O_3\left|W_{(s)},WS_{2(s)},Na_2S_{(s)}\right|Pt \quad (7\text{-V})$$

$$Pt\left|\begin{matrix}\text{Ni-Al alloy}\\(2.36\ \text{a/o Al})\end{matrix},Al_2O_{3(\alpha)}\right|\beta\text{- and }\alpha\text{-}Al_2O_3\left|W_{(s)},WS_{2(s)},Na_2S_{(s)}\right|Pt \quad (7\text{-VI})$$

$$Pt\left|Fe_{(s)},FeO_{(s)}\right|ZrO_2(+CaO)\left|\text{hematite, spinel, aluminum oxide}\right|Pt \quad (8\text{-I})$$

$$Pt\left|Fe_{(s)},\text{wustite, spinel}\right|ZrO_2(+CaO)\left|Fe_{(s)},FeO_{(s)}\right|Pt \quad (8\text{-II})$$

$$Pt\left|Fe_{(s)},FeAl_2O_{4(s)},Al_2O_{3(\alpha)}\right|ZrO_2(+CaO)\left|Fe_{(s)},FeO_{(s)}\right|Pt \quad (8\text{-III})$$

$$Pt\left|\text{Fe-Al alloy}(0.17\ \text{a/o Al}),Al_2O_{3(\alpha)}\right|ZrO_2(+CaO)\left|Fe_{(s)},FeO_{(s)}\right|Pt \quad (8\text{-IV})$$

$$Pt\left|\begin{matrix}\text{Fe-Al alloy}\\(0.17\ \text{a/o Al})\end{matrix},Al_2O_{3(\alpha)}\right|\beta\text{- and }\alpha\text{-}Al_2O_3\left|W_{(s)},WS_{2(s)},Na_2S_{(s)}\right|Pt \quad (8\text{-V})$$

Table (4-11) summarizes the purposes and the cell reactions of the preceding electrochemical cells.

Solid state galvanic cells using calcia stabilized zirconia as solid electrolyte were designed to determine the equilibrium oxygen pressures of coexistences in the Ni-Al-O and Fe-Al-O systems. The cell and cell assembly designed by Davis (40), figure (3-12), were used in this investigation for cells containing calcia stabilized zirconia as solid electrolyte. The 12 inch one end closed tube of calcia stabilized zirconia was supplied by Zirconium Corporation of America, it had a reported composition of 15 m/o CaO. The other dimensions of the tubes were 1/2" outside diameter and 3/8" inside diameter. Every tube used in this investigation showed a leakage resistance to He under a vacuum of 10^{-6} Torr. The tube was fused to a lead glass section which was, in turn, fused to the upper pyrex ground glass joint. The inner compartment of the calcia stabilized zirconia tube was used for the reference electrode. The reference electrodes, Ni,NiO and Fe,FeO coexistences, were shaped in the form of

Cell	Cell reaction	Purpose
(5-I) (5-II) (5-III)	$W_{(s)}+2Na_2S_{(s)}+2M_xO_{(s)}=WS_{2(s)}+2Na_2O_{(\beta)}+2xM_{(s)}$ "where M stands for Cu,Ni, or Fe"	The determination of the Na_2O activities in α-Al_2O_3, β-Al_2O_3 coexistence
(5-IV)	$2Na_{(\ell)}+NiO_{(s)}=Na_2O_{(\beta)}+Ni_{(s)}$	The determination of Na_2O activities in Al,Na, β-Al_2O_3 coexistence
(5-V)	$W_{(s)}+2Na_2S_{(s)}+2NiO_{(s)}=WS_{2(s)}+2Na_2O_{(\beta")}+2Ni_{(s)}$	Determination of Na_2O activities in β-Al_2O_3, β"-Al_2O_3 coexistence
(5-VII)	$W_{(s)}+2Na_2S_{(s)}+2NiF_{2(s)}=WS_{2(s)}+4NaF_{(s)}+2Ni_{(s)}$	To explain the discrepancy betweem the values obtained for the activities of Na_2O in α-Al_2O_3,β-Al_2O_3 coexistence and the values reported by Choudhury (22)
(5-VIII)	$W_{(s)}+2Na_2S_{(s)}+2NiO_{(s)}=WS_{2(s)}+2Na_2O_{(\beta)}+2xM_{(s)}$	To examine the effect of sintering temperature on the activities of Na_2O in the coexistence α-Al_2O_3,β-Al_2O_3

Cell	Cell reaction	Purpose
(6-I)	$Ni_{(a)}+Cu_2O_{(s)}=2Cu_{(s)}+NiO_{(s)}$	To investigate the applicability of using β- and α-Al_2O_3 solid electrolyte to sense reveribly oxygen pressures as high as those of Cu,Cu_2O coexistence and as low as those of Al,α-Al_2O_3, β-Al_2O_3 coexistence
(6-II)	$Fe_{(s)}+NiO_{(s)}=Ni_{(s)}+FeO_{(s)}$	
(6-III)	$\frac{1}{2}W_{(s)}+Na_2S_{(s)}+NiO.xAl_2O_3=Na_2O_{(\beta)}+xAl_2O_{3(\alpha)}+\frac{1}{2}WS_{2(s)}+Ni_{(s)}$	
(6-IV)	$\frac{1}{2}W_{(s)}+Na_2S_{(s)}+FeAl_2O_{4(s)}=Na_2O_{(\beta)}+Al_2O_{3(\alpha)}+\frac{1}{2}WS_{2(s)}+Fe_{(s)}$	
(6-V), (6-VI)	$\frac{4}{3}Al_{(s\text{ or }\ell)}+2Na_2O_{(\beta)}+WS_{2(s)}=2Na_2S_{(s)}+\frac{2}{3}Al_2O_{3(\alpha)}+W_{(s)}$	
(7-I), (7-II), (7-III)	$O_{2(g)}$ (at the cathode compartment = $O_{2(g)}$ at the anode compartment)	The determination of the oxygen pressures in equilibrium with different coexistences that belong to the Ni-Al-O system
(7-IV), (7-V), (7-VI)	$WS_{2(s)}+2Na_2O_{(\beta)}=2Na_2S_{(s)}+O_{2(g)}+W_{(s)}$	

Cell	Cell reaction	Purpose
(8-I) (8-II) (8-III) (8-IV)	$O_{2(g)}$ (at the cathode compartment) = $O_{2(g)}$ at the anode compartment)	The determination of the oxygen pressures in equilibrium with different electrodes that belong to Fe-Al-O system
(8-V)	$QA_{2(s)} + 2Na_2O_{(\beta)} = 2Na_2S_{(s)} + O_{2(g)} + W_{(s)}$	

Table (4-11) The purposes and the cell reactions of the electrochemical cells that designed in this investigation.

pellets, 3/8" in diameter and about 1/8" in thickness, and they contained 1:1, by mole, mixture of the metallic and oxide constituents using the procedure described in section (4.3.2). The pellets were annealed in Pt crucibles for one week at 1000°C under flowing-purified argon atmosphere. Pellets prepared as described in sections (4.3.2) and (4.3.3) were used as the working electrodes. A protective layer, about 2 cm. deep, of powder with the same composition of the standard electrode covered the reference electrode tablet and the bottom section of the platinum wire served to sense the electrode voltage. The spring-loaded α-Al_2O_3 push tube maintained good contact of the solids of the electrode/electrolyte interface.

The outer electrode compartment containing the sample electrode and Pt lead was contained in an α-Al_2O_3 crucible. The electrode tablet/electrolyte interface was completely covered, to a depth of about one inch, by a powder related to the electrode composition.

A chromel-alumel thermocouple was positioned to measure temperature at the bottom of the zirconia tube. Each thermocouple used was calibrated against a Pt - Pt/Rh thermocouple which had been standardised at the National Research Council Laboratories,

A cell was placed vertically inside a mullite tube which was fused to an upper pyrex section which was sealed, in turn, to a pyrex head using an O-ring and metal clamp. The electrical lead connections, the argon inlet and the argon outlet

were positioned to the pyrex head. After sealing the whole assembly, using the O-ring and the metal clamp, the cell assembly was then positioned vertically inside a Nionel tube in the tubular-electric resistance furnace equipped with a Kanthal non-inductively wound heating element. The Nionel tube was grounded to eliminate any possible induced voltage from the furnace windings. A Honeywell Versatronik Controller controlled the cell temperature within ±2°C. The electrolyte-electrodes region of the cell was positioned at the constant temperature zone of the furnace, approximately 5 cm in length.

A cell was evacuated to $\lesssim 10^{-3}$ Torr and flushed with purified argon several times at room temperature, 200, 400, and finally at 1150°C. During measurements a continuous flow of purified argon was held at a head of 4-6 cm Hg. The argon, initially containing < 5 ppm impurities, was purified in the following manner: the gas was passed over copper and unreduced copper oxide catalysts held at 180°C to oxidise CO and H_2 which were then freed by passage through ascarite, $CaSO_4$, and silica jel.

For voltages less than 150 mV, a type K-3 Universial Potentiometer with null detector was used to measure the cell and thermocouple voltages. The potentiometer was standardized against an Eppley Cd-$CdCl_2$ standard cell; the precision of the potentiometer measurements was to ±0.1 mV. Voltages greater than 150 mV were measured on a Dana 3800A digital voltmeter,

with a precision of ±1 mV.

Initially the cell temperature was taken to 1150°C and left at this temperature for a period of 3-4 hours to allow voltage stabilization. Subsequently the potential was very steady, except for cells (7-III) and (8-IV). The electromotive forces were then measured between 1150°C and 850°C at 50°C intervals. When the temperature was changed, a new steady state was reached after about 2 hours. The voltage was recorded after its stabilization and not immediately after reaching the temperature which occured after about 20 minutes. The electromotive forces, which were reproducible, were measured for both increasing and decreasing temperature regions between 850°C and 1150°C. The steady potentials of the calcia stabilized zirconia cells were recorded for a period between 45 minutes and an hour before changing the cell temperature. Cells (7-III) and (8-IV) exhibited instability problems which were not alleviated by temperature cycling or coulometric disturbance.

Cell (5-VII) was constructed to check the activity measurements of Na_2O in the coexistence α-Al_2O_3,β-Al_2O_3 as determined by Choudhury (22). The cell design is shown in figure (4-6). Cathode materials were prepared from a mixture of Ni powder (-200 mesh), anhydrous NiF_2 powder, supplied by Canlab Chemicals, and NaF powder, supplied by J. T. Baker Chemical Co., with the molar rate 1:1:4, respectively. This mixture was tumbled in plastic bottle for about 2 hours and then dried at 80°C for 3 hours. The 2 cm bottom section of a

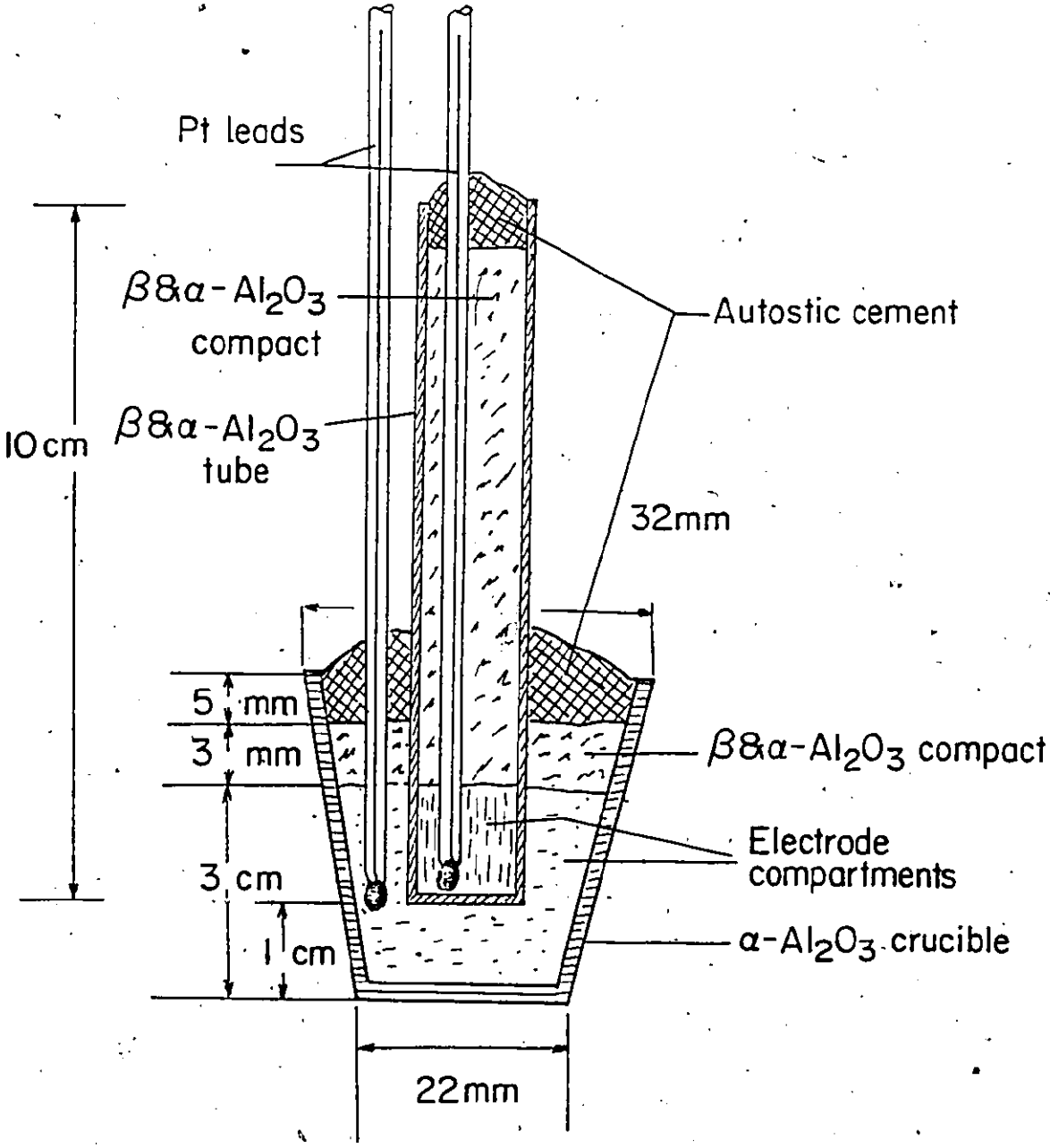

Figure (4-6) The electrochemical cell assembly utilizing β- and α-Al_2O_3 solid electrolyte tube.

10 cm β- and α-Al_2O_3 tube containing the pre-positioned electric lead was filled with this mixture. After compacting this powder in the cathode compartment, it was covered by a 1:1 mixture, by weight, of α- and β-Al_2O_3 powder. Pt electric leads were employed. The anode materials consisted of a 1:1:4 (molar ratio) mixture of W powder, supplied by Fisher Scientific Company, WS_2 powder, supplied by Ventron, and anhydrous Na_2S powder, supplied by Ventron, respectively. This mixture was tumbled in a plastic bottle for 2 hours and dried for 15 hours at 80°C. This mixture in the anode compartment of the cell was covered by an α- and β mixture similar to that used in the cathode compartment. Autostic cement was used to seal the electrode compartments.

Procedures used in operating the calcia stabilized zirconia cells were followed. The temperature of the cell was taken initially to 550°C and left overnight for its potential to stabilize. Cell emfs were measured over the temperature range 550-750°C at 25°C intervals under both increasing and decreasing temperatures. The electromotive force measurements at each temperature were found to be steady and reproducible. When the temperature changed, A new steady potential was reached after a period of 1 to 2 hours. The new temperatures were stabilized after about 20 minutes. The steady potentials shown by cell (5-VII) were recorded for periods up to 45 minutes

before altering the cell temperature.

The design of the other remaining cells was similar to that depicted in figure (4-6) except for the following features:

a) The metal-metal oxide (oxides) electrodes were tablets, 1/4" in diameter and 1/8" in thickness, covered by a protective layer, about 2 cm deep, of a powder with the same composition as the tablets.

b) The compartments of the electrodes which fix the oxygen potentials were sealed by Autostic cement under one atmospheric argon pressure.

c) Tantalum wires were used as the anode electric leads in cell (5-IV) and cell (6-VI) because Pt wires were heavily attacked in Al and Na melts. To correct for the thermocouple effect, Pt wires were welded to Ta wires and the weld regions positioned at the boundary of the constant temperature zone of the furnace. These wires were electrically welded together under vacuum.

d) The Al and Na electrode of cell (5-IV) consisted of pieces of Al, 2 g, and Na, 1 g, covered with β-Al_2O_3 powder. The anodes of cells (6-V) and (6-VI) consisted of an aluminum piece 2 g in weight.

e) Electrodes of cell (5-V) were covered with the mixture of β- and β"-Al_2O_3 powder used in packing the β- and β"-Al_2O_3 tubes during sintering.

The $W_{(s)}, WS_{2(s)}, Na_2S_{(s)}$ electrodes were prepared in the manner described previously. The metal-metal oxide (or oxides), Al and Na, and Al electrodes occupied the inner tube compartments while the outer compartments were occupied by the other electrodes. Ni, NiO and Fe, FeO tablets were prepared as described previously. Cu, Cu_2O electrodes with Cu contents greater than 25 m/o were found to cause coloring of the β- and α-Al_2O_3 tubes and instability in cell potentials; nevertheless, electrodes made from 1:6 (molar ratio) mixture of Cu and Cu_2O, respectively, caused no coloring of the β- and α-Al_2O_3 tube and the potentials obtained were steady and reproducible. The Cu, Cu_2O electrode tablets, 1/4" in diameter and about 1/8" in thickness, were prepared as described in section (4.3.2).

Cells (5-I), (5-II), (5-III), and (5-VIII) were designed to determine the sodium oxide activity in the α- and β-Al_2O_3. They were operated in a manner similar to that used for cell (7-I). After evacuation of the cell assembly, the temperature was raised to 925°C. A cell was left at this temperature overnight and the cell emf subsequently measured at temperatures between 650°C and 925°C under both increasing and decreasing temperature cycles. When the temperature was changed, the emf responded; however, a new steady emf was reached after about 2-3 hours while the stabilization of temperatures occured after only 20 minutes. The solid electrolyte tubes used in cells (5-I), (5-II), and (5-III) were sintered

at 1800°C while that used in cell (5-VIII) was fired at 1550°C.

Cell (5-IV) was fabricated to determine the sodium oxide activity in the coexistence, Al, Na, β-Al_2O_3. The initial working temperature for this cell was 750°C and five days were required for stabilization of the potential. When the cell operating temperature was altered to 700°C, the potential responded more quickly attaining a steady potential after about 3 hours. A similar behaviour was observed between 600°C and 700°C. Over this range steady emfs were recorded for about 40-60 minutes. Cell emfs were measured over this temperature range approaching the required temperature from upper and lower levels. At lower temperatures, the cells showed polarization effects. A cell was depolarized, at a constant temperature between 250°C and 550°C, by applying coulometric charging at 4V for 15 hours. Electrical current passing through the cell was less than 1 μa. The cell voltage dropped to a steady value when the external voltage was removed, which remained constant within ±3 mV for about 15 minutes.

Cell (5-V) was fabricated to measure the activity of Na_2O in the coexistence β- and β''-Al_2O_3 over the temperature range 650-900°C. Operation and response of this cell was similar to that of cell (5-II).

Cells (6-I), (6-II), (6-III), (6-IV), (6-V), and (6-VI) were designed to check the reliability of using β- and α-Al_2O_3 as

an electrolyte to monitor oxygen potentials between those defined by Cu, Cu_2O equilibrium and Al,α-Al_2O_3,β-Al_2O_3 coexistence. The potentials of cell (6-I) were measured between 600°C and 1000°C and those of cell (6-II) were measured between 650 and 1000°C. The emf of cells (6-III) and (6-IV) were measured over the temperature range 650-900°C. Operation and behaviour of the last four cells were similar to those of cells (5-I), (5-II), and (5-III).

The emf of cells (6-V) and (6-VI) were found to decrease steadily at constant temperature. When a 15 ma charging current was applied for 3 minutes at constant temperature, the potential decay curves upon removal of the external current reached constant plateaus after about 2-4 minutes. Durations of these plateaus were between 4 and 9 minutes. Reversibility of a cell emf was checked by discharging the cell through an external circuit momentarily during a plateau period. The emf returned instantaneously to within ±1 mV of the plateau values. This behaviour was observed over the temperature range 550 to 650°C for cell (6-V) and between 675°C and 800°C for cell (6-VI). Figures (4-7) and (4-8) show two decay curves obtained at different temperatures for cell (6-V) and cell (6-VI).

The emfs of cells (7-IV), (7-V), (7-VI) and (8-V) were measured only at 940°C after allowing overnight periods for their potential stabilization. The emfs obtained were very steady over the measuring period (about 1-2 hours). When the

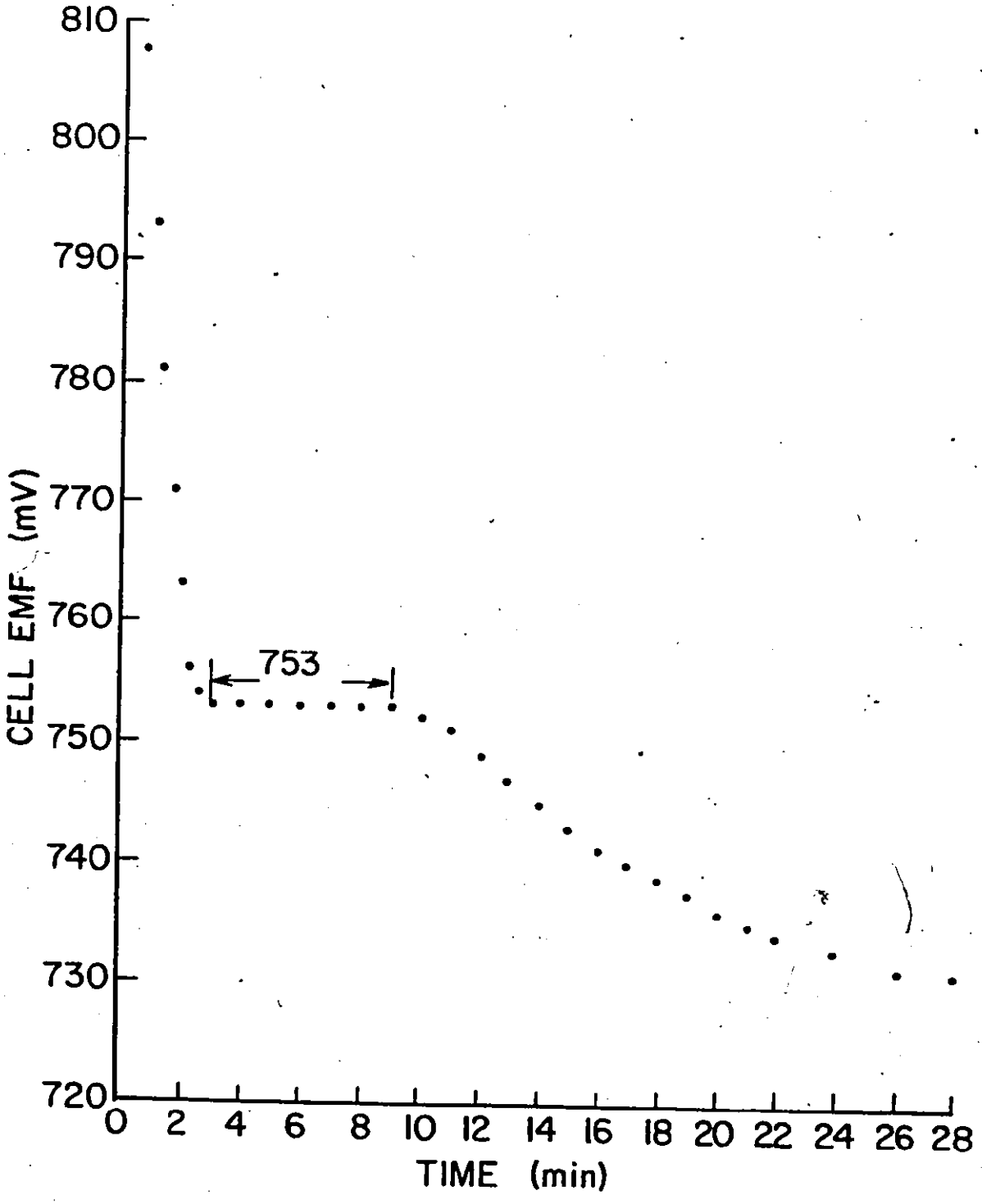

Figure (4-7) The potential decay curve obtained at 650°C for cell (6-V).

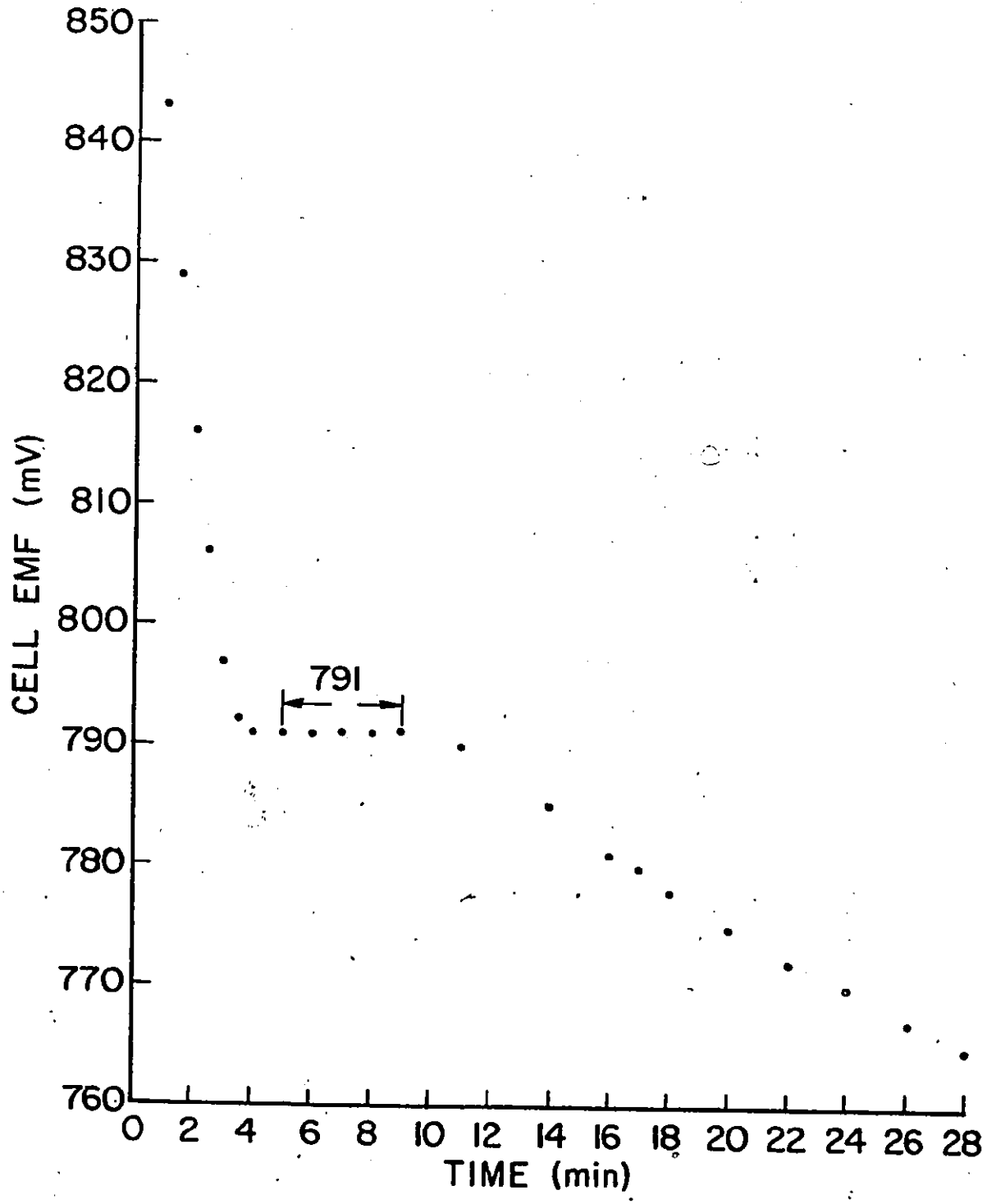

Figure (4-8) The potential decay curve obtained at 775°C for cell (6-VI).

temperature was cycled around 940°C, the emf was found also to return within ±2 mV from its initial value after the temperature was stabilized at 940°C for 5-20 minutes.

Every solid electrolyte tube used in this investigation was dried at 150°C overnight before being charged with an electrode material.

CHAPTER 5

STABILITY OF THE FAST IONIC CONDUCTING PHASES, β- and β"-Al_2O_3, IN THE $NaAlO_2$-Al_2O_3 SYSTEM

5.1 Introduction

Disks prepared from β-Al_2O_3 and α-Al_2O_3 mixtures were used (22) as solid electrolytes in galvanic cells designed to monitor reversibly, over the temperature range 560-660°C, oxygen chemical potentials as low as those imposed by Al,$Al_2O_{3(\alpha)}$ coexistence. However, it was indicated (66-68) that the sodium vapor pressure in equilibrium with β- and α-Al_2O_3 could be relatively high in reducing environments. Equilibrium values of sodium vapor pressure over a mixture of β- and α-Al_2O_3 can be calculated from the thermodynamic data of the chemical reaction

$$\beta\text{-}Al_2O_3(Na_2O.11Al_2O_3) = 11Al_2O_{3(\alpha)} + 2Na_{(g)} + \frac{1}{2}\,O_{2(g)} \cdot$$

This reaction indicates that sodium vapor pressure over the α-Al_2O_3,β-Al_2O_3 equilibrium, $p_{Na(\alpha-\beta)}$, increases with decreasing oxygen potential at constant temperature. Alternatively, the preceding chemical equilibrium can be written as

$$Na_2O_{(\beta)} = 2Na_{(g)} + \frac{1}{2}\,O_{2(g)} \cdot$$

$Na_2O_{(\beta)}$ indicates the sodium oxide in β-Al_2O_3. It is clear from the above reaction that $p_{Na(\alpha-\beta)}$ can be evaluated by determining the activity of sodium oxide of α-Al_2O_3, β-Al_2O_3 coexistence, $a_{Na_2O(\alpha-\beta)}$. Several investigators (22,66-68) determined the values of $a_{Na_2O(\alpha-\beta)}$ over a wide range of temperature (500-1600°C); however, agreement between the different results reaches a discrepancy of about 7 orders of magnitude, for example, at 700°C.

To resolve the discrepancy in the thermodynamic data of β-Al_2O_3, open-circuit emf measurements were carried out to measure $a_{Na_2O(\alpha-\beta)}$. The activity of Na_2O in the coexistence Al,α-Al_2O_3,β-Al_2O_3,$a_{Na_2O(\alpha-\beta-Al)}$, was also determined in our investigation. Open-circuit emf measurements were adopted as the method to determine the activity of Na_2O in the coexistences Al,Na,β-Al_2O_3,$a_{Na_2O(Al-Na-\beta)}$, and β-Al_2O_3,β"-Al_2O_3,$a_{Na_2O(\beta-\beta")}$. There are no reported values for $a_{Na_2O(\alpha-\beta-Al)}$, $a_{Na_2O(Al-Na-\beta)}$, and $a_{Na_2O(\beta-\beta")}$ in the literature: nevertheless, if it is assumed that the sodium oxide activity of β-Al_2O_3 in β-Al_2O_3, α-Al_2O_3 coexistence is independent of oxygen potential, the values of $a_{Na_2O(\alpha-\beta-Al)}$ should be very close to those of $a_{Na_2O(\alpha-\beta)}$. Figure (5-6) illustrates the coexistences that belong to Na-Al-O system at 1000 K.

5.2 Experimental Results

5.2.1 Chemical Equilibration

Sodium contents of aluminum samples equilibrated with α- and β-Al_2O_3 were determined by atomic absorption spectrophotometry. The instrument was calibrated to read directly in concentration. Atomic absorption analyses are shown in table (5-1).

5.2.2 EMF Results

The electrochemical cells (5-I), (5-II), and (5-III) were designed to measure $a_{Na_2O(\alpha-\beta)}$.

$$Pt|W_{(s)},WS_{2(s)},Na_2S_{(s)}|\beta\text{- and }\alpha\text{-}Al_2O_3|Cu_2O_{(s)},Cu_{(s)}|Pt \quad (5\text{-I})$$

$$Pt|W_{(s)},WS_{2(s)},Na_2S_{(s)}|\beta\text{- and }\alpha\text{-}Al_2O_3|NiO_{(s)},Ni_{(s)}|Pt \quad (5\text{-II})$$

$$Pt|W_{(s)},WS_{2(s)},Na_2S_{(s)}|\beta\text{- and }\alpha\text{-}Al_2O_3|FeO_{(s)},Fe_{(s)}|Pt \quad (5\text{-III})$$

Emf data obtained from the above cells over the temperature range 650-925°C are tabulated in table (5-2) and are shown in figures (5-1), (5-2), and (5-3). The straight lines in the figures were obtained by least squares analyses and their equations are described in table (5-3).

Cell (5-IV) was constructed to determine values of $a_{Na_2O(Al\text{-}Na\text{-}\beta)}$ over the temperature range 250-750°C.

$$Ta|Al_{(s\text{ or }\ell)},Na_{(\ell)}|\beta\text{-}Al_2O_3|NiO_{(s)},Ni_{(s)}|Pt|Ta \quad (5\text{-IV})$$

Sample	Annealing temperature (°C)	Annealing time (hrs)	Na concentration in Al (ppm on the atomic scale)
A	1000	10	35 ± 1
B	1000	15	39
C	900	10	19
D	900	15	18
E	800	10	9
F	800	15	9
G	700	10	4
H	700	15	4

Table (5-1) Sodium contents in the metallic phase of the coexistence Al, α-Al_2O_3, β-Al_2O_3.

Temperature (°C)	Cell emf (mV)											
	Cell (5-I)				Cell (5-II)				Cell (5-III)			
650	1098	1100	1103	1101	810	813	815	814	562	564	563	567
700	1076	1074	1078	1077	796	794	795	799	537	540	543	541
750	1053	1053	1055	1052	775	776	777	776	514	514	513	516
800	1028	1027	1029	1030	753	757	756	755	489	491	486	492
850	1005	1003	1006	1008	734	731	734	736	463	465	464	460
900	982	978	980	986	716	714	713	718	439	440	437	438
925	970	968	972	971	704	705	707	708	424	425	426	427

Table (5-2) The variation of cell emf with temperature for cell (5-I), cell (5-II), and cell (5-III).

Cell	Temperature range, (°C)	E(mV) = a(±S_a)-b(±S_b)T(K)				Standard deviation, (mV)
		a	S_a	b	S_b	
(5-I)	650-925	1538	4	0.474	0.004	±2
(5-II)	650-925	1180	4	0.396	0.004	±2
(5-III)	650-925	1032	4	0.506	0.004	±2

Table (5-3) Least squares analyses of emf data from cells (5-I), (5-II), and (5-III).

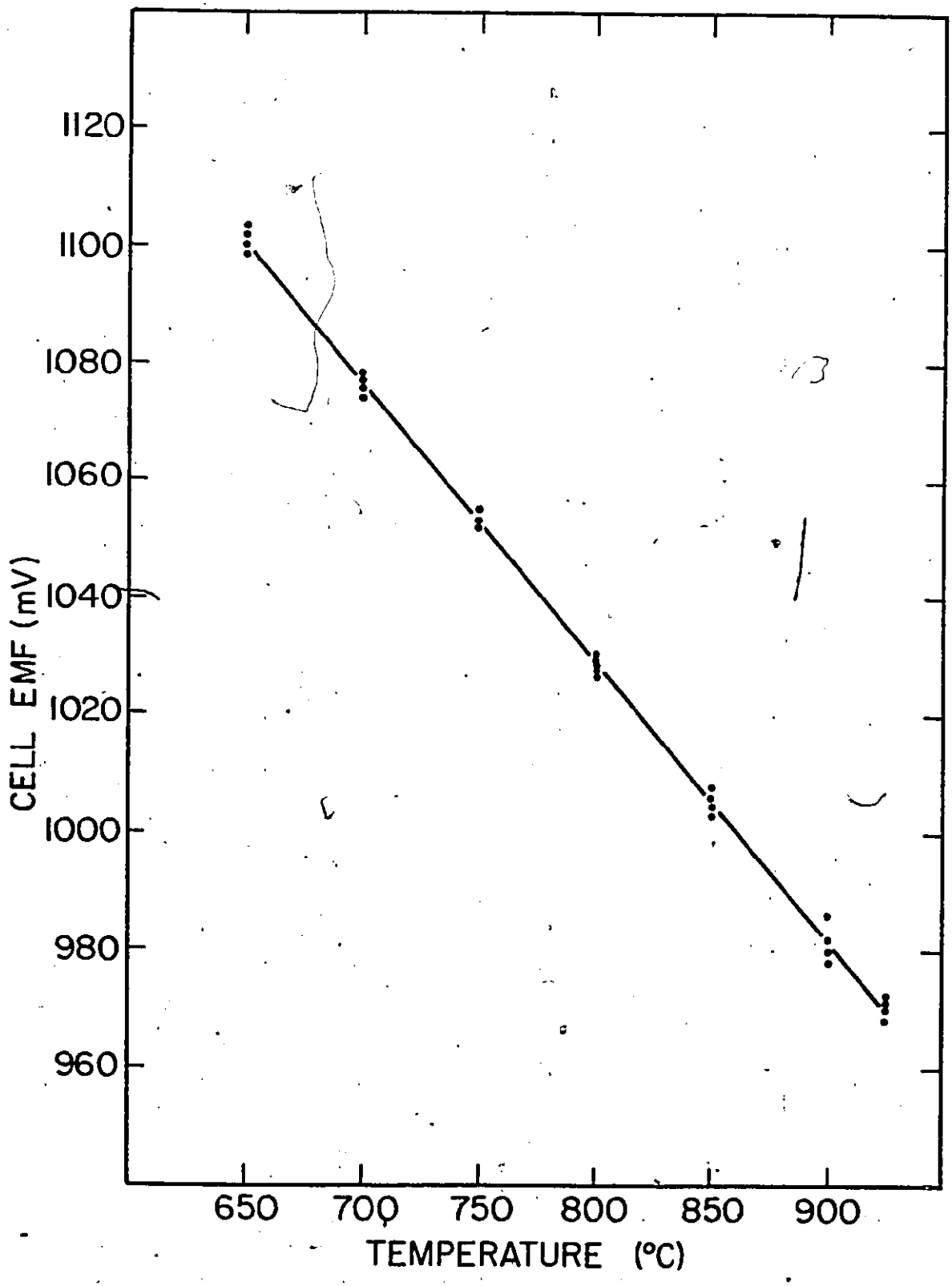

Figure (5-1) Variation of emf with temperature for cell (5-I).

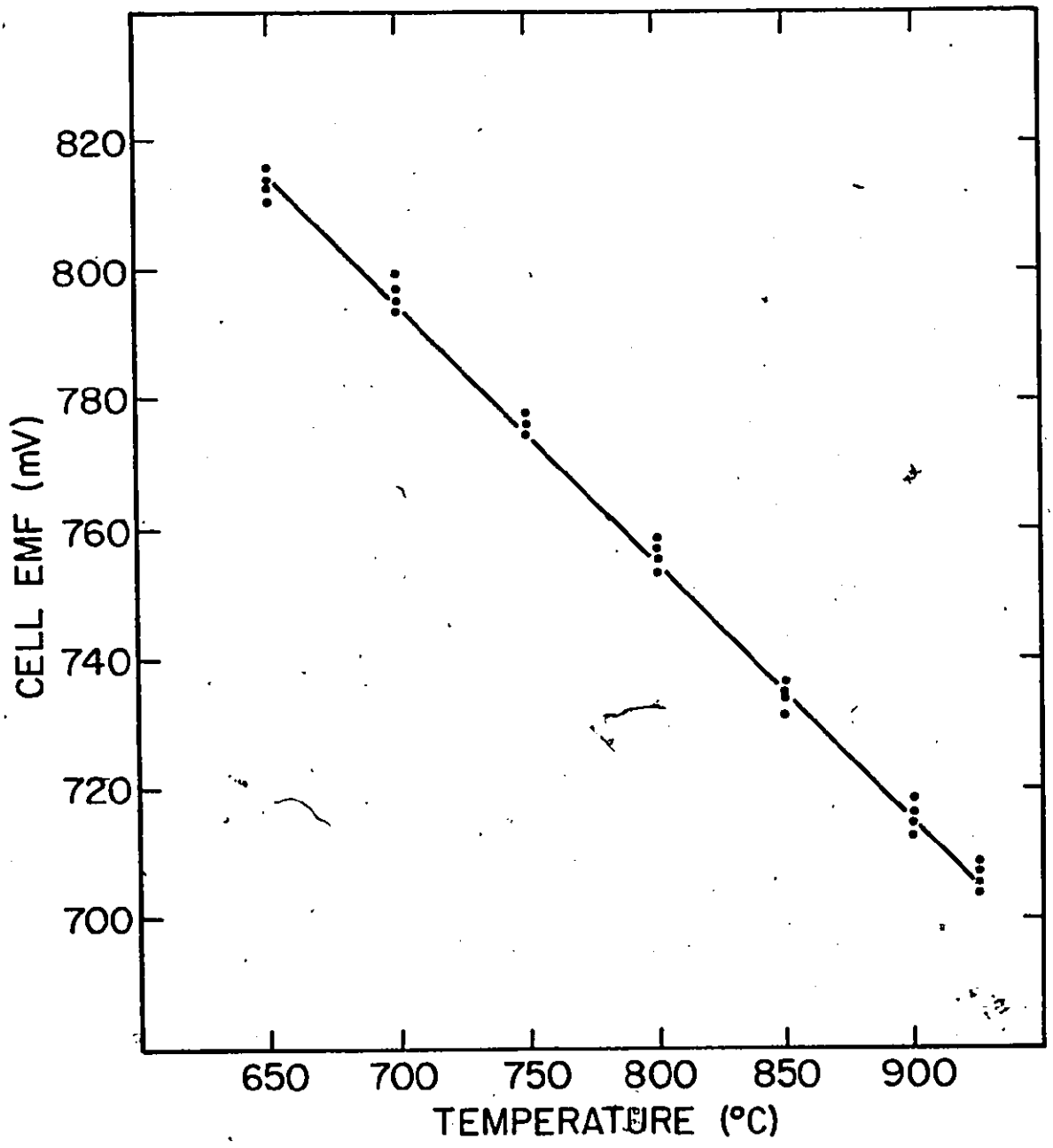

Figure (5-2) Variation of emf with temperature for cell (5-II).

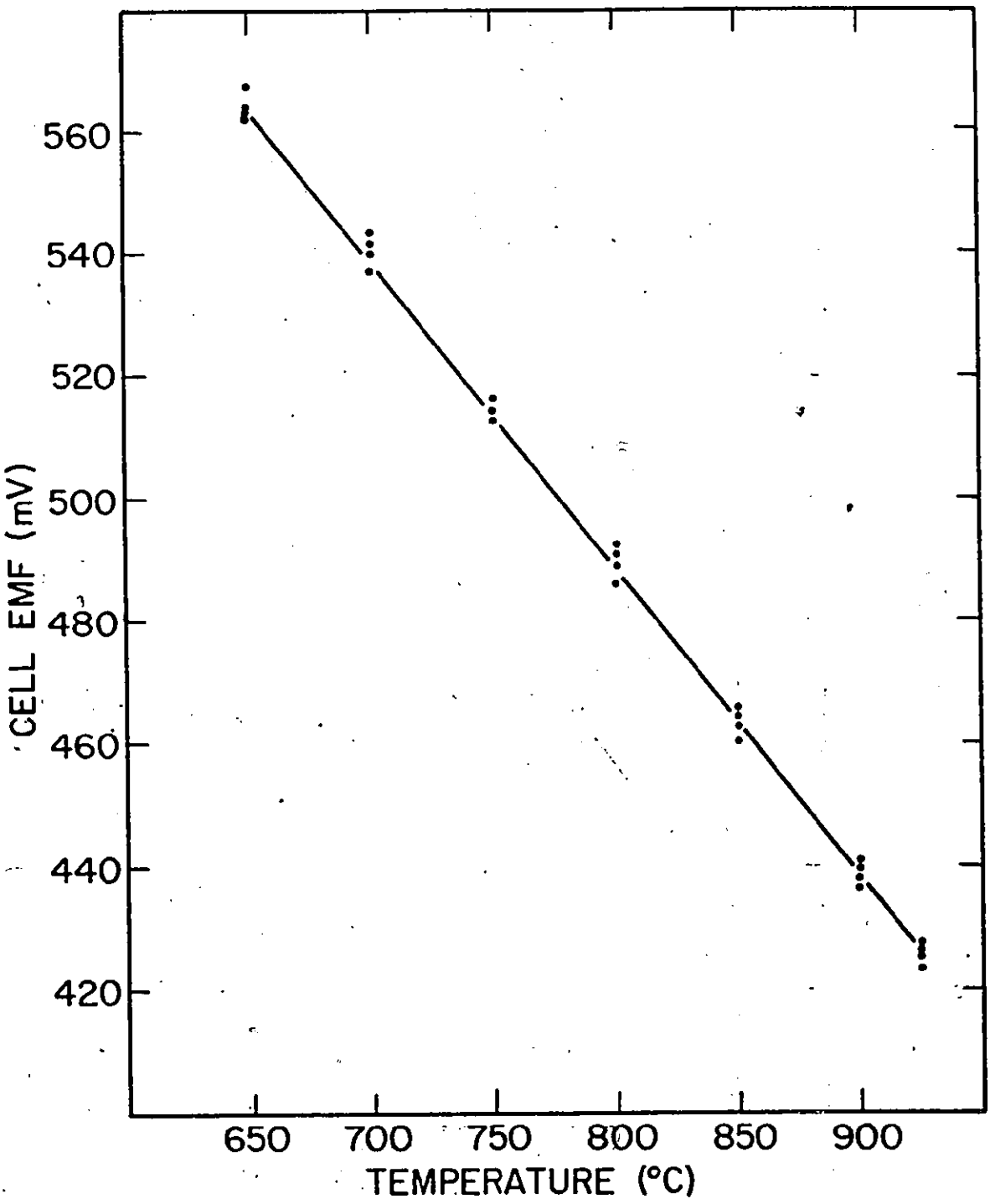

Figure (5-3) Variation of emf with temperature for cell (5-III).

The emf data for the above cell are listed in table (5-4) and plotted in figure (5-4). The straight line in the graph is obtained by least squares analysis of the emf data obtained from cell (5-VI); this line is given by

$$E(mV) = 2107(\pm 3) - 0.324(\pm 0.004)T(K) \pm 3 \quad . \qquad (5.1)$$

To evaluate $a_{Na_2O(\beta-\beta")}$, the emf variation with temperature of cell (5-V) was measured over the range 650-900°C.

$$Pt|W_{(s)},WS_{2(s)},Na_2S_{(s)}|\beta\text{- and }\beta"\text{-}Al_2O_3|Ni_{(s)},NiO_{(s)}|Pt \qquad (5\text{-V})$$

The results obtained for this cell are given in table (5-5) and shown in figure (5-5); least squares analysis of the emf data gives the straight line shown in the figure. This line is described by relation (5.2).

$$E(mV) = 641(\pm 4) - 0.246(\pm 0.004)T(K) \pm 1.5 \quad . \qquad (5.2)$$

5.3 Discussion

5.3.1 Sodium Oxide Activity in Al, α-Al_2O_3, β-Al_2O_3 Coexistence

Equilibrium between aluminum, α-alumina and β-alumina can be represented by the following reaction

$$2Na_{(liq.\ Al)} + \frac{1}{2}\,O_{2(g)} + 11Al_2O_{3(\alpha)} = \beta\text{-}Al_2O_{3(s)} \qquad (5.3)$$

for which

$$\Delta G_{(5.3)} = \Delta G_f^o(\beta\text{-}Al_2O_{3(s)}) - 11\Delta G_f^o(Al_2O_{3(\alpha)}) - RT\ell n a_{Na}^2 \cdot p_{O_2}^{1/2} \qquad (5.4)$$

where $\Delta G_{(5.3)}$ is the free energy change for reaction (5.3), $\Delta G_f^o(\beta\text{-}Al_2O_{3(s)})$ is the standard free energy of formation of $\beta\text{-}Al_2O_{3(S)}$, a_{Na} is the sodium activity in molten Al, and p_{O_2} is the equilibrium oxygen pressure over the Al,$\alpha\text{-}Al_2O_3$, $\beta\text{-}Al_2O_3$ coexistence. Since $\Delta G = 0$ under equilibrium condition, equation (5.4) becomes

$$\Delta G_f^o(\beta\text{-}Al_2O_{3(s)}) = 11\Delta G_f^o(Al_2O_{3(\alpha)}) + RT\ell n a_{Na}^2 \cdot p_{O_2}^{1/2} \quad . \qquad (5.5)$$

But $a_{Na} = x_{Na}\gamma_{Na}$; therefore, equation (5.5) can be written as

$$\Delta G_f^o(\beta\text{-}Al_2O_{3(s)}) = 11\Delta G_f^o(Al_2O_{3(\alpha)}) + RT\ell n x_{Na}^2 \cdot \gamma_{Na}^2 \cdot p_{O_2}^{1/2} \qquad (5.6)$$

where x_{Na} is the atomic fraction of Na in molten Al, and γ_{Na} is the activity coefficient of Na in molten Al.

The standard free energy of formation of $\beta\text{-}Al_2O_3$ was calculated over the temperature range 700-1000°C using equation (5.6) and the data of table (5-6). Values for γ_{Na} were obtained from reference (117) which gives γ_{Na} as a function of temperature over the temperature range 670-900°C. The value of γ_{Na} at 1000°C was extrapolated from the γ_{Na}-T relationship proposed in reference (117). Since a reliable value for p_{O_2} has not been yet determined, the equilibrium oxygen pressure of Al,Al_2O_3 equilibrium was used to calculate $\Delta G_f^o(\beta\text{-}Al_2O_{3(s)})$. The standard free energy of formation of $\alpha\text{-}Al_2O_3$ was obtained from JANAF

Temperature (°C)	Cell emf (mV) (i)				(ii)
750	1776	1774	1777	1773	
700	1792	1793	1791	1789	
650	1806	1810	1804	1805	
600	1824	1825	1822	1827	
550					1840
500					1852
450					1876
400					1890
350					1900
300					1925
250					1935

Table (5-4) Variation of cell emf with temperature for cell (5-IV).

(i) Emf recorded after potential stabilization.
(ii) Plateau emf from the decay curve, after coulometric disturbance.

Temperature (°C)	Cell emf (mV)			
650	416	412	412	413
700	402	404	400	403
750	390	390	388	391
800	375	377	377	376
850	365	364	364	366
900	352	350	355	353

Table (5-5) Emf data for cell (5-V).

Temperature (°C)	700	800	900	1000	Reference
$x_{Na} \times 10^6$	4±1	9±1	18.5±1.5	37±3	*
$RT\ell n\ \gamma_{NA}$	11,920	12,293	12,665	13,038	117
$-\frac{1}{2} RT\ell n\ p_{O_2}$	109,078	106,485	103,891	101,298	118
$-\Delta G^o_f(Al_2O_{3(\alpha)})$	327,234	319,454	311,674	303,894	118

Table (5-6) Data used in calculating $\Delta G^o_f(\beta - Al_2O_{3(s)})$.

*This investigation

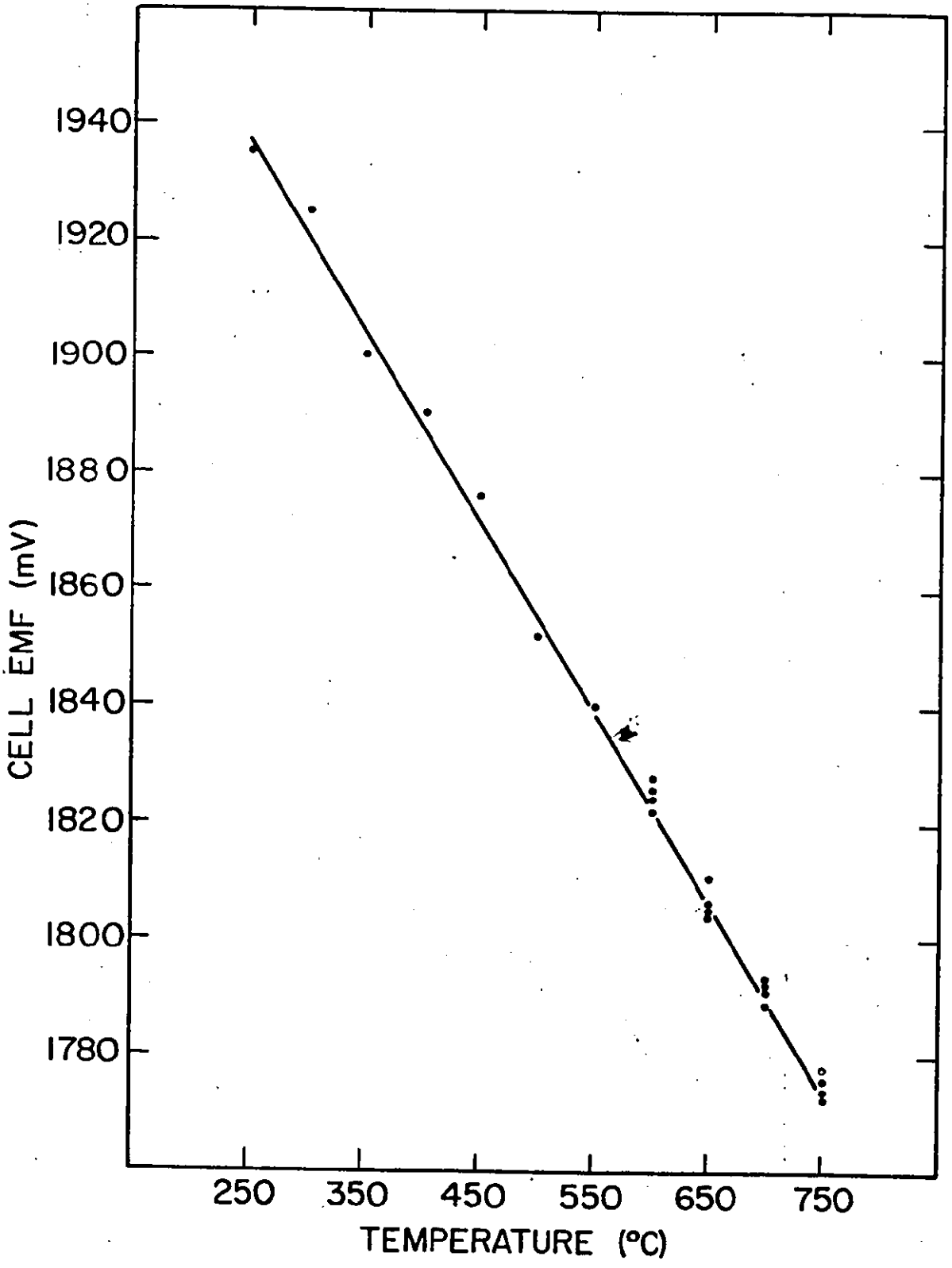

Figure (5-4) Variation of emf with temperature for cell (5-IV).

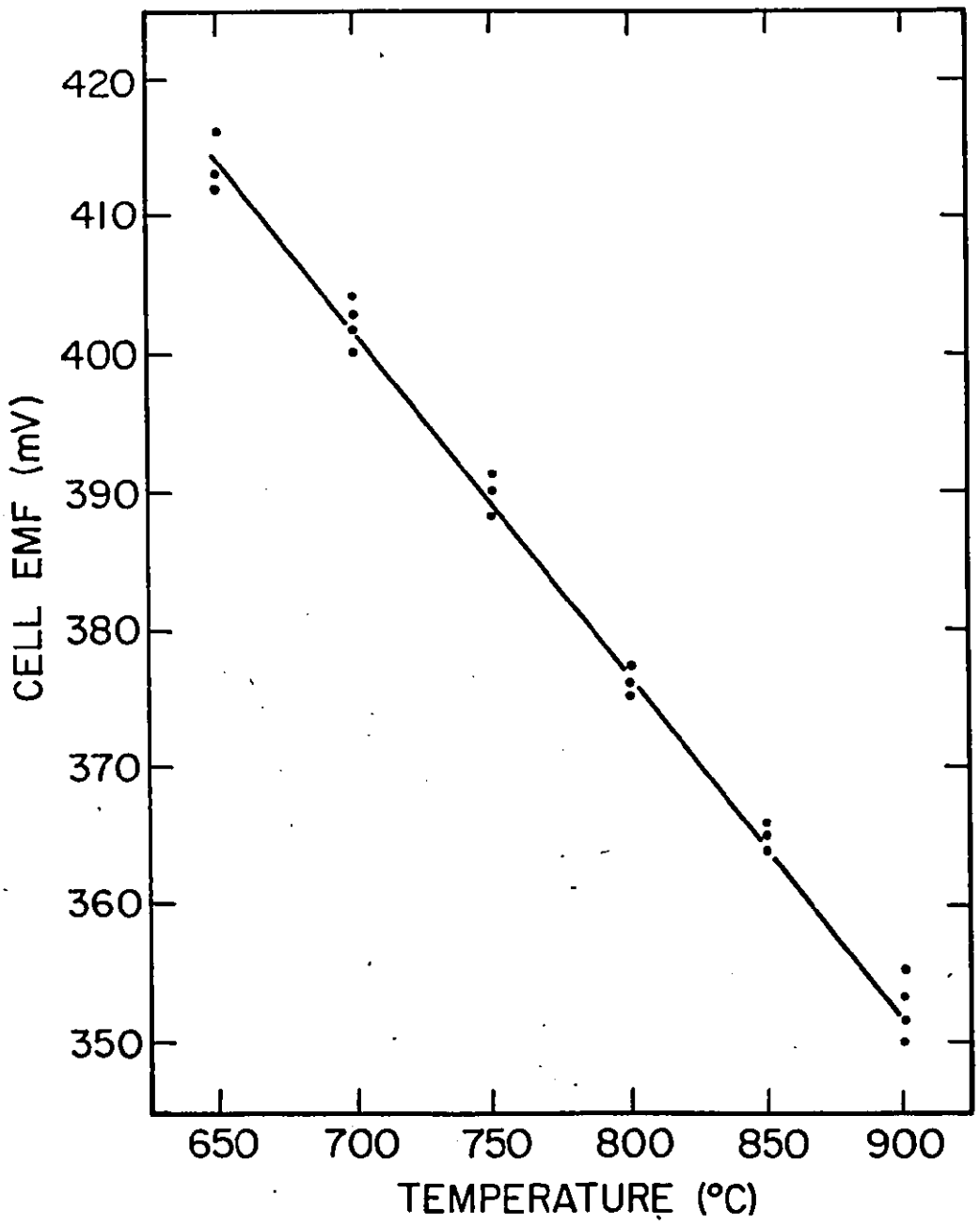

Figure (5-5) Variation of emf with temperature for cell (5-V).

thermochemical tables (118). Table (5-7) lists the values obtained for $\Delta G^{o}_{f(\beta\text{-}Al_2O_{3(s)})}$ to an accuracy of ± 6,000 cal.

The activity of Na_2O in the Al,α-Al_2O_3,β-Al_2O_3 equilibrium can be calculated by considering the following reaction

$$2Na_{(\text{in liq. Al})} + \frac{1}{2} O_{2(g)} = Na_2O_{(\beta)} \quad . \qquad (5.7)$$

At equilibrium, we may write the following expression for reaction (5.7)

$$\Delta G^{o}_{f(Na_2O_{(s)})} = -RT\ell n \frac{a_{Na_2O(\alpha\text{-}\beta\text{-Al})}}{a^2_{Na} \cdot p^{1/2}_{O_2}} \quad .$$

This expression can be rearranged to yield relation (5.8) which gives log $a_{Na_2O(\alpha\text{-}\beta\text{-Al})}$ in terms of the standard free energy of formation of solid Na_2O, $\Delta G^{o}_{f(Na_2O_{(s)})}$, x_{Na}, γ_{Na}, and p_{O_2}.

$$\log a_{Na_2O(\alpha\text{-}\beta\text{-Al})} = - \frac{\Delta G^{o}_{f(Na_2O_{(s)})}}{2.303RT} + \log x^2_{Na} \cdot \gamma^2_{Na} \cdot p^{1/2}_{O_2} \quad . \qquad (5.8)$$

Values of $a_{Na_2O(\alpha\text{-}\beta\text{-Al})}$ were calculated using equation (5.8) with the data of table (5-6) and the values of $\Delta G^{o}_{f(Na_2O_{(s)})}$ which are given in reference (119). The obtained values of $a_{Na_2O(\alpha\text{-}\beta)}$ are reported in table (5-8). The values of $\Delta G^{o}_{f(Na_2O_{(s)})}$ used to calculate $a_{Na_2O(\alpha\text{-}\beta)}$ at 900°C and 1000°C were extrapolated from the lower-temperature values (400K-1100K) of $\Delta G^{o}_{f(Na_2O_{(S)})}$ reported in reference (119).

Temperature (°C)	$\Delta G_f^o(\beta\text{-}Al_2O_{3(s)})$ (cal/mole)
700	-3,732,000
800	-3,645,000
900	-3,557,000
1000	-3,469,000

Table (5-7) The standard free energy of formation of $\beta\text{-}Al_2O_3$

Temperature / (°C)	$\log a_{Na_2O(Al-\alpha-\beta)}$
700	-15.02
800	-13.95
900	-13.03
1000	-12.17

Table (5-8) The activity of Na_2O in the equilibrium $Al, \alpha\text{-}Al_2O_3, \beta\text{-}Al_2O_3$.

5.3.2 Sodium Oxide Activity in α-Al_2O_3,β-Al_2O_3 Coexistence

The over-all cell reaction for cells (5-I), (5-II), and (5-III) can be written as

$$W_{(s)} + 2Na_2S_{(s)} + 2M_xO_{(s)} = WS_{2(s)} + 2Na_2O_{(\beta)} + 2xM \quad (5.9)$$

where M_xO is Cu_2O, NiO, or FeO. The free energy change of reaction (5.9), $\Delta G_{(5.9)}$, can be expressed as

$$\Delta G_{(5.9)} = \Delta G_f^o(WS_{2(s)}) + 2\Delta G_f^o(Na_2O_{(s)}) - 2\Delta G_f^o(Na_2S_{(s)}) - 2\Delta G_f^o(M_xO_{(s)}) + 2RT\ell na_{Na_2O(\alpha-\beta)} \quad (5.10)$$

where:

$\Delta G_f^o(WS_{2(s)})$ is the standard free energy of formation of solid WS_2.

$\Delta G_f^o(Na_2S_{(s)})$ is the standard free energy of formation of solid Na_2S.

$\Delta G_f^o(M_xO_{(s)})$ is the standard free energy of formation of Cu_2O,NiO , or FeO.

We also have the relation

$$\Delta G_{(5.9)} = - 4FE \quad (5.11)$$

where E stands for the open-circuit emf data measured for cell (5-I), cell (5-II), or cell (5-III). Expression (5.12), which gives log $a_{Na_2O(\alpha-\beta)}$ in terms of the standard free energy of formation of the different compounds of reaction (5.9) and E,

can be obtained by combining equation (5.10) and equation (5.11) and substituting for R = 1.987 cal/deg.-mole, F = 23060 cal/V, and ℓn( ) = 2.303 log( ).

$$\log a_{Na_2O(\alpha-\beta)} = \frac{\Delta G_f^o(Na_2S_{(s)}) + \Delta G_f^o(M_xO_{(s)}) - \Delta G_f^o(Na_2O_{(s)}) - \frac{1}{2}\Delta G_f^o(WS_{2(s)})}{4.576\ T(K)}$$

$$- \frac{10.0785\ E(mV)}{T(K)} \quad . \qquad (5.12)$$

Values of $\log a_{Na_2O(\alpha-\beta)}$ can now be calculated using equation (5.12) and the data of table (5-3) and table (5-9). The calculated values of $\log a_{Na_2O(\alpha-\beta)}$ are well described by the linear least-squares equation

$$\log a_{Na_2O(\alpha-\beta)} = - \frac{16457}{T(K)} + 3.63 \quad . \qquad (5.13)$$

Using equation (5.13) and the data of table (5-9) the standard free energy of formation of β-Al_2O_3 from molten aluminum, molten sodium, and gaseous oxygen, over the temperature range 650-925°C is given by

$$\Delta G_f^o(\beta\text{-}Al_2O_{3(s)}) = -4,608,102 + 907.322T(K) \quad . \qquad (5.14)$$

The estimated error in the values of $\Delta G_f^o(\beta\text{-}Al_2O_{3(s)})$ given by equation (5.14) is approximately ± 15 Kcal.

The values of $a_{NA_2O_{(\alpha-\beta)}}$ given by equation (5.13) are about three orders of magnitude higher than the values determined by the chemical equilibration method for $a_{Na_2O(\alpha-\beta)}$, table

Compound	Temperature range, (K)	ΔG_f^o(cal/mole) = A+BT(K)		Standard deviation, (cal)	Reference
		-A	+B		
$Al_2O_{3(\alpha)}$	300-900	400,329	74.8	± 51	118
	1000-1900	402,945	77.8	±122	118
	300-1900	401,625	76.9	±371	118
$Cu_2O_{(s)}$	900-1300	39,925	17.08	±140	13
$FeO_{(s)}$	873-1600	63,235	15.63	±125	13
$Na_2O_{(s)}$	400-1100	100,386	34.9	± 70	119
$Na_2S_{(s)}$	400-1100	105,218	31.4	± 33	119
$NiO_{(s)}$	900-1400	55,965	20.29	±130	13
$WS_{2(s)}$	1370-1565	80,400	37.4	±300	121

Table (5-9) Thermochemical data used in this investigation.

(5-8). If we assume that the sodium oxide content of β-Al_2O_3 which is in equilibrium with α-Al_2O_3 is independent of oxygen pressure, the values of log $a_{Na_2O(\alpha-\beta-Al)}$ should be equal to the values of log $a_{Na_2O(\alpha-\beta)}$. The disagreement may be due to the following reasons:

a) The uncertainties of the thermochemical data of Na_2S and WS_2.

b) During cooling the Al,α-Al_2O_3,β-Al_2O_3 samples, some sodium is rejected from the Al phase during the time for sample to reach room temperature. If the Na contents of the Al phase, as determined experimentally at room temperature, are some 25% less than the actual value at temperature, the value of log $a_{Na_2O(\alpha-\beta-Al)}$ should be higher than those given in table (5-8) by about 0.5.

c) In calculating $a_{Na_2O(\alpha-\beta-Al)}$, it was assumed that the values of p_{O_2} of the equilibrium Al,α-Al_2O_3,β-Al_2O_3 is equal to that of Al,Al_2O_3 coexistence; however, the values of log p_{O_2} of the equilibrium Al,α-Al_2O_3,β-Al_2O_3 calculated by considering the following reaction

$$Na_2O_{(\beta)} + 22Al_{(s \text{ or } \ell)} + \frac{33}{2} O_{2(g)} = \beta\text{-}Al_2O_{3(s)}$$

and using the data of table (5-6) and equation (5.14) is some 0.2 more positive than those of Al,Al_2O_3 equilibria. Therefore, the true values of log $a_{Na_2O(\alpha-\beta-Al)}$ should be higher by about 0.1 which does not account for the whole of three orders of magnitude of discrepancy between the two values of sodium oxide activities.

Choudhury (22) determined the activity of sodium oxide in the coexistence α-Al_2O_3,β-Al_2O_3 over the temperature range 575-625°C by measuring the emf of the cell

$$Ni_{(s)},NaF_{(s)},NiF_2(s)\,|\,\beta\text{- and }\alpha\text{-}Al_2O_3\,|\,Cu_2O_{(s)},Cu_{(s)} \quad \text{(5-VI)}$$

His values for $a_{Na_2O(\alpha-\beta)}$ were about 4 orders of magnitude lower than the values determined in this investigation. Since the uncertainties in the thermodynamic data of Na_2S, WS_2, NiF_2, and NaF are about ± 4 Kcal for each compound, the discrepancy between ours and Choudhury results could be apparently explained by this factor. To examine this assumption, the emf of the cell

$$Pt\,|\,W_{(s)},WS_{2(s)},Na_2S_{(s)}\,|\,\beta\text{- and }\alpha\text{-}Al_2O_3\,|\,NaF_{(s)},NiF_{2(s)},Ni\,|\,Pt \quad \text{(5-VII)}$$

was measured over the temperature range 550-750°C. The experimental data obtained for cell (5-VII) are reported in table (5-10) and can be well-described by the linear equation

$$E^o(mV) = 1146(\pm 2) - 0.098(\pm 0.002)T(K) \pm 1 \,. \quad (5.15)$$

The over-all reaction for cell (5-VII) can be written as

$$W_{(s)} + 2Na_2S_{(s)} + 2NiF_{2(s)} = WS_{2(s)} + 4NaF_{(s)} + 2Ni \quad (5.16)$$

for which

$$2FE^o = \Delta G_f^o(NiF_{2(S)}) + \Delta G_f^o(Na_2S_{(s)}) - 2\Delta G_f^o(NaF_{(s)}) - \tfrac{1}{2}\Delta G_f^o(WS_{2(s)}) \quad (5.17)$$

where $\Delta G_f^o(NiF_{2(s)})$ and $\Delta G_f^o(NaF_{(s)})$ are the standard free energies of formation of $NiF_{2(s)}$ and $NaF_{(s)}$, respectively. The values of $\Delta G_f^o(NiF_{2(s)})$ and $\Delta G_f^o(NaF_{(s)})$, which had been used by Choudhury to calculate log $a_{Na_2O(\alpha-\beta)}$, are given by the following two equations

$$\Delta G_f^o(NiF_{2(s)}) = -156,500+33T(K) \quad \text{cal/mole } (\pm 5,000) \quad 298\text{-}1300K \quad (5.18)$$

$$\Delta G_f^o(NaF_{(s)}) = -136,665+24.995T(K) \quad \text{cal/mole } (\pm 1650) \quad 371\text{-}1178K \quad (5.19)$$

Values for E^o for cell (5-VII) can then be evaluated by combining equations (5.17), (5.18) and (5.19) with the data of table (5-9) for $\Delta G_f^o(WS_{2(s)})$ and $\Delta G_f^o(Na_2S_{(s)})$; The E^o-T relation obtained is given by

$$E^o_{estimated}(mV) = 1123-0.093T(K) \quad (5.20)$$

which is in a fair agreement with the experimental results. Therefore, the uncertainties in the thermodynamic data of WS_2, Na_2S, NaF_2, and NaF may not explain the discrepancy between Choudury's and our results.

In his investigation, Choudhury used solid electrolyte disks which are prepared by sintering at 1690°C for one hour. An electrochemical cell similar to cell (5-III), but using a solid electrolyte tube sintered at 1550°C for three hours, was constructed to examine any sintering-temperature

effect on the values of log $a_{Na_2O(\alpha-\beta)}$. This cell may be represented as

$$Pt|W_{(s)},WS_{2(s)},Na_2S_{(s)}|\beta\text{- and }\alpha\text{-}Al_2O_3(1550)|FeO_{(s)},Fe_{(s)}|Pt \quad (5\text{-VIII})$$

Emf data obtained are shown in table (5-11); these data can be described by the linear relation

$$E(mV) = 1033(\pm 7) - 0.50(\pm 0.01)T(K) \pm 1.5 . \quad (5.21)$$

Comparison between relation (5.21) and the emf-T relation reported in table (5-3) for cell (5-III) indicated that the activity of Na_2O in the coexistence $\alpha\text{-}Al_2O_3, \beta\text{-}Al_2O_3$ does not depend on the solid electrolyte-sintering temperature.

Dewing (68) calculated the activity of Na_2O in the $\alpha\text{-}Al_2O_3, \beta\text{-}Al_2O_3$ coexistence at 1000°C by considering the equilibrium between $\alpha\text{-}Al_2O_3, \beta\text{-}Al_2O_3$, and an AlF_3-NaF melt. The chemical equation for this equilibrium may be written as

$$34Al_2O_3 + 6\ NaF \rightleftharpoons 3Na_2O.11Al_2O_3 + 2AlF_3 . \quad (5.22)$$

The activities of NaF and AlF_3 in the melt were taken from reference (120). He thus obtained the value of -9.816 for log $a_{Na_2O(\alpha-\beta)}$ at 1000°C. The value of log $a_{Na_2O(\alpha-\beta)}$ calculated, at 1000°C, using relation (5.13) is -9.302 while that extrapolated from Choudhury's work is more negative than the value determined in this investigation and the value reported by Dewing by about 4.

Temperature (°C)	Cell emf (mV)	
550	1065	1064
575	1063	1062
600	1060	1060
625	1058	1057
650	1056	1055
675	1053	1053
700	1050	1050
725	1047	1048
750	1045	-

Table (5-10) The variation of cell emf with temperature for cell (5-VII).

Temperature (°C)	Cell emf (mV)
650	571
700	547
750	522
800	499
850	470
900	447

Table (5-11) The dependence of emf on temperature for cell (5-VIII).

Measuring the emf of cell (5-IX),

$$\text{Stainless Steel}|Na_{(\ell)}|\beta\text{-}Al_2O_3|Al_2O_{3(\alpha)},\beta\text{-}Al_2O_3|\text{Stainless Steel} \quad (5\text{-IX})$$

Fray (67) determined a value of -59,032 cal. for the standard free energy of reaction (5.23) at 725°C.

$$Na_2O + 11Al_2O_3 = Na_2O.11Al_2O_3 \ . \quad (5.23)$$

The corresponding value of log $a_{Na_2O(\alpha-\beta)}$ is -12.92. It is possible to calculate a value of -12.86 for log $a_{Na_2O(\alpha-\beta)}$ at 725°C using equation (5.13) which demonstrates a good agreement between ours and Fray's result.

5.3.3 Sodium Oxide Activity in Al, Na, β-Al_2O_3 Coexistence

The over-all cell reaction for cell (5-IV) can be written as

$$2Na_{(\ell)} + NiO_{(s)} = Na_2O_{(\beta)} + Ni_{(s)} \quad (5.25)$$

for which

$$\Delta G_{(5.25)} = \Delta G_f^o(Na_2O_{(s)}) - \Delta G_f^o(NiO_{(s)}) + RT\ell n\, a_{Na_2O(Al\text{-}Na\text{-}\beta)} \quad (5.26)$$

Since $\Delta G_{(5.25)} = -2FE$, where E is the emf of cell (5-IV), we obtain:

$$\log a_{Na_2O(Al\text{-}Na\text{-}\beta)} = \frac{\Delta G_f^o(NiO_{(s)}) - \Delta G_f^o(Na_2O_{(s)})}{4.576T(K)} - \frac{10.0785E(mV)}{T} \quad (5.27)$$

Using expression (5.27), equation (5.1), and data of table (5-9), the log $a_{Na_2O(Al-Na-\beta)}$ vs $\frac{1}{T}$ relation was derived; Equation (5.28) is the result of this derivation.

$$\log a_{Na_2O(Al-Na-\beta)} = -\frac{11,528}{T} + 0.07 \quad . \qquad (5.28)$$

Equation (5.28) indicates that the value of log $a_{Na_2O(Al-Na-\beta)}$ is -11.458 at 1000K, which is about one and a half times more positive than log $a_{Na_2O(\alpha-\beta)}$ at the same temperature.

5.3.4 Sodium Oxide Activity in β-Al_2O_3, β''-Al_2O_3 Coexistence

The over-all cell reaction for cell (5-V) could be written as

$$W_{(s)} + 2Na_2S_{(s)} + 2NiO_{(s)} = WS_{2(s)} + 2Na_2O_{(\beta'')} + 2Ni_{(s)} \qquad (5.29)$$

giving

$$\log a_{Na_2O(\beta-\beta'')} = \frac{\Delta G_f^o(Na_2S_{(s)}) + \Delta G_f^o(NiO_{(s)}) - \Delta G_f^o(Na_2O_{(s)}) - \frac{1}{2}\Delta G_f^o(WS_{2(s)})}{4.576T(K)}$$

$$- \frac{10.0785E(mV)}{T(K)} \quad . \qquad (5.30)$$

Using equation (5.30), equation (5.2), and data of table (5-9), the log $a_{Na_2O_{(\beta-\beta'')}}$ vs $\frac{1}{T}$ relation can be evaluated. The result of this derivation is given by the following relation:

$$\log a_{Na_2O(\beta-\beta'')} = -\frac{10,961}{T} + 2.06 \qquad (5.31)$$

The value of log $a_{Na_2O(\beta-\beta")}$, calculated from equation (5.31), at 1000K is -8.901 which is more positive than log $a_{Na_2O(\alpha-\beta)}$ by about 4.

5.4 The Equilibrium Oxygen Pressure Diagram for Na-Al-O System at 1000K

The equilibrium oxygen pressure of $Al_{(\ell)}, Al_2O_{3(\alpha)}$ can be calculated using the relation

$$P_{O_2} = \exp\left(\frac{\Delta G_f^o(Al_2O_{3(\alpha)})}{1.5RT(K)}\right). \qquad (5.32)$$

At 1000K, $\Delta G_f^o(Al_2O_{3(\alpha)})$ is -325,301 cal/mole (118). The value of p_{O_2} at 1000K for $Al_\ell, Al_2O_{3(\alpha)}$ coexistence is therefore 4×10^{-48} atm.

In this work, we found that the two phases α- and β-Al_2O_3 equilibrate with Al melt at 700°C. The instability of the single phase β-Al_2O_3 in contact with Al was observed by Fray (67). In his work, he found that pellets made from beta-alumina containing an excess of sodium oxide over $Na_2O.11Al_2O_3$ discolored slightly, whereas those made with an excess of alumina remained white when the pellets were left for several hours in molten aluminum. He concluded that the discoloring arose from a reaction at the interface. This reaction could be the leaching of Na from β-Al_2O_3 by Al to attain the equilibrium $Al_{(\ell)}, Al_2O_{3(\alpha)}$, β-$Al_2O_3$. The equilibrium oxygen pressure over $Al_{(\ell)}, Al_2O_{3(\alpha)}$, β-$Al_2O_3$ can be calculated by considering the following reaction:

$$Na_2O_{(\beta)} + 22Al_{(s \text{ or } \ell)} + \frac{33}{2} O_{2(g)} = \beta\text{-}Al_2O_{3(s)} \qquad (5.33)$$

for which

$$\Delta G_f^o(\beta\text{-}Al_2O_{3(s)}) - \Delta G_f^o(Na_2O_{(s)}) = RT\ell n\ p_{O_2}^{16.5} . a_{Na_2O(\alpha-\beta)} .$$

Using the above equation, equation (5.13), equation (5.14), and the value -65,500 cal/mole for $\Delta G^{o}_{f}(Na_2O_{(s)})$ (119), a value of 5×10^{-48} atm. is calculated for the oxygen pressure of $Al_{(\ell)}, Al_2O_{3(\alpha)}, -Al_2O_3$ coexistence at 1000K.

A shift in the intense lines of the X-ray diffraction pattern of α-Al_2O_3 equilibrated with Al melt and/or β-Al_2O_3 was not detected which may indicate a negligible solubility of Na_2O in α-Al_2O_3. The chemical composition of β-Al_2O_3 in equilibrium with Al melt and/or α-Al_2O_3 was not determined in this investigation. Accordingly, the formula of $Na_2O.11Al_2O_3$ (59) is assumed to represent the composition of β-Al_2O_3 in equilibrium with $Al_{(\ell)}$ and/or β-Al_2O_3.

The steady and reproducible results of cell (5-IV) indicate that the two immicible-metallic phases, Al and Na, equilibrate with β-Al_2O_3. The equilibrium oxygen pressure over this coexistence is calculated by considering the equilibrium

$$2Na_{(\ell)} + \frac{1}{2} O_{2(g)} = Na_2O_{(\beta)} \qquad (5.34)$$

for which

$$\Delta G^{o}_{f}(Na_2O_{(s)}) = -RT\ell n\, a_{Na_2O(Al\text{-}Na\text{-}\beta)} \cdot p_{O_2}^{-1/2} . \qquad (5.35)$$

Using the above equation, equation (5.28), and the value -65,500 for $\Delta G^{o}_{f}(Na_2O_{(s)})$, the value 2.8×10^{-52} atm. is calculated for the oxygen pressure of the coexistence $Al_{(\ell)}, Na_{(\ell)}, \beta$-$Al_2O_{3(s)}$ at 1000K.

The maximum solubility of Na in liquid Al at 1000K is approximately 2000 ppm according to Al-Na binary-phase diagram (8). Because of the lack of data for the saturation of Al by Na in the ternary case, the above value of 2000 ppm is taken as the saturation limit of Na in molten Al of the coexistence Al,Na,β-Al_2O_3 at 1000K. No data for the maximum solubility of Al in Na have been reported.

The oxygen pressure in equilibrium with the coexistence $Na_{(\ell)}$,β-Al_2O_3,β"-Al_2O_3 is calculated by considering

$$2Na_{(\ell)} + \frac{1}{2} O_{2(g)} = Na_2O_{(\beta")} \qquad (5.36)$$

for which

$$-\Delta G_f^o(Na_2O_{(s)}) = RT\ell n\, a_{Na_2O(\beta-\beta")} \cdot p_{O_2}^{-1.2} . \qquad (5.37)$$

Substituting for $a_{Na_2O(\beta-\beta")}$ as defined in equation (5.31), and $\Delta G_f^o(Na_2O_{(s)})$ in the above equation, one obtains the value 3.7×10^{-47} atm. for the oxygen pressure in equilibrium with sodium melt, β-Al_2O_3, and β"-Al_2O_3. Again, the compositions of β- and β"-Al_2O_3 of the preceding coexistence will be taken as $Na_2O.9Al_2O_3$ and $Na_2O.7Al_2O_3$, respectively, as indicated by De Vries and Roth (63) in their proposed $Na_2O.Al_2O_3$-Al_2O_3 phase diagram.

Based on the above discussion, the equilibrium oxygen pressure diagram shown in figure (5-6) is proposed.

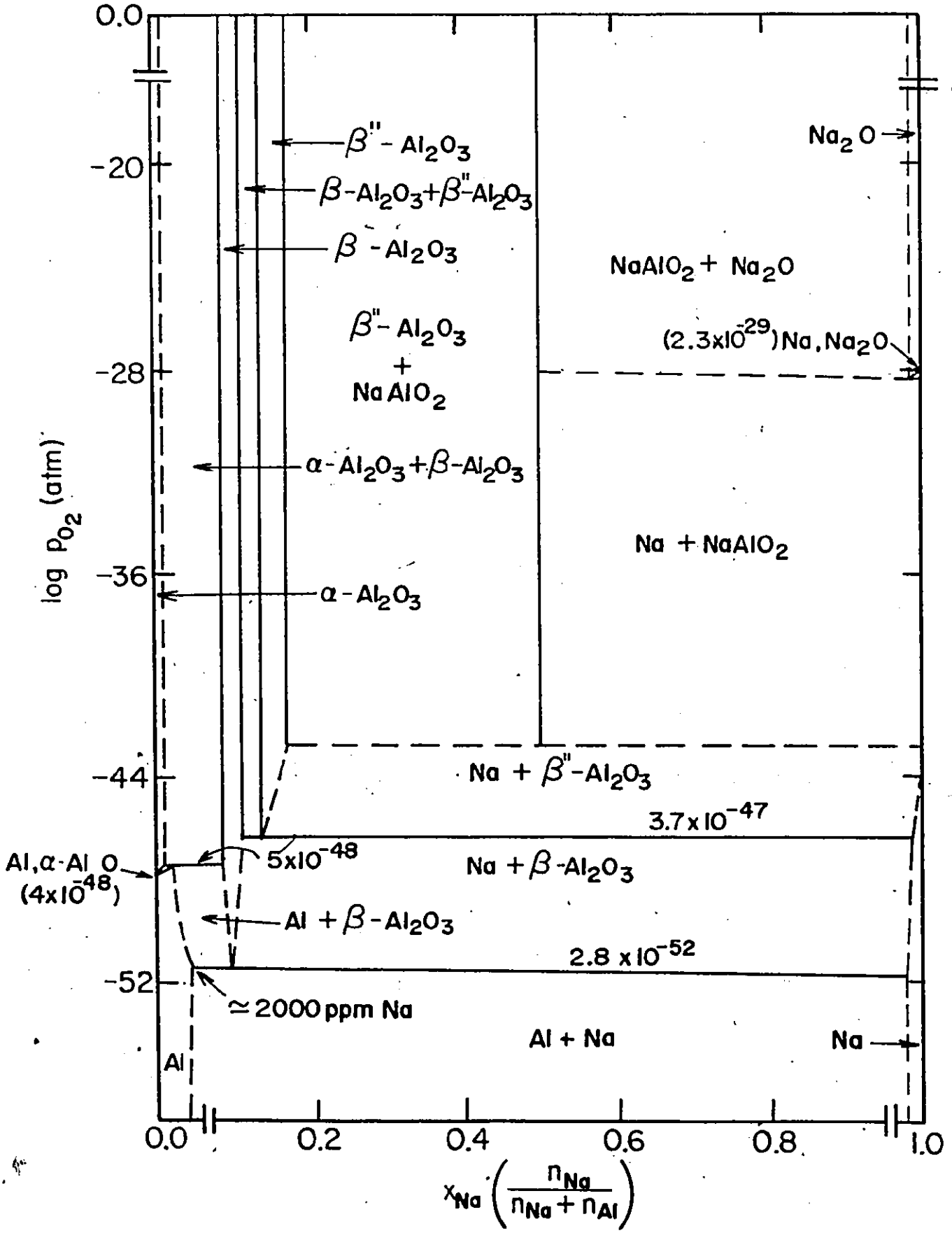

Figure (5-6) The equilibrium oxygen pressure diagram of Na-Al-O system at 1000K.

CHAPTER 6

EMF MEASUREMENTS ON CELLS INVOLVING A MIXTURE OF BETA AND ALPHA ALUMINA AS SOLID ELECTROLYTE WITH ELECTRODES FIXING OXYGEN CHEMICAL POTENTIALS. "RESULTS AND DISCUSSION"

6.1 Introduction

In 1957, Wagner and Kuikkola (6,7) published two papers which suggested the use of the solid solution of calcia stabilized zirconia as a solid electrolyte to monitor the oxygen pressure, reversibly, at high temperatures. Later it was established that this electrolytic behaviour occurs only within an electrolytic domain in the log p_{O_2} - $\frac{1}{T}$ space. Oxygen activities imposed by the Cr, Cr_2O_3 coexistence approximately define the lower electrolytic domain boundary of calcia stabilized zirconia. Outside this limit electrolytic breakdown occurs through electronic conduction which places a limitation on using this solid electrolyte in thermodynamic measurements at high temperatures.

Thoria doped yttria is the other most commonly used solid electrolyte to sense reversibly oxygen potentials. Its lower electrolytic domain boundary occurs at only several orders of magnitude below that of calcia stabilized zirconia. The lack of an oxygen-solid electrolyte which can sense very low oxygen potentials makes the development of a new solid electrolyte,

which is stable and reacts reversibly to oxygen potentials as low as those defined by Al, Al_2O_3 equilibria of great importance.

In our research, emf measurements have been carried out on cells involving solid electrolyte tubes fabricated from a mixture of β- and α-Al_2O_3 together with electrodes fixing oxygen chemical potentials over the temperature range 600-900°C. The cells have been designed to investigate the applicability of using this two phase electrolyte to sense reversibly oxygen pressures as high as those of Cu, Cu_2O coexistence and as low as those of Al, α-Al_2O_3, β-Al_2O_3 coexistence. The experimental results obtained as well as the analysis will be given and discussed in this chapter.

6.2 Electrochemical Cell Measurements

The dependences of emf upon temperature, between 600°C and 1000°C, for the cells

$$Pt|Ni_{(s)}, NiO_{(s)}|\beta\text{- and } \alpha\text{-}Al_2O_3|Cu_{(s)}, Cu_2O_{(s)}|Pt \qquad (6.I)$$

$$Pt|Fe_{(s)}, FeO_{(s)}|\beta\text{- and } \alpha\text{-}Al_2O_3|Ni_{(s)}, NiO_{(s)}|Pt \qquad (6.II)$$

are given in table (6-1) and shown in figures (6-1) and (6-2). The lines through these points were obtained by least squares analyses of the experimental data; the lines are described in table (6-2). In the above two cells, the anodes and cathodes are oxygen chemical potential electrodes.

Emf measurements were made also for the following cells

$$Pt|W_{(s)},WS_{2(s)},Na_2S_{(s)}|\beta\text{- and }\alpha\text{-}Al_2O_3|Ni_{(s)},spinel,Al_2O_{3(\alpha)}|Pt \quad (6\text{-III})$$

$$Pt|W_{(s)},WS_{2(s)},Na_2S_{(s)}|\beta\text{- and }\alpha\text{-}Al_2O_3|Fe_{(s)},FeAl_2O_{4(s)},Al_2O_{3(\alpha)}| \quad (6\text{-IV})$$

$$Pt|Al_{(s)}|\beta\text{- and }\alpha\text{-}Al_2O_3|W_{(s)},WS_{2(s)}Na_2S_{(s)}|Pt \quad (6\text{-V})$$

$$Pt|Ta|Al_{(\ell)}|\beta\text{- and }\alpha\text{-}Al_2O_3|W_{(s)},WS_{2(s)},Na_2S_{(s)}|Pt \quad (6\text{-VI})$$

The emf temperature data of these cells are listed in tables (6-3) and (6-4) and plotted graphically in figures (6-3), (6-4), and (6-5). The lines which appear in the figures were obtained by least squares analyses of the emf data; the lines are described in table (6-5). The cathodes of cells (6-III) and (6-IV) fix the oxygen chemical potentials while the anodes, made of $W_{(s)},WS_{2(s)},Na_2S_{(s)}$ coexistence, fix the sodium chemical potential. The opposite situation is encountered in cells (6-V) and (6-VI); i.e., the anodes are coexistences which fix the oxygen chemical potentials while the cathodes are made of $W_{(s)},WS_{2(s)}$, $Na_2S_{(s)}$ coexistence.

Temperature (°C)	emf (mV)	
	Cell (6-I)	Cell (6-II)
600	288	-
650	285	251
700	281	256
750	278	262
800	275	266
850	271	271
900	268	276
950	264	282
1000	[illegible]0	286

Table (6-1) The emf-temperature data for cells (6-I), and (6-II).

Cell	Temperature range (°C)	E(mV)=a(±S_a)+b(±S_b)T(K)				Standard deviation (mV)
		a	S_a	b	S_b	
(6-I)	600-1000	349	1	-0.069	0.001	±0.4
(6-II)	650-1000	158	2	0.100	0.001	±0.5

Table (6-2) Least squares analyses of the emf data of cell (6-I) and cell (6-II).

Temperature (°C)	emf(mV)						
	Cell (6-III)				Cell (6-IV)		
650	706	706	705	707	434	435	432
700	684	682	686	683	412	412	410
750	662	661	663	663	388	387	389
800	640	642	641	638	363	363	363
850	617	616	618	618	337	336	335
900	595	594	596	594	313	314	314

Table (6-3) The emf-temperature data for cells (6-III), and (6-IV).

Temperature (°C)	emf (mV)			
	Cell (6-V)		Cell (6-VI)	
550	724	725	-	
575	733	732	-	
600	740	741	-	
625	747	748	-	
650	754	753	-	
675	-		763	760
700	-		768	769
725	-		774	777
750	-		782	783
775	-		791	790
800	-		795	798

Table (6-4) The emf-temperature data for cells (6-V) and (6-VI)

Cell	Temperature range, (°C)	$E(mV) = a(\pm S_a) + b(\pm S_b)T(K)$				Standard deviation, (mV)
		a	S_a	b	S_b	
(6-III)	650-900	1117	3	-0.444	0.003	±2
(6-IV)	650-900	884	5	-0.486	0.004	±2
(6-V)	550-650	485	7	0.292	0.008	±1
(6-VI)	675-800	493	9	0.283	0.009	±2

Table (6-5) Least squares analyses of emf data of cells (6-III), (6-IV), (6-V), and (6-VI).

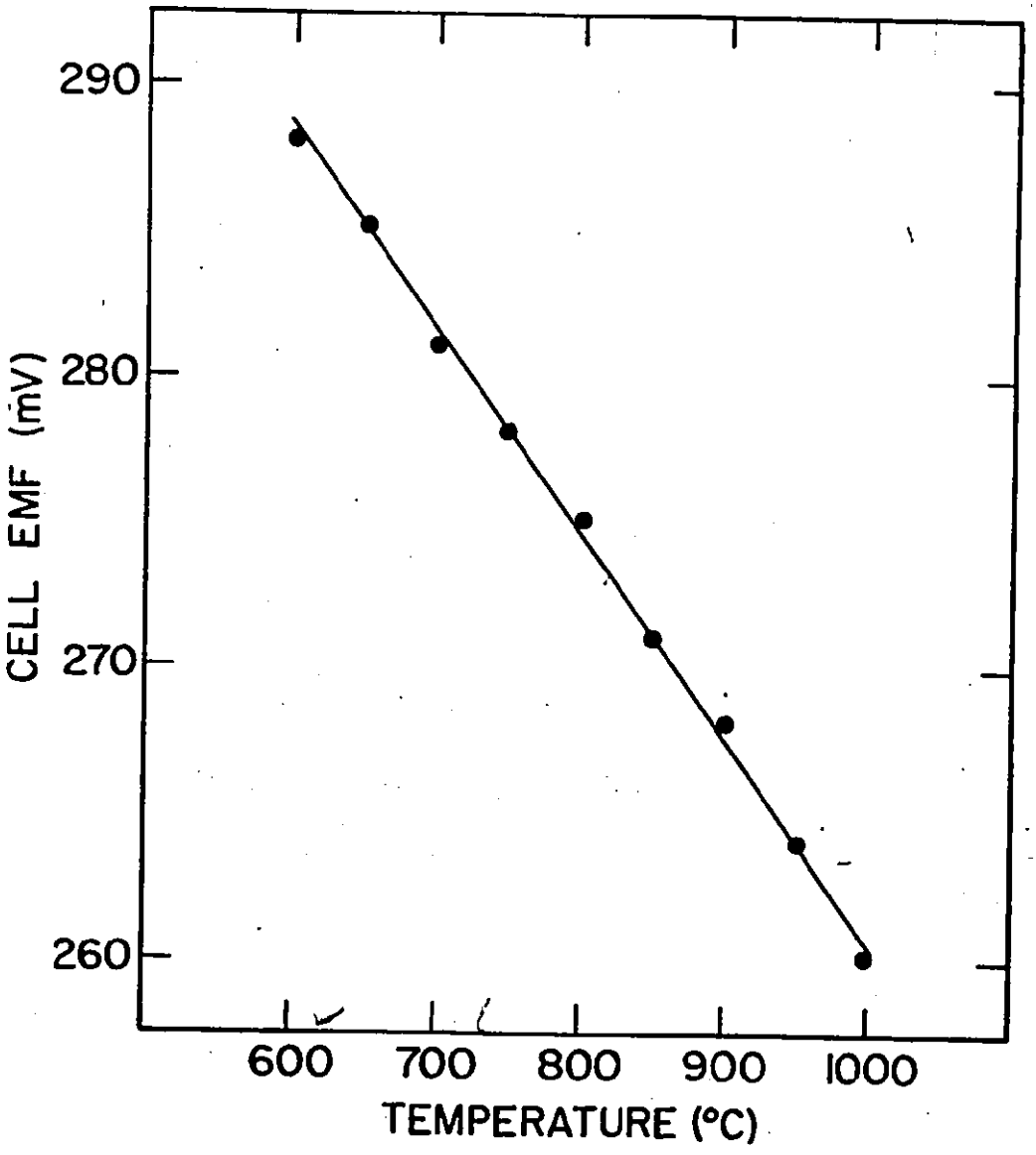

Figure (6-1) Variation of emf with temperature for cell (6-I).

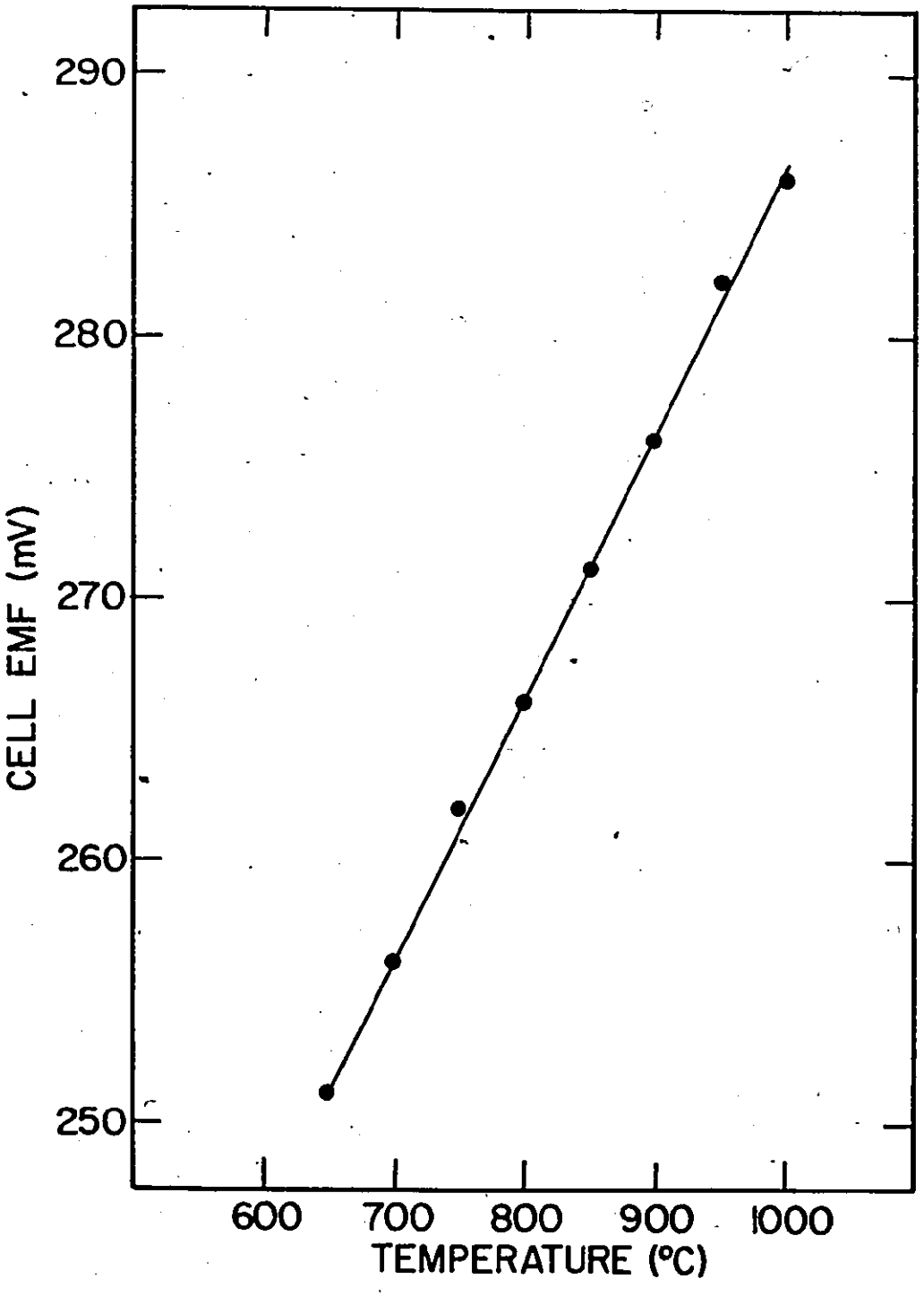

Figure (6-2) Variation of emf with temperature for cell (6-II).

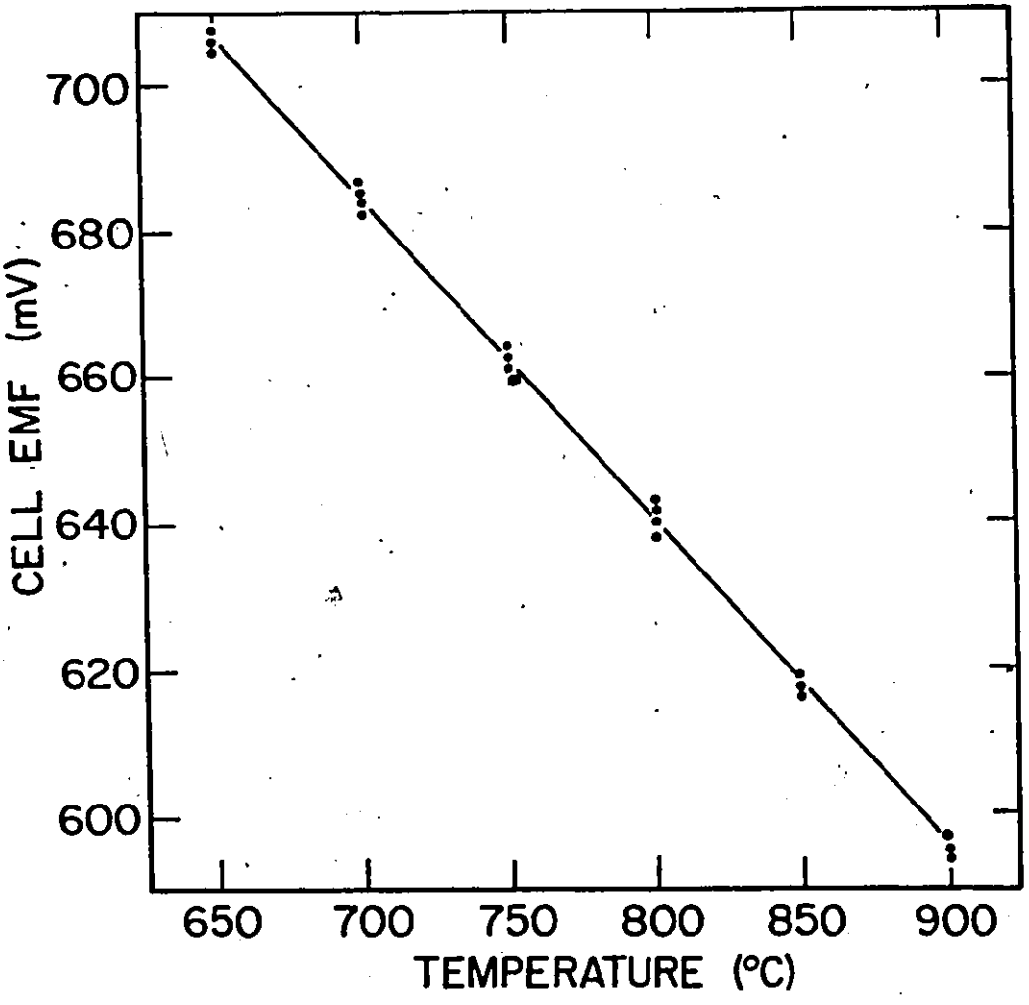

Figure (6-3) The dependence of emf on temperature for cell (6-III).

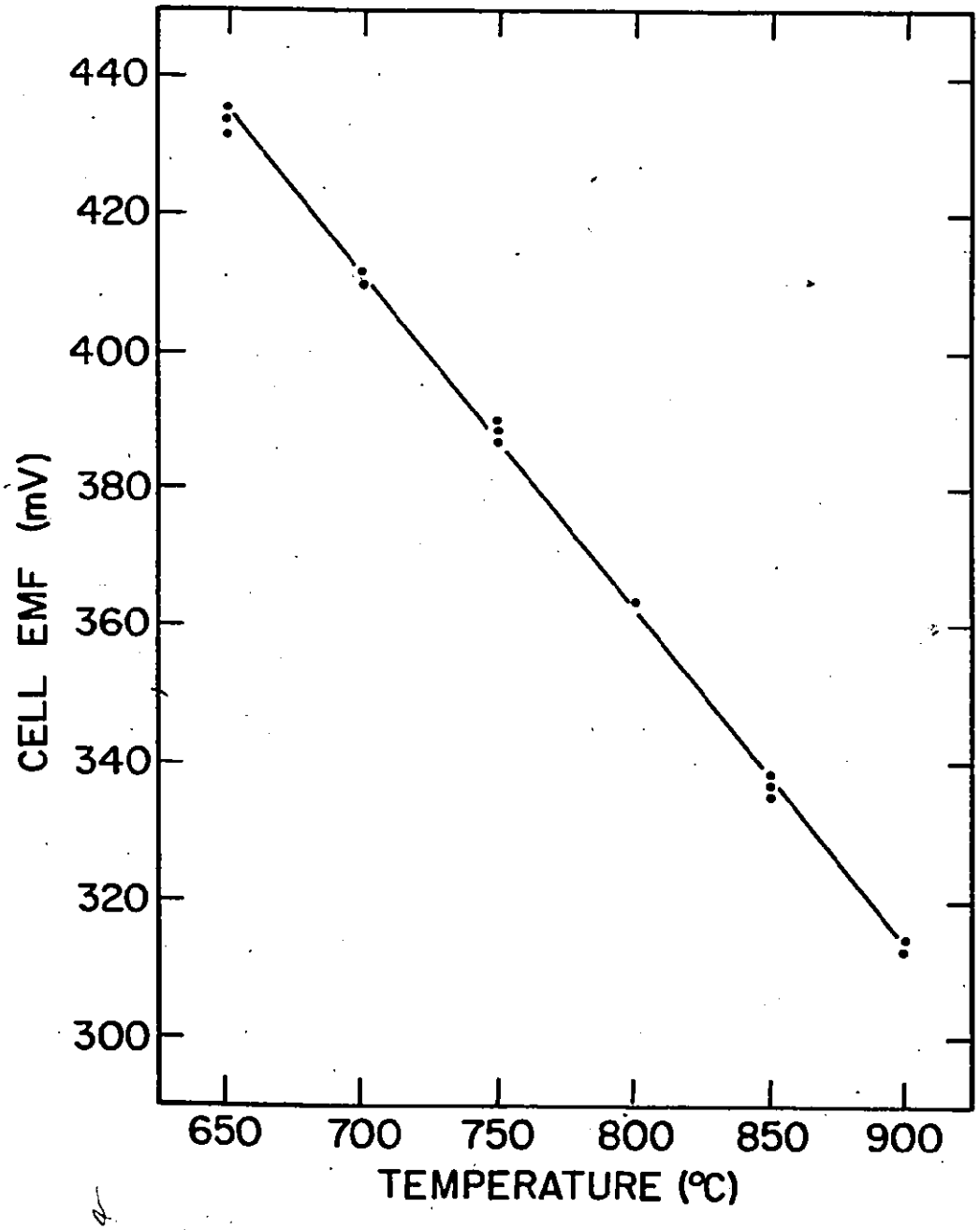

Figure (6-4) Variation of emf with temperature for cell (6-IV).

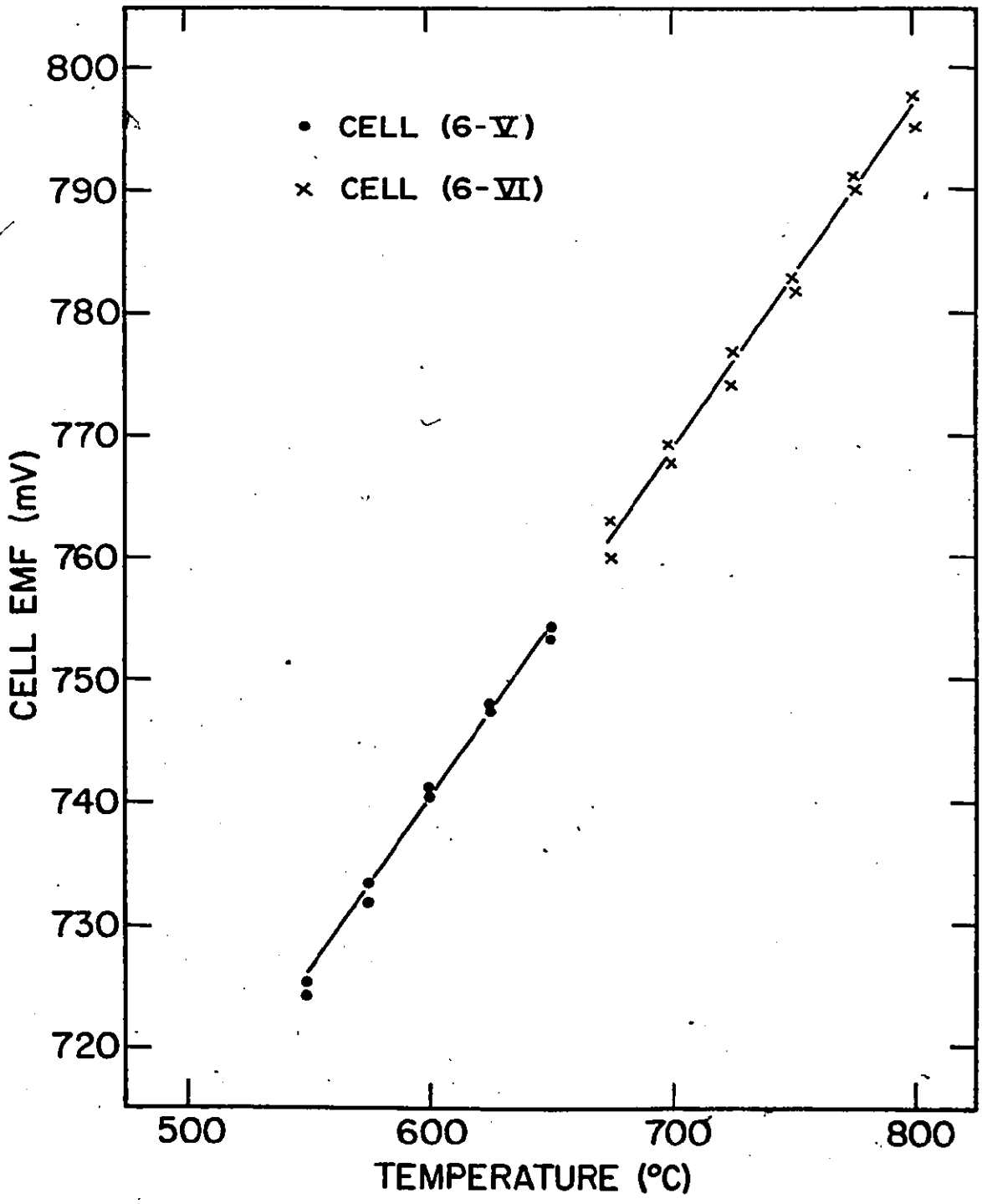

Figure (6-5) The variation of the emf with temperature for cells (6-V), and (6-VI).

6.3 Discussion

Emf-T relation for cell (6-I) is plotted in figure (6-1) and described in table (6-2). The results obtained by Steele and Alcock (91) and Charette and Flengas (92) for the cell

$$Ni_{(s)},NiO_{(s)}\,|\,ZrO_2(+CaO)\,|\,Cu_2O_{(s)},Cu_{(s)}$$

along with our results of cell (6-I) are plotted in figure (6-6). Choudhury's data (22) for a cell similar to cell (6-I) are shown also in figure (6-6). The least-squares best fit of Charette and Flengas data between 924K and 1328K is given by

$$E(mV) = 346.68-0.07046T(K) \pm 0.19\ mV\ . \qquad (6.1)$$

The agreement between the emf-T relation obtained in this investigation for cell (6-I), table (6-2), and equation (6.1) is very good.

Several investigators (6, 7, 91, 92) have measured the emf developed by the cell

$$Fe_{(s)},FeO_{(s)}\,|\,\text{oxygen conducting solid electrolyte}\,|\,NiO_{(s)},Ni_{(s)}.$$

The results of the present investigation for cell (6-II) as well as the results from other investigations have been plotted in figure (6-7).

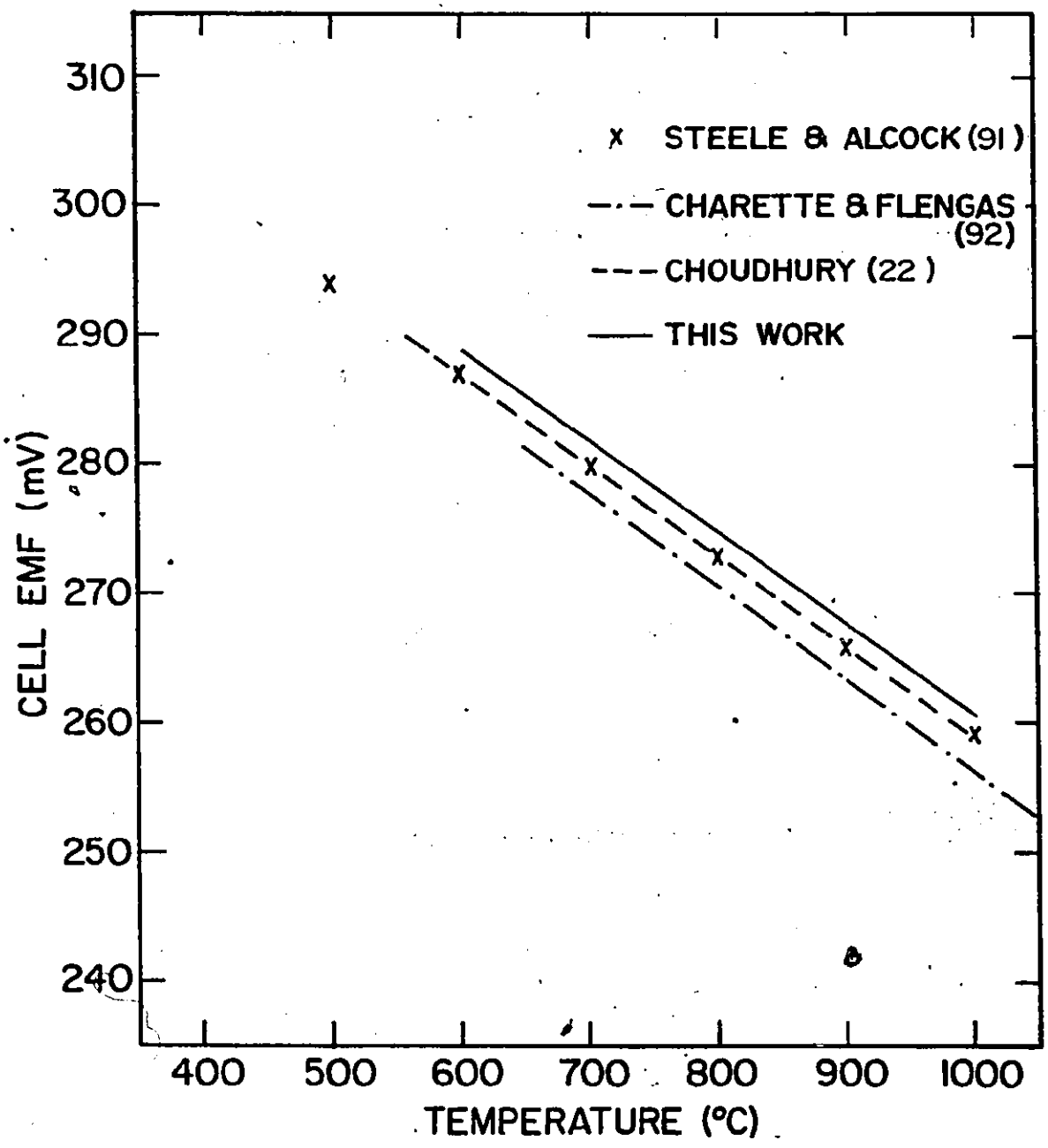

Figure (6-6) Temperature dependence of emf for Ni,NiO||Cu_2O,Cu cell.

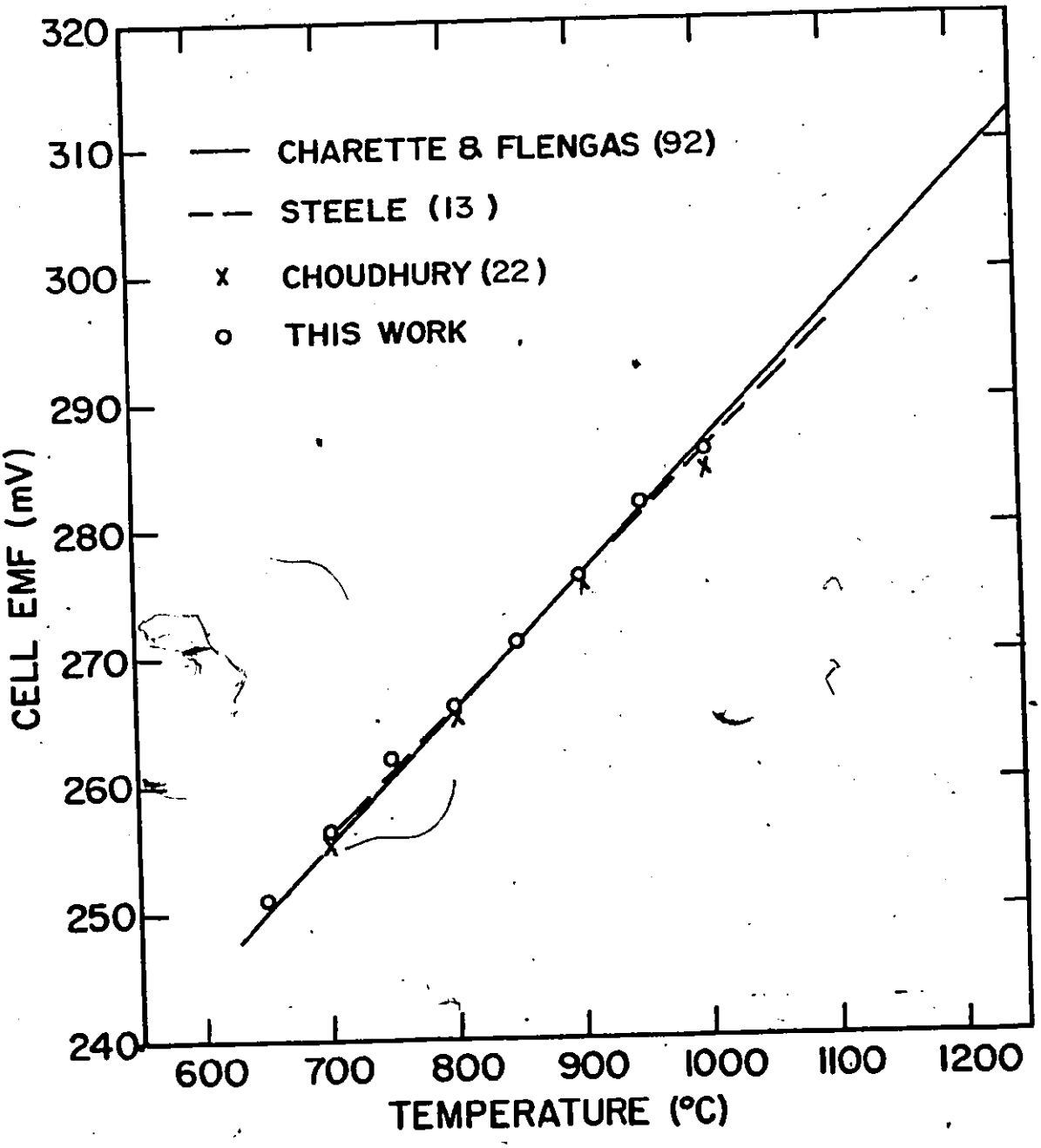

Figure (6-7) Temperature dependence of emf for Fe,FeO||NiO,Ni cell.

A least-squares analysis of published data has been carried out by Steele (13); the line obtained from Steele's analysis is described by:

$$E(mV) = 157.6+0.101T(K) \pm 0.86\ mV \quad (6.2)$$

Comparison between the emf-T relation obtained in our investigation for cell (6-II), $E = 158.4+0.100T$ and relation (6.2) gives excellent agreement.

The good agreement between the results of cells (6-I) and (6-II) and the emf data in the literature for cells with similar electrode systems but having an oxygen ion conducting solid electrolyte indicates that the oxygen-fixing coexistences Cu,Cu_2O, Ni,NiO, and Fe,FeO show reversible behaviour in contact with β- and α-Al_2O_3 solid electrolyte.

The free energy of formation of nickel spinel was determined by Tretjakow and Schmalzried (33) by using a galvanic cell of the type

$$Ni,spinel,Al_2O_{3(\alpha)}\,|\,ZrO_2(+CaO)\,|\,O_2$$

Table (6-6) lists the values of the free energy of formation of the spinel from NiO and α-Al_2O_3 as determined by Tretjakow and Schmalzried. Jacob and Alcock (34) have reported the following relation

$$\Delta G(cal) = -1,499-2.31T(K) \pm 150\ cal \quad (6.2)$$

for the free energy of formation of $NiO.xAl_2O_3$ from its oxide.

Temperature (K)	1000	1100	1200	1300	1400	1500
ΔG (cal/mole)	-10,200	-7,000	-5,200	-4,000	-3,250	-3,000

Table (6-6) The free energy of formation of nickel spinel from $NiO_{(s)}$ and $Al_2O_{3(\alpha)}$ (33).

The values of ΔG given by equation (6.2) decrease with temperature which contradicts Tetrjakow and Schmalzried results.

The steady and reproducible potentials exhibited by cell (6-III) have made it possible not only to see the applicability of using the two-phase solid electrolyte to sense the oxygen potential of the coexistence Ni, spinel, $Al_2O_{3(\alpha)}$ but also to determine the free energy of formation of nickel spinel. The over-all cell reaction for cell (6-III) may be written as

$$\frac{1}{2} W_{(s)} + Na_2S_{(s)} + NiO.xAl_2O_3 = Na_2O_{(\alpha-\beta)} + xAl_2O_{3(\alpha)} + \frac{1}{2} WS_{2(s)} + Ni \qquad (6.3)$$

for which

$$\Delta G^{o}_{6.3} = -2FE - RT\ell n\, a_{Na_2O_{(\alpha-\beta)}}$$

Since

$$\Delta G^{o}_{(6.3)} = \Delta G^{o}_{f}(Na_2O_{(s)}) + x\Delta G^{o}_{f}(Al_2O_{3(\alpha)}) + \frac{1}{2} G^{o}_{f}(WS_{2(s)})$$

$$- \Delta G^{o}_{f}(Na_2S_{(s)}) - \Delta G_{f}(NiO.xAl_2O_3)$$

therefore

$$\Delta G_{f}(NiO.xAl_2O_3) = 2FE + RT\ell n\, a_{Na_2O_{(\alpha-\beta)}} + \Delta G^{o}_{f}(Na_2O_{(s)}) + x\Delta G^{o}_{f}(Al_2O_{3(\alpha)})$$

$$+ \frac{1}{2} \Delta G^{o}_{f}(WS_{2(s)}) - \Delta G^{o}_{f}(Na_2S_{(s)}) \qquad (6.4)$$

where, $\Delta G_f(NiO.xAl_2O_3)$ is the free energy of formation of spinel. The free energy change of the reaction

$$NiO_{(s)} + xAl_2O_{3(\alpha)} = NiO.xAl_2O_3 \qquad (6.5)$$

is given by

$$\Delta G_{(6.5)} = \Delta G_f(NiO.xAl_2O_3) - \Delta G_f^o(NiO_{(s)}) - x\Delta G_f^o(Al_2O_{3(\alpha)}). \qquad (6.6)$$

Combining equation (6.4) and equation (6.6) yields

$$\Delta G_{(6.5)} = 2FE + RT\ell n\, a_{Na_2O_{(\alpha-\beta)}} + \Delta G_f^o(Na_2O_{(s)}) + \frac{1}{2}\Delta G_f^o(WS_{2(s)}) - \Delta G_f^o(NiO_{(s)}) - \Delta G_f^o(Na_2S_{(s)}). \qquad (6.7)$$

The dependence of $\Delta G_{(6.5)}$ on temperature can be obtained using equation (6.7), equation (5.13), and the data of tables (5-9) and (6-5). The evaluated equation for the free energy change of reaction (6.5) is given by

$$\Delta G_{(6.5)} = -3,227 - 1.29T \qquad (6.8)$$

The estimated error in the values of $\Delta G_{(6.5)}$, given by equation (6.8), is about ± 1500 cal. The agreement between equation (6.8) and equation (6.2) is fairly good while both equations are in a clear disagreement with Tretjakow and Schmalzeried results.

To examine the applicability of using the β- and α-Al_2O_3 solid electrolyte to monitor reversibly an oxygen potential as

low as that of $Fe_{(s)}, FeAl_2O_{4(s)}, Al_2O_{3(\alpha)}$ equilibria, the emf of the solid state-galvanic cell (6-IV) was measured. The best line through the emf data of cell (6-IV) can be represented by

$$E(mV) = 884(\pm 5) - 0.486(\pm 0.004)T(K) \quad . \qquad (6.9)$$

The over-all cell reaction of cell (6-IV) may be written as

$$\frac{1}{2} W_{(s)} + Na_2S_{(s)} + FeAl_2O_{4(s)} = Na_2O_{(\beta)} + Al_2O_{3(\alpha)} + \frac{1}{2} WS_{2(s)} + Fe_{(s)} \qquad (6.10)$$

for which

$$-2FE = \Delta G_f^o(Al_2O_{3(\alpha)}) + \Delta G_f^o(Na_2O_{(s)}) + \frac{1}{2} \Delta G_f^o(WS_{2(s)}) - \Delta G_f^o(Na_2S_{(s)})$$
$$- \Delta G_f^o(FeAl_2O_{4(s)}) + RT\ell n\, a_{Na_2O(\alpha-\beta)} \quad . \qquad (6.11)$$

Rearranging equation (6.11) we obtain

$$\Delta G_f^o(FeAl_2O_4) = \Delta G_f^o(Al_2O_{3(\alpha)}) + \Delta G_f^o(Na_2O_{(s)}) + \frac{1}{2} \Delta G_f^o(WS_{2(s)})$$
$$- \Delta G_f^o(Na_2S_{(s)}) + RT\ell n\, a_{Na_2O(\alpha-\beta)} + 2FE \quad . \qquad (6.12)$$

The standard free energy change of the following reaction

$$2Fe_{(s)} + O_{2(g)} + 2Al_2O_{3(\alpha)} = 2FeAl_2O_{4(s)} \qquad (6.13)$$

is given by

$$\Delta G^o_{(6.13)} = 2\Delta G_f^o(FeAl_2O_{4(s)}) - 2\Delta G_f^o(Al_2O_{3(\alpha)}) \quad . \qquad (6.14)$$

Multiplying equation (6.12) by two and adding to equation (6.14) yields

$$\Delta G^{o}_{(6.13)} = 2\Delta G^{o}_{f}(Na_2O_{(s)}) + \Delta G^{o}_{f}(WS_{2(s)}) - 2\Delta G^{o}_{f}(Na_2S_{(s)}) + 2RT\ell n\, a_{Na_2O(\alpha-\beta)} + 4FE \quad . \qquad (6.15)$$

$\Delta G^{o}_{(6.13)}$-T relation can be evaluated using equation (6.15), equation (6.9), equation (5.13), and the data of table (5-9). The determined $\Delta G^{o}_{(6.13)}$-T relation, over the temperature range 650-900°C, is given by

$$\Delta G^{o}_{(6.13)} = -139,877+32.79T(K) \quad . \qquad (6.16)$$

The estimated error in the values of $\Delta G^{o}_{(6.13)}$ is ±2 Kcal. A solid oxide galvanic cell using calcia stabilized zirconia and calcia stabilized zirconia in combination with thoria doped yttria as electrolyte was used (50) to determine the free energy change of reaction (6.13). The results of that investigation, equation (6.17), are found to be in excellent agreement with the results of the present work.

$$\Delta G^{o} = -139,790+32.83T(K)\pm 300 \text{ cal. } (750\text{-}1536°C). \qquad (6.17)$$

Steady and reproducible electrical potentials exhibited by cell (6-IV) as well as the excellent agreement between our results for $\Delta G^{o}_{(6.13)}$ and results obtained from solid oxide

galvanic cells demonstrate that β- and α-Al_2O_3 solid electrolyte senses an oxygen potential as low as that of $Fe,FeAl_2O_4,Al_2O_{3(\alpha)}$ reversibly between 650°C and 900°C.

Cell (6-V) and cell (6-VI) were designed to examine the behaviour of the two-phase β- and α-Al_2O_3 tubes as solid electrolyte to sense reversibly the extremely low oxygen partial pressure of $Al,\alpha\text{-}Al_2O_3,\beta\text{-}Al_2O_3$ coexistence. Although we have found that the emf of cell (6-V) and cell (6-VI) decrease steadily with time, at a constant temperature, the instability problem of these two cells was partially overcome by coulometric disturbance of the cell. The change of emf with time was then followed at each temperature to determine the decay curve of the cell emf. Reversible emf plateaus with duration times between 4 and 9 minutes were obtained.

The over-all cell reaction for cell (6-V), or cell (6-VI), can be written as

$$\frac{4}{3}\,Al_{(s\text{ or }\ell)} + 2Na_2O_{(\beta)} + WS_{2(s)} = 2Na_2S_{(s)} + \frac{2}{3}\,Al_2O_{3(\alpha)} + W \qquad (6.18)$$

for which

$$-6FE = \Delta G_f^o(Al_2O_{3(\alpha)}) + 3\Delta G_f^o(Na_2S_{(s)}) - \frac{3}{2}\,\Delta G_f^o(WS_{2(s)}) - 3\Delta G_f^o(Na_2O_{(s)}) - 3RT\ell n\, a_{Na_2O(\alpha-\beta)} \qquad (6.19)$$

Rearrangement of equation (6.19) yields

$$\Delta G_f^o(Al_2O_{3(\alpha)}) = 3RT\ell n\, a_{Na_2O(\alpha-\beta)} + 3\Delta G_f^o(Na_2O_{(s)})$$

$$+ \frac{3}{2}\Delta G_f^o(WS_{2(S)}) - 3\Delta G_f^o(Na_2S_{(s)}) - 6FE \ . \qquad (6.20)$$

The dependence of $\Delta G_f^o(Al_2O_{3(\alpha)})$ on temperature can be obtained using equation (6.20), equation (5.13), and the data of tables (5-9) and (6-5). This is given by equation (6.21) between 550°C-650°C and by equation (6.22) between 675°C-800°C.

$$\Delta G_f^o(Al_2O_{3(\alpha)}) = -399{,}232+76.03T(K) \text{ cal/mole} \qquad (6.21)$$

$$\Delta G_f^o(Al_2O_{3(\alpha)}) = -400{,}338+77.27T(K) \text{ cal/mole} \ . \qquad (6.22)$$

The estimated error in the values of the free energy of formation of α-Al_2O_3 given by the preceding two equations is about ± 1 Kcal. The values of $\Delta G_f^o(Al_2O_{3(\alpha)})$ given by equations (6.21) and (6.22) are more positive than the values given in JANAF tables by about 3 Kcal. However, the agreement is good in view of the fact that the emf results are for $Al_2O_{3(\alpha)}$ equilibrated in a ternary system.

6.4 Summary

The emfs of cells (6-I)-(6-VI) were measured. A coulometric disturbance was needed to overcome the steady decrease of the emf of cell (6-V) and cell (6-VI) with time at constant temperature. This problem was not encountered in the case of the other four cells where potentials were very steady. Analyses of the emf data obtained from the six cells demonstrated that the two-phase β-Al_2O_3 and α-Al_2O_3 tubes reacted reversibly as a solid electrolyte to oxygen pressures as high as those imposed by Cu,Cu_2O equilibrium and as low as those of Al,α-Al_2O_3,β-Al_2O_3 co-existence. The most commonly used solid-oxide electrolytes conduct electronically (n-conduction) at oxygen pressures higher than that of Al,Al_2O_3 by approximately 10 orders of magnitude over the temperature range 600-900°C. The results from this investigation demonstrate that β- and α-Al_2O_3 solid electrolyte has the advantage over other solid-oxide electrolytes to be used as an oxygen probe to monitor extremely low oxygen potentials.

CHAPTER 7

NICKEL-ALUMINUM-OXYGEN SYSTEM

"RESULTS AND DISCUSSION"

7.1 Electrochemical Cell Measurements

Temperature dependences of the electromotive forces of the following two cells

$$Pt|Ni_{(s)},NiO_{(s)},NiAl_2O_4|ZrO_2(+CaO)|Ni_{(s)},NiO_{(s)}|Pt \qquad (7\text{-I})$$

$$Pt|Ni_{(s)},\text{spinel},Al_2O_{3(\alpha)}|ZrO_2(+CaO)|Ni_{(s)},NiO_{(s)}|Pt \qquad (7\text{-II})$$

which represent Ni,NiO,$NiAl_2O_4$ equilibria and Ni,spinel,$Al_2O_{3(\alpha)}$ coexistence, respectively, combined with Ni,NiO as reference electrode are listed in table (7-1) and plotted in figures (7-1) and (7-2). The lines shown in the figures were obtained by least squares analyses of the emf data, equations describing these linear plots are given on the graphs.

Cell (7-III) which is similar to the above cells but with Ni-Al alloy(0.15 a/o Al),$Al_2O_{3(\alpha)}$ anode exhibited electrical instability which was not amenable to correction by coulometric disturbance or by temperature cycling of the cell.

$$Pt|\begin{matrix}\text{Ni-Al alloy}\\(0.15\text{ a/o Al})\end{matrix},Al_2O_{3(\alpha)}|ZrO_2(+CaO)|Ni_{(s)},NiO_{(s)}|Pt \qquad (7\text{-III})$$

This instability problem can be explained on the basis of electronic conduction in the solid electrolyte when the oxygen

Temperature (°C)	Cell emf (mV)						
	Cell (7-I)				Cell (7-II)		
850	4.2	4.4	4.5	4.3	117	116	117
900	4.4	4.5	4.5	4.4	120	118	119
950	4.7	4.6	4.5	4.5	120	123	121
1000	4.6	4.7	4.8	4.8	124	125	125
1050	4.9	4.8	4.8	5.0	127	126	127
1100	5.0	5.1	5.0	5.3	128	130	129
1150	5.4	5.3	5.3	5.3	130	130	131

Table (7-1) The dependence of emf on temperature for cells (7-I) and (7-II).

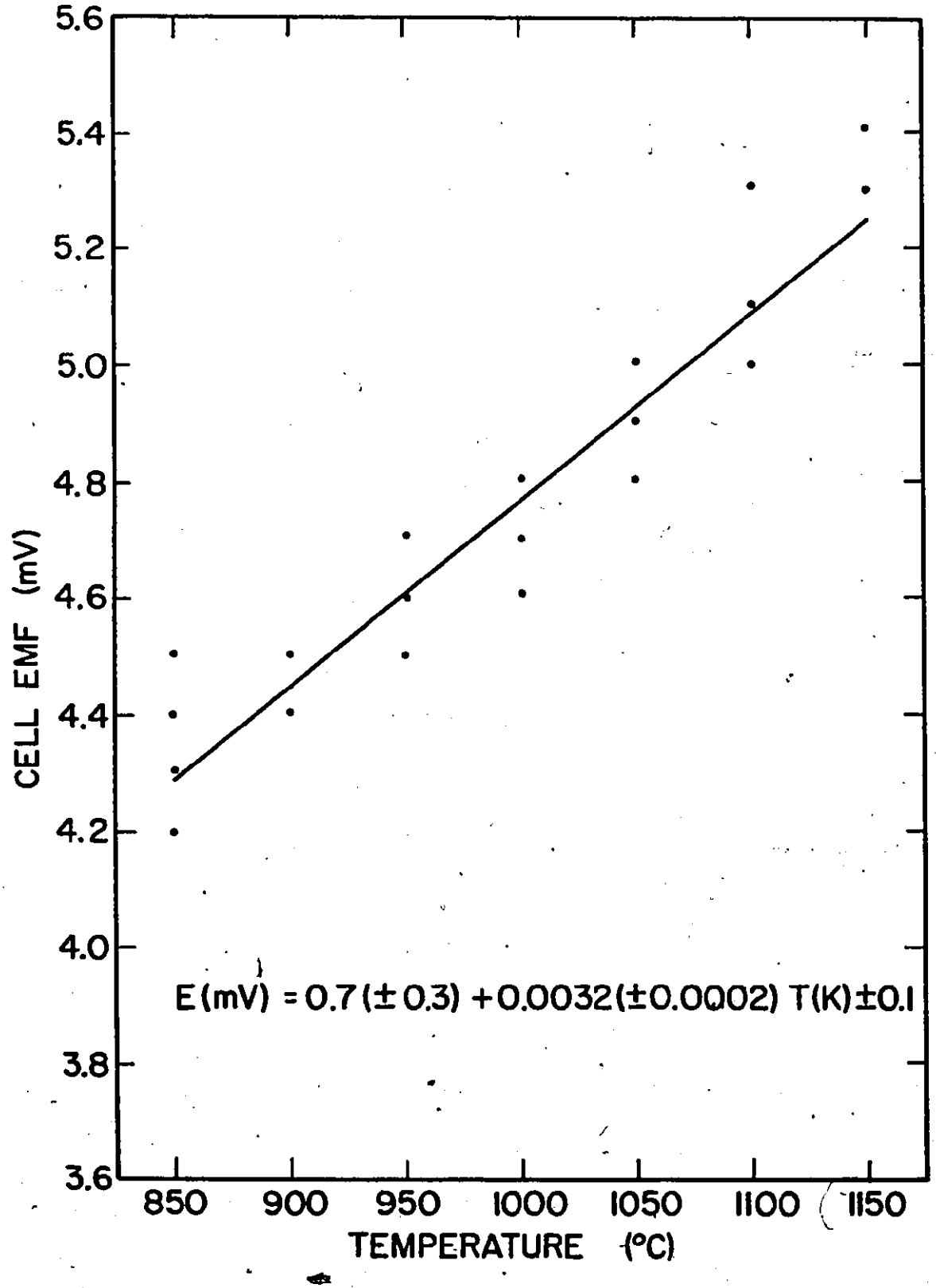

Figure (7-1) The variation of emf with temperature for cell (7-I).

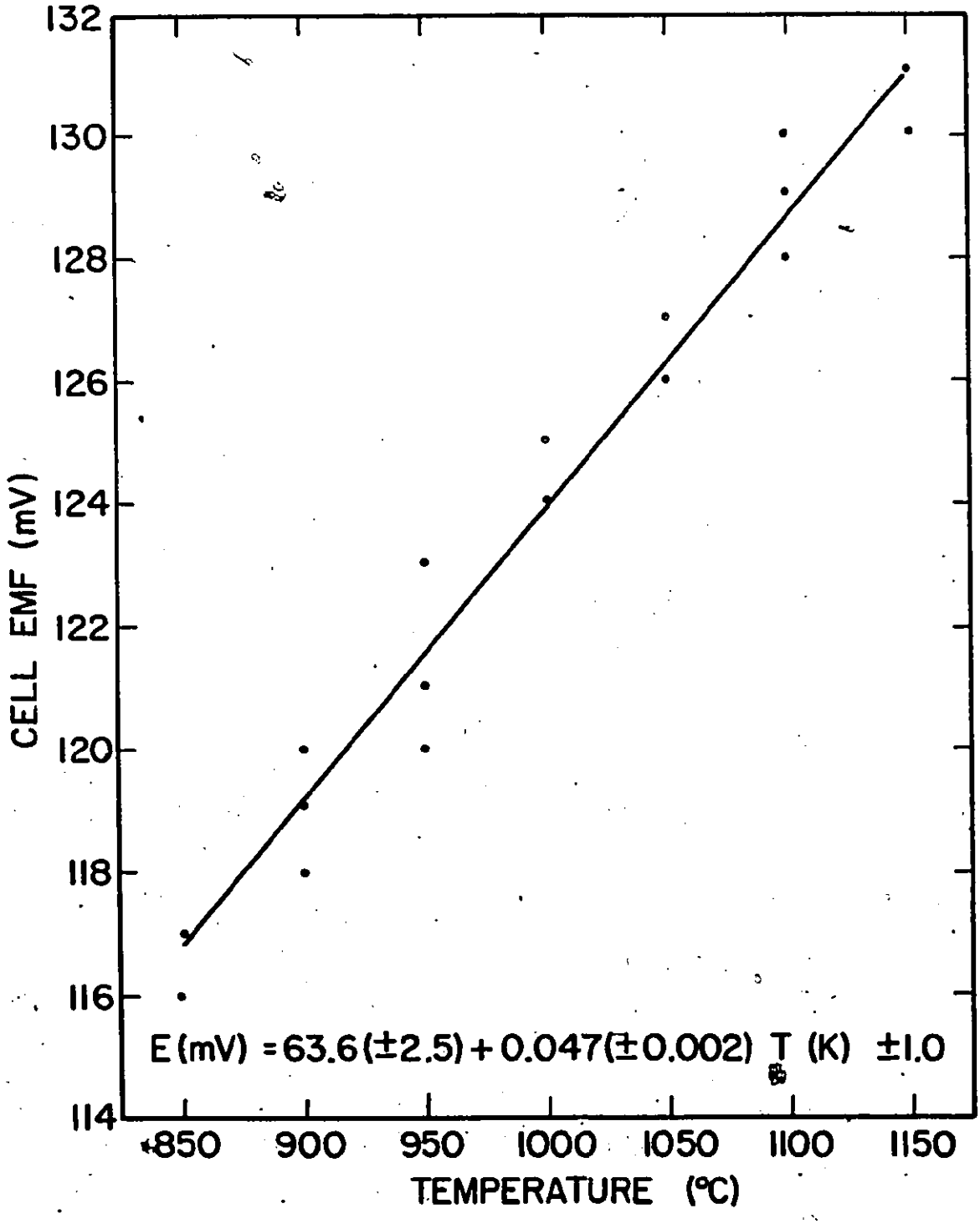

Figure (7-2) The variation of emf with temperature for cell (7-II).

pressures imposed by the coexistence Ni-0.15 a/o Al alloy,$Al_2O_{3(\alpha)}$ are below the values of oxygen potentials defined by the lower electrolytic domain boundary of calcia stabilized zirconia.

The following three cells

$$Pt|{}^{\text{Ni-Al alloy}}_{\text{(0.15 a/o Al)}},Al_2O_{3(\alpha)}|\beta\text{-and }\alpha\text{-}Al_2O_3|W_{(s)},WS_{2(s)},Na_2S_{(s)}|Pt \quad (7\text{-IV})$$

$$Pt|{}^{\text{Ni-Al alloy}}_{\text{(1.19 a/o Al)}},Al_2O_{3(\alpha)}|\beta\text{- and }\alpha\text{-}Al_2O_3|W_{(s)},WS_{2(s)},Na_2S_{(s)}|Pt \quad (7\text{-V})$$

$$Pt|{}^{\text{Ni-Al alloy}}_{\text{(2.36 a/o Al)}},Al_2O_{3(\alpha)}|\beta\text{- and }\alpha\text{-}Al_2O_3|W_{(s)},WS_{2(s)},Na_2S_{(s)}|Pt \quad (7\text{-VI})$$

were designed using β- and α-Al_2O_3 as solid electrolyte to determine the equilibrium oxygen pressures of coexistences of the type Ni-Al alloy,$Al_2O_{3(\alpha)}$. The aluminum contents of the alloys were between 0.15 a/o and 2.36 a/o. The electromotive forces of these three cells were measured at 940°C. In contrast to cell (7-III) the emfs shown by these three cells were steady and reproducible. The emf values obtained for cells (7-IV), (7-V) and (7-VI) were 19±1 mV, 119±2 mV, and 151±1 mV, respectively.

7.2 Metallography

Figures (7-3)-(7-8) are photographs showing features of pellets belonging to the NiO-Al_2O_3 system. NiO-$NiAl_2O_4$ pellets annealed between 1000°C and 1700°C had the appearance shown in figure (7-3). Tablet surfaces in contact with the α-Al_2O_3 container were completely blue while the upper surfaces and the cross sections of the tablets exercised no change in color upon annealing. This indicated that the crucible-tablet interaction, α-Al_2O_3+NiO=spinel, was limited only to the con-

tact region during an equilibration period. The presence of a metallic phase as well as a change in color, from green-blue to grey, were observed, figure (7-4), for $NiO-NiAl_2O_4$ pellets annealed at 1800°C under argon atmospheres. The metallic phase located at the pellet surfaces was of globular form. $NiO-NiAl_2O_4$ pellets annealed at 1800°C in air had features similar to those shown in figure (7-4) except that the nickel spinel layer formed at the crucible-pellet contacts were more pronounced, figure (7-5).

$Spinel-Al_2O_{3(\alpha)}$ pellets were annealed between 1000°C and 1900°C at intervals of 100°C. Figure (7-6) gives the typical features observed for the air-annealed pellets. Although some coloring of the $\alpha-Al_2O_3$ containers was observed at the contact region, figure (7-7), it was not as severe as that observed in the case of $NiO-NiAl_2O_4$ tablets, figure (7-8). Samples annealed at 1800°C and 1900°C under atmospheric argon pressure showed color changes, figures (7-9) and (7-10).

The microstructures of polished-annealed samples of $Ni, spinel, Al_2O_{3(\alpha)}$ and 0.15 a/o Al-Ni alloy, $Al_2O_{3(\alpha)}$ were revealed, figures (7-11-a) and (7-12-a), using scanning electron microscopy. Ni- and Al-K_α radiation mapping for the two samples are shown in figures (7-11-b); (7-11-c); (7-12-b) and (7-12-c). The polished sample of $Ni-NiO-NiAl_2O_4$ showed poor contrast. Consequently it was difficult to obtain a micrograph for this sample revealing the different phases,

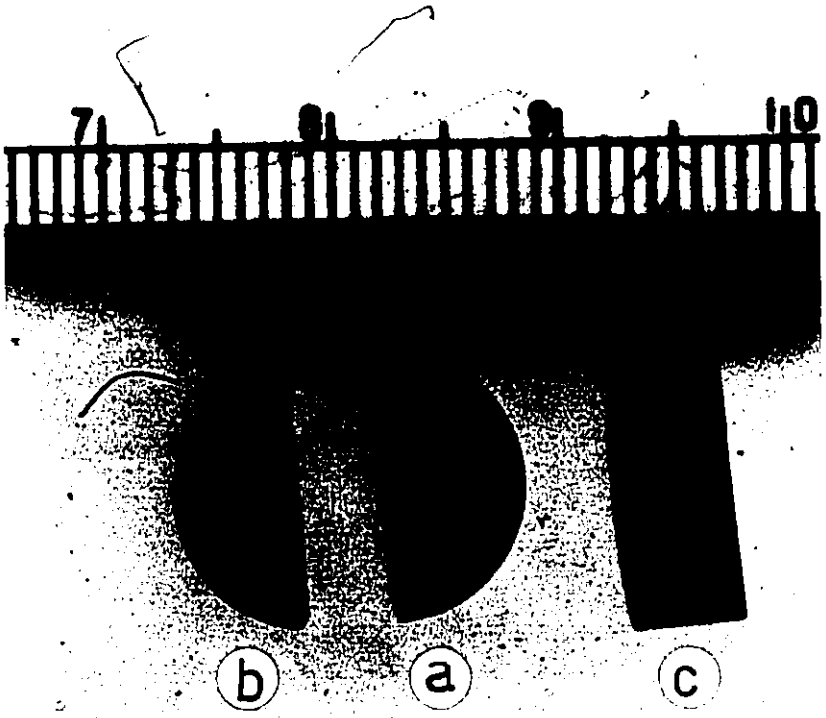

Figure (7-3) Photograph showing the upper surface (a), the lower surface (b), and the cross section (c) of air annealed NiO-$NiAl_2O_4$ tablet at 1600°C.

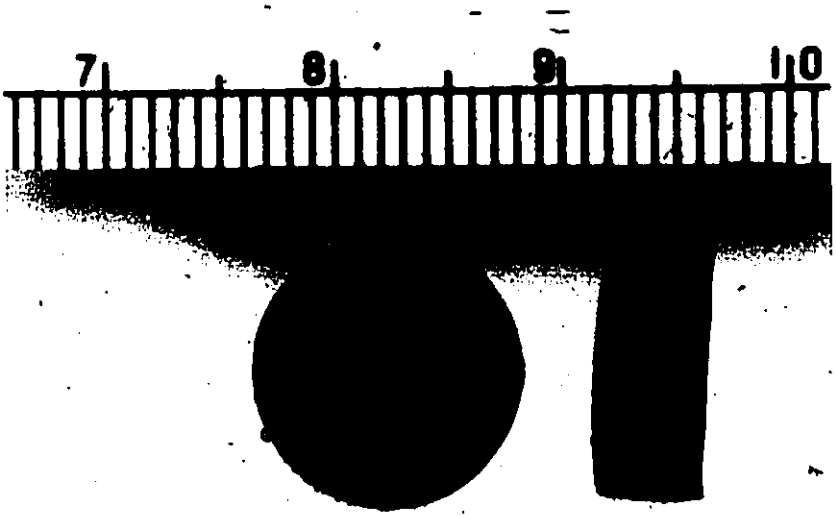

Figure (7-4) Photograph showing the surface and the cross section of $NiO-NiAl_2O_4$ pellet after annealing at 1800°C in argon atmosphere for 20 hours.

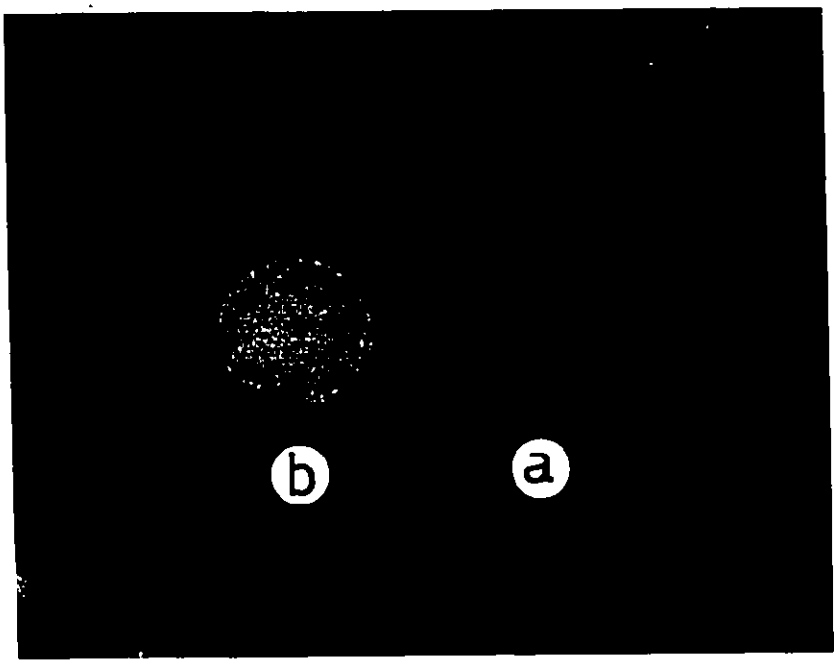

Figure (7-5) Photograph showing the upper surface (a) and the lower surface (b) of air annealed NiO-Ni at 1800°C.

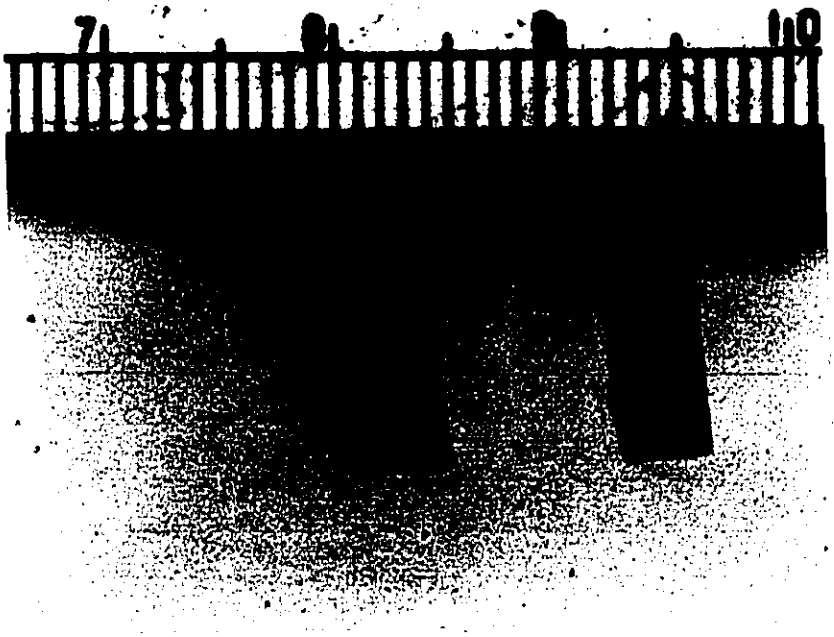

Figure (7-6) Photograph showing the surface and the cross section of air annealed spinel-$Al_2O_{3(\alpha)}$ tablet at 1700°C.

Figure (7-7) Photograph showing the contact region of the α-Al_2O_3 crucible with spinel-$Al_2O_{3(\alpha)}$ pellet after air annealing at 1700°C.

Figure (7-8) The contact region of the α-Al_2O_3 crucible with NiO-$NiAl_2O_4$ pellet after air annealing at 1700°C.

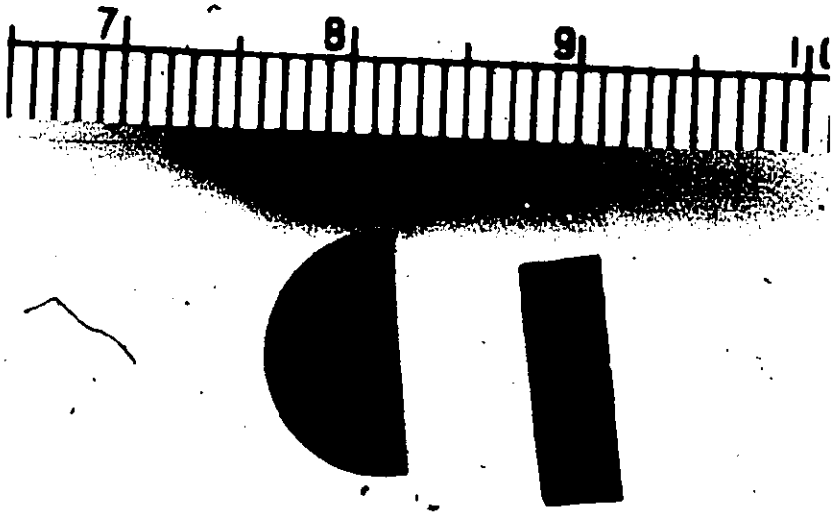

Figure (7-9) The surface and the cross section of spinel-$Al_2O_{3(\alpha)}$ tablet after annealing at 1800°C under argon atmosphere for 14 hours.

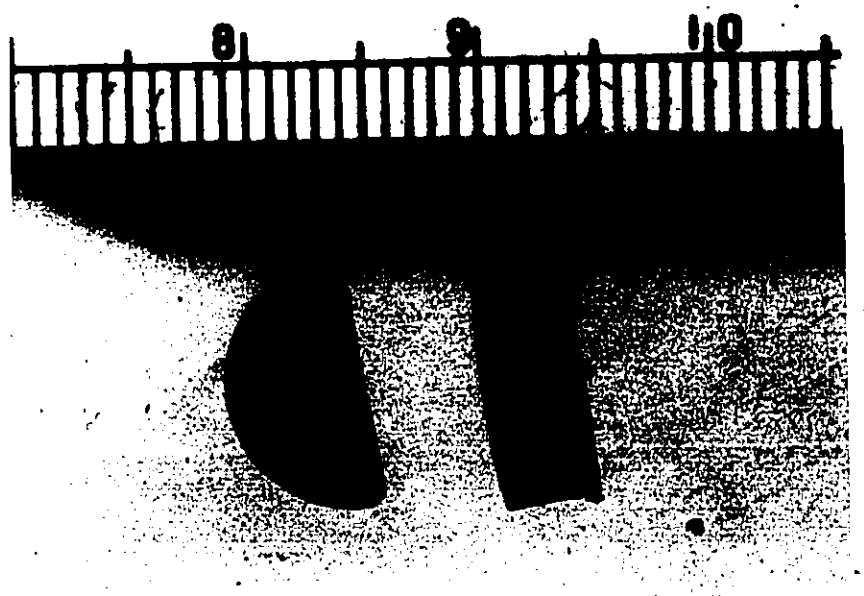

Figure (7-10) The surface cross section of spinel-$Al_2O_{3(\alpha)}$ tablet after annealing at 1920°C in argon atmosphere for three hours.

Figure (7-11) a) Scanning electron micrograph of the Ni, spinel, $Al_2O_{3(\alpha)}$ sample. b) Ni-K_α radiation mapping. c) Al-K_α radiation mapping. The alloy phase shown in the figure is substantially pure Ni.

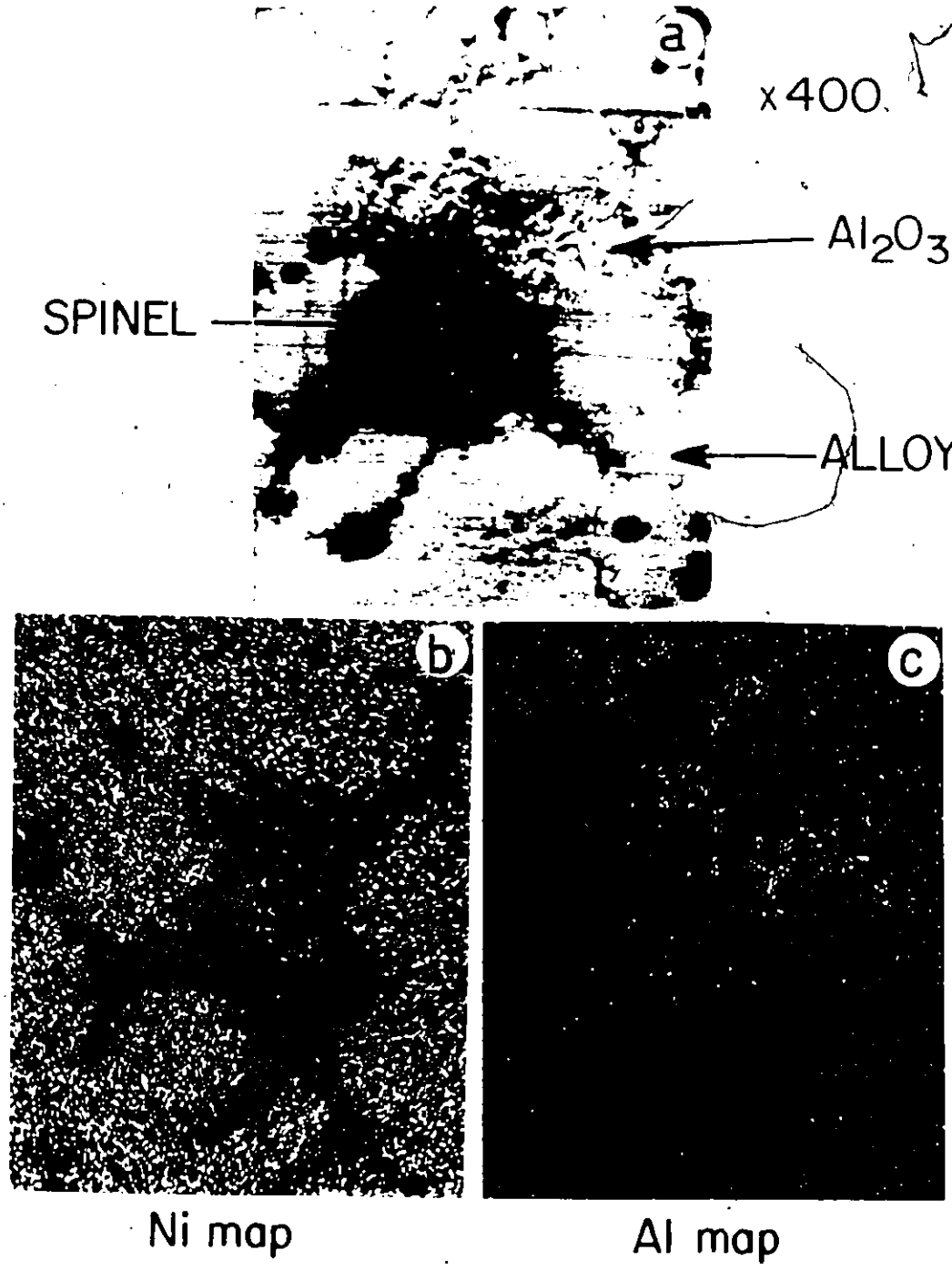
a)
x400
$Al_2O_3(\alpha)$
SPINEL
ALLOY
b)
c)
Ni map
Al map

Figure (7-12) a) Scanning electron micrograph of the 0.15 a/o Al-Ni alloy, $Al_3O_{3(\alpha)}$ sample. b) Ni-K_α radiation mapping. c) Al-K_α radiation mapping.

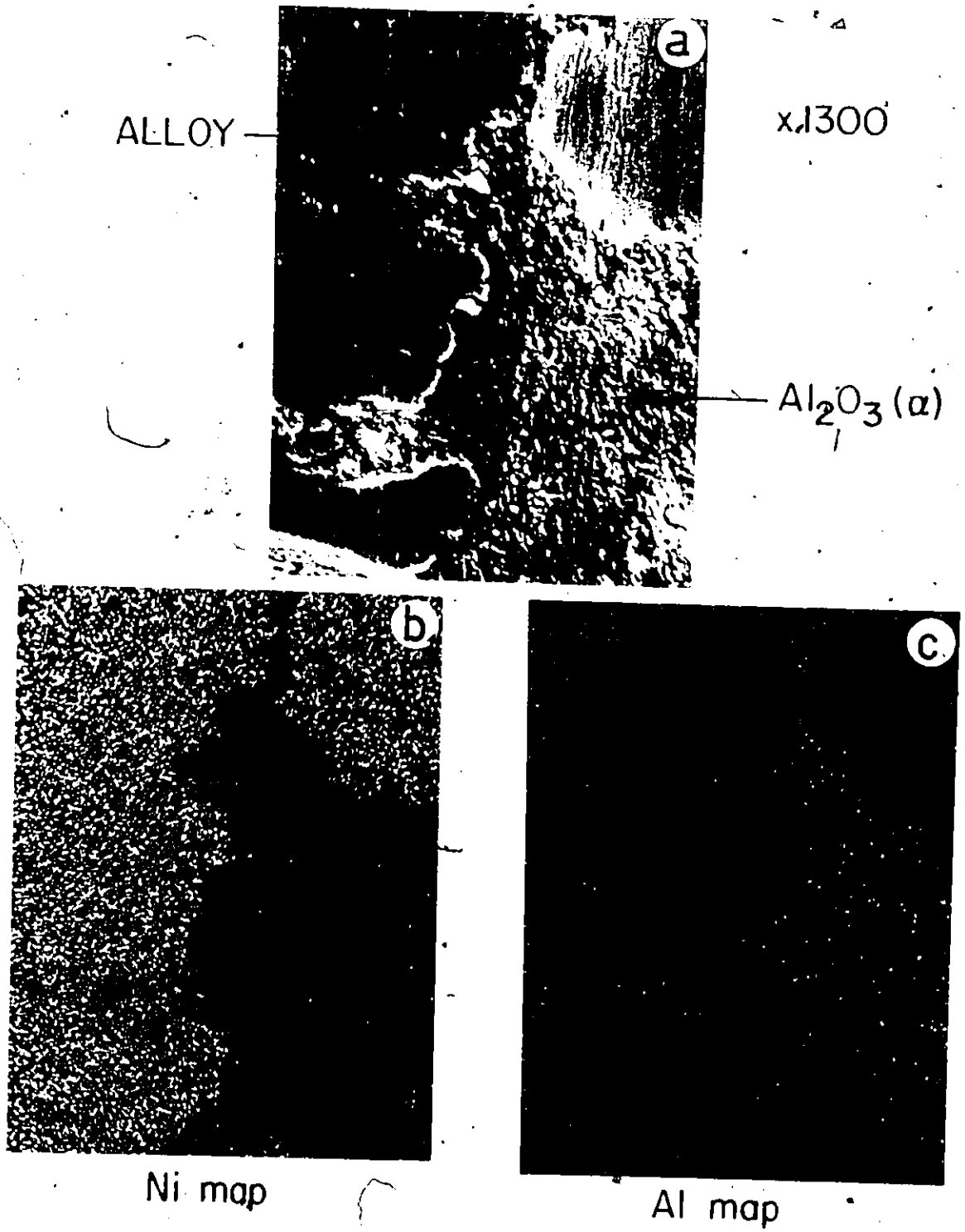
a
ALLOY
x1300
Al_2O_3 (α)
b
Ni map
c
Al map

however, the presence of the three phases was detected by electron probe microanalysis, section (7-4). The oxide phases of some samples tended to preferentially abrade during the polishing procedure and the resultant voids are shown, in some cases, in the figures.

7.3 X-ray Analysis

The phases in the $NiO-Al_2O_3$ system identified using the powder X-ray diffraction method with Ni filtered Cuk_α radiation are summarized in table (7-2).

7.4 Electron Probe Microanalyses

The spot counting procedure was used to quantitatively determine the compositions of the equilibrated phases. Every sample was initially scanned by the electron-probe beam to obtain a qualitative estimate of the constituents of each annealed sample. Figures (7-13)-(7-17) illustrate the nickel and aluminum profiles in several $NiO-Al_2O_3$ samples. Profiles shown in figures (7-13) and (7-14) were obtained from $NiO-NiAl_2O_4$ and spinel-$Al_2O_{3(\alpha)}$ tablets, respectively, annealed at 1600°C and 1700°C, respectively. The profiles obtained from the other air-annealed $NiO-NiAl_2O_4$ or spinel-$Al_2O_{3(\alpha)}$ tablets exhibited the same features of figures (7-13) and (7-14), respectively. The Ni and Al profiles of figure (7-13) indicate the presence of NiO and $NiAl_2O_4$ as the only phases in the $NiO-NiAl_2O_4$ tablet while the profiles of figure (7-14) testify to the presence of spinal and Al_2O_3 as the only phases in the spinel-Al_2O_3 pellets.

Pellet	X-ray-detected phases
SA19AR	NiO + spinel + α-Al_2O_3
SA19AI	spinel + α-Al_2O_3
SA18AR	α-Al_2O_3
SA18AI	spinel + α-Al_2O_3
NS18AR	Ni + α-Al_2O_3
NS18AI	NiO + $NiAl_2O_4$
SA17	spinel + α-Al_2O_3
NS17	NiO + $NiAl_2O_4$
SA16	spinel + α-al_2O_3
NS16	NiO + $NiAl_2O_4$
SA15	spinel + α-Al_2O_3
NS15	NiO + $NiAl_2O_4$
SA14	spinel + α-Al_2O_3
NS14	NiO + $NiAl_2O_4$
SA13	spinel + α-Al_2O_3
NS13	NiO + $NiAl_2O_4$
SA12	spinel + α-Al_2O_3
NS12	NiO + $NiAl_2O_4$
SA11	spinel + α-Al_2O_3
NS11	NiO + $NiAl_2O_4$
SA10	spinel + α-Al_2O_3
NS10	NiI + $NiAl_2O_4$

Table (7-2) X-ray powder diffraction results of annealed samples from NiO-Al_2O_3 system.

The Ni and Al profiles obtained from the surface of the NS18AR sample is shown in figure (7-15). The nickel profile reflects the globular shape of nickel metal formed on the pellet surface; the profiles indicate also the formation of Al_2O_3 during annealing the surface. Figure (7-16) illustrates the profiles obtained from the surface, figure (7-16-a), and the cross section, figure (7-16-b), of the SA18AR pellet. The surface profile reflects the absence of Ni or any Ni compound at the sample surface since only Al_2O_3 was detected. The profiles obtained from the pellet cross section indicated also the absence of NiO in the surface region to a depth of 300 μm; however, NiO and nickel spinel were detected at greater depths within the pellet. Ni and Al profiles obtained within the cross section of SA19AR are shown in figure (7-17). The profiles reflected the presence of NiO, nickel spinel, and α-Al_2O_3 with the spinel phase particularly concentrated at the inner region of a tablet, see also figure (7-10).

Al-K_α and Ni-K_α X-ray radiation signals were used to determine quantitatively phase compositions. The intensities of these X-ray signals obtained from the equilibrated phases of the NiO-Al_2O_3 and Ni-Al-O systems are tabulated in tables (7-3) and (7-4), respectively. Each intensity value is the average of thirty two-intensity values taken at different spots of a phase. Background, dead time, atomic number, absorption, and fluorescence corrections were applied to get the composition of each phase. Column five of table (7-3) gives the composi-

Sample	Phase	Intensity of the electron probe X-ray signal				Chemical formula of the oxide
		Al	Ni	Al	Ni	
SA19AI	Nickel spinel	60019	30768	15837	4045	$(Ni_{0.377}Al_{2.416})O_4$
	Aluminum oxide	60019	30768	22713	397	$(Ni_{0.027}Al_{1.982})O_3$
NS18AI	Nickel spinel	60915	31029	8801	8793	$(Ni_{0.957}Al_{2.029})O_4$
	Nickel Oxide	60915	31029	412	22703	$(Ni_{0.917}Al_{0.056})O$
SA18AI	Nickel spinel	60915	31029	12504	5414	$(Ni_{0.555}Al_{2.297})O_4$
	Aluminum oxide	60915	31029	22845	342	$(Ni_{0.023}Al_{1.985})O_3$
NS17	Nickel spinel	61243	30700	8658	8901	$(Ni_{0.983}Al_{2.011})O_4$
	Nickel oxide	61243	30700	320	22541	$(Ni_{0.934}Al_{0.044})O$
SA17	Nickel spinel	61243	30700	11593	5778	$(Ni_{0.619}Al_{2.254})O_4$
	Aluminum oxide	61243	30700	22941	333	$(Ni_{0.023}Al_{1.985})O_3$
NS16	Nickel spinel	61018	30415	8792	8999	$(Ni_{0.981}Al_{2.013})O_4$
	Nickel oxide	61018	30415	300	22495	$(Ni_{0.938}Al_{0.041})O$
SA16	Nickel spinel	61018	30415	11041	6020	$(Ni_{0.661}Al_{2.226})O_4$
	Nickel oxide	61018	30415	23004	318	$(Ni_{0.022}Al_{1.985})O_3$

(continued next page)

Sample	Phase	Intensity of the electron probe x-ray signal				Chemical formula of the oxide
		Al	Ni	Al	Ni	
NS15	Nickel spinel	64243	30923	8853	8939	$(Ni_{0.998}Al_{2.001})O_4$
	Nickel oxide	64243	30923	270	22564	$(Ni_{0.946}Al_{0.036})O$
SA15	Nickel spinel	64243	30923	11007	7094	$(Ni_{0.754}Al_{21.64})O_4$
	Aluminum oxide	64243	30923	23679	383	$(Ni_{0.026}Al_{1.982})O_3$
NS14	Nickel spinel	63212	31197	8716	9021	$(Ni_{0.998}Al_{2.002})O_4$
	Nickel oxide	63212	31197	252	22808	$(Ni_{0.949}Al_{0.034})O$
SA14	Nickel spinel	63212	31197	10609	7372	$(Ni_{0.779}Al_{2.148})O_4$
	Aluminum oxide	63212	31197	23328	374	$(Ni_{0.026}Al_{1.983})O_3$
NS13	Nickel spinel	63917	30747	8812	8891	$(Ni_{0.998}Al_{0.032})O_4$
	Nickel oxide	63917	30747	236	22481	$(Ni_{0.952}Al_{0.032})O$
SA13	Nickel spinel	63917	30747	10551	7410	$(Ni_{0.797}Al_{2.136})O_4$
	Aluminum oxide	63917	30747	23652	338	$(Ni_{0.023}Al_{1.984})O_3$
NS12	Nickel spinel	61045	30992	8423	8905	$(Ni_{0.994}Al_{2.004})O_4$
	Nickel oxide	61045	30992	184	22807	$(Ni_{0.961}Al_{0.026})O$
SA12	Nickel spinel	61045	30992	9923	7523	$(Ni_{0.809}Al_{2.127})O_4$
	Aluminum oxide	61045	30992	23799	284	$(Ni_{0.018}Al_{1.988})O_3$

(continued next page)

Sample	Phase	Intensity of the electron probe x-ray signal				Chemical formula of the oxide
		Al	Ni	Al	Ni	
NS11	Nickel spinel	59924	2980	8340	8590	$(Ni_{0.99}Al_{2.007})O_4$
	Nickel oxide	59924	2980	163	22399	$(Ni_{0.965}Al_{0.023})O$
SA11	Nickel spinel	59924	29804	9652	7384	$(Ni_{0.824}Al_{2.118})O_4$
	Aluminum oxide	59924	29804	23201	251	$(Ni_{0.017}Al_{1.988})O_3$
NS10	Nickel spinel	60487	32009	8339	9243	$(Ni_{0.997}Al_{2.002})O_4$
	Nickel oxide	60487	32009	187	23494	$(Ni_{0.96}Al_{0.027})O$
SA10	Nickel spinel	60487	32009	9718	8001	$(Ni_{0.830}Al_{2.114})O_4$
	Aluminum oxide	60487	32009	22612	320	$(Ni_{0.021}Al_{1.986})O_3$

Table (7-3) Electron probe results for samples from $NiO-Al_2O_3$ system.

Sample	Phase	Intensity of the electron probe x-ray signal				Al and Ni weight present in the alloy		Chemical formula of the oxide
		Al	Ni	Al	Ni	Al	Ni	
NSN	Nickel Oxide	58916	32306	256	23556	-	-	$(Ni_{0.944}Al_{0.037})O$
	Nickel spinel	58986	32306	8134	9386	-	-	$(NiAl_2O_4$
	Nickel	58986	32306	1	32304	-	-	-
SAN	Nickel spinel	58986	32306	9496	8108	-	-	$(Ni_{0.830}Al_{2.113})O_4$
	Aluminum oxide	58986	32306	21983	30	-	-	$(Ni_{0.020}Al_{1.987})O_3$
	Nickel	58986	32306	1	32296	-	-	-
NA0.1A	Alloy	58986	32306	13	32257	0.08	99.87	-
	Aluminum oxide	58986	32306	22059	288	-	-	$(Ni_{0.019}Al_{1.987})O_3$
NA0.5A	Alloy	59461	33093	98	32861	0.55	99.47	-
	Aluminum oxide	59461	33093	22238	264	-	-	$(Ni_{0.017}Al_{1.988})O_3$
NA1.0A	Alloy	59461	33093	198	32667	1.10	98.96	-
	Aluminum oxide	59461	33093	22297	248	-	-	$(Ni_{0.016}Al_{1.989})O_3$

(continued next page)

Sample	Phase	Intensity of the electron probe x-ray signal				Al and Ni weight present in the alloy		Chemical formula of the oxide
		Al	Ni	Al	Ni	Al	Ni	
NA12A	Alloy	60665	30259	2374	25629	12.16	86.99	-
	Aluminum oxide	60665	30259	22643	191	-	-	$(Ni_{0.013}Al_{1.991})O_3$
NA22A	Alloy	60665	30259	4603	22271	22.05	77.11	-
	Aluminum oxide	60665	30258	22684	162	-	-	$(Ni_{0.011}Al_{1.992})O_3$
NA27A	Alloy	60614	30317	5826	20969	27.00	73.03	-
	Aluminum oxide	60614	30317	22691	143	-	-	$(Ni_{0.010}Al_{1.993})O_3$
NA30A	Alloy	60614	30317	6736	19668	30.30	69.03	-
	Aluminum oxide	60614	30317	22677	137	-	-	$(Ni_{0.010}Al_{1.994})O_3$
NS35A	Alloy	60614	30317	8002	18399	34.75		-
	Aluminum oxide	60614	30317	22703	118	65.04	-	$(Ni_{0.008}Al_{1.994})O_3$

Table (7-4) Electron probe results for samples from Ni-Al-O system.

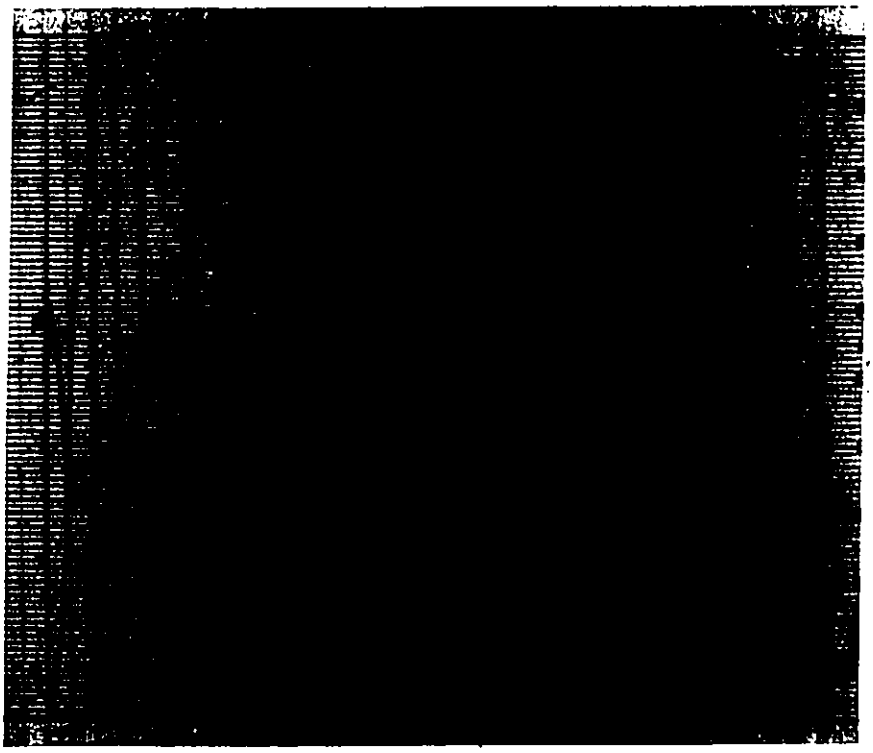

Figure (7-13) Microprobe scan along the cross section of air annealed NS16 tablet; the red trace represents the intensity of Al-K_α signal while the blue reflects the Ni-K_α intensity.

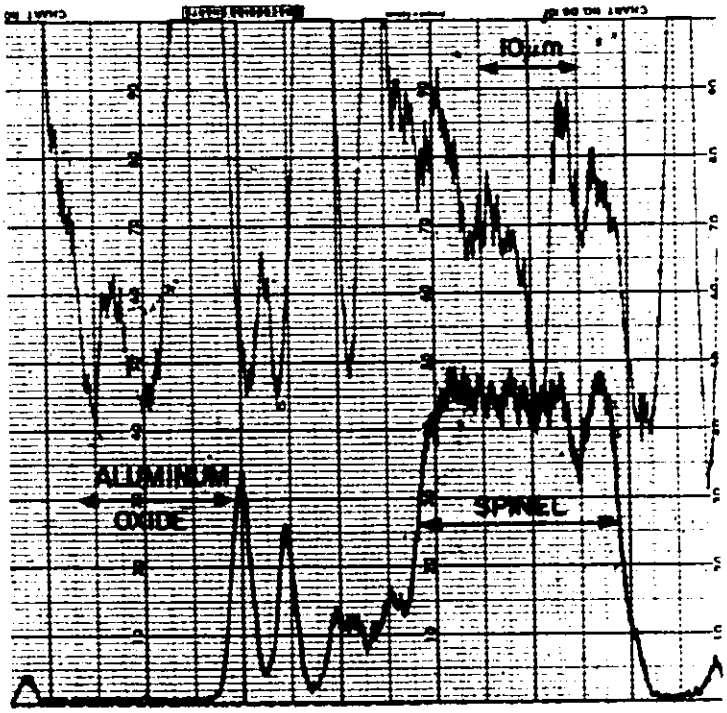

Figure (7-14) Microprobe scan along the cross section of spinel-$Al_2O_{3(\alpha)}$ pellet annealed at 1700°C.

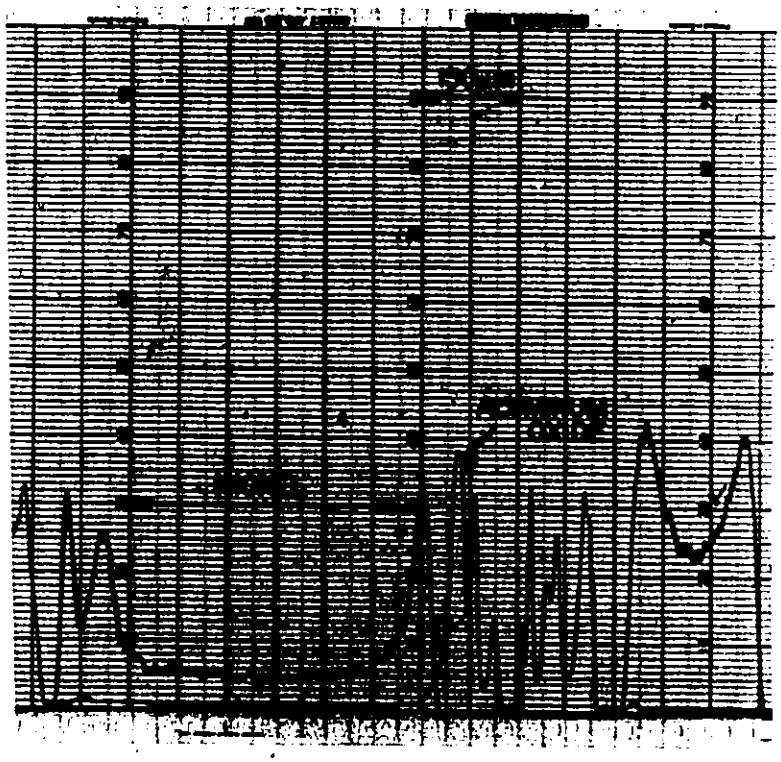

Figure (7-15) Microprobe scan along the surface of annealed NS18AR sample.

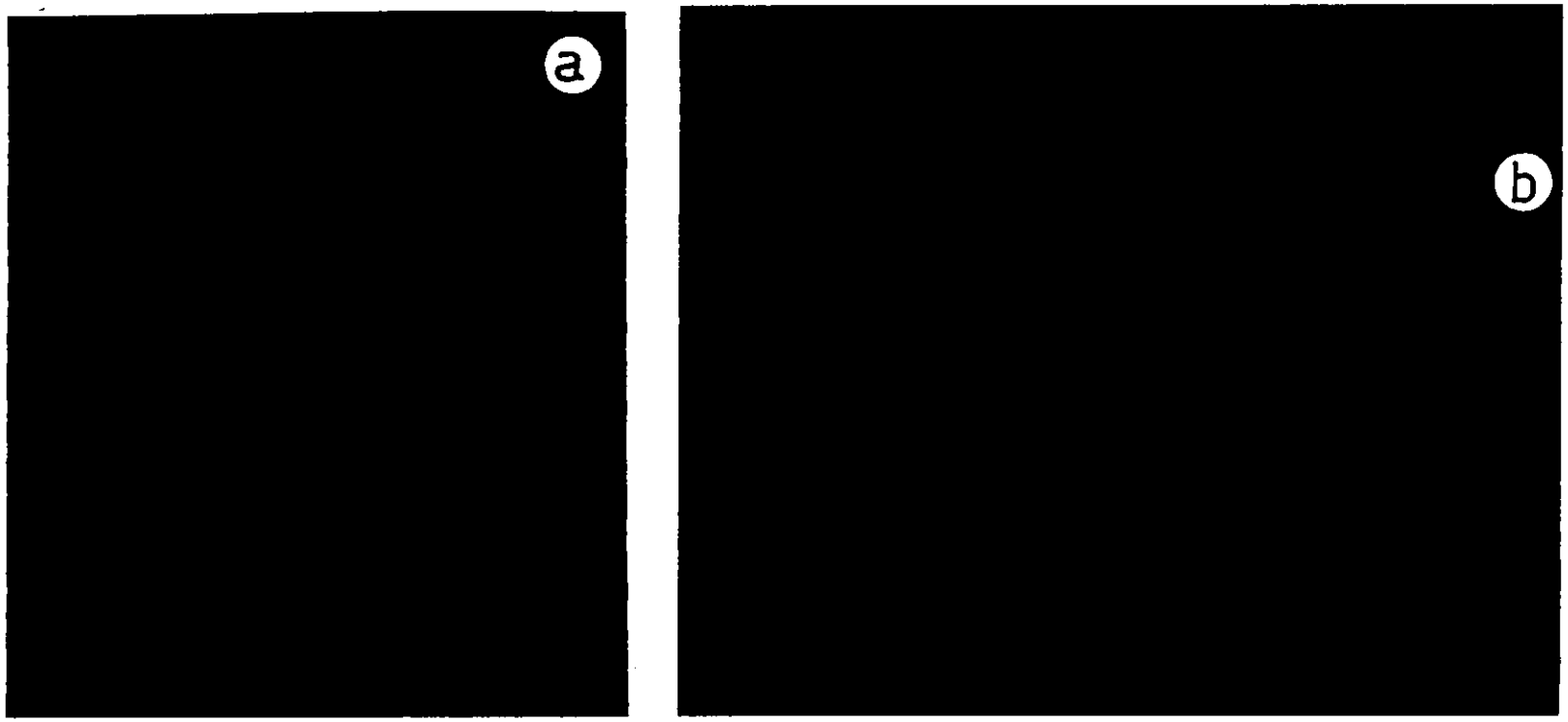

Figure (7-16) Ni and Al profiles obtained from the surface (a) and the cross section (b) of annealed SA18AR tablet.

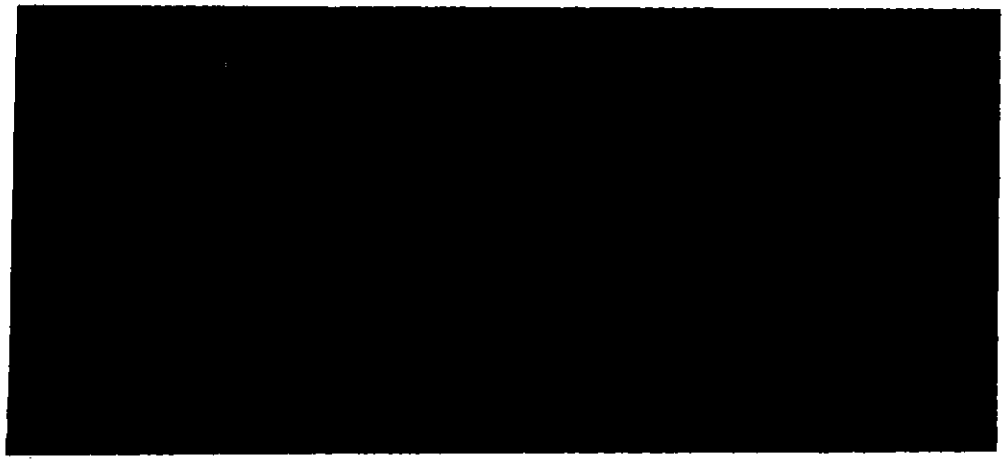

Figure (7-17) Electron microprobe scan obtained from the cross section of annealed SA19AR pellet.

tion, in chemical formula form, of the equilibrated phases in the $NiO-Al_2O_3$ system. The values obtained for the chemical compositions of phases in the annealed tablets of Ni-Al-O system are listed in table (7-4); column five lists the alloy composition while column six gives the oxide chemical formula. It was not possible to analyze for aluminum in the metallic phases of the NSN and SAN samples since the Al-K_α signals obtained were of the order of the background obtained from the standard Ni sample of 99.99% purity.

7.5 Discussion

7.5.1 Nickel Oxide-Aluminum Oxide System

Nickel spinel was the only phase encountered in this system as a ternary oxide at temperatures in the range 1000-1900°C. The electron probe results indicated that the spinel/(nickel oxide-spinel) boundary is independent of temperature from 1000° to 1800°C and occurs at the stoichiometric composition $NiAl_2O_4$ within a relative error of 2%. The probe results demonstrated also that an alumina-rich spinel exists in equilibrium with $\alpha-Al_2O_3$. The composition of spinel at the alumina-rich boundary changes with temperature; as the temperature increases, the spinel becomes richer in alumina. The alumina contents of this spinel in terms of mole percent are listed in table (7-5). These values were calculated from the compositions given in table (7-3). Al and Ni solubilities in NiO

and α-Al_2O_3, respectively, are also given in table (7-5). The electron probe results for NiO-Al_2O_3 are compiled in figure (7-18).

Two equilibrium diagrams, figures (2-4) and (2-5), were previously proposed in the literature. The spinel/(nickel oxide-spinel) boundary was given at the stoichiometric composition in both diagrams which is in good agreement with our results. However, the two proposed diagrams differ significantly about the position of the alumina-rich boundary. Comparison of figures (7-18), (2-4), and (2-5) indicates that the alumina contents of the alumina-rich spinel in equilibrium with α-Al_2O_3 determined in this investigation are in fair agreement with those given by spinel/(spinel-aluminum oxide) boundary proposed in figure (2-4). The results also demonstrate that the solubility of aluminum in nickel oxide increases from approximately 1 a/o at 1000°C to 3 a/o at 1800°C. This solubility was reflected in the shape of the NiO-Al_2O_3 diagram proposed by Phillips et al. (31). In contradiction to the observation of these authors, however, solubility of nickel in α-Al_2O_3 was detected in this investigation. This nickel content did not change measurably with temperature between 1000°C and 1900°C. An average value of 0.45±0.1 a/o was estimated to represent the nickel solubility in aluminum oxide. The aluminum oxide solid solution range was proposed in figure (7-18) to signify this nickel solubility.

Temperature (°C)	Al_2O_3 content of alumina-rich spinel (m/o)	Al solubility in NiO (a/o)	Ni solubility in α-Al_2O_3 (a/o)
1000	56.0	1.4	0.42
1100	56.2	1.2	0.34
1200	56.8	1.3	0.36
1300	57.3	1.6	0.46
1400	58.0	1.7	0.52
1500	58.9	1.8	0.52
1600	62.7	2.1	0.44
1700	64.5	2.2	0.46
1800	67.4	2.8	0.46
1900	76.2	-	0.54

Table (7-5) Phase relations in NiO-Al_2O_3 system over the temperature range 1000-1900°C.

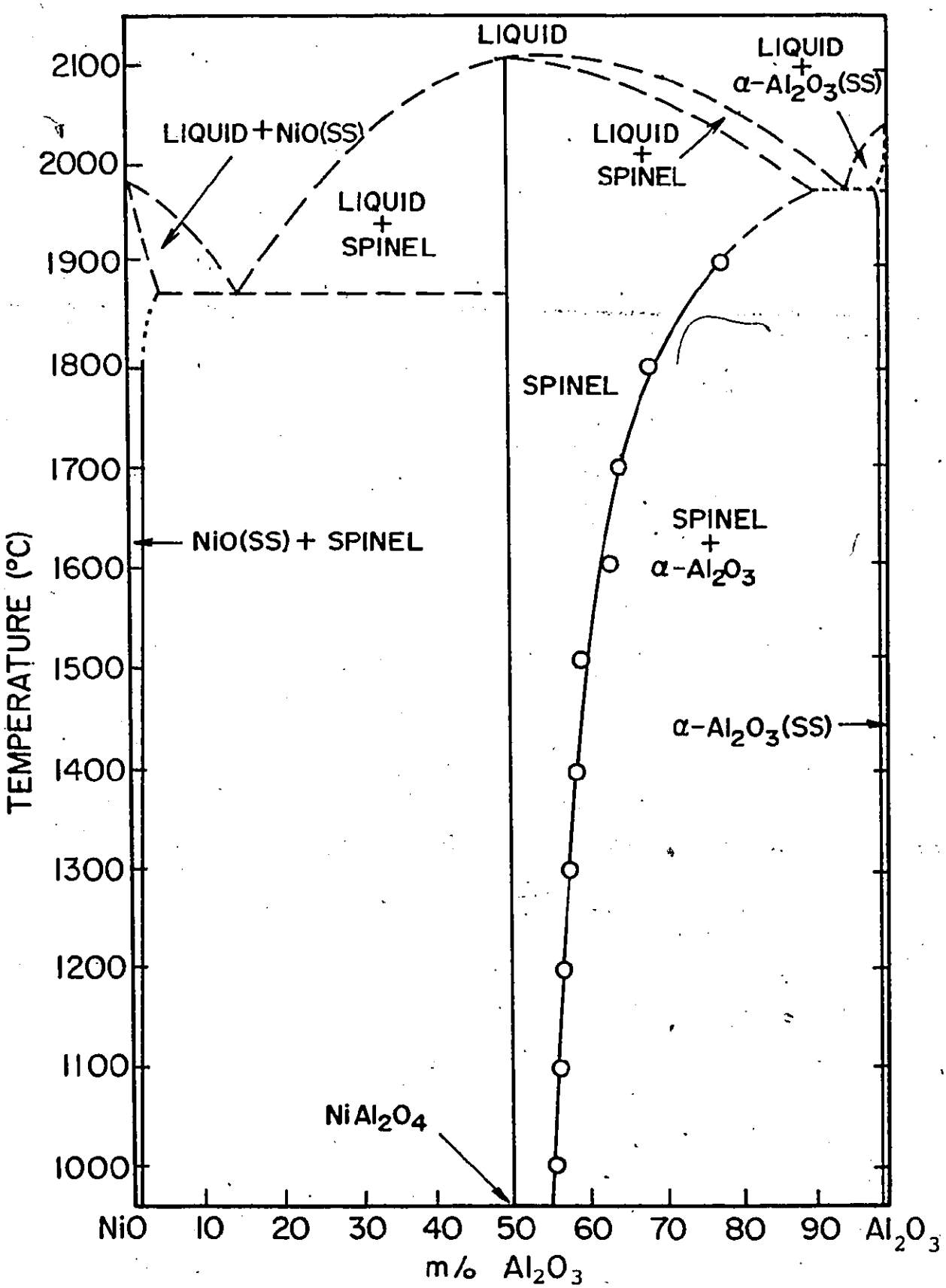

Figure (7-18) Equilibrium diagram for the system $NiO-Al_2O_3$.

$NiO-NiAl_2O_4$ tablets when annealed in argon become unstable; the formation of Ni as well as $\alpha-Al_2O_3$ indicated that NiO vaporized and/or decomposed. The dissociation pressure of pure NiO at 1800°C is 1.45×10^{-3} atm. which is much higher than the partial pressure of oxygen in the argon atmosphere (oxygen impurity content is less than 5 ppm). This large difference in oxygen potential explains the instability of NiO exposed in argon. The spinel of the spinel-$Al_2O_{3(\alpha)}$ tablets annealed in argon at 1800°C and 1900°C was also unstable; however, no metallic phase was formed in this case which suggested that the NiO content of the spinel was vaporized into the gaseous environment.

7.5.2 Nickel-Aluminum-Oxygen Isotherm at 1000°C

The electron microprobe results obtained from phases in this system are summarized in table (7-4). Analysis for Al in the metallic phases of $Ni-NiO-NiAl_2O_4$ and $Ni-NiO-NiAl_2O_4$ coexistences were not possible because Al-K_α radiation intensities obtained were of the order of Al background intensity. These negative results indicate, nevertheless, that nickel containing only a few ppm aluminum is compatible with these coexistences at 1000°C. Results obtained from the electron microprobe investigation of Ni-Al-O samples indicated the following:

a) Nickel spinel equilibrated with NiO and Ni at 1000°C is stoichiometric while the spinel phase of the coexistence

Ni-spinel-$Al_2O_{3(\alpha)}$ contains 56 m/o alumina. The same composition was determined for the spinel, table (7-5), of spinel-$Al_2O_{3(\alpha)}$ system.

b) The solubility of Al in NiO of Ni-NiO-$NiAl_2O_4$ coexistence is 1.87 a/o at 1000°C which is slightly larger than 1.40 a/o determined in NiO equilibrated with $NiAl_2O_4$.

c) α-Al_2O_3 of the coexistence Ni-spinel-$Al_2O_{3(\alpha)}$ contains 0.4 a/o Ni.

d) The solubility of nickel in α-Al_2O_3 equilibrated with Ni-Al alloys decreases with increasing Al content of the alloy. At 1000°C, α-Al_2O_3 in equilibrium with Ni-0.07 w/o Al alloy contains 0.38 a/o Ni; this solubility is 0.16 a/o Ni in α-Al_2O_3 equilibrated with Ni-34.75 w/o Al alloy.

To my knwoledge, no attempt has been previously made to propose Ni-Al-O isotherms. However, based on the preceding results and the available data for the binary systems Al-Ni, Ni-O, and Al-O that discussed in chapter two, the isotherm shown in figure (7-19) is proposed for Ni-Al-O system at 1000°C. In this diagram, the extent of NiO and α-Al_2O_3 phase fields and the curve representing the oxygen solubility in the Ni-Al alloys have been enlarged. The limiting compositions of the metallic phases are taken from the Ni-Al equilibrium diagram (8).

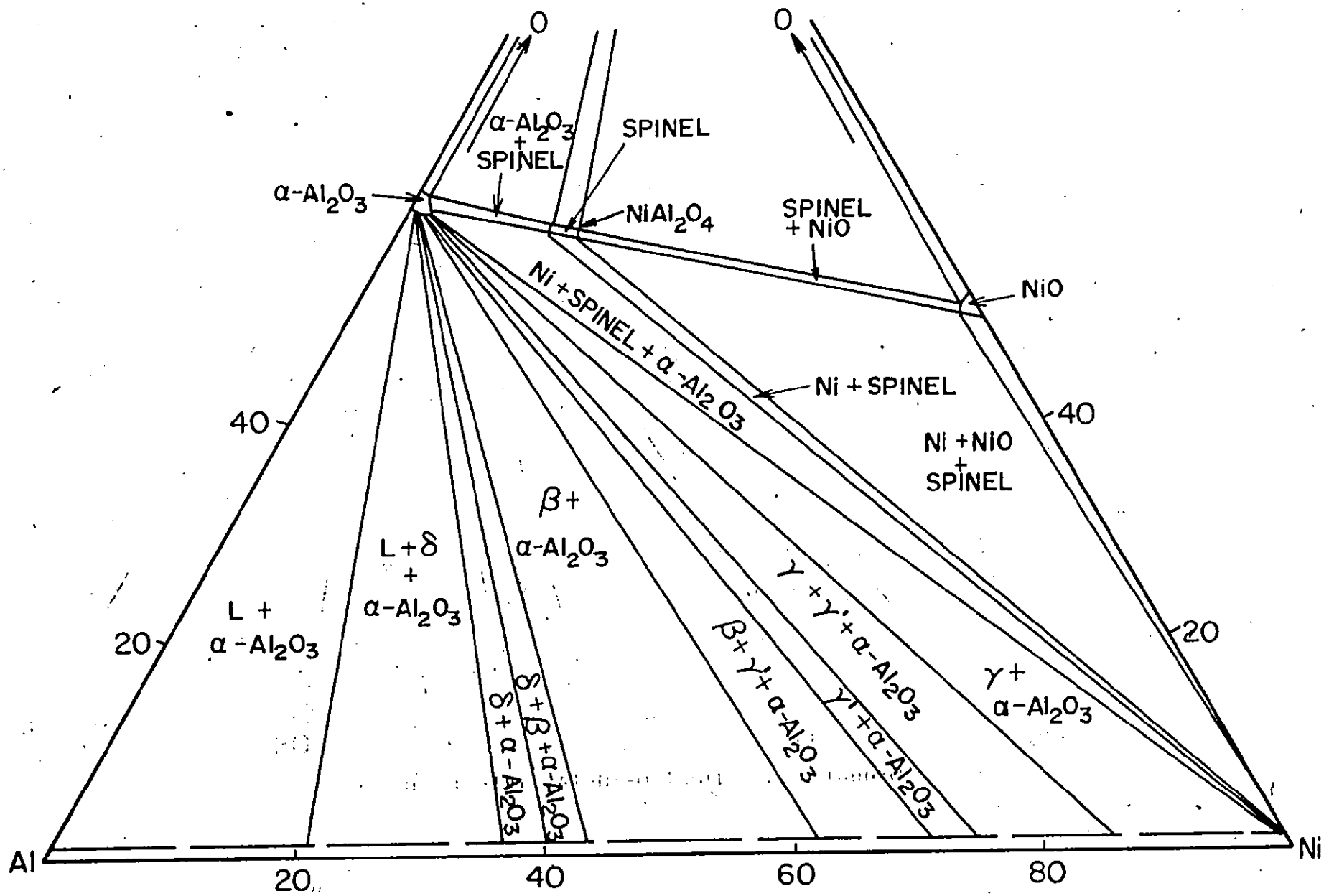

Figure (7-19) Al-Ni-O isotherm at 1000°C.

7.5.3 Cell Electromotive Force Analyses

The electromotive forces, E, of cells (7-I) and (7-II) are given by the relation

$$E = \frac{RT}{4F} \ln \frac{P^c_{O_2}}{P^a_{O_2}} , \qquad (7.1)$$

providing that the cells are at constant temperature and pressure, operate reversibly, and the solid electrolyte responds ionically. $P^c_{O_2}$ is the dissociation pressure of NiO to Ni and oxygen and $P^a_{O_2}$ is the equilibrium oxygen pressure over the working electrode. The dissociation pressure of NiO is given by the following relation

$$\log P^c_{O_2} = \frac{2\Delta G^o_f(NiO_{(s)})}{2.303\ RT} \qquad (7.2)$$

where $\Delta G^o_f(NiO_{(s)})$ is the standard free energy of formation of NiO in cal per mole of NiO. Using the relation proposed by Steele (13) for $\Delta G^o_f(NiO_{(s)})$, relation (7.2) becomes

$$\log p^c_{O_2}(atm) = - \frac{24,460}{T(K)} + 8.87 . \qquad (7.3)$$

Combining equation (7.1) and equation (7.3) yields relation (7.4) which defines $\log p^a_{O_2}$ in terms of E.

$$\log p^a_{O_2}(atm) = - \frac{24,460}{T(K)} + 8.87 - \frac{4FE}{2.303RT} . \qquad (7.4)$$

The emf-T relations for cells (7-1) and (7-II) are given by relations (7.5) and (7.6), respectively.

$$E(mV) = 0.7 + 0.0032T(K) \quad . \qquad (7.5)$$

$$E(mV) = 63.6 + 0.047T(K) \quad . \qquad (7.6)$$

Substituting for E in equation (7.4) gives equations (7.7) and (7.8) which represent the dependence of the equilibrium oxygen pressure of NSN and SAN electrodes, respectively, on temperature.

$$\log p^a_{O_2}(atm) = -\frac{24,474}{T(K)} + 8.81 \qquad (7.7)$$

$$\log p^a_{O_2}(atm) = -\frac{25,742}{T(K)} + 7.92. \qquad (7.8)$$

The estimated error in the values of $\log p^a_{O_2}$ given by relations (7.7) and (7.8) is ±0.1.

The over-all reaction for cells (7-IV), (7-V), and (7-VII) can be written as

$$WS_{2(s)} + 2(Na_2O)_\beta = 2\,Na_2S_{(s)} + O_{2(g)} + W_{(s)} \qquad (7.9)$$

for which

$$\Delta G_{(7.9)} = 2\Delta G^o_f(Na_2S_{(s)}) - 2\Delta G^o_f(Na_2O_{(s)}) - \Delta G^o_f(WS_{2(s)}) - 2RT\ell n\, a_{Na_2O(\alpha-\beta)} + RT\ell n\, p_{O_2} \qquad (7.10)$$

Substituting for $\Delta G_{(7.9)}$, $\Delta G_{(7.9)} = -4FE$, in equation (7.10) and rearranging, we obtain

$$RT\ell n\, p_{O_2} = 2\Delta G^o_f(Na_2O_{(s)}) + \Delta G^o_f(WS_{2(s)}) + 2RT\ell n\, a_{Na_2O(\alpha-\beta)} - 2\Delta G^o_f(Na_2S_{(s)}) - 4FE \quad . \qquad (7.11)$$

The equilibrium oxygen pressures over the working electrodes of cells (7-IV), (7-V), and (7-VI) were calculated at 940°C using equation (7.11), equation (7.13), and data from table (5.9). The values for p_{O_2} (atm) in equilibrium with the working electrodes of cells (7-IV), (7-V), and (7-V) were 5.7×10^{-24}, 1.2×10^{-25}, and 3.7×10^{-26}, respectively, with an error of 0.5 order of magnitude.

7.5.4 Free Energy of Formation of Nickel Spinel

The phase field Ni-spinel-$Al_2O_{3(\alpha)}$ can be described by the following two equilibria:

$$2Al_{(\text{in nickel})} + \frac{3}{2}\,O_{2(g)} = Al_2O_{3(\alpha)} \qquad (7.12)$$

$$(1-x)Ni+(2+y)Al_{(\text{in nickel})}+2O_{2(g)} = Ni_{(1-x)}Al_{2+y}O_4 \qquad (7.13)$$

Activities of Al in Ni, which is in equilibrium with nickel spinel and α-Al_2O_3 were determined, table (7-6), by considering the first equilibrium over the temperature range 800-1150°C. For this reaction, we write:

$$\Delta G^{o}_{f}(Al_2O_{3(\alpha)}) = -\,RT\,n\,\frac{a_{Al_2O_{3(\alpha)}}}{a_A^2\cdot P_{O_2}^{3/2}} \qquad (7.14)$$

where $a_{Al_2O_{3(\alpha)}}$ is the activity of α-Al_2O_3, a_{Al} is the activity of Al, and P_{O_2} is the equilibrium oxygen pressure of the invariant system Ni, spinel, $Al_2O_{3(\alpha)}$. Assuming unit activity for α-Al_2O_3 and rearranging equation (7.14) we obtain

T(°C)	850	900	950	1000	1050	1100	1150
Log a_{Al}	-19.45	-18.51	-17.65	-16.86	-16.12	-15.44	-14.81

Table (7-6) The activities of the aluminum of the alloy of the invariant system Ni-spinel-$Al_2O_{3(\alpha)}$.

$$\log a_{Al} = 0.5\left(\frac{\Delta G^{o}_{f(Al_2O_{3(\alpha)})}}{2.303RT} - 1.5 \log P_{O_2}\right) \qquad (7.15)$$

Data of table (7-6) were calculated using equation (7.15), equation (7.8) and the relation reported in table (5-9) for $\Delta G^{o}_{f(Al_2O_{3(\alpha)})}$ between 1000K-1900K.

The standard free energy of formation of nickel spinel can be calculated by considering the second equilibrium. However, an essential parameter in this determination is the activity of $NiAl_2O_4$ in the alumina-rich spinel which, to my knowledge, is not reported in the literature. To avoid a major assumption, the free energy change of reaction (7.16) will be calculated instead of $\Delta G^{o}_{f(NiAl_2O_{4(s)})}$.

$$Ni + \frac{1}{2} O_2 + xAl_2O_3 = NiO{\cdot}xAl_2O_3 \; . \qquad (7.16)$$

For this equilibrium we can write:

$$\Delta G_{(7.16)} = \frac{1}{2} RT\ell n \, P_{O_2} \; . \qquad (7.17)$$

Combining equation (7.17) and equation (7.8) yields:

$$\Delta G_{(7.16)} = -58{,}898+18.1T(K) \; . \qquad (7.18)$$

The free energy change of reaction (7.19) can then be calculated by subtracting the temperature relation of $\Delta G^{o}_{f(NiO_{(s)})}$ from equation (7.18).

$$NiO_{(s)} + xAl_2O_{3(\alpha)} = NiO{\cdot}xAl_2O_3 \; . \qquad (7.19)$$

The result of the calculation is

$$\Delta G_{(7.17)} = -2,933-2.19T(K) \quad . \qquad (7.20)$$

The estimated error in the value of $\Delta G_{(7.17)}$ is ±800 cal. The free energy change of reaction (7.17) was determined in chapter 6 using cell (6-III) which utilized β- and α-Al_2O_3 as solid electrolyte. Equation (6.8) gives the temperature dependence of the free energy change of reaction (7.17) as determined by cell (6-III). The agreement between equation (7.18), equation (6.8), and the results of Jacob and Alcock (34) for the same reaction is good.

7.5.5 Thermodynamic Properties of Nickel-Aluminum Alloys

Determinations of equilibrium oxygen pressures of Ni-0.15 a/o Al, $Al_2O_{3(\alpha)}$; Ni-1.19 a/o Al, $Al_2O_{3(\alpha)}$ and Ni-2.36 a/o Al,$Al_2O_{3(\alpha)}$ equilibria at 940°C using galvanic cells with β- and α-Al_2O_3 solid electrolytes made it possible to evaluate the Al activities in the metallic phases, Ni-Al alloys, of these electrodes. Equilibrium between metal and oxide phases of these electrodes can be represented by equation (7.12) for which relation (7.15) was derived; this equation was then used to determine a_{Al} in the alloy. The estimated values of Al activities in nickel alloys containing 0.15 a/o Al, 1.19 a/o Al, and 2.36 a/o Al were 4.39×10^{-11}, 8×10^{-10}, 1×10^{-9} (referred to liquid aluminum), respectively, at 940°C. Al activities in nickel equilibrated with nickel spinel and α-Al_2O_3 over the temperature range 850-1150°C were calculated

in section (7.5.5). The utilization of $W_{(s)}, WS_{2(s)}, Na_2S_{(s)}$ coexistence as reference electrodes in cells (7-IV), (7-V), and (7-VI) places a limitation in studying the thermodynamic properties of coexistences of the type Ni-Al alloy, $Al_2O_{3(\alpha)}$ at 1000°C using these cells because Na_2S melts at 950°C.

7.5.6 Equilibrium Oxygen Pressure Diagram for Ni-Al-O System at 1000°C

The equilibrium oxygen pressures associated with the electrodes NSN and SAN were determined, equations (7.7) and (7.8), between 850°C and 1150°C using galvanic cells with calcia stabilized zirconia as solid electrolyte. The equilibrium oxygen pressures associated with Ni-Al alloys containing 0.15 a/o Al, 1.19 a/o Al, and 2.35 a/o Al were determined at 940°C using galvanic cells with β- and α-Al_2O_3 as solid electrolytes and $W_{(s)}WS_{2(s)}$, and $Na_2S_{(s)}$ as reference electrode. The presence of Na_2S as a constituent of the reference electrode limited the operation of cells (7-IV), (7-V), and (7-VI) at higher temperatures because Na_2S melts at 950°C. However, the oxygen pressures of the working electrodes of cells (7-VI), (7-V), and (7-VI) at 1000°C would be about one order of magnitude higher than those determined at 940°C.

Equilibrium oxygen pressure associated with alloys of higher Al contents at 1000°C were calculated using relation (7.21) which was derived by considering reaction (7.12).

$$\log P_{O_2} = \frac{2}{3}\left(\frac{\Delta G_f^{o}(Al_2O_{3(\alpha)})}{2.303RT(K)} - 2 \log a_{Al}\right) . \quad (7.21)$$

Activity data of Al reported in references (29) were then used to calculate the variation of $\log P_{O_2}$ with Al contents in the alloys. The calculated values of $\log P_{O_2}$ are shown in table (7-7).

The dependence of oxygen pressure on the nickel contents of Ni-Al alloys is shown in figure (7-19). The equilibrium oxygen pressure decreases from 4.5×10^{-11} which corresponds to Ni/NiO coexisting electrode at 1000°C to 3.9×10^{-11} atm which is the equilibrium oxygen pressure associated with the invariant nickel $Ni-NiO-NiAl_2O_4$. Aluminum contents of the alloys of this invariant system and also of the system Ni, spinel, $Al_2O_{3(\alpha)}$ were too small to be detected by the electron probe. However, assuming that the activity coefficient of Al is constant over the composition range 0-0.15 at/o Al, the aluminum contents of these alloys could be determined from the thermodynamic data of these invariant systems. Results indicate that a ppm of Al is sufficient to stabilize α-Al_2O_3. Equilibrium oxygen pressure decreases with increasing Al content, of the alloy until it reaches at 1000°C, 1.68×10^{-35} atm corresponding to that of the $Al/Al_2O_{3(\alpha)}$ equilibrium.

Atomic percent of Al	a_{Al}	log P_{O_2} (atm.)
5.0	2.15×10^{-7}	-25.88
10.0	2.20×10^{-6}	-27.23
14.3	1.20×10^{-5}	-28.21
23.0	1.20×10^{-5}	-28.21
27.5	3.00×10^{-5}	-28.74
36.3	3.00×10^{-5}	-28.74
40.0	5.30×10^{-5}	-29.07
45.0	1.30×10^{-4}	-29.59
50.0	7.20×10^{-3}	-31.92
55.5	5.40×10^{-2}	-33.08
59.0	5.40×10^{-2}	-33.08
60.4	1.02×10^{-1}	-33.45
63.0	5.34×10^{-1}	-34.41
79.0	5.34×10^{-1}	-34.41
85.0	6.91×10^{-1}	-34.56
87.5	8.04×10^{-1}	-34.65
90.0	8.60×10^{-1}	-34.69
95.0	9.38×10^{-1}	-34.74
98.0	9.58×10^{-1}	-34.75
99.5	9.68×10^{-1}	-34.76

Table (7-7) Dissociation pressure of α-Al_2O_3 in equilibrium with Ni-Al alloys.

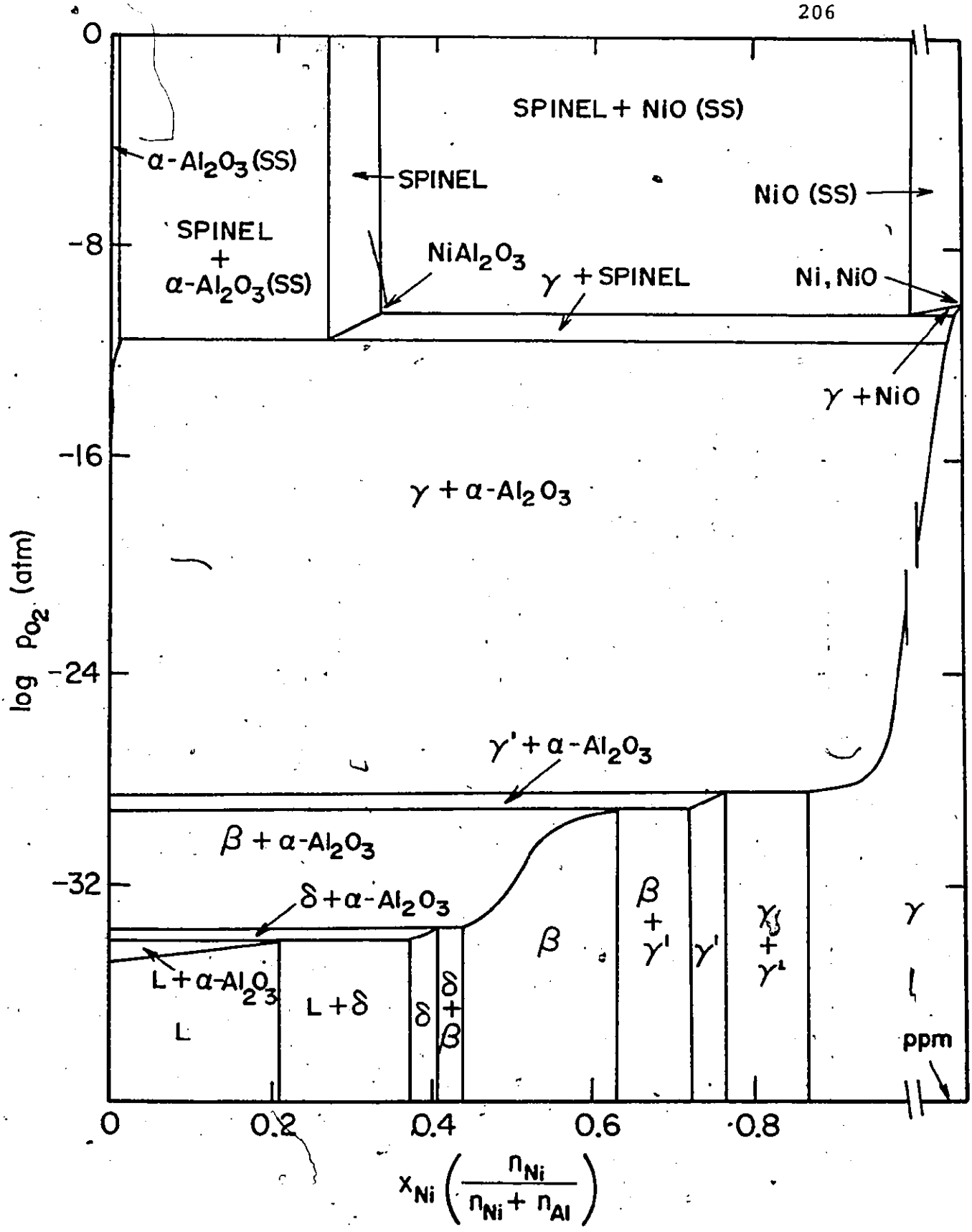

Figure (7-20) Equilibrium oxygen pressure diagram for Ni-Al-O system at 1000°C.

CHAPTER 8

IRON-ALUMINUM-OXYGEN SYSTEM

"RESULTS AND DISCUSSION"

8.1 Electrochemical Cell Measurements

The emfs at several temperatures for cells (8-I), (8-II), and (8-III) are given in table (8-1) and shown in figures (8-1), (8-2), and (8-3). The lines through these points were obtained by least squares analyses as described in table (8-2).

$$Pt|Fe_{(s)},FeO_{(s)}|ZrO_2(+CaO)|\text{hematite,spinel},Al_2O_{3(\alpha)}|Pt \quad (8\text{-I})$$

$$Pt|Fe_{(s)},\text{spinel,wustite}|ZrO_2(+CaO)|Fe_{(s)},FeO_{(s)}|Pt \quad (8\text{-II})$$

$$Pt|Fe_{(s)},\text{spinel},Al_2O_{3(\alpha)}|ZrO_2(+CaO)|Fe_{(s)},FeO_{(s)}|Pt \quad (8\text{-III})$$

Over the temperature range 850-1100°C the emf of the cell

$$Pt|\text{Fe-Al alloy}_{(s)}(0.17\ \text{a/o Al}),Al_2O_{3(\alpha)}|ZrO_2(+CaO)|Fe_{(s)},FeO_{(s)}|Pt \quad (8\text{-IV})$$

decreased steadily with time at a constant temperature. To overcome this problem, coulometric disturbance of the cell was attempted at temperature; however, the instability problem was found to persist. A temperature cycling disturbance was also

Temperature (°C)	Cell emf (mV) Cell (8-I)			Cell (8-II)				Cell (8-III)		
850	503	505	505	6	7	7	6	124	125	123
900	518	516	516	8	7	8	8	123	124	124
950	527	529	530	8	9	9	8	124	122	123
1000	542	542	540	9	9	9	10	122	123	123
1050	555	554	555	10	9	10	10	122	122	122
1100	566	568	567	11	13	11	10	121	121	120
1150	582	580	581	12	13	11	12	119	119	119

Table (8-1) Variation of cell emf with temperature for cells (8-I), (8-II), and (8-III).

Cell	Temperature range (°C)	$E(mV) = (\pm S_a) + b(\pm S_b)T(K)$ a	S_a	b	S_b	Standard deviation (mV)
(8-I)	850-1150	218	3	0.2547	0.002	± 1
(8-II)	850-1150	-13	1.4	0.0175	0.001	± 1
(8-III)	850-1150	142	2	-0.0157	0.002	± 1

Table (8-2) Emf-T relations obtained for cell (8-I), cell (8-II) and cell (8-III).

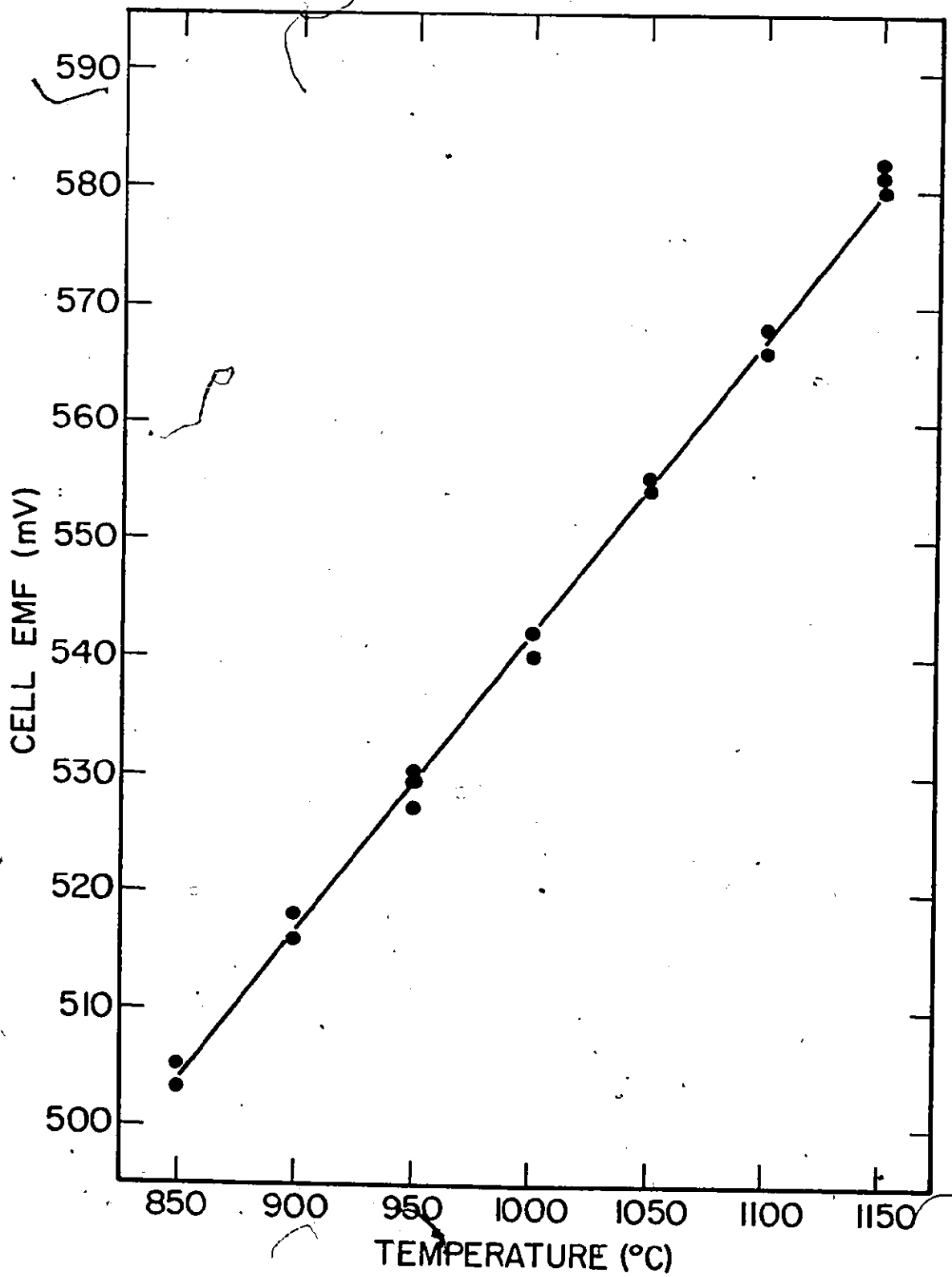

Figure (8-1) Variation of emf with temperature for cell (8-I).

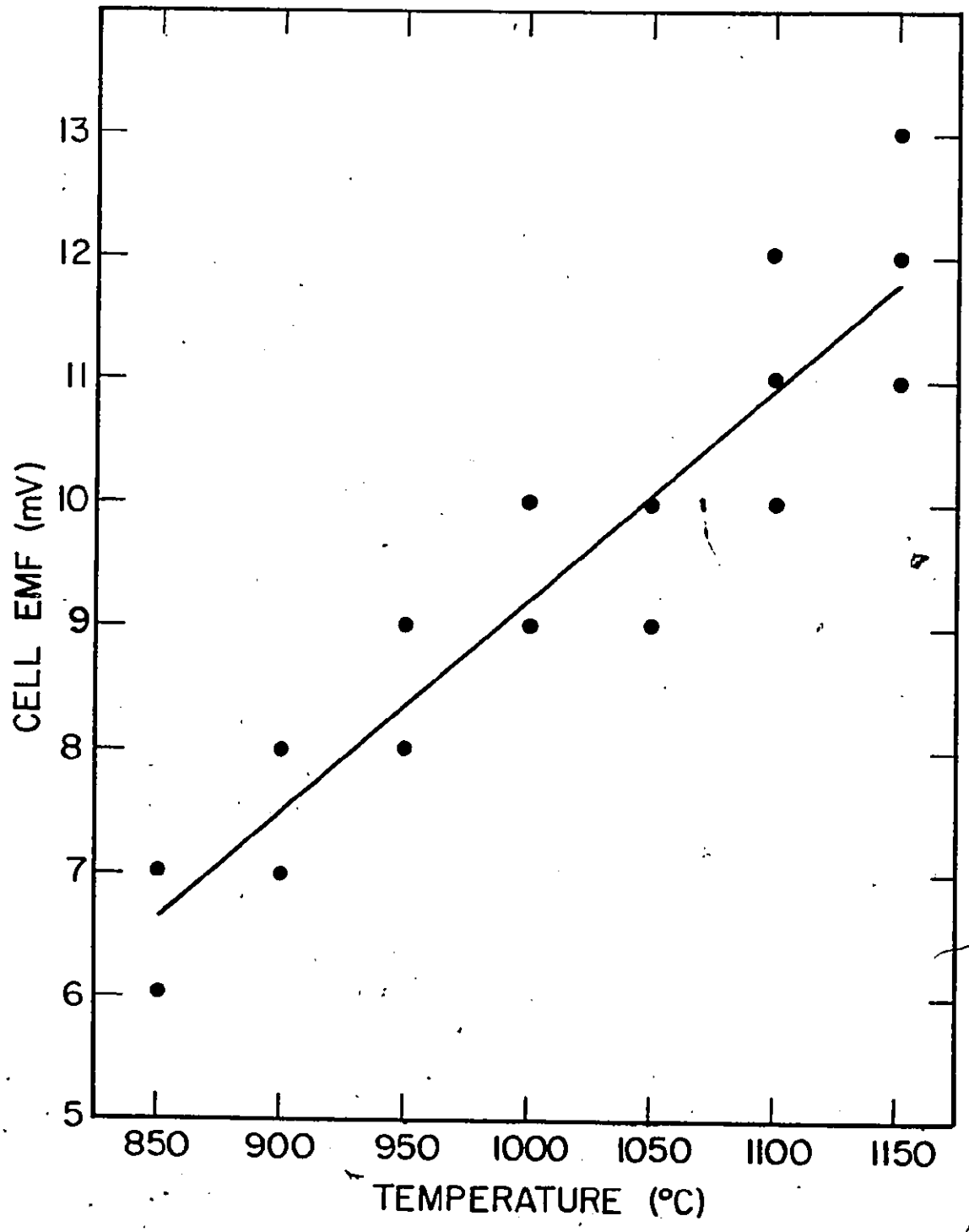

Figure (8-2) Variation of emf with temperature for cell (8-II).

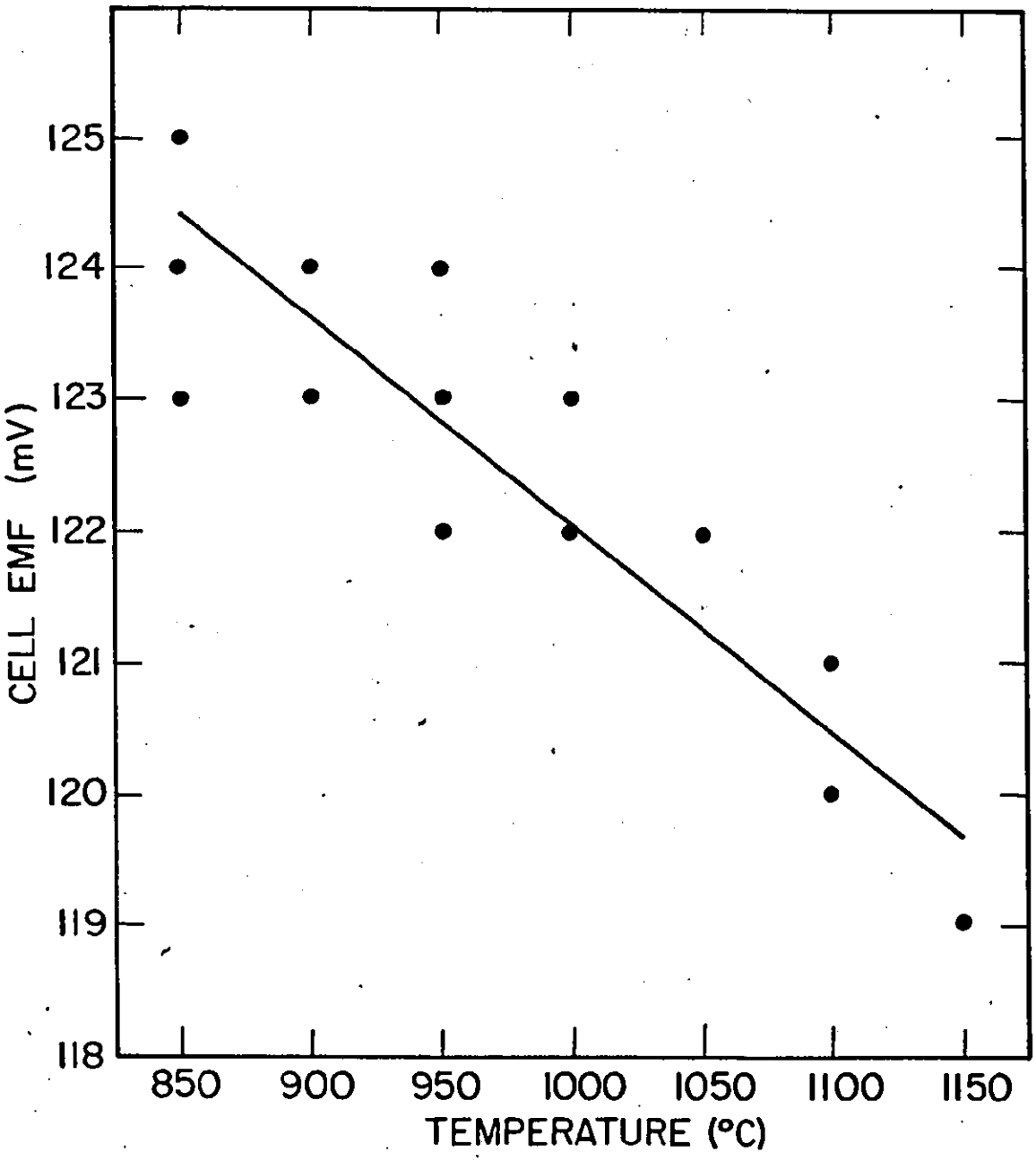

Figure (8-3) Variation of emf with temperature for cell (8-III).

not effective in giving reproducible results. The instability problem of cell (8-IV) can be due to electrolytic breakdown of ZrO_2(+CaO) if the oxygen potential imposed by the coexistence Fe-0.17 a/o Al alloy, α-Al_2O_3 is outside the electrolytic domain.

Cell (8-V) was constructed, using β- and α-Al_2O_3 as solid electrolyte, to determine the oxygen potential in equilibrium with Fe-0.17 a/o Al alloy,Al_2O_3 coexistence.

$$Pt\left|\begin{matrix}\text{Fe-Al alloy}\\(0.17\text{ a/o Al})\end{matrix}\right.,Al_2O_3\,|\,\beta\text{- and }\alpha\text{-}Al_2O_3\,|\,W_{(s)},WS_{2(s)},Na_2S_{(s)}\,|\,Pt \qquad (8\text{-V})$$

The emf was measured only at 940°C. In contrast to cell (8-IV) the emf of cell (8-V) was steady and reproducible. The emf value obtained at 940°C was 403±2 mV.

8.2 Metallography

Scanning electron micrographs in figures (8-4-a) and (8-5-a) illustrate the microstructure of the polished-annealed specimens of wustite-spinel-iron (WSI3) and Fe-0.17 a/o Al alloy,$Al_2O_{3(\alpha)}$ (IA0.1A), respectively. X-ray radiation mapping revealed the microstructure of these samples. Figures (8-4-b) and (8-5-b) show Fe-K_α radiation mapping of WSI3 and IA0.1A samples, respectively, while figures (8-4-c) and (8-5-c) illustrate Al-K_α radiation mapping for WSI3 and IA0.1A specimens.

Figure (8-4) a) Scanning electron micrograph of the Fe, wustite, spinel sample that annealed at 1000°C. b) Fe-K_α radiation mapping. c) Al-K_α radiation mapping. The alloy phase of the sample is substantially pure Fe.

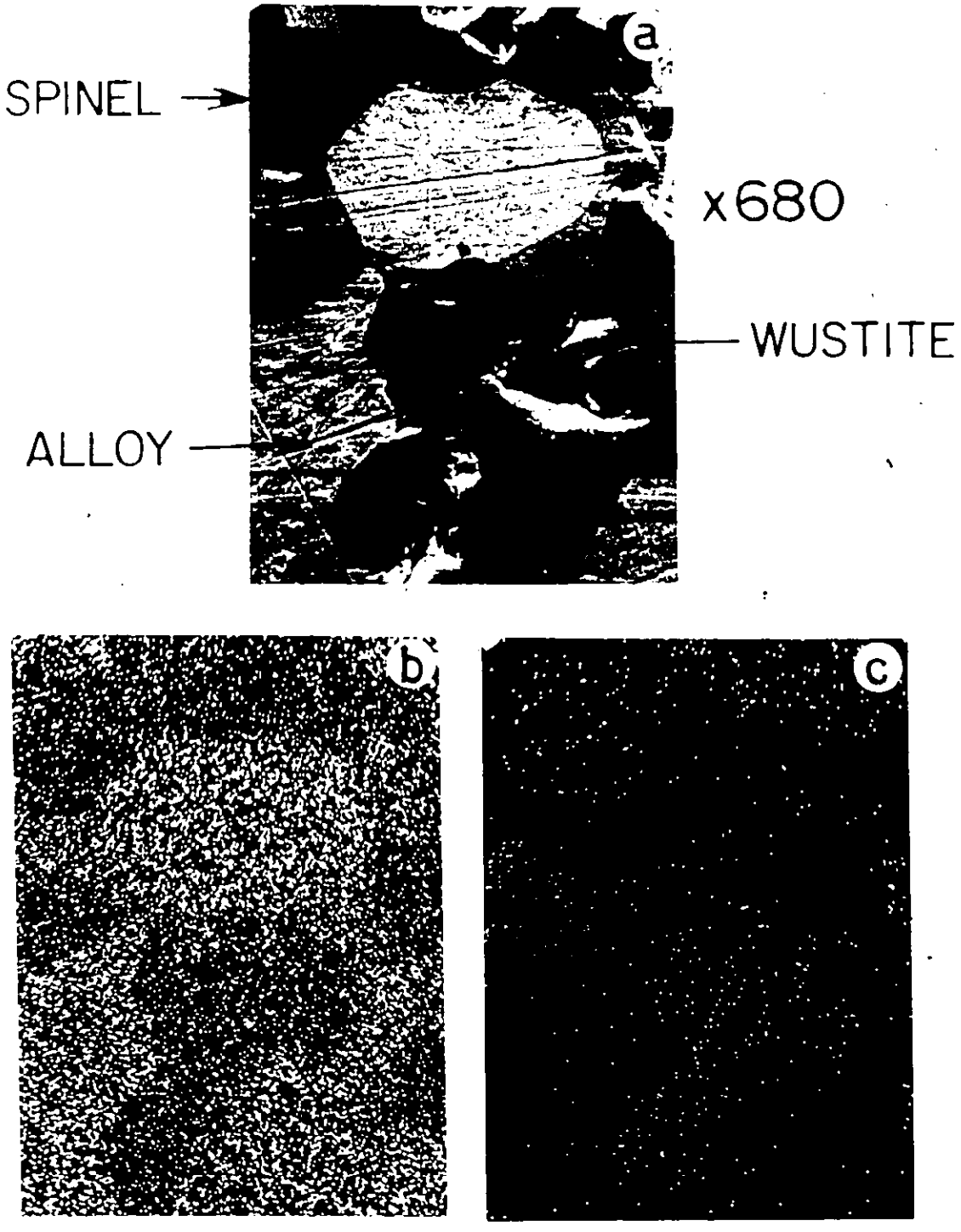
a
SPINEL
x680
WUSTITE
ALLOY
b
c
Fe map
Al map

Figure (8-5) a) Scanning electron micrograph of the IA0.1A sample. b) Fe-K_α radiation mapping. c) Al-K_α radiation mapping.

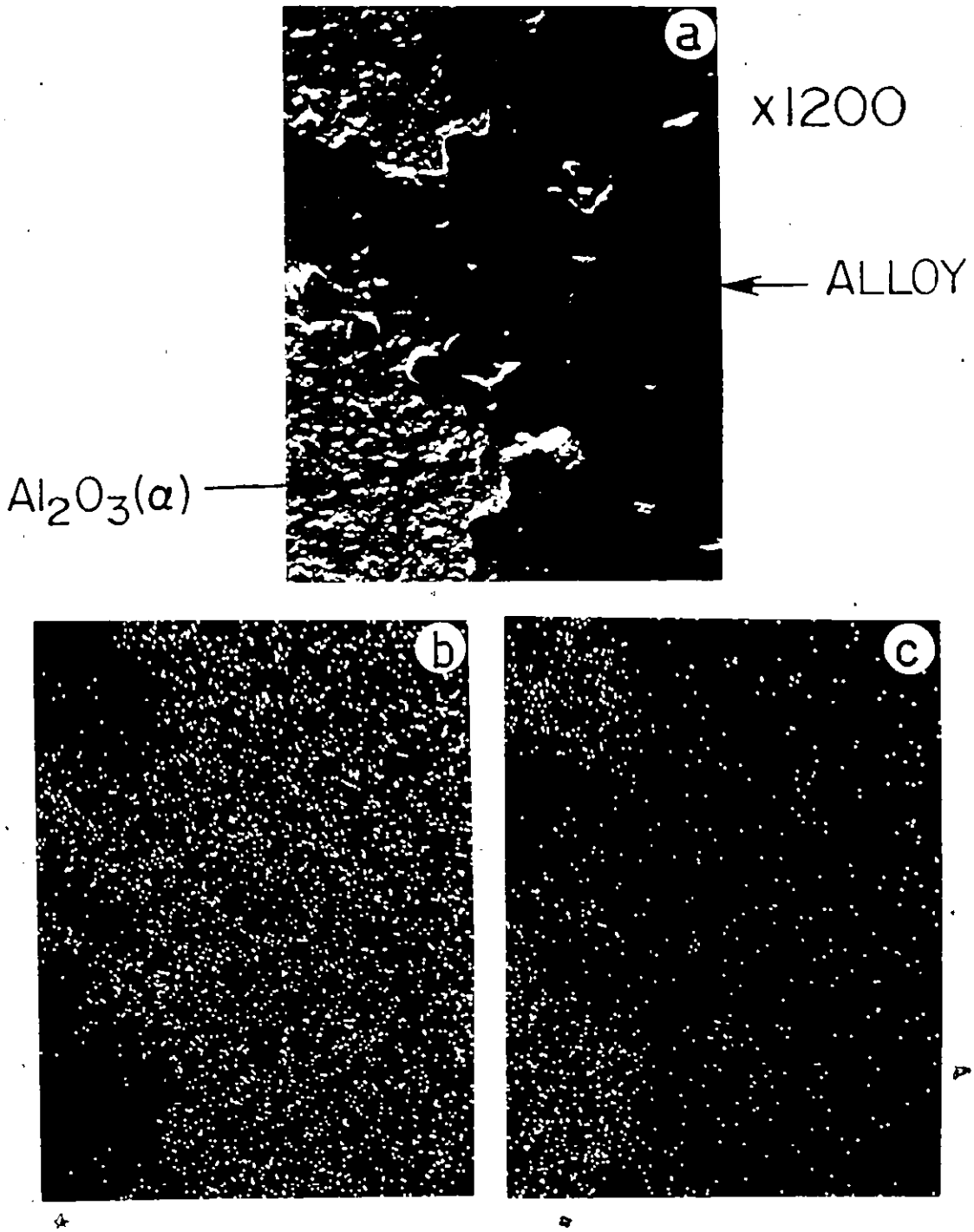
a
x1200
ALLOY
$Al_2O_3(\alpha)$
b
c
Fe map
Al map

Polished samples of hematite-spinel-aluminum oxide (HSA) and spinel-aluminum oxide-iron (SAI) exhibited poor contrast. To overcome this difficulty, the samples were scanned by the electron probe beam to obtain a qualitative estimate of the phases in each sample. Figure (8-6) illustrates the iron and aluminum profiles obtained. It is possible from these observations to predict the presence of three phases in each equilibrated sample. During the polishing procedure, the oxide phases of the samples tended to be preferentially abraded. the resultant voids are shown, in some cases, in the figures.

8.3 The Electron Microprobe Analyses

Results of the electron probe analyses for Fe-Al-O samples are reported in table (8-3). The reported intensities of X-ray signal were obtained from Al-K_α and Fe-K_α lines. Each value is the arithmetical mean of thirty two spot-detected values taken at different regions of an equilibrated phase. Background, dead time, atomic number, absorption, and fluorescence corrections were applied to get the composition of each phase. Obtained compositions are listed in columns five and six of table (8-3). Column five gives the composition of the metallic phases and column ~~six~~ shows the determined chemical composition of the oxide phases.

Intensities of Al-K_α radiation obtained from the metallic phases of WSI and SAI samples were of the order of background

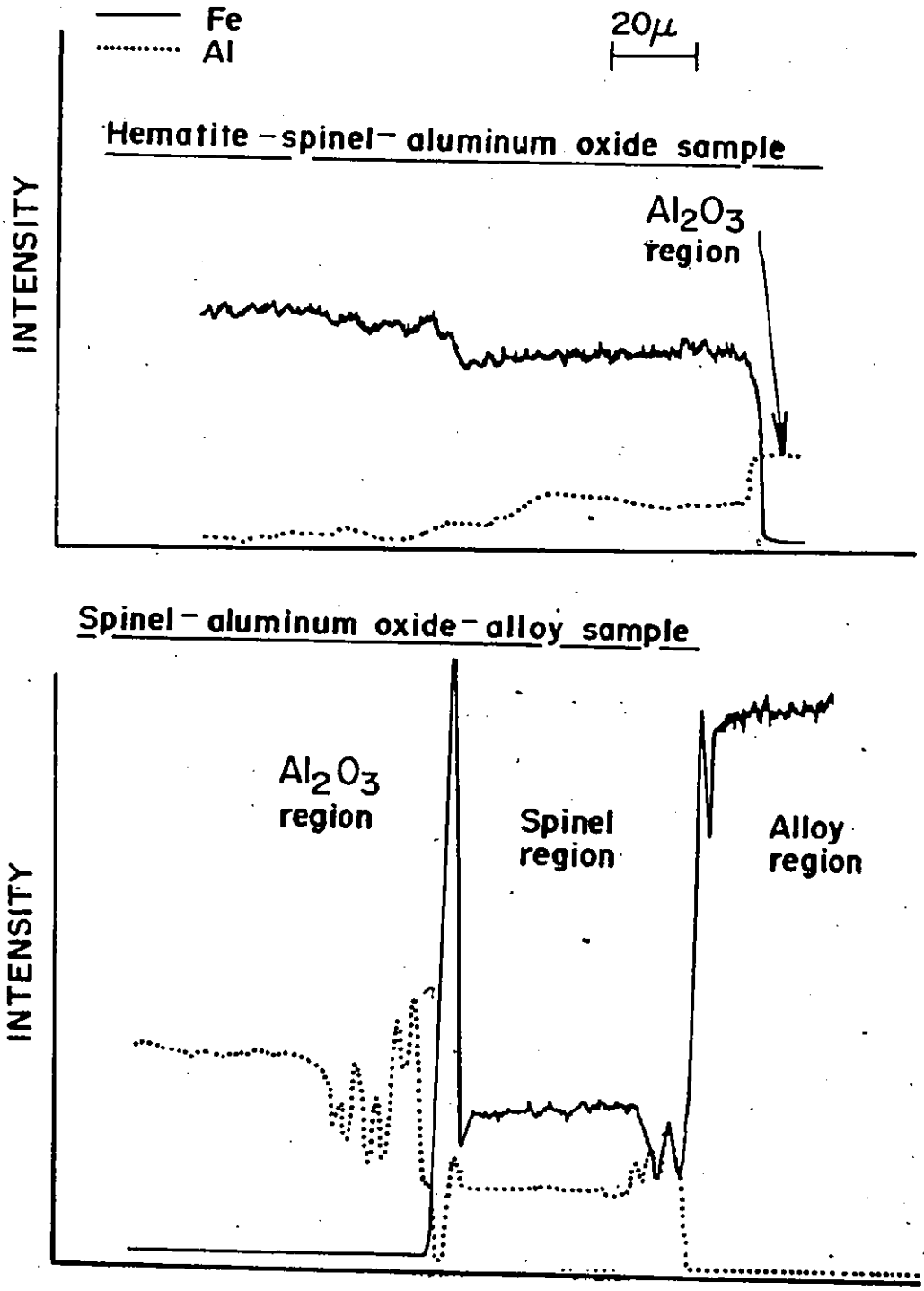

Figure (8-6) Microprobe scan along the sample.

Sample	Phase	Intensity of the electron probe X-ray signal				Al and Ni weight percent in the alloy		Chemical formula of the oxide
		Standards		Samples				
		Al	Fe	Al	Fe	Al	Fe	
WSI1	Wustite	60123	39103	94	28515	-	-	$(Fe_{0.983}Al_{0.011})O$
	Spinel	60123	39103	7996	12825	-	-	$(Fe_{1.227}Al_{1.849})O_4$
SAI1	Spinel	60123	39103	9138	11418	-	-	$(Fe_{1.057}Al_{1.962})O_4$
	Aluminum oxide	60123	39103	22315	401	-	-	$(Fe_{0.023}Al_{1.985})O_3$
WSI2	Wustite	61039	39217	82	28614	-	-	$(Fe_{0.986}Al_{0.009})O$
	Spinel	61039	39217	7613	13409	-	-	$(Fe_{1.304}Al_{1.797})O_4$
SAI2	Spinel	61039	39217	9270	11443	-	-	$(Fe_{1.056}Al_{1.962})O_4$
	Aluminum oxide	61039	39217	22680	392	-	-	$(Fe_{0.023}Al_{1.985})O_3$
WSI3	Wustite	60073	39714	60	28991	-	-	$(Fe_{0.989}Al_{0.007})O$
	Spinel	60073	39714	7268	14138	-	-	$(Fe_{1.356}Al_{1.763})O_4$
SAI3	Spinel	60073	39714	9112	11569	-	-	$(Fe_{1.057}Al_{1.962})O_4$
	Aluminum oxide	60073	39714	9112	383	-	-	$(Fe_{0.022}Al_{1.986})O_3$

(continued next page)

Sample	Phase	Intensity of the electron probe X-ray signal				Al and Ni weight percent in the alloy		Chemical formula of the oxide
		Standards		Samples				
		Al	Fe	Al	Fe	Al	Fe	
IA0.1A	Alloy	60013	38213	17	38155	0.08	99.87	-
	Aluminum oxide	60013	38213	22460	379	-	-	$(Fe_{0.022}Al_{1.985})O_3$
IA0.5A	Alloy	60013	38213	108	37983	0.49	99.54	-
	Aluminum oxide	60013	38213	22500	370	-	-	$(Fe_{0.021}Al_{1.986})O_3$
IA1.5A	Alloy	60013	38213	334	37501	1.49	98.49	-
	Aluminum oxide	60013	38213	22510	361	-	-	$(Fe_{0.021}Al_{1.986})O_3$
IA3A	Alloy	60013	38213	714	37111	3.17	97.80	-
	Aluminum oxide	60013	38213	22590	347	-	-	$(Fe_{0.020}Al_{1.987})O_3$
IA10A	Alloy	61522	39584	2432	34786	10.18	90.00	-
	Aluminum oxide	61522	39584	23001	313	-	-	$(Fe_{0.018}Al_{1.988})O_3$
IA20A	Alloy	61522	39584	5032	30388	19.90	80.17	-
	Aluminum oxide	61522	39584	23024	272	-	-	$(Fe_{0.016}Al_{1.990})O_3$

(continued next page)

Sample	Phase	Intensity of the electron probe X-ray signal				Al and Ni weight percent in the alloy		Chemical formula of the oxide
		Standards		Samples				
		Al	Fe	Al	Fe	Al	Fe	
IA25A	Alloy	61522	39584	6569	28188	25.14	75.17	-
	Aluminum oxide	61522	39584	23120	249	-	-	$(Fe_{0.014}Al_{1.991})O_3$
IA30A	Alloy	61522	39584	8109	26038	30.01	30.13	-
	Aluminum oxide	61522	39584	23224	223	-	-	$(Fe_{0.013}Al_{1.992})O_3$

Table (8-3) Electron microprobe analyses for Fe-Al-O samples.

signals obtained from the standard sample of pure iron (99.99) therefore, it was not possible to determine the aluminum content in the metallic phases of these samples using the electron probe technique. The electron probe results obtained in this investigation for Fe-Al-O system indicated the following:

a) Wustite in equilibrium with iron and iron spinel dissolves 0.55 a/o Al at 1300°C, 0.45 a/o Al at 1150°C, and 0.35 a/o Al at 1000°C.

b) The composition of the spinel phase which is in equilibrium with aluminum oxide and iron is independent of temperature in the range 1000-1300°C and could be represented by the formula $FeO.(0.48\pm0.03)Al_2O_3$.

c) Spinel in equilibrium with wustite and iron is richer in iron and its composition is temperature dependent, table (8-4); the spinel becomes richer in iron with decreasing temperature.

d) Iron-aluminum alloys equilibrate with aluminum oxide which contains iron ions in its lattice. The solubility of iron in α-Al_2O_3 was found to decrease with increasing the Al contents of the metallic phase for tablets annealed at 1000°C. The iron content of the aluminum oxide of IA0.1A sample is 0.44 a/o and drops to 0.26 a/o for aluminum oxide in equilibrium with iron alloy containing 30 w/o Al.

e) The solubility of iron in α-Al_2O_3 equilibrated with spinel and iron is constant, 0.45 a/o, over the temperature range 1000-1300°C.

Annealing temperature (°C)	Aluminum oxide content in iron spinel, (m/o)
1300	42.97
1150	40.79
1000	39.40

Table (8-4) The composition data of iron spinel equilibrated with wustite and iron.

8.4 Discussion

8.4.1 Introduction

Emfs of cells (8-I), (8-II), and (8-III) can be described by the relation

$$E = \pm \frac{RT}{4F} \ln \frac{p_{O_2}}{p^{o}_{O_2}} \qquad (8.1)$$

providing that the cells are at constant temperature and pressure, operate reversibly, and the solid electrolyte behaves ionically. p_{O_2} is the equilibrium oxygen pressure over the working electrode and $p^{o}_{O_2}$ is the equilibrium oxygen pressure over the standard electrode.

The dissociation pressure of wustite in equilibrium with iron, over the temperature range 873-1600K, is given by the relation (13)

$$\log p^{o}_{O_2}(\text{atm.}) = - \frac{27,637}{T(K)} + 6.831 \; . \qquad (8.2)$$

Equilibrium oxygen pressures over HSA, WSI and SAI electrodes were evaluated over the temperature range 850-1150°C by using equation (8.1), equation (8.2) and the data of table (8-2). The calculated values of $\log p_{O_2}$ are listed in table (8-5).

The over-all cell reaction of cell (8-V) can be written as

$$2(Na_2O)_{\beta} + WS_{2(s)} = O_{2(g)} + 2Na_2S_{(s)} + W_{(s)} \qquad (8.3)$$

Electrode	$-\log p_{O_2}$ (atm.)						
	850°C	900°C	950°C	1000°C	1050°C	1100°C	1150°C
HSA	8.7	7.8	7.0	6.3	5.6	5.0	4.4
WSI	17.88	16.85	15.89	15.01	14.20	13.45	12.75
SAI	20.01	18.85	17.79	16.81	15.90	15.06	14.28

Table (8-5) The equilibrium oxygen pressures over HSA, WSI, and SAI electrodes.

for which

$$\Delta G_{(9.3)} = -4FE = 2\Delta G_f^o(Na_2S_{(s)}) - 2\Delta G_f^o(Na_2O_{(s)} - \Delta G_f^o(WS_{2(s)})$$

$$+ RT\ell n\ p_{O_2} - 2RT\ell n\ a_{Na_2O(\alpha-\beta)} \quad . \qquad (8.4)$$

The oxygen pressure in equilibrium with the coexistence Fe-0.17 a/o Al,$Al_2O_{3(\alpha)}$ at 940°C was obtained utilizing equation (8.4), the data of table (5-9), and the measured value of E for cell (8-V). The estimated value of the oxygen pressure in equilibrium with IA0.1A coexistence at 940°C is 2.3×10^{-30} atm. ($\log p_{O_2} = -29.6$). Under such oxygen potential, calcia stabilized zirconia exhibits electronic conduction which explains the unsteady behaviour observed for cell (8-IV).

For an error in emf measurement of ± 3 mV, which is larger than the standard deviation of the least squares lines, and an error of ± 5°C in the recorded temperature, the calculated values of $\log p_{O_2}$ (atm.) have an estimated error of ± 0.2 atm. The resultant p_{O_2} values, combined with the electron probe results, as well as the available data in the literature for Fe-Al-O system were used to determine the equilibrium oxygen pressure diagram for this system.

8.4.2 Standard Free Energy of Formation of $FeAl_2O_4$

Equilibrium between the alloy and the oxide phases in the spinel-$Al_2O_{3(\alpha)}$-iron phase field of the Fe-Al-O system can be represented by the following two equilibria

$$2Al_{(\text{in iron})} + \frac{3}{2} O_{2(g)} = Al_2O_{3(\alpha)}$$

$$Fe_{(s)} + 2Al_{(\text{in iron})} + 2O_{2(g)} = FeAl_2O_{4(s)} .$$

Activities of aluminum, a_{Al}, of the metallic phase in equilibrium with $Al_2O_{3(\alpha)}$ and $FeAl_2O_{4(s)}$ were calculated, by considering the first reaction, over the temperature range 850-1150°C using the relation

$$\log a_{Al} = 0.5\left(\frac{\Delta G_f^o(Al_2O_{3(\alpha)})}{2.303RT(K)} - 1.5 \log p_{O_2}\right) \qquad (8.5)$$

where p_{O_2} is the equilibrium oxygen pressure over the spinel-$Al_2O_{3(\alpha)}$-iron electrode calculated in the previous section. To obtain equation (8.5), it was assumed that the activity of $Al_2O_{3(\alpha)}$ is unity because iron is at very small solubility in Al_2O_3. Obtained activities are tabulated in table (8-6).

Considering the second equilibrium, the standard free energy of formation of $FeAl_2O_4$, $\Delta G_f^o(FeAl_2O_{4(s)})$, was calculated using the formula

$$\Delta G_f^o(FeAl_2O_{4(a)}) = 2RT\ell n(a_{Al} \cdot p_{O_2}) . \qquad (8.6)$$

Unit activities of iron and spinel are assumed in this case. The calculated values of $\Delta G_f^o(FeAl_2O_{4(s)})$ are listed in table (8-7). The estimated error in these values is ± 700 cal/mole.

Temperature (°C)	850	900	950	1000	1050	1100	1150
$\log a_{Al}$	-15.77	-14.98	-14.25	-13.58	-12.96	-12.39	-11.86

Table (8-6) Activities of Al of the alloy phase which is in equilibrium with $FeAl_2O_4$ and α-Al_2O_3.

Temperature (°C)	850	900	950	1000	1050	1100	1150
$-\Delta G^{o}_{f}(FeAl_2O_{4(s)})$ (cal/mole)	367,790	363,226	358,669	354,105	349,484	344,970	340,469

Table (8-7) The standard free energy of formation of $FeAl_2O_4$.

Least squares analysis of the values of $\Delta G^{o}_{f}(FeAl_2O_{4(s)})$ yielded relation (8.7) over the temperature range 850-1150°C.

$$\Delta G^{o}_{f}(FeAl_2O_{4(s)}) = -470,195+91.2T(K) \quad . \qquad (8.7)$$

The standard free energy change of the following reaction

$$2Fe_{(s)} + O_{2(g)} + 2Al_2O_{3(\alpha)} = FeAl_2O_{4(s)} \qquad (8.8)$$

was calculated by combining relation (8.7) with the data of table (5-9). The calculated values for the standard free energy change of reaction (8.8), $\Delta G^{o}_{(8.8)}$, are represented by the following relation

$$\Delta G^{o}_{(8.8)} = - 139.732+32.8T(K) \quad . \qquad (8.9)$$

The above relation is in a very good agreement with the results of Chan et al.(50).

8.4.3 Thermodynamic Properties of Fe-Al Alloys

The unsteady behaviour of cell (8-IV) indicated the limitation of using calcia stabilized zirconia as a solid electrolyte to determine the equilibrium oxygen pressure of coexistence of the type Fe-Al alloy, $Al_2O_{3(\alpha)}$ over the temperature range 850-1100°C. On the other hand, cell (8-V) has shown a steady and reproducible potential at 940°C. The solid electro-

lyte used in cell (8-V) was a sintered tube of β- and α-Al_2O_3 mixture. The measured emf value of cell (8-V) at 940°C was used to calculate the equilibrium oxygen pressure of the co-existence Fe-Al alloy containing about 0.1 w/o Al, $Al_2O_{3(\alpha)}$. The estimated value of p_{O_2} of this coexistence is 2.3×10^{-30} atm. at 940°C. The activity of Al in this alloy can be estimated by considering relation (8.5). Its resultant value is 2.6×10^{-6} (referred to liquid aluminum as standard state).

Values of Al activities in the Fe-Al system over the range 5-75 a/o Al at 900°C have been reported in reference (46). Table (8-8) gives the values of Al activity and the partial molal quantities of Al reported in the preceding reference. Aluminum activities in Fe-Al alloys have been calculated at 1000°C using the data of table (8-8) and the following relation

$$(\log a_{Al})_{T_2} - (\log a_{Al})_{T_1} = \frac{\Delta\bar{H}}{4.575}\left(\frac{1}{T_2} - \frac{1}{T_1}\right). \quad (8.10)$$

In the above relation, the value of $\Delta\bar{H}$ is assumed to be constant. The calculated values of Al activity at 1000°C are shown in table (8-8).

8.4.4 The Equilibrium Oxygen Pressure Diagram of Fe-Al-O System at 1000°C

In this investigation the equilibrium oxygen pressure over three electrodes, HSA, WST, and SAI was determined over the temperature range 850-1150°C. The oxygen pressure in

Atomic percent of Al	a_{Al}		$-\Delta\bar{H}_{Al}$	$-\Delta\bar{G}_{Al}$	$-\Delta\bar{S}_{Al}$
	900°C	1000°C	(cal/g. atom)	(cal/g. atom)	(cal/g. atom-K)
5	3.8×10^{-4}	8.6×10^{-4}	24,400	18,400	5.12
10	8.1×10^{-4}	1.8×10^{-3}	23,000	16,600	5.45
15	1.5×10^{-3}	3.1×10^{-3}	21,600	15,200	5.45
20	2.45×10^{-3}	4.9×10^{-3}	20,300	14,000	5.37
25	3.7×10^{-3}	7×10^{-3}	19,000	13,050	5.07
30	5.5×10^{-3}	1×10^{-2}	17,600	12,140	4.65
35	8.3×10^{-3}	1.4×10^{-2}	16,200	11,180	4.28
40	1.35×10^{-2}	2.2×10^{-2}	14,800	10,020	4.07
45	2.6×10^{-2}	4.1×10^{-2}	13,500	8,530	4.23
50	5.5×10^{-2}	8.3×10^{-2}	12,200	6,760	4.64
52	9.8×10^{-2}	1.4×10^{-1}	11,600	5,420	5.26
60	9.8×10^{-2}	1.4×10^{-1}	11,400	5,420	5.12
67	1.3×10^{-1}	1.9×10^{-1}	11,100	4,780	5.35
70	1.3×10^{-1}	1.9×10^{-1}	10,900	4,780	5.21
75	4.0×10^{-1}	5.1×10^{-1}	7,300	2,150	4.39

Table (8-8) The thermodynamic functions of Al in Fe-Al solid alloys (referred to liquid aluminum).

equilibrium with the coexistence Fe-Al alloy containing 0.17 a/o Al, $Al_2O_{3(\alpha)}$ was determined at 940°C by using cell (8-V). The value obtained for this oxygen pressure, 2.3×10^{-30} atm., which lies outside the electrolytic domain of calcia stabilized zirconia, explains the unsteady behaviour observed for cell (8-IV).

The dissociation pressure of $Al_2O_{3(\alpha)}$ in equilibrium with alloys containing 5 a/o up to 75 a/o Al have been calculated at 1000°C using the data of table (8-8) and relation (8.11)

$$\log p_{O_2}(\text{atm.}) = \frac{2}{3}\left(\frac{\Delta G_f^o(Al_2O_{3(\alpha)})}{2.303RT(K)} - 2\log a_{Al}\right) . \qquad (8.11)$$

The obtained values of p_{O_2} are listed in table (8-9).

Figure (8-7) shows the oxygen pressure diagram for the Fe-Al-O system at 1000°C. The diagram has been compiled from the results of this investigation and the data of table (8-9) at 1000°C.

At 1000°C the equilibrium oxygen pressure, decreases from 3.2×10^{-6} atm. (42) which is imposed by the Fe_2O_3,Fe_3O_4 coexistence to 5×10^{-7} atm. which is the equilibrium oxygen pressure associated with the invariant hematite-spinel-$Al_2O_{3(\alpha)}$. The metallic atomic fraction of iron, $x_{Fe} = \frac{n_{Fe}}{n_{Fe}+n_{Al}}$, in each phase of the coexistence hematite-spinel-$Al_2O_{3(\alpha)}$ are 0.89, 0.91, and 0.04, respectively. These latter values were determined from the Fe-Al-O isotherm at 1000°C which is proposed in reference (49). The oxygen pressure in equilibrium with the

Atomic percent of Al	log p_{O_2} (atm.)
5	-30.69
10	-31.11
15	-31.43
20	-31.69
25	-31.90
30	-32.11
35	-32.30
40	-32.56
45	-32.92
50	-33.33
52	-33.64
60	-33.64
67	-33.81
70	-33.81
75	-34.38

Table (8-9) Dissociation pressure of α-Al_2O_3 in equilibrium with Fe-Al alloys at 1000°C.

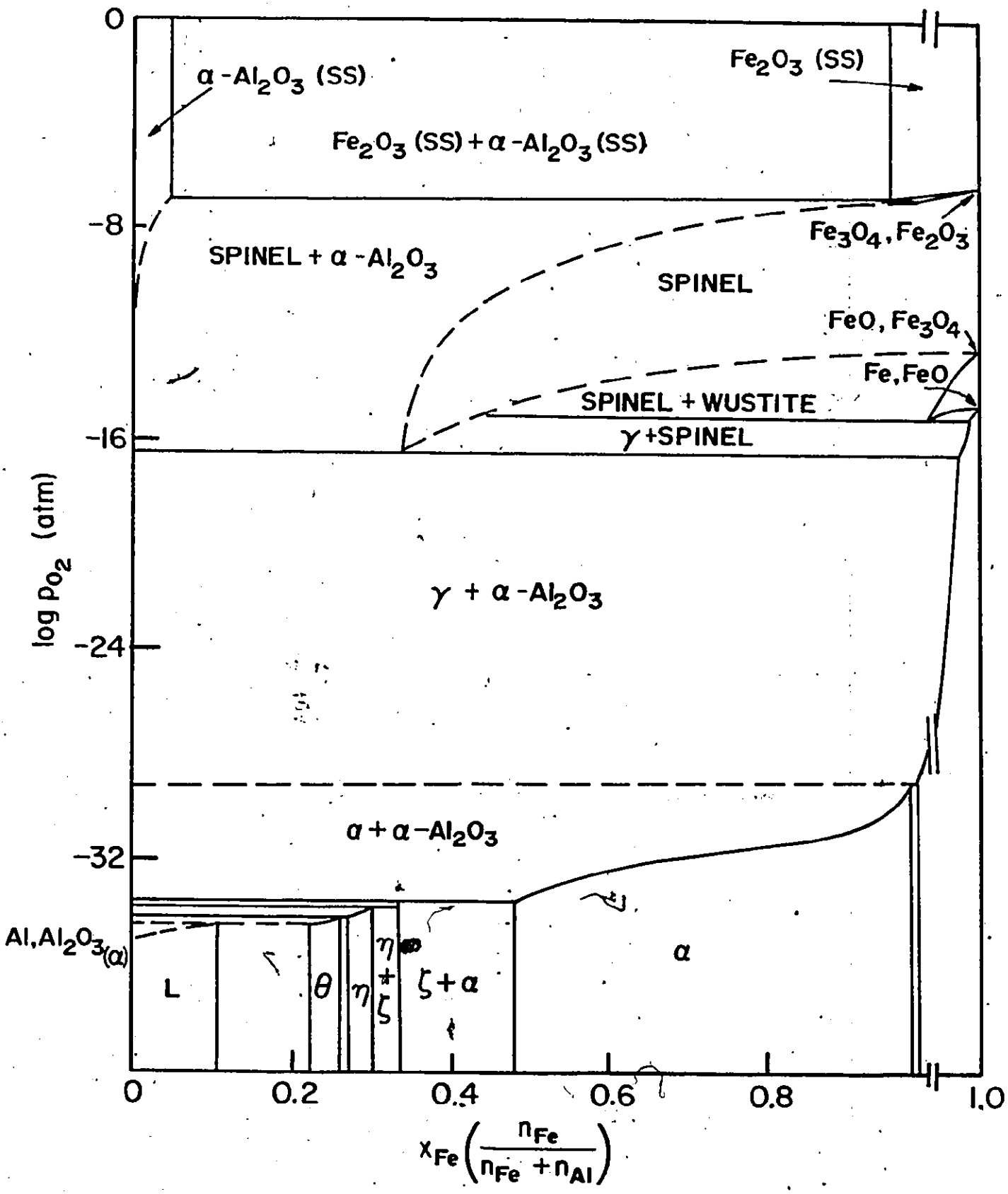

Figure (8-7) The equilibrium oxygen pressure diagram for Fe-Al-O system at 1000°C.

coexistences Fe_3O_4,FeO and FeO,Fe are 1.7×10^{-13} (40), and 1.3×10^{-15} (13), respectively, at 1000°C.

Over the temperature range 850-1150°C the equilibrium oxygen pressures associated with the invariant wustite-spinel-iron have been found to be lower than those corresponding to the coexistence Fe,FeO. Aluminum solubility in the wustite of this invariant system and the composition of spinel, table (8-4), were determined at 1000°C using the electron probe microanalysis technique.

Al contents of the metallic phase of WSI samples and also of the system spinel-Al_2O_3-iron are too small to be detected by the electron probe, however, assuming that the activity coefficient of Al is constant over the composition range 0.0-0.17 a/o Al, the Al contents of these alloys could be determined from the thermodynamic data of these invariant systems. Results indicate that a ppm of Al in the alloy is sufficient to stabilize α-Al_2O_3.

[redacted] equilibrium oxygen pressure decreases with increasing Al content of the alloy until it reaches, at 1000°C, 1.68×10^{-35} atm corresponding to that of Al,$Al_2O_{3(\alpha)}$ equilibria. The equilibrium oxygen pressures corresponding to the invariants γ-α-Al_2O_3 and θ-L-Al_2O_3 have not been determined due to the lack of required thermodynamic data. Fe contents of Al_2O_3 in equilibrium with alloys containing up to 50 a/o

Al have been determined and given in table (8-3). Also the composition of spinel in equilibrium with iron and Al_2O_3 was found to be very close to the stoichiometric composition, $FeAl_2O_4$, over the temperature range 1000-1300°C.

CHAPTER 9

GENERAL DISCUSSION AND CONCLUSIONS

9.1 Stability of β-Alumina

Chemical stability of an ionic solid which shows an electrolytic domain is an essential topic to be investigated before attempting to utilize the material as a solid electrolyte in practical applications. Therefore, it was necessary to investigate the stability of β-Al_2O_3 of the coexistence β- and α-Al_2O_3 before using ceramic tubes made from a mixture of these materials to monitor oxygen potentials. The dependence of sodium oxide activity in the coexistence β- and α-Al_2O_3 upon temperature is a good indication of the stability of β-Al_2O_3 in the solid electrolyte tubes; however, this representation does not serve to indicate directly the effect of oxygen potential on the stability of β-Al_2O_3. The variation of equilibrium sodium vapor pressure, $P_{Na(\alpha-\beta)}$, over β- and α-Al_2O_3 mixtures with temperature and oxygen pressure is a direct way for examining the stability of β- and α-Al_2O_3 electrolyte tubes.

The variation of $P_{Na(\alpha-\beta)}$ with temperature and oxygen pressure can be estimated by considering the following reaction

$$2Na_{(v)} + \frac{1}{2} O_{2(g)} + 11Al_2O_{3(\alpha)} = \beta\text{-}Al_2O_3 \qquad (9.1)$$

for which

$$\Delta G^{o}_{(9.1)} = RT\ell n(P^{1/2}_{O_2} \cdot P^{2}_{Na(\alpha-\beta)}). \qquad (9.2)$$

But $\Delta G^{o}_{(9.1)}$ is also given by:

$$\Delta G^{o}_{(9.1)} = \Delta G^{o}_{f}(\beta\text{-}Al_2O_{3(s)})_v - 11\Delta G^{o}_{f}(Al_2O_{3(\alpha)}). \qquad (9.3)$$

Therefore

$$RT\ell n(P^{1/2}_{O_2} \cdot P^{2}_{Na(\alpha-\beta)}) = \Delta G^{o}_{f}(\beta\text{-}Al_2O_{3(s)})_v - 11\Delta G^{o}_{f}(Al_2O_{3(\alpha)}) \qquad (9.4)$$

The standard free energy change of formation of $\beta\text{-}Al_2O_3$ from liquid sodium, liquid aluminum, and oxygen was given by equation (5.14) as follows

$$\Delta G^{o}_{f}(\beta\text{-}Al_2O_{3(s)}) = -4,608,102+907.322T(K). \qquad (9.5)$$

The phase transformation of sodium from liquid to monoatomic gas occurs at 1176.9K (118) with ΔH_v = 23,285 cal/mole. Therefore, for the following reaction

$$Na_{(\ell)} \rightarrow Na_v$$

the free energy is given by relation (9.6).

$$\Delta G^{o}_{v}(Na) = 23285-19.785T(K) . \qquad (9.6)$$

Multiplying equation (9.6) by two and subtracting from relation (9.5) yields relation (9.7) which gives $\Delta G^{o}_{f}(\beta\text{-}Al_2O_{3(s)})_v$-T relation over the range 650-925°C.

$$\Delta G_f^{\circ}(\beta\text{-}Al_2O_{3(s)})_v = -4{,}654{,}672+946.892T(K) \quad . \quad (9.7)$$

Combining equation (9.4), equation (9.7) and the $\Delta G_f^{\circ}(Al_2O_{3(\alpha)})$-T relation given in table (5-9) yields relation (9.8) which gives the dependence of $P_{Na(\alpha-\beta)}$ on temperature and oxygen pressure.

$$\log(P_{O_2}^{1/2} \cdot P_{Na(\alpha-\beta)}^{2}) = -\frac{48{,}576}{T} + 19.91 \quad . \quad (9.8)$$

Equation (9.8) was used to construct figure (9-1) which shows the variation of $P_{Na(\alpha-\beta)}$ with temperature, between 650°C and 925°C, at oxygen potentials imposed by ambient atmosphere, P_{O_2} = 0.21 atm., Fe,FeO equilibrium, and $Al,Al_2O_{3(\alpha)}$ equilibrium. The log $P_{Na(\alpha-\beta)}$ - $\frac{1}{T}$ relations shown in the figure were obtained by substituting for the corresponding P_{O_2} in relation (9.8). The dissociation temperature, defined as the temperature at which log $P_{Na(\alpha-\beta)}$ = 0.0, was calculated by considering log $P_{Na(\alpha-\beta)}$ - $\frac{1}{T}$ relations given in figure (9-1). Under an atmosphere with oxygen potential equal to that of the $Al,Al_2O_{3(\alpha)}$ equilibria, β-Al_2O_3 dissociates at 1076°C, while dissociation occurs at 1834°C in environments with an Fe,FeO imposed-oxygen potential. The estimated error in the above values of temperatures is ±35°C. On the same figure, a plot of the values of the equilibrium sodium vapour pressure over β- and α-Al_2O_3 mixture in air reported in reference (66) between 1300K and 1900K are shown. Although Weber's values were determined over a different temperature range, the agreement between our values of log $P_{Na(\alpha-\beta)}$ (in air) and values extrapolated from Weber's results is fairly good. We therefore

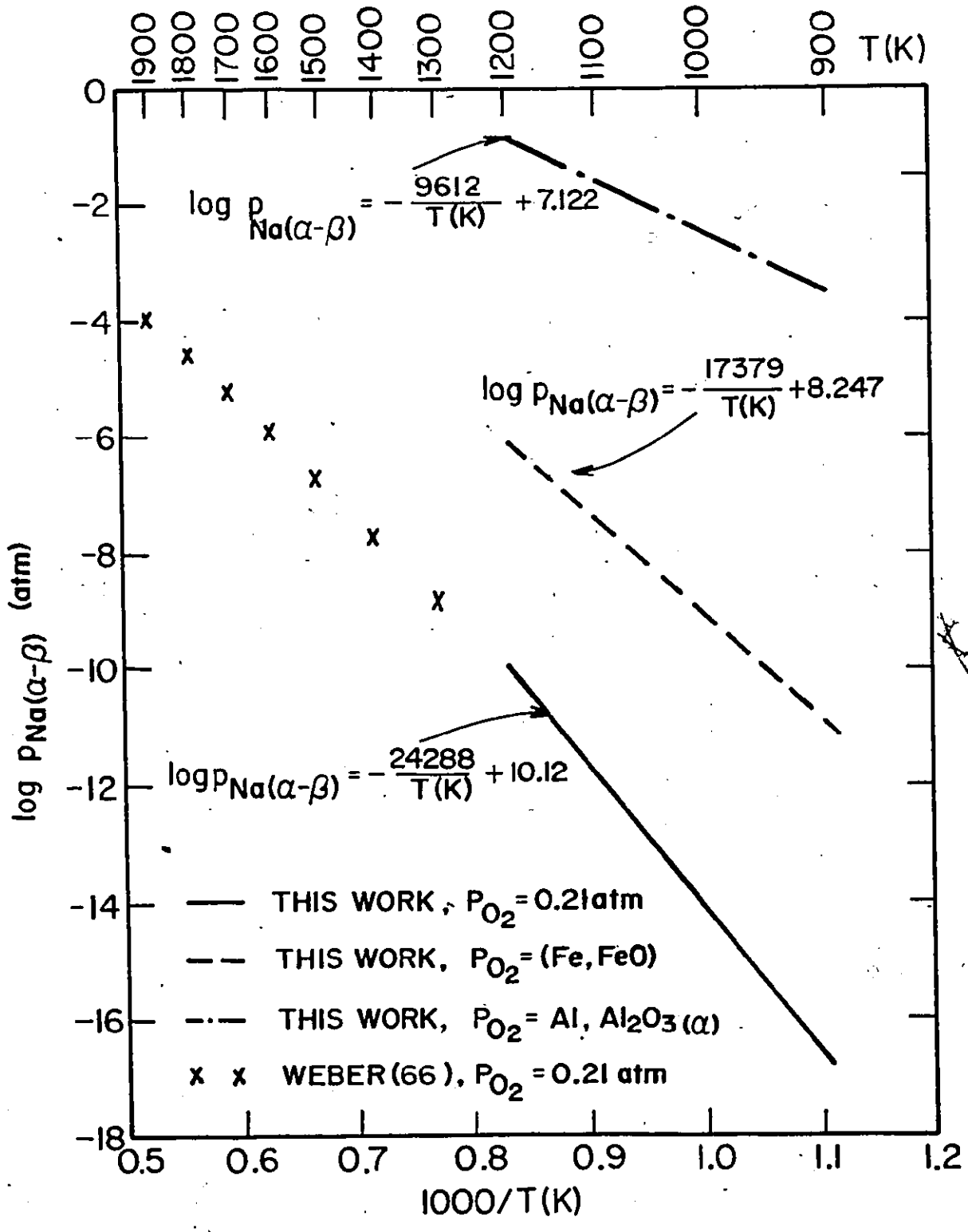

Figure (9-1) The variation of $P_{Na(\alpha-\beta)}$ with temperature and oxygen pressure.

conclude the following:

1 - At temperatures higher than 1000°C, β-Al_2O_3 of the coexistence α- and β-Al_2O_3 is unstable in open systems with equilibrium oxygen pressures as those defined by $Al, Al_2O_{3(\alpha)}$ equilibria.

2 - β-Al_2O_3 equilibrated with α-Al_2O_3 becomes more stable with increasing oxygen potential at constant temperature. The dissociation temperature is approximately 1900°C in environments with an Fe,FeO imposed-oxygen potential.

3 - At a fixed oxygen potential, β-Al_2O_3 becomes more stable with decreasing temperature.

9.2 β- and α-Alumina Mixtures as Solid Electrolytes for Oxygen Probe

Activities of sodium oxide in α- and β-Al_2O_3 coexistence were determined using galvanic cells, (5-I), (5-II), and (5-III), with β- and α-Al_2O_3 electrode tubes. One electrode fixes the sodium potential, $W_{(s)}, WS_{2(s)}, Na_2S_{(s)}$ coexistence, and the other fixes the oxygen potential, Cu-Cu_2O, Ni-NiO, or Fe-FeO coexistence. The emf values obtained from these cells were steady and reproducible indicating a reversible response of the electrolyte to the different electrodes, i.e. β- and α-Al_2O_3 behaved reversibly in contact with the oxygen potentials of Cu-Cu_2O, Ni-NiO, and Fe-FeO. Cells (6-I) and (6-II) were designed to closely examine this behaviour at temperatures between 600°C and 1000°C. The measured emf values were in

excellent agreement with previous published data for similar cells with oxygen-conducting solid electrolyte, $ZrO_2(+CaO)$ or $ThO_2(+YO_{1.5})$. However, the construction of a cell was very difficult because the two electrode compartments were sealed under argon atmospheres.

To ease this construction difficulty, the $W_{(s)},WS_{2(s)},Na_2S_{(s)}$ electrode was employed in cells (6-III), (6-IV), (6-V), and (6-VI). The oxygen fixing electrodes of cells (6-III) and (6-IV) were $Ni_{(s)},Ni_{1-x}Al_{2+y}O_4,Al_2O_{3(\alpha)}$, and $Fe_{(s)},FeAl_2O_{4(s)},Al_2O_{3(\alpha)}$ coexistences, respectively, and the electromotive forces were measured between 650°C and 900°C. These cells yielded steady reproducible potentials which enabled one to determine the free energy of formation of nickel spinel from its oxide constituents, equation (6.8), and the standard free energy change of reaction (6.13), equation (6.16). The free energy of formation of nickel spinel, equation (7.20), and the standard free energy change of reaction (6.13), equation (8.9), were also determined using cells with calcia stabilized zirconia as solid electrolyte. The agreement between equation (6.8) and equation (7.20) is fairly good, while excellent agreement is obtained between equation (6.16) and (8.9). Although the potentials of cells (6-I), (6-II), (6-III), and (6-IV) took a period to stabilize after temperature stabilization, coulometric disturbance or thermal cycling was not needed to obtain steady and reproducible results. The steady behaviour

of the emf was attained in few cases for periods of 48 hours.

In contradiction to the behaviour of the previous cells, coulometric disturbance was needed to overcome the unsteady behaviour at a constant temperature of cells (6-V) and (6-VI). A charging current of 15 ma was applied for three minutes; the change of emf with time was then followed to determine the cell emf decay curve. Reversible emf plateaus with duration times between 4 and 9 minutes were obtained. The free energy of formation of α-Al_2O_3 between 550°C and 800°C was calculated from equations (6.21) and (6.22) by considering reaction (6.18) of cells (6-V) and (6-VI). The obtained values of $\Delta G^{o}_{f}(Al_2O_{3(\alpha)})$ were more positive than the values given in JANAF tables (118) by approximately 3 Kcal. An alternative method for expressing the over-all reaction in cells (6-V) and (6-VI) is

$$WS_{2(s)} + 2Na_2O_{(\beta)} = 2Na_2S_{(s)} + O_{2(g)} + W_{(s)} \qquad (9.9)$$

for which

$$\Delta G_{(9.9)} = -4FE = 2\Delta G^{o}_{f}(Na_2S_{(s)}) - \Delta G^{o}_{f}(WS_{2(s)}) - 2\Delta G^{o}_{f}(Na_2O_{(s)})$$

$$+ RT\ell n\, P_{O_2} - 2RT\ell n\, a_{Na_2O(\alpha-\beta)} \qquad (9.10)$$

Rearranging equation (9.9) we obtain

$$\log P_{O_2} = \frac{\Delta G^{o}_{f}(WS_{2(s)}) + 2\Delta G^{o}_{f}(Na_2O_{(s)}) - 2\Delta G^{o}_{f}(Na_2S_{(s)}) - 4FE}{2.303RT.(K)}$$

$$+ 2\log a_{Na_2O(\alpha-\beta)} \qquad (9.11)$$

where P_{O_2} is the equilibrium oxygen pressure of $Al, Al_2O_{3(\alpha)}$, β-Al_2O_3 coexistence.

The variation of log P_{O_2} with temperature for $Al, Al_2O_{3(\alpha)}$, β-Al_2O_3 coexistence was calculated using equation (9.11), the emf-T relation for cell (6-V) or cell (6-VI), table (6-5), and the data of table (5-9) for $\Delta G^o_f(WS_{2(s)})$, $\Delta G^o_f(Na_2O_{(s)})$, and $\Delta G^o_f(Na_2S_{(s)})$. The estimated log P_{O_2} vs $\frac{1}{T}$ relations are given by relations (9.12) and (9.13).

$$\log P_{O_2} = -\frac{58,162}{T(K)} + 11.07 \quad [550°C\text{-}650°C] \qquad (9.12)$$

$$\log P_{O_2} = -\frac{58,323}{T(K)} + 11.26 \quad [675°C\text{-}800°C] \; . \qquad (9.13)$$

The corresponding values for the equilibrium oxygen pressure of $Al, Al_2O_{3(\alpha)}$, $P^*_{O_2}$, were calculated using the data of table (5-9) for $\Delta G^o_f(Al_2O_{3(\alpha)})$ over the temperature ranges 300-900K and 1000-1900K. The estimated relations are given by equations (9.14) and (9.15).

$$\log P^*_{O_2} = -\frac{58,322}{T} + 10.90 \quad [300K\text{-}900K] \qquad (9.14)$$

$$\log P^*_{O_2} = -\frac{58,703}{T} + 11.33 \quad [1000K\text{-}1900K]. \qquad (9.15)$$

Comparisons between (9.12) and (9.14), and equations (9.13) and (9.15) indicate that the values of log P_{O_2} is about 0.2 higher than log $P^*_{O_2}$. The higher values of log P_{O_2} thus explain the positive deviation of the standard free energy of formation of Al_2O_3 calculated from the emf data of cells (6-V) and (6-VI).

The above discussion indicates that solid electrolyte tubes of β- and α-Al_2O_3 were successfully used to monitor reversible oxygen pressures as high as those of Cu,Cu_2O coexistence (1.6×10^{-9} atm. at 800°C) between 600°C and 1000°C, and as low as those of Al,$Al_2O_{3(\alpha)}$, β-Al_2O_3 equilibria, (8.2×10^{-44} atm. at 800°C) between 550°C and 800°C. This solid electrolyte responded reversibly to any change in the oxygen pressure of cell [A],

$$W_{(s)},WS_{2(s)},Na_2S_{(s)}\,|\,\beta\text{-}Al_2O_3\,|\,Na_2CrO_{4(\ell)},P_{O_2},Cr_2O_{3(s)} \qquad (A)$$

which was designed by Liang and Elliott (112) to measure the standard free energy of formation of $Na_2CrO_{4(\ell)}$ between 1100K and 1220K. The values of oxygen pressure in the cathode compartment of this cell varied between 5×10^{-2} atm. and 1.0 atm. It is feasible now to make the following conclusions:

1 - β- and α-Al_2O_3 solid electrolyte tubes responded reversibly to an oxygen pressure that varies between 1.0 atm. and that imposed by Al,$Al_2O_{3(\alpha)}$, β-Al_2O_3 equilibria (10^{-43} atm. at 800°C) between 550°C and 1000°C.

2 - Potentials of cells (6-I), (6-II), (6-III), and (6-V) stabilized after few hours at temperature.

3 - The unsteady behaviour of cells (6-V) and (6-VI) was overcome by coulometric disturbance. Reversible emf plateau were observed for periods between 4 and 9 minutes.

4 - Although the values of $P_{Na(\alpha-\beta)}$ are relatively high in environments with Al,$Al_2O_{3(\alpha)}$, β-Al_2O_3 imposed oxygen

potentials, the static design adopted for the galvanic cells that utilized β- and α-Al_2O_3 electrolyte minimized sodium leaching from the β-Al_2O_3 structure.

9.3 Aluminum,α-Alumina,β-Alumina Equilibrium

In section (5.2.1) Na contents in the metallic phase of Al,α-Al_2O_3,β-Al_2O_3 coexistence, which determined by atomic absorption spectrophotometry were reported. Values of $\Delta G_f^o(\beta\text{-}Al_2O_{3(s)})$, table (5-7),calculated from these results were more negative by about 15 Kcal. than the values obtained from the emf results, equation (5.14). The reasons for this discrepancy were discussed in section (5.3.2). One reason advanced was sodium rejection from the aluminum phase during the time for a sample to reach room temperature.

The determination of the equilibrium oxygen pressure of Al,α-Al_2O_3,β-Al_2O_3 coexistence in section (9.2),which was based upon the assumption that the sodium oxide content of β-Al_2O_3 in equilibrium with α-Al_2O_3 is independent of oxygen pressure, can be utilized to determine the sodium level in the aluminum phase. Chemical equilibrium between the different phases in this coexistence can be described by the following reaction

$$2Na_{(\text{in liq Al})} + \frac{1}{2}\,O_{2(g)} + 11Al_2O_{3(\alpha)} = \beta\text{-}Al_2O_3 \quad (9.16)$$

for which

$$\Delta G_f^o(\beta\text{-}Al_2O_{3(s)}) - 11\Delta G_f^o(Al_2O_{3(\alpha)}) = RT\ell n\, P_{O_2}^{1/2}\cdot a_{Na}^2 \quad (9.17)$$

Rearranging equation (9.17), we obtain

$$\log a_{Na} = \frac{\Delta G^{o}_{f}(\beta\text{-}Al_2O_{3(s)}) - 11\Delta G^{o}_{f}(Al_2O_{3(\alpha)})}{4.606RT(K)} - \frac{1}{4}\log p_{O_2} \quad (9.18)$$

The variation of $\log a_{Na}$ was evaluated over the temperature range 675-800°C using equation (9.18), equation (5.14), equation (9.13), and $\Delta G^{o}_{f}(Al_2O_{3(\alpha)})$ vs T relation given in table (5-9) between 1000K and 1900K. The determined relation is

$$\log a_{Na} = -\frac{4618}{T} + 2.81 \quad (9.19)$$

Dewing (117) proposed that the activity coefficient of sodium in liquid aluminum, γ_{Na}, is given by

$$\log \gamma_{Na} = (\frac{1812}{T} + 0.82)x^2_{Al} \quad (9.20)$$

where x_{Al} stands for the atom fraction of Al in the melt. Since $a_{Na} = \gamma_{Na}x_{Na}$, equation (9.19) can be written as

$$\log x_{Na} = -\frac{4618}{T} + 2.81 - \log \gamma_{Na} \quad (9.21)$$

Subtracting equation (9.20) from equation (9.21) and assuming that $x_{Al} \simeq 1.0$, one obtains:

$$\log x_{Na} = -\frac{6480}{T} + 1.99 \quad (9.22)$$

Equation (9.22) gives the dependence of x_{Na} on T for extremely dilute solutions of sodium in the aluminum phase of Al, $\alpha\text{-}Al_2O_3$, $\beta\text{-}Al_2O_3$ coexistence. Thus, aluminum in this three-phase coexistence dissolves 24 ppm of sodium at 700°C and 100

ppm of sodium at 800°C. The estimated error in the values of this solubility is ±60 ppm. These sodium levels in the metallic phase are about one order of magnitude higher than those determined experimentally and reported in section (5.2.1).

The high level of sodium in aluminum required to attain Al, α-Al_2O_3, β-Al_2O_3 equilibrium possibly explains the unsteady behaviour of cells (6-V) and (6-VI). Dissolution of the electrolyte would occur by the following reaction

$$\beta\text{-}Al_2O_3 \rightarrow \alpha\text{-}Al_2O_3 + 2Na_{(\text{in Al})} + \frac{1}{2} O_{2(g)} \qquad (9.23)$$

at the aluminum-electrolyte interface. This reaction leads to formation of α-Al_2O_3, which could not be experimentally confirmed. However, leaching of sodium could occur without destruction of the β-Al_2O_3 structure, as depicted by reaction (9.24),

$$Na_{Na}^{x} + e' \rightarrow Na_{(\text{in Al})} + V_{Na}^{\cdot} \qquad (9.24)$$

Thus, cell polarization could occur which would be removed by coulometric disturbance as experimentally found.

9.4 The Equilibrium Oxygen Pressure Diagram of Na-Al-O System at 1000K

Figure (5-6) shows the equilibrium oxygen pressure diagram of sodium-aluminum-oxygen system at 1000K. The most critical part of this diagram with respect to developing an oxygen probe based on β- and α-Al_2O_3 electrolyte is the Al, α-Al_2O_3, β-Al_2O_3 invariant system. In section (9.2) we found

that the equilibrium oxygen pressure of this coexistence which defines the lower level of oxygen potential that can be sensed by β- and α-Al_2O_3 probe is about two to five times higher than that of Al,$Al_2O_{3(\alpha)}$ equilibrium. However, the applicability of this probe to sense this very low oxygen potential is limited to the temperature range $T \leq 1000°C$ because the equilibrium sodium pressure increases with temperature. According to relation (9.22), the sodium content of aluminum equilibrated with α-Al_2O_3 and β-Al_2O_3 is about 36 ppm at 1000K. At sodium contents lower than this value, β-Al_2O_3 becomes unstable in contact with aluminum melt. However, as indicated in this investigation and also by Fray (67) the transformation reaction of β-Al_2O_3 to α-Al_2O_3, reaction (9.23), is very slow and unsubstantial at temperatures at least up to 800°C.

9.5 Nickel Oxide-Aluminum Oxide System

The nature and compositions of phases in this system were studied at temperatures between 1000°C and 1900°C. The results signified the importance of modifying the NiO-Al_2O_3 equilibrium diagram proposed in reference (31) to include an α-Al_2O_3 solid solution range. An average value of 0.45±0.1 a/o was found to represent the Ni solubility in α-Al_2O_3 between 1000°C and 1900°C. On the other hand, NiO dissolved more Al with increasing temperature; the solubility increased from

1.0 a/o Al at 1000°C to 3 a/o Al at 1800°C. The chemical formula $NiAl_2O_4$ was found to represent the composition of the spinel in equilibrium with NiO while alumina-rich spinel was found to equilibrate with α-Al_2O_3. Compositions of this alumina-rich spinel are summarized in table (7-5).

9.6 Nickel-Aluminum-Oxygen Isotherm at 1000°C

An isotherm for this system at 1000°C is proposed, figure (7-6). Compositions of the equilibrated phases were determined by analyzing annealed pellets that corresponded to different composition points on this isotherm. The results of this study are discussed and are represented in section (7.5.2). The following two conclusions are made based on the electron microprobe analyses and the emf results described in chapter 7:

1 - alumina-rich spinel, $Ni_{0.83}Al_{2.113}O_4$, and α-Al_2O_3 containing small amount of Ni, 0.4 a/o Ni, equilibrate practically with pure Ni. Thermodynamic calculations demonstrated that less than 1 ppm of Al in Ni is sufficient to stabilize α-Al_2O_3. Of course, less than this amount of Al is needed to stabilize NiO (containing 1.87 a/o Al)-$NiAl_2O_3$-Ni coexistence.

2 - The Ni solubility in α-Al_2O_3 equilibrated with Ni-Al alloys decreases with increasing Al content of the alloy.

9.7 Iron-Aluminum-Oxygen System

The phase relation in this system can be summarized as follows:

1 - Fe-Al alloys equilibrate at 1000°C with α-Al_2O_3 that dissolves a small amount of Fe; the iron solubility in Al_2O_3 decreases with increasing Al content of the alloy.

2 - Between 1000°C and 1300°C, $FeAl_2O_4$ and α-Al_2O_3 or wustite and spinel each coexist with substantially pure Fe.

3 - Wustite of the coexistence wustite-spinel-iron dissolves 0.55 a/o Al at 1300°C, 0.45 a/o Al at 1150°C, and 0.35 a/o Al at 1000°C.

4 - With increasing temperature, the spinel vertex of the wustite-spinel-iron field increases in alumina content (table 8-4).

5 - The composition of the spinel phase of the $FeAl_2O_4$-α-Al_2O_4-Fe coexistence is essentially stoichiometric.

9.8 Nickel-Nickel Oxide-Spinel Phase Field

The equilibrium oxygen pressure over this phase field was determined over the temperature range 850°-1150°C using a galvanic cell with calcia stabilized zirconia as solid electrolyte, cell (7-I). The variation of log P_{O_2} with temperature for this phase field is given by equation (7.7). In the temperature range 850°-1150°C the equilibrium oxygen pressure over this coexistence is lower than that defined by Ni,NiO equilibrium by about 0.15 order of magnitude. The activity

of NiO in this field can be determined by considering the equilibria between the different phases. This phase equilibrium can be represented by the following reaction

$$Ni + \frac{1}{2} O_2 = NiO$$

for which $\Delta G^o_f(NiO_{(s)}) = -RT\ell n\ a_{NiO}/P_{O_2}^{1/2}$

Since $\Delta G^o_f(NiO_{(s)}) = RT\ell n\ P_{O_2}^{*1/2}$,

therefore $$\log a_{NiO} = \frac{1}{2} \log (P_{O_2}/P^*_{O_2}) \qquad (9.23)$$

where $P^*_{O_2}$ is the dissociation pressure of pure NiO. An average value of 0.921±0.002, over the temperature range 850°-1150°C, was obtained for a_{NiO} by substituting for P_{O_2}, equation (7.7), and $P^*_{O_2}$, equation (7.3), into equation (9.23).

9.9 Iron-Wustite-Spinel Phase Field

The galvanic cell (8-II) with calcia stabilized zirconia as solid electrolyte was used to determine the equilibrium oxygen pressure over wustite-spinel-iron coexistence between 850°C and 1150°C. The determined values of $\log P_{O_2}$ are reported in table (8-5). The equilibrium between iron and wustite of this phase field can be described by the following reaction

$$Fe + \frac{1}{2} O_2 = FeO$$

for which $$\Delta G_f^o(FeO) = -RT\ell n \frac{a_{FeO}}{P_{O_2}^{1/2}}$$

Since $$\Delta G_f^o(FeO) = \frac{1}{2} RT\ell n P_{O_2}^*$$

therefore $$\log a_{FeO} = \frac{1}{2} \log (P_{O_2}/P_{O_2}^*) \qquad (9.24)$$

where $P_{O_2}^*$ is the dissociation pressure of wustite to pure iron. Equation (9.24), equation (8.2), and the data of table (8-5) for log P_{O_2} of wustite-spinel-iron coexistence were used to calculate a_{FeO}. The estimated values of a_{FeO} was found to decrease from 0.89 at 850°C to 0.83 at 1150°C.

9.10 Nickel-Spinel-Aluminum Oxide Phase Field

The equilibrium oxygen pressure imposed by this coexistence between 850°C and 1150°C was determined using cell (7-II) and between 650°C and 900°C using cell (6-III). Equation (7.8) gives the dependence of the obtained values of log P_{O_2} on temperature. The spinel of this field is not stoichiometric and its composition changes with temperature. It was therefore not possible to define a standard state for nickel spinel and to calculate the standard free energy of formation of nickel spinel. Notwithstanding, the free energy change of reaction (7.19), $NiO + xAl_2O_3 = NiO.xAl_2O_3$, was estimated over the temperature range 650°C-1150°C. The results obtained in this investigation as well

as the results available in the literature are represented in figure (9.2).

9.11 Iron-Spinel-Aluminum Oxide Phase Field

Contrary to the nickel spinel of the coexistence Ni-spinel-$Al_2O_{3(\alpha)}$; the iron spinel of the corresponding phase field is stoichiometric, $FeAl_2O_4$, over the temperature range 650°C-1150°C. Therefore, it was possible to determine the standard free energy change of the reaction

$$2Fe_{(s)} + O_{2(g)} + 2Al_2O_{3(\alpha)} = 2FeAl_2O_{4(s)}. \qquad (9.25)$$

The variation of the standard free energy change of the reaction (9.25) with temperature was determined between 650°C and 900°C using cell (6-IV) which utilized β- and α-Al_2O_3 as solid electrolyte; cell (8-III) with calcia stabilized zirconia as solid electrolyte was used to estimate the variation of $\Delta G^{o}_{(9.25)}$ on temperature over the range 850°-1150°C. The agreement between the two results, equations (6.16) and (8.9) and the data reported in literature (50, 51) for $\Delta G^{o}_{(9.25)}$ is excellent. The equilibrium oxygen pressure of this coexistence was estimated to be about two orders of magnitude less that that of Fe,FeO coexistence at 1000°C.

9.12 Nickel (or Iron)-Aluminum Alloy, Aluminum Oxide Coexistence

The equilibrium oxygen pressure over electrodes of the type Ni or Fe)-Al alloy, $Al_2O_{3(\alpha)}$. were determined at

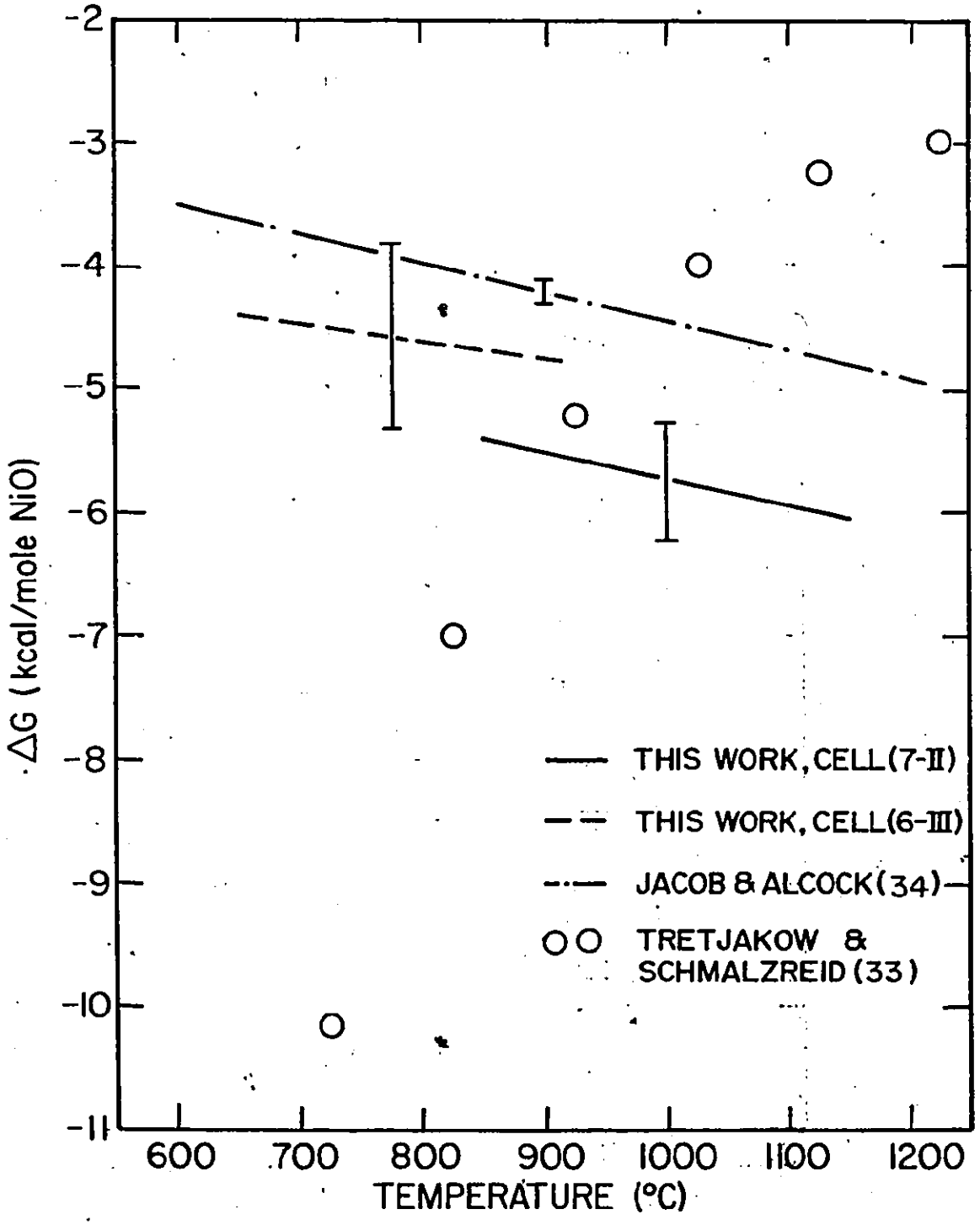

Figure (9-2) The free energy of formation of nickel spinel from NiO and Al_2O_3.

940°C using galvanic cells with β- and α-Al_2O_3 as solid electrolyte and $W_{(s)}, WS_{2(s)}, Na_2S_{(s)}$ coexistence as reference electrode. The melting point of Na_2S is 950°C which limits the use of $W_{(s)}, WS_{2(s)}, Na_2S_{(s)}$ as a reference electrode at higher temperature. The dissociation pressure of aluminum oxide equilibrated with nickel-aluminum alloys at 940°C was found to decrease from 5.7×10^{-24} atm. when the alloy contained 0.15 a/o Al to 3.7×10^{-26} atm. for Ni-2.36 a/o Al alloy at 940°C. By considering the formation reaction of α-Al_2O_3, the activity data of Al in the Ni-Al alloys equilibrated with aluminum oxide were determined for alloys containing between 0.15 a/o Al and 2.36 a/o Al at 940°C. This aluminum activity increases from 4.39×10^{-11} at 0.15 a/o Al to 1.9×10^{-9} for 2.36 a/o alloys when referred to liquid aluminum as the standard state.

The dissociation pressure of aluminum oxide equilibrated with iron containing 0.17 a/o Al (2.3×10^{-30} atm., at 940°C) was determined using cell (8-V) which contained β- and α-Al_2O_3 as solid electrolyte and $W_{(s)}, WS_{2(s)}, Na_2S_{(s)}$ as reference electrode. The aluminum activity in this alloy is 2.6×10^{-6}, referred to liquid aluminum as standard state. The unsteady behaviour displayed by the galvanic cells containing calcia stabilized zirconia as solid electrolyte with Ni-0.15 a/o Al (or Fe=0.17 a/o Al), $Al_2O_{3(\alpha)}$ coexistences occured since the equilibrium oxygen pressure over these electrodes were sufficiently low to cause electrolyte breakdown.

9.13 Equilibrium Oxygen Pressure Diagram for Ni-Al-O System at 1000°C

Equilibrium oxygen pressures determined in this investigation at 1000°C for coexistences in this ternary system as well as the values of dissociation pressure of aluminum oxide calculated by considering the activity data of aluminum (29) in the Ni-Al binary system were compiled in figure (7-19). The main features in this diagram are:

1 - At the Ni-rich side of the diagram, the equilibrium oxygen pressure changes drastically lower with increasing aluminum content in the alloy.

2 - The oxide of the baser metal, α-Al_2O_3, coexist practically over the whole compositional range of Ni-Al alloys.

3 - Spinel and/or nickel oxide coexist only with substantially pure nickel.

9.14 Equilibrium Oxygen Pressure Diagram for Fe-Al-O System At 1000°C

The dependence of the equilibrium oxygen pressures on the aluminum content of Fe-Al alloys is shown in figure (8-7). the equilibrium oxygen pressure over the coexistences hematite-spinel-aluminum oxide, wustite-spinel-iron, spinel-aluminum oxide-iron were determined at 1000°C in this investigation. The dissociation pressure of α-Al_2O_3 equilibrated with Fe-0.19 a/o Al alloy was measured at 940°C using cell (7-V). There is a steep drop in log P_{O_2} with aluminum alloy content at the iron

rich side of the diagram. Wustite and/or spinel are practically in equilibrium with pure iron since α-Al_2O_3 is nearly compatible with the alloys over their entire compositional range.

REFERENCES

1. C. Wagner, Corrosion Science, 9, 91 (1969).

2. J. S. Kirkaldy, Can. Met. Quart., 8, 35 (1969).

3. D. E. Coats and A. D. Dalvi, J. Oxidation of Metals 2, 331 (1970).

4. W. W. Smeltzer, Defects and Transport in Oxides, edited by M. S. Seltzer and R. I. Jaffee, Plenum Press, 475 (1974).

5. W. W. Smeltzer and D. P. Whittle, J. Electrochem. Soc., 125, 1116 (1978).

6. K. Kiukkola and C. Wagner, J. Electrochem. Soc., 104, 308 (1957).

7. K. Kiukkola and C. Wagner, J. Electrochem. Soc., 104, 379 (1957).

8. M. Hansen, Constitution of Binary Alloys, McGraw-Hill Book Company (1958).

9. R. P. Elliott, Constitution of Binary Alloys, First Supplement, McGraw-Hill Book Company (1965).

10. F. A. Shunk, Constitution of Binary Alloys, First Supplement, McGraw-Hill Book Company (1969).

11. D. P. Bogatskii, Zhur. Obshchei Khim., 21, 3 (1951), in Russian; Chem. Abstr., 46, 7861 (1952).

12. Emile Rutner and Gerald L. Haury, J. of Chem. Eng. Data., 19, 19 (1974).

13. B.C.H. Stale, Electromotive Measurements in High Temperature Systems, edited by C. B. Alcock, American Elsevier Publishing Co. Ltd. (1968).

14. H. Yanagida and F. A. Kroger, J. Am. Ceram. Soc., 51, 700 (1968).

15. M. Hock and H. L. Johnston, J. Am. Chem. Soc., 76, 2560 (1954).

16. E. Baur and R. Brunner, Z. Electrochem., 40, 154 (1934).

17. R. F. Porter et al., J. Chem. Phys., 23, 339 (1955).

18. L. Brewer and A. W. Searcy, J. Am. Chem. Soc., 73, 5408 (1951).

19. J. Browart et al., J. Chem. Phys., 32, 1366 (1960).

20. W. D. Treadwell and L. Terebesi, Helv. Chim. Acta, 16, 922 (1933).

21. D. Ghosh and D.A.R. Kay, J. Electrochem. Soc., 124, 1836 (1977).

22. N. S. Choudhury, J. Electrochem. Soc., 120, 1663 (1973).

23. V. Vlack, Materials Science for Engineers, Addison-Wesley, New York, 64 and 505 (1978).

24. R. W. Guard and J. H. Westbrook, Trans. AIME, 215, 871 (1959).

25. A. Taylor and N. J. Doyle, J. Apply. Cryst., 5, 201 (1972).

26. T. Hughes et al., J. Apply. Phys., 42, 3705 (1971).

27. A. Steiner and K. L. Komarek, Trans. AIME, 230, 786 (1964).

28. R. E. Hanneman and A. U. Seybolt, Trans. AIME, 245, 434 (1969).

29. S. C. Schaefer, Rep. No. 7993, USA Bureau of Mines (1975).

30. O. Kubaschewski, Trans. Faraday Soc., 54, 814 (1958).

31. B. Phillips et al., J. Am. Ceram. Soc., 46, 579 (1963).

32. Anne-Marie LeJus, Ph.D. Thesis, University of Paris (1964).

33. J. D. Tretjakow and H. Schmalzried, Berichte der Bunsengesellschaft, 69, 396 (1965).

34. K. T. Jacob and C. B. Alcock, J. Solid State Chem., 20, 79 (1977).

35. L. S. Darken and R. W. Gurry, J. Am. Chem. Soc., 67, 1398 (1945).

36. L. S. Darken and R. W. Gurry, J. Am. Chem. Soc., 68, 798 (1946).

37. H. G. Sockel and H. Schmalzried, Berichte Bunsengesellschaft, 72, 745 (1968).

38. P. Vallet and P. Raccah, Mem. Sc. Rev. Met., 62, 1 (1965).

39. H. F. Rizzo et al., J. Electrochem. Soc., 116, 266 (1969).

40. H. Davies, Ph.D. Thesis, McMaster University (1973).

41. P. Kofstas, Nonstoichiometry, Diffusion, and Electrical Conductivity in Binary Metal Oxides, Wiley-Interscience (1972).

42. P.E.C. Pryant and W. W. Smeltzer, J. Electrochem. Soc., 116, 1409 (1969).

43. A. J. Bradley and A. H. Jay, J. Iron Steel Inst., 125, 339 (1932).

44. R. G. Davies, Trans. AIME, 230, 903 (1964).

45. G. Lutjering and H. Warlimont, Acta Metall., 12, 1460 (1964).

46. J. Eldridge and K. L. Komarek, Trans. AIME, 230, 226 (1964).

47. S. V. Radcliffe et al., Acta Metall., 9, 169 (1961).

48. A. Muan, J. Am. Sci., 256, 413 (1958).

49. L. M. Atlas and W. K. Sumida, J. Am. Ceram. Soc., 41, 158 (1958).

50. J. C. Chan et al., Canad. Met. Quart., 12, 439 (1973).

51. T. N. Rezukhina et al., Russ. Jour. Phys. Chem., 37, 358 (1963).

52. T.C.M. Pillay et al., J. Am. Ceram. Soc., 43, 583 (1960).

53. C. J. Stournaras, Ph.D. Thesis, McMaster University (1977).

54. Ford Motor Co., Science, 154, 828 (1966).

55. G. A. Rankin and H. E. Merwin, J. Am. Chem. Soc., 38, 568 (1916).

56. L. T. Brownmiller and R. H. Bogue, J. Res. Nat. Bur. Std., 32, 289 (1932).

57. J. Gallup, J. Am. Ceram. Soc., 18, 144 (1935).

58. R. R. Ridgway et al., Trans. Electrochem. Soc. 70, 71 (1936).

59. C. A. Beevers and M.A.S. Ross, Z. Krist., 97, 59 (1937).

60. Y. Yao and J. T. Kummer, J. Onorg. Nucl. Chem., 29, 2453 (1967).

61. N. Weber and A. F. Benero, Presented at the Amer. Ceram. Meeting, Philadelphia, May (1970).

62. J. Thery and D. Briacon, Compt. Rend., 254, 2782 (1962).

63. R. C. DeVries and W. L. Roth, J. Am. Ceram. Soc., 52, 364 (1969).

64. C. N. Poulieff et al., Mat. Res. Bul., 13, 323 (1978).

65. Y. Le Cars et al., Compt. Rend. Acad. Sci., Paris, Series C, 274, 4 (1972).

66. J. T. Kummer, Progr. Solid State Chem., 7, 141 (1972).

67. D. J. Fray, Met. Trans. B, 8, 153 (1977).

68. E. W. Dewing, Special Communication.

69. H. Schmalzried and A. D. Pelten, Special Communication.

70. R. A. Rapp, Physiochemical Measurements in Metal Research, Part 2, Wiley-Interscience, New York (1978).

71. W. L. Worrel, Special Communication.

72. J. W. Patterson, J. Electrochem. Soc., 118, 1033 (1971).

73. P. Kofstad and D. J. Rucicka, J. Electrochem. Soc., 110, 181 (1963).

74. T. Mitsuhashi and Y. Fujiki, J. Am. Ceram. Soc., 56, 493 (1973).

75. B. C. Weber, J. Am. Ceram. Soc., 39, 197 (1956).

76. T. Y. Tien and E. C. Subbarao, J. Chem. Phys., 39, 1041 (1963).

77. P. Ducvez et al., J. Am. Ceram. Soc., 35, 107 (1952).

78. F. Hund, Z. Phys. Chem., 199, 142 (1952).

79. A. Cocco, Chemica Ind., Milano, 41, 882 (1959).

80. A. M. Diness and R. Roy, Solid State Commun., 3, 123 (1965).

81. R. E. Carter and W. L. Roth, "Electromotive force measurements in High Temperature Systems", ed. C. B. Alcock, American Elsevier Publishing Co. Ltd. (1968).

82. D. J. Poulton and W. W. Smeltzer, J. Electrochem. Soc., 117, 378 (1970).

83. D. L. Douglas and C. Wagner, J. Electrochem. Soc., 113, 671 (1966).

84. F. A. Kroger, J. Am. Ceram. Soc., 49, 215 (1966).

85. C. Wagner, Z. Physik. Chem., B21, 25 (1933).

86. C. B. Alcock and J. C. Chan, Can. Met. Quart., 11, 559 (1972).

87. M. Iwase and T. Mori, Met. Trans., 9B, 653 (1978).

88. C. R. Peters et al., Acta Cryst, B27, 1826 (1971).

89. N. M. H. Fallah, Master thesis, McMaster University (1977).

90. R. A. Rapp, Trans. AIME, 227, 371 (1963).

91. B.C.H. Steele and C.B. Alcock, Trans. AIME, 233, 1359 (1965).

92. G. G. Charette and S.J. Flengas, J. Electrochem. Soc., 115, 796 (1968).

93. J.W. Patterson et al., ibid, 114, 752 (1967).

94. R. Baker and J. M. West, J. Iron Steel Inst., 204, 212 (1966).

95. R. J. Fruehan et al., Trans. Met. Soc. AIME, 245, 1501 (1969).

96. W. L. Worrell, Thermodynamics, IAEA, Vienna, 1, 131 (1966).

97. H. Schmalzried, Proc. Int. Symp. Met. Chem., London, MNSO (1972).

98. C. M. Diaz and F. D. Richardson, Electromotive Force Measurements in High Temperature System, Pub. Inst. Mining and Met., p. 29 (1968).

99. T. A. Ramanarayanan and W. L. Worrell, Can. Met. Quart., 13, 325 (1974).

100. B. Porter and M. Feinleib, J. Electrochem. Soc., 103, 300 (1956).

101. R. Galli et al., Electrochim. Acta, 18, 1013 (1973).

102. J. H. Kennedy and A. F. Sammells, J. Electrochem. Soc., 119, 1609 (1972).

103. B. V. Joglekar, Master Thesis, McMaster University (1972).

104. J. Fally et al., J. Electrochem. Soc., 120, 1296 (1973).

105. G. G. Farrington, J. Electrochem. Soc., 123, 1213 (1976).

106. R. N. Powers, J. Electrochem. Soc., 122, 490 (1975).

107. R. N. Powers and S. P. Mitoff, J. Electrochem. Soc., 122, 226 (1975).

108. J. H. Kennedy and A. Foissy, J. Electrochem. Soc., 122, 482 (1975).

109. L. J. Miles and I. W. Jones, Proc. Brit. Ceram. Soc., 19, 179 (1971).

110. J. S. Lundsgaard and R. J. Brook, J. Mat. Sci., 8, 1519 (1973).

111. . L. Franciset al., Am. Ceram. Soc. Bull., 50, 615 (1971).

112. W. W. Liang and J. F. Elliott, J. Electrochem. Soc., 123, 617 (1976).

113. A.D. Morrison et al., J. Am. Ceram. Soc., 58, 41 (1975).

114. W. Byckalo et al., Am. Ceram. Soc. Bull., 55, 286 (1976).

115. M. River and A. D. Pelton, Am. Ceram. Soc. Bull., 57, 183 (1978).

116. A. Dalvi, Senior Editor, The Electron Probe Micro-Analyzer, a McMaster University Publication, Hamilton, Canada (1969).

117. E. D. Dewing, Met. Trans., 1, 1691 (1970).

118. JANAF Thermochemical Tables, Second Edition (1971).

119. J. F. Elliott and M. Gleiser, Thermochemistry for Steelmaking, Addison-Wesley Publishing Company, Inc., (1960).

120. E. W. Dewing, Met. [illegible]., 3, 495 (1972).

121. J. P. Hager and J. F. Elliott, Trans. Met. Soc. AIME, 239, 513 (1967).

122. T. Elkasabgy, Ph.D. Thesis, McMaster University (1978).